Elucidating Novel Regulators of Cytokinesis

Dissertation der Fakultät für Biologie

der Ludwig-Maximilians-Universität München

Sriyash Mangal

Delhi, 2019

Diese Dissertation wurde angefertigt
unter der Leitung von

Dr. Esther Zanin

im Bereich von
Fakultät für Biologie, Biozentrum
an der Ludwig-Maximilians-Universität München

Erstgutachter: Dr. Esther Zanin
Zweitgutachter: Prof. Christof Osman
Tag der Abgabe: 10.12.2019
Tag der mündlichen Prüfung: 05.06.2020

Erklärung

Ich versichere hiermit an Eides statt, dass meine Dissertation selbständig und ohne unerlaubte Hilfsmittel angefertigt worden ist. Die vorliegende Dissertation wurde weder ganz, noch teilweise bei einer anderen Prüfungskommission vorgelegt. Ich habe noch zu keinem früheren Zeitpunkt versucht, eine Dissertation einzureichen oder an einer Doktorprüfung teilzunehmen.

_____

Delhi, den 10 Dezember 2019

Sriyash Mangal

Declaration

I hereby declare that the research presented in this thesis was carried out by me and contributions of other people have been duly acknowledged within the text. The thesis has not been submitted or presented to any other examination board, either as a whole or in parts. The research described here has not been published except from that mentioned in the section “Publications originating from this thesis”.

_____

Delhi, 10th December 2019

Sriyash Mangal

Publications originating from this thesis

Mangal, S., Sacher, J., Kim, T., Osório, D.S., Motegi, F., Carvalho, A.X., Oegema, K., and Zanin, E. (2018). TPXL-1 activates Aurora A to clear contractile ring components from the polar cortex during cytokinesis. The Journal of Cell Biology *217*, 837–848.

Mangal, S., Zielich, J., Lambie, EJ., Zanin E. (2018). Rapamycin-induced protein dimerization as a tool for C. elegans research. microPublication Biology. https://doi.org/10.17912/W2BH3H.

Zeilich, J., Mangal, S., Zanin, E., Lambie, EJ. (2018). Establishment of a CRISPR/Cas9-based strategy for inducible protein dimerization. microPublication Biology. 10.17912/W2208R

Acknowledgements

I would like to thank my supervisor Dr. Esther Zanin for giving me the opportunity to work in her lab and sharing her wisdom, insight and expertise with me. Further, I want to thank my collaborators Dr. Marc Bickle, Dr. Martin Stoeter, and Cordula Andree for their contributions in conducting RNAi screen. Special thanks to Prof. Barbara Conradt for sharing her lab space and equipment and Thesis Advisory Committee members Prof. Marc Bramkamp, PD Dr. Annette Müller-Taubenberger, Dr. Marc Bickle for their insights and feedback.

I would like to thank my colleagues Jennifer, Fabian, Hai, Laura, Ryan, Anna, and Jeffrey for their valuable inputs, help and cooperation. Special thanks to my family for their patience and support.

Contents

List of Figures

List of Tables

Abbreviations

General abbreviations

SAC	Spindle assembly checkpoint
GAP	GTPase activating protein
GEF	Guanine Nucleotide Exchange Factor
GTP	Guanine tri-phosphate
GDP	Guanine di-phosphate
PBS	Poly-basic sequence
PH domain	Pleckstrin homology domain
RNAi	RNAi interference
siRNA	Short interfering RNA
RNA	Ribonucleic acid
HeLa	Cancer cell line from Henrietta Lacks
DMEM	Dulbecco's modified Eagle's medium
AZD	Aurora B inhibitor AZD1152-HQPA
MK5108	Aurora A inhibitor
DMSO	Dimethylsulfoxide
GFP	Green fluorescent protein
HCL	Hydrochloric acid
UV	Ultraviolet
TCA	Trichloroacetic acid
BSA	Bovine serum albumin
PBS	Phosphate buffer saline
DNA	Deoxyribonucleic acid
MosSCI	Mos1-mediated single-copy insertion
NEBD	Nuclear envelope breakdown
MTs	Microtubules
PCR	Polymerase chain reaction
FACS	Fluorescence activated cell sorting
GPCRs	G-protein coupled receptors

BSA	Bovine serum albumin
Da	Dalton
DIC	Differential interphase contrast microscopy
C. elegans	*Caenorhabditis elegans*
D. melanogaster	*Drosophila melanogaster*
E. coli	*Escherichia coli*
S. cerevisae	*Sacharomyces cerevisae*
X. laevis	*Xenopus laevis*
µl	Microlitre
ml	Millilitre
min	minutes
s	seconds
PAGE	Polyacrylamide gel electrophoresis
PBS (buffer)	Phosphate buffer saline
SDS	Sodium dodecyl sulphate
UTR	Untranslated region
WT	Wild type

Gene abbreviations

Gene Symbol	**Gene Name**	**Species**
ect-2	epithelial cell transforming 2	*H. sapiens*
RhoA	ras homolog family member A	*H. sapiens*
MgcRacGAP	Rac GTPase-Activating Protein	*H. sapiens*
Cyk-4	Cytokinesis defect 4	*C. elegans*
MKLP1 or *KIF23*	Mitotic Kinesin Like Protein 1	*H. sapiens*
Rac	Rac family small GTPase	*H. sapiens*
RhoB	ras homolog family member B	*H. sapiens*
RhoC	ras homolog family member C	*H. sapiens*
ROCK	Rho kinase	*H. sapiens*
MYPT	Myosin phosphate	*H. sapiens*
CPC	Chromosomal passenger complex	*H. sapiens*
INCENP	Inner centromere protein	*H. sapiens*
MP-GAP	Mitotic phase GTPase activating protein	*H. sapiens*
rga-3	Rho GTPase activating protein 3	*C. elegans*

rga-4	Rho GTPase activating protein 4	*C. elegans*
PRC1	Protein regulator of cytokinesis 1	*H. sapiens*
KIF4	Kinesin family member 4A	*H. sapiens*
PLK1	Polo like kinase 1	*H. sapiens*
PP1	Protein phosphatase 1	*H. sapiens*
CENP-E	Centromere protein E	*H. sapiens*
ESCRT-III	Endosomal Sorting Complex Required for Transport III	*H. sapiens*
Sept7	Septin 7	*H. sapiens*
PKN2	Protein Kinase N2	*H. sapiens*
NuMA	Nuclear mitotic apparatus	*H. sapiens*
FRB	FKBP12-rapamycin binding	*H. sapiens*
FKBP-12	FK506 binding protein	*H. sapiens*
BUB1B	Budding Uninhibited By Benzimidazoles 1B	*H. sapiens*
PLK4	Polo like kinase 4	*H. sapiens*
AURKA	Aurora A kinase	*H. sapiens*
AURKB	Aurora B kinase	*H. sapiens*
air-1	Aurora A kinase	*C. elegans*
Eg5/KIF11	Kinesin family member 11	*H. sapiens*
KIF2A	Kinesin family member 2A	*H. sapiens*
KIF18A	Kinesin family member 18A	*H. sapiens*
CKS2	CDC28 protein kinase regulatory subunit 2	*H. sapiens*
CRHR2	corticotropin releasing hormone receptor 2	*H. sapiens*
EIF3H	eukaryotic translation initiation factor 3H	*H. sapiens*
POLE3	DNA polymerase epsilon 3	*H. sapiens*
PTBP1	polypyrimidine tract binding protein 1	*H. sapiens*
DDX6	DEAD box helicase 6	*H. sapiens*
DGKG	diacylglycerol kinase gamma	*H. sapiens*
ETFA	electron-transfer-flavoprotein A	*H. sapiens*
FOXC1	forkhead box C1	*H. sapiens*
IHH	indian hedgehog	*H. sapiens*
PPP2CB	protein phosphatase 2, catalytic subunit beta	*H. sapiens*
PPP4C	protein phosphatase 4, catalytic subunit	*H. sapiens*
PRSS38	Serine protease 38	*H. sapiens*
SLC18A2	solute carrier family 18 member 2	*H. sapiens*

TCEA1	transcription elongation factor A1	*H. sapiens*
UBE2L3	Ubiquitin-conjugating enzyme E2L 3	*H. sapiens*
TPXL-1	Targeting protein for *Xenopus* Klp2-like	*C. elegans*
NMY-2	Non-muscle myosin II	*C. elegans*
HCP-4	CENPC like protein 4	*C. elegans*
mTOR	Mammalian target of rapamycin	*H. sapiens*

Abstract

Cytokinesis is the final event of cell division in which the mother cell splits into two daughter cells. During cytokinesis, the contractile ring is carefully positioned between the separating chromosomes by anaphase spindle. While the spindle midzone, located between segregating chromosomes, promotes the accumulation of contractile ring components at the equator, the centrosomal microtubule asters prevent the accumulation of contractile ring proteins at the cell poles. Despite rigorous research, the identity of aster derived inhibitory molecules(s) remains elusive and how cytokinesis regulators like Ect2 and RhoA are activated in a narrow equatorial zone is not properly understood. To identify novel regulators of this signalling pathway, high-throughput RNAi screen was performed in HeLa cells and cortical localization of contractile ring component GFP-tagged anillin was analyzed manually. In total, 7553 genes comprising druggable human genome were screened and 18 new genes were identified to play a role in regulating anillin localization at cell poles or equator. Among the 18 new candidate genes, Protein Kinase N2 (PKN2) and Septin 7 were the two most exciting candidates as they directly interact with RhoA and anillin, respectively and were further characterized. PKN2, a known RhoA effector, inhibited anillin localization on the cell poles whereas contractile ring component Septin 7 promoted anillin localization at the cell equator. Remarkably, the role of PKN2 and Septin7 in regulating anillin location during anaphase was found to be conserved in *C. elegans* one-cell embryos.

It was previously shown that TPXL-1 mediated activation of Aurora A during anaphase is required for clearing anillin from the anterior pole in *C. elegans* one-cell embryos. To investigate whether Aurora A plays a similar role in clearing other contractile ring proteins from the anterior pole, localization of f-actin was analysed in TPXL-1 depleted embryos using a f-actin binding probe LifeAct fused to mKate2. Similar to anillin, TPXL-1 was found to be involved in clearing f-actin from the anterior pole during anaphase and the clearing defect was confirmed not to be a consequence of altered microtubule dynamics. Moreover, ectopic localization of Aurora A at the cell cortex induced by inhibiting PP6, a phosphatase that negatively regulates Aurora A activation, led to a significant reduction in anillin localization at cell equator and poles. Consistent with the observations in *C. elegans*,

inhibition of Aurora A in HeLa cells by small molecular inhibitor MK-5108 resulted in increased accumulation of anillin on the polar cortex and a wider anillin zone at cell equator. Based on these findings, it is proposed that TPXL-1 activates Aurora A on the microtubule asters which diffuses to the adjacent cell poles and inhibits localization of contractile ring proteins. Finally, a rapamycin-inducible dimerization system was established in *C. elegans* using FRB and FKBP-12 domains of mTOR signaling pathways. In future, this protein dimerization tool can be used to target Aurora A and TPXL-1 to the plasma membrane and determine whether ectopic localization of TPXL-1 and Aurora A, without inhibiting PP6, can result in anillin localization defects. In summary, high-throughput RNAi screen revealed 18 new regulators of cytokinesis, two of which (Sept7 and PKN2) were further validated in HeLa cells and *C. elegans* one-cell embryos. In addition, Aurora A was shown to restrict the localization of contractile ring proteins to the cell equators in both the model systems.

1. Introduction

1.1 Cytokinesis in animal cells

Cell division is essential for reproduction and maintenance of living organisms. The cell cycle has two main phases, interphase and mitotic phase (or M-phase). During interphase, animal cells grow in size (G1 phase) and DNA is replicated (S-phase). In M-phase DNA is condensed into structures called chromosomes (Prophase) which are aligned at the center of the cell by the bipolar mitotic spindle (Metaphase; Figure 1). Once all the chromosomes are correctly attached to the spindle microtubules, spindle assembly checkpoint (SAC) is satisfied and sister chromatids separate along opposite poles of the mitotic spindle (Figure 1). This mitotic phase where chromosome segregation occurs is called anaphase. Finally, a cytokinetic furrow assembles at the cell equator between the segregated chromosomes which ingresses to divide the cell into two daughter cells (Figure 1). Thus, cytokinesis is the last phase of mitosis that partitions the contents of mother cell between two daughter cells. For successful cell division, it is essential that the cell contents including replicated genomic material, organelles and centrosomes are equally distributed between the two daughter cells. Thus, precise temporal and spatial regulation of cytokinesis is crucial for maintaining normal ploidy of the genome. Early constriction of the contractile ring before complete chromosome separation could damage the integrity of the genetic material resulting in aneuploidy. Similarly, failure of cytokinesis can lead to accumulation of tetraploid or polyploid cells which are genetically unstable and prone to oncogenic transformations (Davoli and de Lange, 2011; Dewhurst et al., 2014; Ganem et al., 2014). Defects in cytokinesis can also lead to other diseases such as Lowe Syndrome, female infertility, and Wiskott-Aldrich syndrome (Lacroix and Maddox, 2012). Another outcome of failed cell division is increase in number of centrosomes which can lead to formation of multipolar spindles, aneuploidy and development of extra cilia (Bettencourt-Dias et al., 2011).

To ensure equivalent inheritance of genetic material in the resulting daughter cells, contractile ring is assembled and constricted in response to active signalling between mitotic spindle and the cell cortex (Verma et al., 2019; Green et al., 2012). During anaphase, overlapping bundles of microtubules, referred to as spindle midzone, are formed between the segregating chromosomes (Figure 1). Ect2, a RhoA Guanine Nucleotide Exchange Factor (RhoA-GEF), is activated and recruited to the spindle midzone in a MgcRacGAP (Rac GTPase-Activating Protein) or CYK-4 (in *C. elegans*) dependent manner (Figure 2; Nishimura and Yonemura, 2006; Somers and Saint, 2003; Yüce et al., 2005; Zhao and Fang, 2005). MgcRacGAP/CYK-4 is a subunit of heteromeric complex called centralspindlin which localizes to the spindle midzone (Pavicic-Kaltenbrunner et al., 2007). The other subunit of centralspindlin is MKLP1 (Mitotic Kinesin Like Protein 1) and both the subunits are arranged in a heterotetrameric complex. Ect2 is then loaded to the plasma membrane where it activates the small GTPase RhoA, which in turn directs the assembly of contractile ring at the equatorial cortex comprising of actin and septin filaments, the cross-linker protein anillin and the motor protein myosin II (Figure 2 and 3A). In parallel to spindle midzone driven RhoA activation at the cell equator, inhibitory signal(s) from microtubule asters prevent the accumulation of active RhoA and contractile ring proteins at the cell poles (Bement et al., 2005; Foe and Dassow, 2008; Mangal et al., 2018; Murthy and Wadsworth, 2008; Werner et al., 2007; Zanin et al., 2013). As a result, assembly of the contractile ring is confined to the equatorial plane between the segregating chromosomes. Finally, the contractile ring constricts followed by membrane abscission leading to formation of two daughter cells.

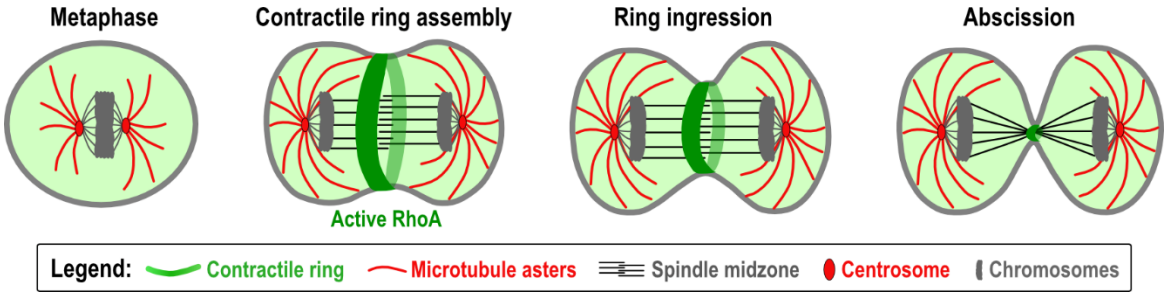

Figure 1: Schematic representation of cytokinesis in animal cells. During anaphase, chromosome segregation is followed by assembly and ingression of a contractile ring at the centre of the cell to ensure equal inheritance of the genetic material between the newly formed daughter cells. The connection between the two daughter cells is cleaved much later in in a process called abscission. Active RhoA, which localizes at the cell equator, directs the ring assembly and ingression.

1.2 RhoA directs contractile ring assembly

Human genome encodes twenty Rho GTPases but only RhoA, Cdc42 and Rac are intensively studied for their roles in cytokinesis (Haga and Ridley, 2016; Hodge and Ridley, 2016; Heasman and Ridley, 2008; Sit and Manser, 2011). Rho GTPases regulate cytoskeleton during many cellular processes like cell migration and adhesion, polarity establishment and cytokinesis (Heasman and Ridley, 2008; D'Avino et al., 2015; Jordan and Canman, 2012). RhoA, a small GTPase, is required for contractile ring assembly and constriction by regulating actomyosin contractility in many different model organisms and localizes to the site of furrow formation (Bement et al., 2005; 2006; Drechsel et al., 1997; Glotzer, 2004; Jantsch-Plunger et al., 2000; Kishi et al., 1993; Mabuchi et al., 1993; Prokopenko et al., 1999; Takaishi et al., 1995; Yonemura et al., 2004). RhoB and RhoC are closely related to RhoA but have roles other than in cytokinesis (Hakem et al., 2005; Liu Ax et al., 2001). Rho GTPases cycle between GTP and GDP bound states (Figure 2) which is regulated by GEF and GAP (GTPase-activating proteins) proteins. During cytokinesis, Ect2 GEF converts RhoA-GDP to active GTP-bound state by exchanging GDP molecule with GTP and MP-GAP (or RGA-3 and RGA-4 in *C. elegans*; Figure 2) accelerates conversion of RhoA-GTP back to inactive GDP-bound state by inducing the hydrolysis of GTP to GDP.

Upon conversion to GTP-bound state by Ect2 GEF, RhoA directs the assembly of contractile ring by promoting accumulation of the constituent proteins to the cell cortex (Figure 2). RhoA promotes actin nucleation and polymerization by activation of profilin and diaphanous-related formins, respectively (Castrillon and Wasserman, 1994; Evangelista et al., 2002; Severson et al., 2002; Watanabe et al., 2008). In addition, RhoA activates the motor protein myosin through Rho Kinase (ROCK), which directly phosphorylates myosin light chain and also inhibits its dephosphorylation by myosin phosphatase (MYPT). Besides actin and myosin, contractile ring also contains anillin and septins. Anillin interacts with actin, myosin, RhoA, and plasma membrane thereby acting as a cross-linker protein which stabilizes cleavage furrow (Sun et al., 2015; D'Avino et al., 2015; Gregory et al., 2008; Piekny and Glotzer, 2008; Piekny and Maddox, 2010). Thus, RhoA orchestrates both the formation of the cleavage furrow and its constriction, thereby playing a central role in cytokinetic signalling cascade.

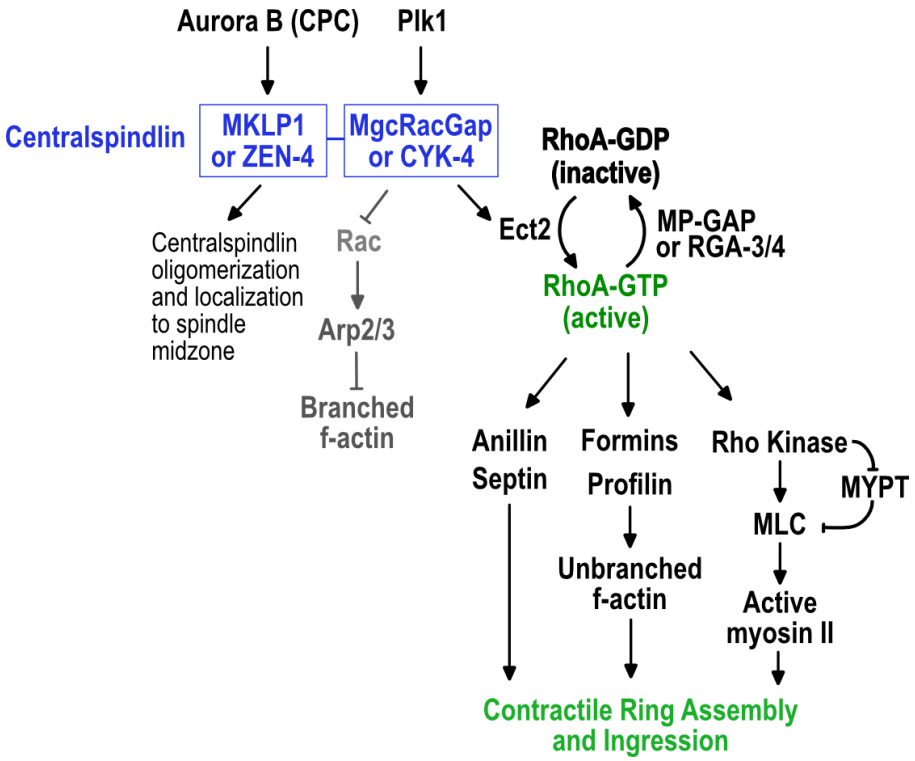

Figure 2: Cell signalling during cytokinesis. Aurora B of CPC phosphorylates centralspindlin subunit MKLP1 and releases 14-3-3 binding, thereby allowing oligomerization of centralspindlin and its stable recruitment to the spindle midzone. Plk1 phosphorylates centralspindlin subunit MgcRacGap which then recruits and activates Ect2 at the spindle midzone. Ect2 converts GDP-bound RhoA in to GTP-bound active form. RhoA activation is opposed by GTPase activating protein M phase GAP (MP-GAP) or RGA-3/4 (in *C. elegans*) which converts RhoA-GTP back to RhoA-GDP. Active RhoA directs the assembly and ingression of the contractile ring by triggering recruitment of anillin and septins to the cell cortex, promoting actin polymerization through formins and profilin, and activating motor protein myosin II through Rho kinase. GAP activity of CYK-4 inhibits Rac which supresses branching of f-actin filaments, thereby, supporting the assembly of the contractile ring.

1.3 Mitotic spindle positions the contractile ring

In animal cells, the position of contractile ring assembly is regulated by signalling between anaphase spindle and the cell cortex. As early as 1985, Raymond Rappaport, the godfather of cytokinesis, showed that changing the position of mitotic spindle induced regression of the old cleavage furrow and formation of new furrow near the midplane of displaced mitotic spindle in echinoderm eggs (Rappaport, 1985). According to the widely accepted hypothesis the spindle midzone promotes the accumulation of contractile ring proteins at the cell equator (equatorial simulation by midzone; Cao and Wang, 1996; Kawamura, 1977; Nishimura and Yonemura, 2006; Somers and Saint, 2003; Wheatley and Wang, 1996; Yüce et al., 2005;

Zhao and Fang, 2005) (Figure 3A), whereas dynamic microtubule asters (polar relaxation) or kinetochores provide inhibitory signals that prevent the accumulation of contractile ring proteins at the polar cortex (Bement et al., 2005; Foe and Dassow, 2008; Mangal et al., 2018; Murthy and Wadsworth, 2008; Rodrigues et al., 2015; Werner et al., 2007; Zanin et al., 2013; Zhou and Wang, 2008) (Figure 3C). In addition, a small subset of stable microtubules that extend all the way from the asters to the equatorial cortex are also thought to contribute stimulatory signals which promote cleavage furrow formation (equatorial simulation by astral microtubules; Canman et al., 2003; Foe and Dassow, 2008; Rappaport, 1961; Rieder et al., 1997; Verma and Maresca, 2019) (Figure 3B). The latter hypothesis was first proposed very early based on the experiments of Rappoport (Rappaport, 1961) and Reider (Rieder et al., 1997), who showed that two asters of independent spindles that are not connected by a spindle midzone induced formation of an ectopic furrow between them. Using advanced microscopy techniques, Verma et. al. have recently showed in *Drosophila* cells that centralspindlin and Aurora B kinase localize to plus-tips of equatorial microtubule asters which locally recruit Ect2 to the equatorial cortex and activate RhoA (Verma and Maresca, 2019), thereby providing the mechanistic insights for this emerging hypothesis. Aurora B kinase is a component of Chromosomal Passenger Complex (CPC) together with, INCENP (Inner Centromere Protein), Borealin and Survivin which phosphorylates MKLP1 of centralspindlin to induce its oligomerization and stable association with the plasma membrane (Basant et al., 2015; Douglas et al., 2010; Hu et al., 2008). Finally, polarity proteins have also been shown to specify the position of the contractile ring independent of the mitotic spindle in *Drosophila* neuroblasts (Cabernard et al., 2010) and *C. elegans* one-one cell embryos (Jordan et al., 2016).

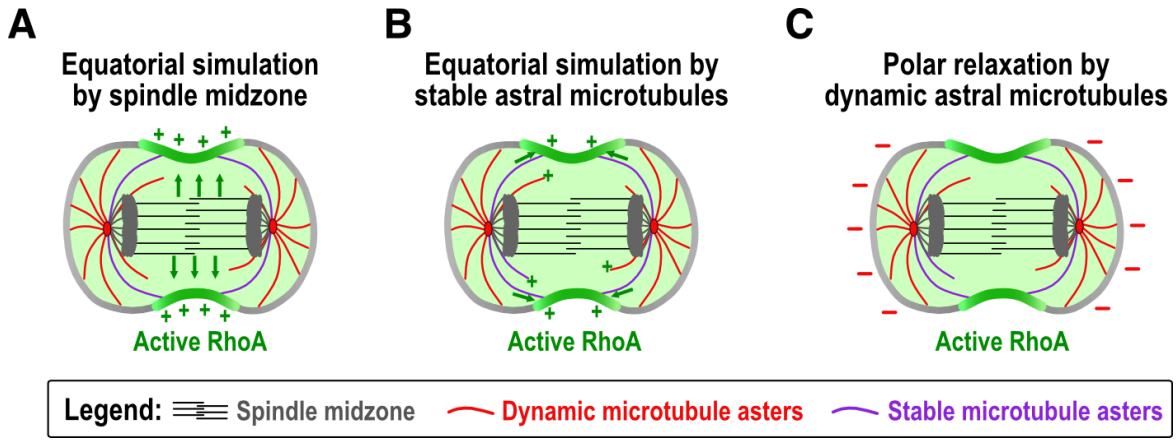

Figure 3: Models showing how mitotic spindle positions the cleavage furrow during cytokinesis. (A) Equatorial simulation by spindle midzone. Signals from the spindle

midzone promote accumulation of contractile ring proteins at the equatorial cortex. (**B**) **Equatorial simulation by stable astral microtubules.** A small number of stable microtubules from the asters, that reach equatorial cortex, carry stimulatory signals which promote contractile ring assembly and ingression. (**C**) **Polar relaxation by dynamic astral microtubules.** Astral microtubules provide inhibitory cues which prevent accumulation of contractile ring proteins on the polar cortex, thereby ensuring correct position for assembly of the contractile ring. (Adapted from Oegema and Mitchison, 1997)

1.4 Precise regulation of active RhoA flux is critical for cortical patterning during anaphase

Active RhoA invariably appears in a narrow zone at the site of contractile ring assembly during cell division across different model organisms and directs the assembly of contractile ring (Bement et al., 2005; Foe and Dassow, 2008; Murthy and Wadsworth, 2008; Rodrigues et al., 2015; Werner et al., 2007; Zanin et al., 2013; Zhou and Wang, 2008). Consistent with the notion that spindle and cortex communicate with each other, repositioning of spindle in sea urchin embryos led to translocation of zone of active RhoA followed by formation of a new cleavage furrow (Bement et al., 2005). In addition, theoretical modelling argues that maintenance of RhoA in a narrow equatorial zone also requires a balance between active and inactive state of RhoA (Bement et al., 2006). Since RhoA has very low rate of intrinsic GAP activity (Zhang et al., 2000), RhoA flux model proposed that maintaining a narrow zone of RhoA would be very difficult without a RhoA GAP. The identity of RhoA GAP, however, remained elusive for many years. In early days, the GAP domain of CYK-4 was proposed to be involved in inactivation of RhoA (Jantsch-Plunger et al., 2000; Miller and Bement, 2009). However, other reports argued that the CYK-4 GAP domain inhibits Rac and promots RhoA activation, and thus is required for successful cytokinesis (Bastos et al., 2012; Jantsch-Plunger et al., 2000; Kawashima et al., 2000; Touré et al., 1998; Canman et al., 2008; Loria et al., 2012; Miller and Bement, 2009; Yamada et al., 2006; Zavortink et al., 2005). Finally in 2013, Zanin and co-workers showed in a milestone publication that MP-GAP counteracts the activation of RhoA in human cells. Moreover, distantly related orthologs of MP-GAP in *C. elegans*, RGA-3 and RGA-4, were shown to similarly inactivate RhoA during first embryonic division (Schmutz et al., 2007; Schonegg et al., 2007; Zanin et al., 2013). MP-GAP inhibition (in HeLa cells and *C. elegans* one-cell embryo) led to ectopic membrane protrusions and hypercontractile cortex due to excessive active RhoA (Figure 4E; Zanin et al., 2013). Surprisingly, MP-GAP depletion in HeLa cells did not show broader equatorial localization of RhoA (Figure 4C). Earlier studies had recorded an increase in the equatorial zone width of

RhoA upon elimination of astral microtubules by nocodazole treatment (Figure 4D). Interestingly, when microtubule asters were eliminated by nocodazole reatment in MP-GAP depleted cells, RhoA localized all around the cortex and a zone of RhoA at the equator ceased to exist (Zanin et al., 2013; Figure 4E). Thus, in the absence of astral microtubules MP-GAP contributes in regulating the amount of active RhoA on the cell cortex.

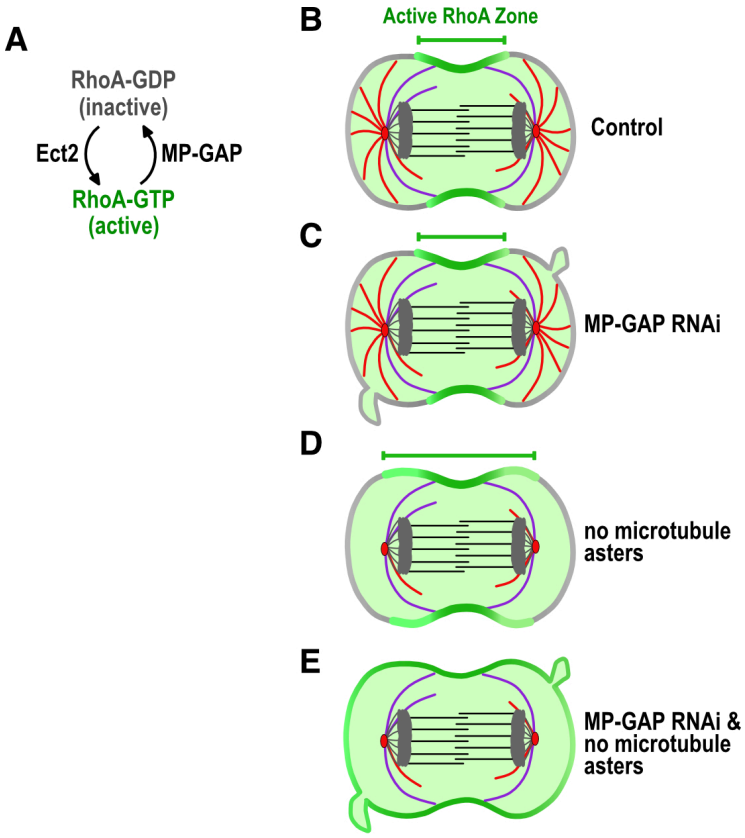

Figure 4: Flux of RhoA through the GTPase cycle is crucial for cortical patterning in anaphase. (**A**) RhoA activation is opposed by MP-GAP during anaphase in human cells. (**B**) Schematic representation of a wild type anaphase cell where active RhoA is confined to a narrow equatorial zone. (**C**) Depletion of MP-GAP leads to increased RhoA activation resulting in ectopic membrane protrusions but RhoA zone width is not altered. (**D**) Depolymerization of astral microtubules with low-dose nocodazole treatment results in broader zone of RhoA accumulation (**E**) Depletion of active RhoA in absence of microtubule asters results in membrane protrusions and broader zone of RhoA accumulation. Part of the figure scheme is adapted from Green et al., 2012; Based on findings of Zanin et. al., 2013.

1.5 Spindle midzone promotes the accumulation of contractile ring proteins

The array of anti-parallel overlapping microtubules that forms between the segregating chromosomes at anaphase onset is called spindle midzone or central spindle. Their minus end is oriented towards the cell poles and the plus ends are interdigitated at the centre of the array (Euteneuer and McIntosh, 1980). Formation of spindle midzone requires microtubule cross-linker protein PRC1 (Protein Regulator Of Cytokinesis 1), two kinesins – KIF4A (Kinesin Family Member 4A) and MKLP1, and kinase activity of Plk1 (Polo like kinase 1) and CPC (Glotzer, 2009). PRC1 cross-links antiparallel microtubules enabling them to assemble as a bundle (Bieling et al., 2010; Gaillard et al., 2008; Janson et al., 2007; Loïodice et al., 2005). PRC1 is also required to recruit KIF4A at the site of microtubule overlap where KIF4A supresses the growth of microtubule plus ends, thereby confining the zone of overlapping microtubules within the central spindle (Bieling et al., 2010; Kurasawa et al., 2004; Zhu and Jiang, 2005). KIF4A inhibition leads to wider spindle midzone with longer zone of overlapping microtubules. As a result, midzone microtubules fail to align properly and RhoA accumulates in a broader zone at the cell equator (Hu et al., 2011; Kurasawa et al., 2004; Zhu and Jiang, 2005). PRC1 depletion in human cells and *C. elegans* one-cell embryos disrupts spindle midzone but does not prevent successful cytokinesis (Mollinari et al., 2005; Verbrugghe and White, 2004). Inhibition of CPC in human cells (Zhu et al., 2005), *Drosophila* (Giet and Glover, 2001) and *C. elegans* (Severson et al., 2000; Lewellyn et al., 2010; Speliotes et al., 2000) inhibits cytokinetic furrow ingression ultimately resulting in failed division. Similarly, depleting components of centralspindlin (MKLP1 or CYK-4) in human cells (Zhu et al., 2005) or *C. elegans* (Severson et al., 2000; Jantsch-Plunger et al., 2000; Canman et al., 2008; Severson et al., 2000; Lewellyn et al., 2010; Powers et al., 1998; Raich et al., 1998) also inhibits the furrow ingression leading to failure of cytokinesis. Inhibition of Plk1 prevents elongation of spindle midzone, contractile ring assembly and ring ingression leading to failure fo cytokinesis (Brennan et al., 2007; Burkard et al., 2007; Petronczki et al., 2007).

Constitutive phosphorylation of centralspindlin leads to its sequestration by 14-3-3 protein. CPC phosphorylates MKLP1 of centralspindlin and releases 14-3-3 binding (Figure 2), thereby allowing multimerization of centralspindlin and its stable recruitment to the spindle midzone (Douglas et al., 2010; Giet and Glover, 2001; Guse et al., 2005; Hauf et al., 2003; Hu et al., 2008; Kaitna et al., 2000; Severson et al., 2000; Verbrugghe and White, 2004; Zhu

et al., 2005). Once centralspindlin complex localizes to the spindle midzone, Plk1 phosphorylates midzone localized substrates, primarily PRC1 and MKLP2 (Neef et al., 2007; 2003) to promote its own localization to the spindle midzone. In addition, Plk1 phosphorylates centralspindlin's CYK-4 subunit on the N-terminus (Burkard et al., 2009; Wolfe et al., 2009) which then binds and recruits RhoA-GEF Ect2 to the spindle midzone (Figure 2). This binding relieves autoinhibition of Ect2 by its BRCT domains and Ect2 is loaded on the adjoining cell membrane where it activates RhoA and triggers contractile ring formation (Burkard et al., 2009; Chalamalasetty et al., 2006; Tatsumoto et al., 1999; Wolfe et al., 2009). In human cells, Ect2 associates with plasma membrane with the poly-basic sequence (PBS) and Pleckstrin homology (PH) domain (Kotýnková et al., 2016; Su et al., 2011) and in *C. elegans* C-terminus of Ect2 has been shown to be important for membrane binding (Chan and Nance, 2013). Recently, this widely accepted hypothesis was questioned by Kotýnková et al. as they showed that Ect2 binding to CYK-4 and subsequent recruitment to the spindle midzone is dispensable for contractile ring assembly and constriction (Kotýnková et al., 2016). Instead, they showed that Ect2 can localize to plasma membrane without interacting with CYK-4 and this membrane-bound pool of Ect2 is critical for successful cytokinesis. Consistent with this finding, Ect2 homologs in *Drosophila* and *C. elegans* localize to the plasma membrane but not on the spindle midzone (Motegi and Sugimoto, 2006; Prokopenko et al., 1999). Nevertheless, spindle midzone plays an important role in cytokinesis (Glotzer, 2005) and there is substantial evidence which shows that spindle midzone provides a diffusible stimulatory signal, Ect2, which triggers the formation of contractile ring (Cao and Wang, 1996; Kawamura, 1977; Nishimura and Yonemura, 2006; Somers and Saint, 2003; Wheatley and Wang, 1996; Yüce et al., 2005; Zhao and Fang, 2005). The molecular mechanism of how active Ect2 is loaded on the equatorial membrane is yet not properly understood and continues to be an area of active research.

1.6 Astral microtubules confine contractile ring proteins to the cell equator

While the spindle midzone provides stimulatory signals for contractile ring assembly, simultaneous inhibitory signals from microtubule asters have been proposed to prevent the accumulation of contractile ring proteins on the polar cortex. In addition, one recent study has implicated a role of kinetochores in clearing contractile ring proteins from the cell poles. It was shown that, as the chromosomes move close to the polar cortex during anaphase, kinetochore-localized protein phosphatase 1 (PP1) promotes removal of filamentous actin

from the polar cortex in *Drosophila* and cultured human cells (Rodrigues et al., 2015). However, this seems not to be the case in *C. elegans* early embryos which are much bigger in size and anaphase kinetochores are farther away from the polar cortex (Mangal et al., 2018). Besides, there is accumulating evidence from different model systems, which supports the notion that microtubule asters indeed inhibit contractility at the cell poles. For instance, selective elimination of dynamic astral microtubule through laser ablation or drug treatments led to broader zone of active RhoA in sea urchin embryos (Dassow, 2009; Foe and Dassow, 2008), *X. laevis* (Bement et al., 2005) and mammalian cells (Murthy and Wadsworth, 2008; Zanin et al., 2013) (Figure 5A-C). Similarly, laser ablation of one centrosome aster in sea urchin embryos shifted the zone of active RhoA towards the ablated centrosome (Dassow, 2009) (Figure 5D). Notably, the wider RhoA zone observed in the absence of asters was not caused by an increase in the total amount of active RhoA. Thereby, suggesting that asters modulate the distribution of active RhoA or contractile signals rather than generating them (Lewellyn et al., 2010). Further support for this notion came from *C. elegans* embryos and grasshopper spermatocytes. In *C. elegans*, artificial displacement of the mitotic spindle to the posterior side of the embryo prevented myosin accumulation on the posterior side and restricted myosin localization to the anterior cortex (Werner et al., 2007). Similar positioning of asters on one side of the grasshopper spermatocytes resulted in cortical accumulation of actin on the opposite side of the cell (Chen et al., 2008). Furthermore, Lewellyn et. al (2010) revealed that cleavage furrow formation in *C. elegans* embryos is inhibited when centrosomal asters are positioned too close together regardless of the normal spindle midzone. Similarly, studies in anucleate cells have shown that contractile ring can only form when the intra-centrosomal distance is smaller than the distance between centrosome and the cortex (Canman, 2009; Dassow, 2009). In conclusion, dynamic microtubule asters corral active RhoA in a narrow zone at the cell equator thereby playing a key role in accurately positioning the contractile ring. In spite of plentiful evidence for aster-based inhibitory signal, the molecular identity of such signal remains to be unknown.

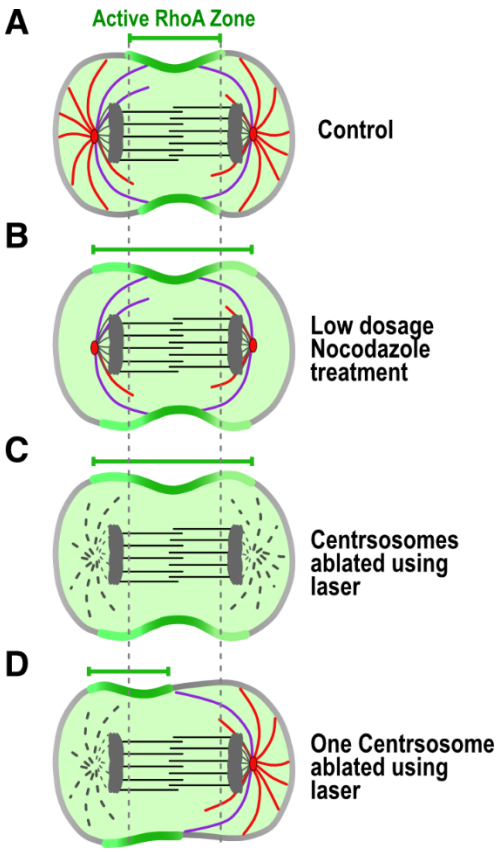

Figure 5: Microtubule asters confine contractile signals to the cell equator. (**A**) Schematic representation of a wild type anaphase cell in which accumulation of active RhoA is confined to a narrow equatorial zone by signals from microtubule asters. (**B**) Upon selective disassembly of dynamic astral microtubules by treatment with drugs such as Nocodazole, zone of active RhoA broadens. (**C**) Similarly, disassembly of asters by laser ablation of both centrosomes leads to wider zone of RhoA accumulation and (**D**) laser ablation of one centrosome displaces the zone of active RhoA towards the pole having ablated centrosome. The figure scheme is adapted from Green et al., 2012.

1.7 Contractile ring ingression and abscission

After the contractile ring assembles in the correct position, the ring must completely constrict and two daughter cells must separate from each other by a process called abscission. Structurally, contractile ring is composed of actin filaments, anillin, filaments of motor myosin II and septin filaments (Green et al., 2012). In different model systems, the contractile ring has been observed to be 0.1-0.2 µm thin but the ring width is variable between less than a micron to approximately 20 µm (Kamasaki et al., 2007; Schroeder, 1990). To initiate cleavage furrow formation, contractile ring should be linked to the plasma membrane. Since anillin binds to all three contractile ring components – actin, septin and myosin II and bears membrane binding PH domain, anillin seems to stabilize and link the

contractile ring with the plasma membrane (D'Avino et al., 2015; Gregory et al., 2008; Piekny and Glotzer, 2008; Piekny and Maddox, 2010). The contractile ring ingression is induced by RhoA by activating motor protein myosin II through ROCK (D'Avino et al., 2015) and interestingly, the ring constricts at similar rates across different model organisms (Biron et al., 2005; Calvert et al., 2011; Carvalho et al., 2009; Ma et al., 2012; Zumdieck et al., 2007). It is assumed that the force required for constriction of the contractile ring is generated by sliding of myosin filaments over actin filaments, just like in muscles (Biron et al., 2005). However, the organization of actomyosin filaments in sarcomere-like arrays (similar to muscles) has not been reproducibly observed in electron micrographs of different model systems (Green et al., 2012). Moreover, it was shown in COS-7 cells that myosin II filaments incapable of sliding over actin filaments could ingress cytokinetic furrow in absence of endogenous myosin II (Ma et al., 2012). Thus, the dynamins of contractile ring ingression is not entirely clear.

As the contractile ring constricts, the overlapping microtubules of spindle midzone get tightly packed which prevents further ingression of the contractile ring. In addition, the contractile ring cannot simply cut through the plasma membrane since it is positioned underneath the membrane. Thus, the cells reach a point where the ring cannot constrict any further, leaving the two daughter cells connected by an intracellular bridge. This intracellular bridge is wider (~1.5 μm) at the centre as compared to the two much narrower outer flanks (~0.2 μm) and is referred to as midbody. Thus, the midbody originates from the spindle midzone. During furrow ingression, spindle midzone proteins are relocated to three distinct regions of maturing midbody in Plk1 dependent manner (Hu et al., 2012). KIF4A and PRC1 stay in the microtubule overlap region of the midbody core, Ect2 and centralspindlin translocate to the midbody ring to colocalize with RhoA and anillin, and MKLP2, CENP-E (Centromere Protein E) and Aurora B concentrate in the two flanking regions of midbody (Hu et al., 2012). Similar to its role in stabilizing contractile ring, anillin is also required for midbody ring assembly and its stable attachment to cell membrane (Kechad et al., 2012; Somma et al., 2002). The two flanking regions of the midbody core serve as the docking and cleavage sites for the Endosomal Sorting Complex Required for Transport III (ESCRT-III). At the end of mitosis, Plk1 and Aurora B are degraded which allows ESCRT-III to finally cut the intracellular bridge giving rise to two completely separated daughter cells (Green et al., 2012). ESCRT complexes also play important roles in other processes which also involve membrane scission like viral budding and formation of multivesicular bodies (Schmidt and Teis, 2012).

1.8 Gaps in current understanding of cytokinesis

Despite decades of research, precise regulation of cortical patterning during cytokinesis remains inadequately understood (Figure 6). For instance, how Ect2 is loaded on the cell membrane and how its activity is controlled to activate RhoA only at the equatorial membrane is not clear yet. Furthermore, the molecular identity of aster derived inhibitory signal(s), which prevent RhoA accumulation outside equatorial plane, remains to be identified. These gaps in the current knowledge may be attributed to the missing regulators of cytokinesis that have not been identified yet.

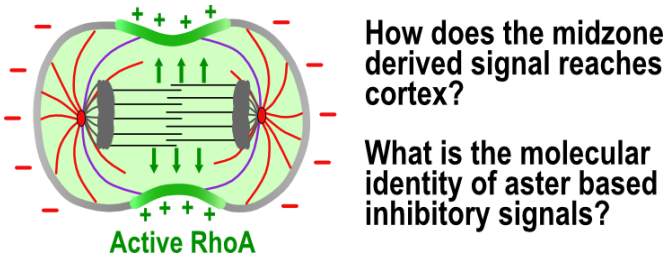

Figure 6: Major gaps in the current understanding of cytokinesis. Schematic showing stimulatory and inhibitory signalling by mitotic spindle and highlights the gaps in our present knowledge of cortical patterning during cytokinesis.

In the past, several genome-wide RNAi screens have been conducted in human cells (Kittler et al., 2007; 2004; Mukherji et al., 2006; Neumann et al., 2006; 2010), *Drosophila* (Eggert et al., 2004) and *C. elegans* (Sönnichsen et al., 2005) to identify regulators of cell division. The human and *Drosophila* studies had wider focus on different aspects of cell division. To find genes involved in regulation of cytokinesis, binucleated and multinucleated cells were counted in these studies. For instance, genome-wide RNAi screen in HeLa cells carried out by Kittler et. al. (2007), employed laser scanning cytometry to assess any changes in the genome ploidy upon gene silencing. Similarly, the screen performed in *Drosophila* cells exclusively relied on multinucleation assay to identify cytokinesis regulators after inhibiting the function of genes by RNAi interference (RNAi) or treatment with chemical compounds (Eggert et al., 2004). Importantly, altering cortical contractility does not always result in cytokinesis failure. For example, depletion of MP-GAP, which opposes RhoA activation, leads to formation of large ectopic protrusions due to uncontrolled RhoA activity but does not prevent furrow ingression (Zanin et al., 2013). As a result, MP-GAP was not identified in any of the above mentioned screens. A more sophisticated screen conducted by Mitocheck consortium scored phenotypes such as cell division, survival and migration by time-lapse

imaging of fluorescently labelled chromsosomes in human cells after RNAi treatment (Neumann et al., 2006; 2010). However in none of the screens, a contractile ring marker such as RhoA or anillin was used to directly analyse contractile ring assembly and localization of contractile ring proteins during anaphase. Therefore, it is highly probable that crucial regulators of cytokinesis were missed in the previous studies due to their experimental design and wider focus on cell division.

2. Aim

The current gaps in the knowledge of cytokinesis can be attributed to unidentified signalling molecules of the stimulatory and inhibitory pathways that regulate contractile ring assembly. Although previous genetic screens have discovered important regulators of cytokinesis (Eggert et al., 2004; Kittler et al., 2004; 2007; Mukherji et al., 2006; Neumann et al., 2006; 2010; Sönnichsen et al., 2005), they may have missed regulators due to their experimental design. The aim of my doctoral research was to identify new regulators of cortical patterning during cytokinesis. To this end, I carried out a high-content RNAi screen in human cells in collaboration with Dr. Marc Bickle and Dr. Martin Stoeter of the Screening Facility at the Max Planck Institute of Molecular Cell Biology and Genetics (MPI-CBG) in Dresden, Germany. Their contributions in the project are clearly marked in the text. We screened a set of 7,553 genes which comprises the druggable human genome library. In our high-content RNAi screen, novel regulators of cytokinesis that promote or inhibit cortical accumulation of contractile ring protein anillin were identified by cortex-wide analysis of changes in anillin localization (Figure 10A) after knocking down expression of each gene in the library.

Previous Work of my thesis advisor Dr. Esther Zanin suggested a role of the kinase Aurora A in clearing anillin from the polar cortex in *C. elegans* one-cell embryos. Therefore, I aimed to investigate the similar involvement of Aurora A in polar clearing of another contractile ring protein f-actin. Since Aurora-A activity was supressed by depleting TPXL-1, I also measured the affects of *tpxl-1(RNAi)* on microtubule growth and dynamics in *C. elegans* one-cell embryos. Finally, I investigated whether the function of Aurora A in restricting localization of anillin on the cell poles is conserved in human cells.

3. Material and Methods

3.1 Screening Methodology for high-content screen in HeLa cells

3.1.1 Transfection of siRNAs

Four different siRNAs targeting each gene were pooled together from Dharmacon ON-TARGETplus human druggable-genome library using Biomek FXp (Beckman) liquid handling robot. To prepare the transfection mix, 5µl of 100nM control and gene specific siRNAs were transferred to 384-well µClear plates using Tecan 384-head liquid handling robot and 5µl Opti-MEM containing 0.05µl transfection reagent INTERFERin was added. HeLa cells expressing anillin-GFP and mKate2-α-tubulin were trypsinized and re-suspended in DMEM supplemented with 10% FBS, 1% Penicillin/Streptomycin. The number of cells in the suspension was measured using the CASY Cell Counter. The cell suspension was diluted to 62,500 cells/ml and 40µl of this solution containing 2,500 cells was added to the wells having transfection mix using Multidrop Combi dispenser (Thermo Fischer Scientific).

3.1.2 Cell cycle synchronization and Fixation

Cell cycle was synchronized with two consecutive thymidine blocks followed by transient MG132 arrest to increase the number of anaphase cells. Twenty-four hours after the transfection, cells were incubated with 0.5mM thymidine for 16 hours, released for 8 hours by washing out thymidine and treated again with 0.5mM thymidine for 16 hours. Thymidine was again washed off and cells were allowed to continue in cell cycle for 7.5 hours. Finally, 5µM MG132 was added for two hours to allow accumulation of metaphase cells. MG132 was washed off and cells were released for 110 mins followed by fixation with 4% formaldehyde for 20 mins at room temperature using Matrix WellMate liquid dispenser (Thermo Scientific). To wash out thymidine and MG132, culture medium was exchanged with fresh pre-warmed medium (DMEM with 10% FBS and 1% Pen-Strep) four and five times respectively using Tecan 384 liquid handling robot which was optimized to prevent washing away of loosely attached mitotic cells. After fixation, formaldehyde was removed by 4

washes with 1x PBS using Tecan 96-head liquid handling robot integrated with PowerWasher 384. Finally, 1x PBS containing 1.5µg/ml DAPI and 0.02% sodium azide was added to stain DNA and prevent microbial growth.

3.1.3 Drug Treatments

Plk1 inhibition and elimination of astral microtubules are known to alter the anillin localization during anaphase. Therefore, these two treatments were also included as additional controls. For Plk1 inhibition, 100nM BI2536 was added 40 mins before fixation and to depolymerize astral microtubules during anaphase 70nM nocodazole was added 10 mins before fixation.

3.2 Cell Culture Techniques

3.2.1 Maintenance and freezing of HeLa cell lines

HeLa cell lines used in this study are listed in Table 5 (Section 3). Cells were grown at 37°C with 5% CO2 in high-glucose Dulbecco's modified Eagle's medium (DMEM) supplemented with 10% superior fetal bovine serum and 1% Penicillin/Streptomycin. The expression of the transgenes was induced by addition of 0.2 µg/mL tetracycline 24-48hrs before starting the experiments. For freezing HeLa cell lines, cells were grown in T75 cell culture flask to 90% confluency. After trypsinization, cells were re-suspended in fresh medium and centrifuged at 1000 rpm for 5 mins. The cell pellet was re-suspended in 4ml 1x freezing solution and frozen as 1ml aliquots in cryotubes at -80°C and in liquid nitrogen tanks.

3.2.2 siRNA transfection and drug treatments

To deplete endogenous proteins by RNAi, gene specific siRNA was diluted in 200 µl Opti-MEM and 2 µl of the transfection reagent INTERFERin was added. Volume of siRNA was calculated according to the required final concentration in 1 ml volume. After 15 mins of incubation of transfection mix at room temperature, the 200 µl transfection mix was added to each well (of 12-well plate or 2 well imaging chambers) having freshly seeded cells in 800 µl of the culture medium. To deplete NuMA by RNAi, Lipofectamine RNAiMAX transfection reagent was used according to the manufacturer's instructions. In all cases, control cells were similarly treated with an equivalent concentration of the non-targeting siRNA. Cell cycle was synchronized with a double thymidine block as described in section 3.1.2 and the cells were either fixed or imaged live 8 hours after the release from second thymidine block. To inhibit

Aurora A activity, MK-5108 was added to a final concentration of 10 µM just prior to filming; ~60% of treated cells arrested in mitosis and ~40% went into anaphase. Cortical anillin distribution was measured in cells that entered anaphase between 25-60 mins after MK-5108 addition. To inhibit Aurora B activity, AZD1152-HQPA was added to a final concentration of 200nM; ~30% of the cells arrested in mitosis and 70% entered anaphase. Cortical anillin distribution was measured in cells that entered anaphase between 2 and 3hrs after AZD addition. For pH3(Ser28) and pLATS2(Ser83) staining to assess the efficiency and specificity of the inhibitor treatments, cells were treated with 10µM MK-5108 for 30 or 60min and with 200nM AZD for 2 or 3hrs. To investigate the localization of endogenous anillin in fixed samples after Aurora A inhibition, the cell cycle was synchronized with a double thymidine block to increase the number of anaphase cells and 10µM MK-5108 was added 30 or 45min before fixation. To depolymerize astral microtubules during anaphase, 70nM nocodazole was added 10min before fixation. Stocks of 10mM MK-5180, 10mM AZD and 1mg/ml nocodazole were prepared in DMSO and a 100mM stock of thymidine was made in 1xPBS. Control cells were treated with an equivalent concentration of DMSO.

3.2.3 Generation of stable cell lines

To establish a cell line expressing anillin-GFP and mKate2-α-tubulin, previously described BAC-integrated mouse anillin-GFP cell line (Zanin et al., 2013) was transfected with a plasmid encoding mKate2-α-tubulin (Section 3.4) using X-tremeGENE 9 (by following manufacturer's instructions). Stable integrants were selected by treatment with blasticidin and single clones were isolated by fluorescence-activated cell sorting (FACS). Cell lines expressing RNAi resistant mNeonGreen PKN2 and Septin-7 (Section 3.4) were generated by co-transfecting HeLa Flp-In TRex host cell line, which expresses Tet repressor and has FRT integration site, with Flp recombinase expression plasmid pOG44 and pcDNA5/FRT/TO vector containing either PKN2 or Septin7 cDNA. Clones having stable integration of the transgene were selected by treatment with 300 µg/µl hygromycin for 7-10 days.

3.2.4 Immunofluorescence

For immunostainings, HeLa cells were grown on 12mm round glass coverslips (Roth, P233.1) coated with poly-L-lysine. For coating, glass coverslips were washed in 1M HCL at 50-60^{o}C for 5 hours, cooled down to room temperature and rinsed in distilled water 5 times. Coverslips were then rinsed in absolute ethanol and dried between two sheets of whatman paper. These cleaned coverslips were incubated with 15 ml of 1 mg/ml poly-L-lysine solution in a 50 ml tube for 1 hour with gentle rocking. Then, coverslips were washed 5 times in

distilled water and rinsed with absolute ethanol. Coverslips were dried between two sheets of whatman paper and sterilized by UV light in cell culture hood for 1 hour. Prior to fixation, cells were washed once in 1x PBS. To stain phosphorylated myosin light chain (pMLCser19), histone H3 (pH3Ser28) and LATS2 (pLATS2Ser83) cells were fixed with 4% formaldehyde (Thermo Scientific #28908; dilute to 4% in 1xPBS) for 20min at room temperature. To stain anillin, Septin-7, PKN2 and Plk-1 cells were fixed with -20°C-cold 100% methanol for 5min. To stain RhoA, cells were fixed with ice-cold 10% TCA for 15min on ice and washed three times wit 1x PBS containing 30mM Glycine. As a next step in all cases, cells were washed with 1x PBS buffer and permeabilized with 1x PBS buffer containing 0.1% Triton X-100 (PBST) for 2min followed by 1hr blocking with 4% BSA-PBST. Samples were incubated with desired primary antibodies listed in Table 11 (Section 3) overnight at 4°C. Coverslips were washed 3x in 1x PBST and secondary antibodies (Thermo Fischer) were incubated with Hoechst 33258 (Sigma) for 1hr at room temperature. Coverslips were washed 3x in PBST buffer and covered by mounting medium (see Table 14 in Section 3).

3.2.5 Image Quantification

a. Cortical localization of anillin and myosin

Unprocessed raw images were used for all quantifications in Fiji (Schindelin et al., 2012). To measure anillin or myosin accumulation in human cells a line was drawn around the entire cell cortex in Fiji (called a linescan) and pixel intensities along the line were recorded (Figure 10A). After subtracting the cytoplasmic anillin fluorescence intensity from each value, the mean polar (0-10%, 40-60%, 90-100% cell length) and equatorial (20-30%, 70-80%) fluorescent intensity was calculated for each cell. The anillin zone width was defined as the width of peak at half maximum anillin fluorescence intensity (Figure 18A). Mean fluorescence intensities at the equatorial and polar cortex, and the mean zone width were calculated using data analysis software Knime (Section 3.9) (http://www.knime.org).

b. Spindle midzone length

To measure the spindle midzone length, a 15-pixel wide line was drawn across the anillin-GFP channel and the distance between the two minima of the fluorescent intensity was defined as midzone length (Figure 38G). In fixed cells, length of the spindle midzone was measured by a linescan drawn across the Hoechst (DNA) channel and the distance between the two maxima was defined as spindle midzone length (Figure 18B). The data was analyzed in Knime.

c. Fluorescence intensity of pH3 and pLATS2

The mean centrosomal pLATS2(Ser83) intensity was measured in a circular region centered at the centrosome (Figure 37C). The pH3(Ser28) fluorescent intensity was calculated by drawing a region around the chromosome mass in the Hoechst channel and measuring in the pH3 channel (Figure 37D). The mean cytoplasmic signal measured in a small box was subtracted from the pLATS2(Ser83) and pH3(Ser28) fluorescence intensity. Data analysis was performed in Excel.

3.3 *C. elegans* Techniques

3.3.1 Maintenance and freezing worm strains

C. elegans strains used in this study are listed in Table 6 (Section 3). Strains were grown on NGM plates having a thin lawn of OP50 *E. coli* at 20°C according to the standard procedures (Stiernagle, 2006). Two strains, OD314 and ZAN43, were maintained at 23°C or 25°C due to silencing of the GFP-anillin transgene at lower temperatures. To freeze *C. elegans* strains, 10 L4 stage worms were transferred to four medium NGM plates and grown until the plates were starved of the bacterial food source. These plates mainly having larvae were washed with 3.5ml M9 buffer and collected in a 15ml tube. Equal volume of 2x freezing solution was added to the tube, mixed and aliquoted in 5 cryotubes. The tubes were stored at -80°C.

3.3.2 Generation of strains by MosSCI

Single-copy transgenes were integrated at specific chromosomal loci using the Mos1 mediated single copy gene insertion (MosSCI) method (Frøkjær-Jensen et al., 2008). To obtain single-copy insertions on chromosome II or IV, young EG6699 or EG8081 adults were injected with pCFJ350 plasmid containing the desired transgene (listed in Table 10 in Section 3) together with plasmids encoding co-injection markers (pMA122, pGH8, pCFJ190, pCFJ104) and the transposase (pCFJ601). Heat shock was performed at 34°C for 1hr after 7-10 days, and surviving worms were screened for the absence of the mCherry-tagged array markers. The worms thus identified to have stably integrated transgene were singled on fresh NGM plates and F1 progenies were screened for homozygosity marked by complete absence of progenies showing *unc* phenotype.

3.3.3 dsRNA production, RNAi and Lethality assay

To generate dsRNAs, the targeting region was amplified from *C. elegans* cDNA or genomic DNA with the primers containing T7 promoter sequence listed in Table 9 (Section 3). PCR products were purified and used as template for transcribing dsRNA in vitro with T7 RNA polymerase using MEGAscript Kit as per manufacturer's instruction. dsRNA was purified using the MEGAclear Kit by following the manufacture's instruction. Purified dsRNA was injected in to the gut of young adults and their embryos were filmed after 24-28 hours at 20°C for all genes except *nmy-2, rga-3, rga-4, unc-59, unc-61* and *pkn-1*. Young Adults injected with *pkn-1, unc-59* or *unc-61* dsRNAs were filmed after 40-48hrs at 20°C and those injected with *nmy-2, rga-3* or *rga-4* were imaged 16-20 hours after injection at 20°C. For co-depletion experiments dsRNAs were mixed at 1:1 ratio.

3.3.4 Immunofluorescence

For immunostaining of *C. elegans* embryos, gravid hermaphrodites were cut open in 10µl M9 buffer on glass slides coated with 0.1% poly-L-lysine. Egg shell of the embryos was freeze-cracked in liquid nitrogen followed by fixation for 20min in 100% methanol cooled down to -20°C. Slides were washed in 1xPBS (0.2% Tween) for 5 mins and incubated with the desired primary antibodies listed in Table 11 (Section 3) at 4°C overnight. Slides were washed thrice in 1xPBS (0.2% Tween) and incubated with appropriate secondary antibodies for 1hr at room temperature and 1µg/ml Hoechst 33258. Embryos were covered by the mounting medium (see Table 14 in Section 3) and a coverslips was fixed on the top.

3.3.5 Image Quantification

a. Cortical localization of anillin and NMY-2

Anillin or NMY-2 localization in a *C. elegans* embryo was measured by two linescans along the cell cortex, each extending from mid-anterior pole to the mid-posterior pole (Figure 24E). The cytoplasmic background intensity was measured in a small box close to the posterior pole and subtracted from each value in the linescan. The mean fluorescence intensity at the anterior pole (0-10%), posterior pole (90-100%) and equator (45-55%) was calculated over time. Anillin or myosin fluorescence intensity was normalized to the mean anterior or equatorial fluorescence intensity in controls 180s after NEBD and has been stated in figure legends. NEBD was defined as the time point when nuclear mCherry::histone equilibrated with the cytoplasm. In absence of mCherry::histone, NEBD was defined as the time point when NG::Anillin or GFP::NMY-2 equilibrated with the cytoplasm. In strains without any of

the three fluorescence markers, NEBD was defined as the time point when the border of nucleus disappeared in DIC images. In few embryos, site of polar body extrusion led to bright fluorescent signal at the anterior cortex, therefore, such cortices were excluded from the analysis.

b. Microtubule dynamics

Microtubule nucleation and growth rates were measured in the *C. elegans* strain expressing microtubule end binding protein EBP-2::GFP as previously described (Srayko et al., 2005). EBP-2::GFP images were acquired at 400 msec intervals for 1 min at 25°C of one cell embryos during metaphase (50-100s after NEBD) or anaphase (160-220s or 255-315s after NEBD) by live-cell imaging. To measure microtubule nucleation rate, an arc (29-30 µm long) was drawn 9 µm away from the anterior centrosome and underneath the anterior polar cortex in Fiji. Kymographs were generated for the 1 min recording and EBP-2::GFP dots were manually counted. To measure microtubule growth rate, Fiji Manual Tracking plugin was used to manually track the individual EBP-2::GFP dots originating from the anterior centrosome. The position of EBP-2::GFP dot with respect to the centrosome was plotted at each time interval and the microtubule growth rate was calculated as the slope of each line in Excel. Microtubule growth rate was analyzed in at least three embryos and 8-12 MTs were tracked for each embryo.

3.4 Transgene Construction

To generate pcDNA6 mammalian expression plasmid having mKate2-tagged α-tubulin, sequences encoding mKate2, α-tubulin and pcDNA6 plasmid were amplified from Addgene plasmids #37132 (Shcherbakova et al., 2012), # 31930 (Subach et al., 2009) and #40201 (Shuda et al., 2011) respectively, and assembled together by Gibson cloning (NEB, E2611; pEZ170). To generate mNeonGreen-tagged PKN2 (pEZ299) and Septin-7 (pEZ292), their sequences were amplified from the cDNA of HeLa cells and inserted next to the mNeonGreen sequence in pcDNA5/FRT/TO expression plasmid by Gibson cloning. To confer RNAi resistance, four and five silent point mutations in the siRNA binding site of PKN2 and Septin-7 sequences respectively were introduced in the DNA primers. To generate GST-tagged fragment of anillin for production and purification of antibodies, anillin cDNA sequence encoding for amino acids 417-687 (Piekny and Glotzer, 2008) was inserted into pGEX-4T plasmid next to the GST tag (pEZ154). To generate GST-tagged MP-GAP for antibody purification, MP-GAP cDNA was inserted into pGEX-4T bacterial expression plasmid next to GST tag (pEZ229). To generate transgene encoding FRB-GFP-PH, FRB

sequence was codon-optimized (Redemann et al., 2011) and an intron was introduced between amino acids 25(K)-26(G). In addition, 'threonine' 2098 was mutated to 'leucine' to allow binding of rapamycin derivatives to FRB domain. The resulting DNA sequence was synthesized by Eurofins. Plasmid backbone pCFJ350 having *mex-5* and *tbb-2* regulatory sequences, GFP-PH and FRB domain were amplified by PCR and assembled together by Gibson cloning (pEZ156). To generate transgene encoding mCherry-FKBP12, FKBP12 sequence was codon-optimized (Redemann et al., 2011) and an intron was introduced between amino acids 35(K)-36(K). The resulting DNA sequence of FKBP12 was synthesized by Eurofins. FKBP-12 and plasmid backbone pCFJ350 having mex-5 and tbb-2 regulatory sequences along with mCherry flurophore, were amplified by PCR and assembled together by Gibson cloning (pEZ159). DNA sequencing was performed to confirm the sequences of obtained plasmids as dsscribed in section 3.4.7. All clonings were performed by Gibson assembly (NEB, E2611) as described in sections 3.4.1-3.4.7. All plasmid used are listed in Table 10 (Section 3) and DNA primers are listed in Table 3 (Section 3.4.1).

3.4.1 Amplification of DNA by Polymerase Chain Reaction (PCR)

All template DNA sequences including gene of interest and plasmid backbone were amplified by PCR using the below mentioned reaction composition (Table 1) and thermo-cycler conditions (Table 2). Phusion polymerase was used in all the PCR reactions. Primers used for molecular cloning are listed in Table 3 below. To visualize the PCR products, 2 µl of PCR products were mixed with 1x EZ-Vision Loading Buffer (VWR, N472-KIT) and loaded on 0.8% agarose gel. DNA bands were allowed to resolve at 120V for 20 mins to 45 mins depending on the size of DNA products.

Table 1: Chemical composition of each PCR reaction

S. No.	Ingredient	Volume (for 50 µl reaction)
1.	5x Phusion buffer	10 µl
2.	2 mM dNTPs mix	5 µl
3.	50 pmol/µl forward DNA primer	0.5 µl
4.	50 pmol/µl reverse DNA primer	0.5 µl
5.	DNA template (1:100 diluted)	1 µl
6.	Phusion Polymerase	0.5 µl
7.	MilliQ water	32.5 µl

Table 2: Thermo-cycler temperature settings

Step	Name of Step	Temperature	Duration
1.	Initial denaturation	98°C	30 sec
2.	Denaturation	98°C	10 sec
3.	Annealing	Annealing Temperature (see Table 3)	30 sec
4.	Elongation	72°C	1 min for 2 kb
5.	Repeat steps 2-4, 29 times		
6.	Final elongation	72°C	10 min
7.	Cooling down	12°C	20 min

Table 3: List of DNA primers (synthesized by Eurofins) and their annealing temperature

Name	Sequence (5' to 3')	Used for	Annealing Temp.	Resulting Plasmid
EZ569	CGGAATTCCCGTCTTCATC TACTACCCATTTAGCAC	Amplifying a part of anillin sequence	55°C	pEZ154
EZ570	ATCGTCAGTCAATTGAGTT CCTGCATTTTCTGTTTGA			
EZ571	AGGAACTCAATTGACTGA CGATCTGCCTCGC	Amplifying pGEX-4T plasmid backbone	58°C	
EZ572	GTAGATGAAGACGGGAAT TCCGGGGATCCAC			
EZ657	GACCCAAGCTGGCCACCA TGGTGAGCGAGC	Amplifying mKate2 sequence	61°C	pEZ170
EZ658	CTGAGTCCGGATCTGTGC CCCAGTTTGCTAGG			
EZ659	GAGGAATACTAAAAACCC GCTGATCAGCCTC	Amplifying pcDNA6 plasmid backbone	54°C	
EZ660	ACCATGGTGGCCAGCTTG GGTCTCCCTATAG			
EZ661	TGGGGCACAGATCCGGAC TCAGATCTCGAG	Amplifying α-tubulin sequence	54°C	
EZ662	CAGCGGGTTTTTAGTATTC CTCTCCTTCTTCCTC			
EZ947	CGGAATTCCCGGCTACTTC ATGTGAACTCACC	Amplifying MP-GAP sequence	54°C	pEZ229
EZ948	ATCGTCAGTCACATTTGTG AACTTTCAGAAACTG			
EZ949	GTTCACAAATGTGACTGA CGATCTGCCTCGC	Amplifying pGEX-4T plasmid backbone	60°C	
EZ950	CATGAAGTAGCCGGGAAT TCCGGGGATCCAC			

EZ1217	CCAGATTCACCCACTACC ATTAAAGTAAATTCAAAA CCTCTCTTCACCG	Amplifying the plasmid pcDNA5 having Sept7-NG to with primers having point mutations to confer RNAi resistance to PKN2.	60ºC	pEZ292
EZ1218	CGGTGAAGAGAGGTTTTG AATTTACTTTAATGGTAGT GGGTGAATCTGG			
EZ1096	GCATGGCGTCCAACCCCG AACG	Amplifying part of NG and PKN2 with primers having point mutations to confer RNAi resistance.	58ºC	pEZ266
EZ1101	AGAACCTAGGGTATCTAA CTTCATCATTTACAATACT GTCAAAAAC			
EZ1097	CGCGGCCGCTTAACACCA ATCAGCAATGTAGTC	Amplifying part of NG and PKN2 with primers having point mutations to confer RNAi resistance to PKN2.	55ºC	
EZ1100	GAAGTTAGATACCCTAGG TTCTTATCTACAGAAGCC			
EZ1098	TGATTGGTGTTAAGCGGC CGCGGGCCCGTTTAA	Amplifying plasmid backbone pcDNA5	63ºC	
EZ1099	CGTTCGGGGTTGGACGCC ATGCTGCCGCTGCCCTTGT AC			
EZ575	GGCAGAAGTAAATGCAAG ATCCTTTCAAGC	Amplifying plasmid backbone of pCFJ350 and mex-5 promoter sequence	54ºC	pEZ156
EZ576	GCCAGAGGATCATTCTCT GTCTGAAACATTCAATTG			
EZ577	AGACAGAGAATGATCCTC TGGCACGAGATGTG	Amplifying FRB sequence	58ºC	
EZ578	CTCATAGTACCTCCACCTC CCTTGGAGATACGACGGA AGACG			
EZ579	AGGGAGGTGGAGGTACTA TGAGTAAAGGAGAAGAAC TTTTCAC	Amplifying GFP-PH sequence	55ºC	
EZ580	GGATCTTGCATTTACTTCT GCCGCTGGTCC			
EZ591	CAAGCTCGAGTAAATGCA AGATCCTTTCAAGC	Amplifying plasmid backbone of pCFJ350 having mex-5 promoter, mCherry and tbb-2 sequence	54ºC	pEZ159
EZ594	TAGTACCTCCACCTCCCTT ATAC			
EZ592	TATAAGGGAGGTGGAGGT ACTATGGGAGTCCAAGTC GAGACC	Amplifying FKBP12 sequence	60ºC	
EZ593	ATCTTGCATTTACTCGAGC TTGAGGAGCTCGAC			

3.4.2 Purification of PCR products

Before purifying the PCR products, plasmid template was cleaved with DpnI restriction enzyme (1 µl in 50 µl PCR products) for 1 hour at 37ºC. PCR products were purified using the Macherey-Nagel NucleoSpin Gel and PCR Clean-up kit (#740609250) according to the manufacturer's instructions.

3.4.3 Gibson assembly

PCR products were mixed together with 2x Gibson Assembly master-mix (NEB, #4767707) in an Eppendorf tube according to the manufacturer's instructions (NEB, E2611) and incubated at 50ºC for 1 hour.

3.4.4 Transformation of chemical competent *E. coli* DH5α

Chemical competent DH5α cells were thawed on ice for 20 mins. 6 µl of the Gibson reaction mix from previous step was added to 50 µl of DH5α cells and incubated on ice for 20 mins. Then, this mix of cells and gibson reaction was incubated at 42ºC for 45 seconds and immediately transferred to ice for 2 mins. Cells were then allowed to recover from the heat shock in 1 ml LB broth at 37ºC for 1 hour and were plated in LB-plates containing appropriate antibiotic for selecting positive clones. The plates were incubated at 37ºC overnight.

3.4.5 DNA purification from bacterial colonies

Few of the bacterial colonies growing on the LB-plates (with antibiotic selection marker) were picked and cultured at 37ºC overnight in 2 ml LB broth containing appropriate antibiotic for selection. Bacteria were pelleted at 10,000 rpm for 5 mins and the pellet was resuspended in 100 µl solution-1 having 100 µg/ml RNase A, followed by addition of 200 µl of solution-2. Tubes were incubated at room temperature for 5 mins and 150 µl of solution-3 was added. Tubes were then incubated on ice for 10 mins. Afterwards, tubes were centrifuged at 13,000 rpm for 10 mins at 4ºC and supernatant was transferred to new Eppendorf tubes. 1 ml ice-cold absolute ethanol was mixed with the supernatant and centrifuged at 13,000 rom for 10 mins. Supernatant was discarded and pellet was rinsed with 70% ethanol followed by centrifugation at 13,000 rpm for 10 mins. Supernatant was again discarded and the pellet was air dried for about 15 mins. Finally, the pellet was dissolved in 30 µl TE buffer and stored at -20ºC

3.4.6 DNA sequencing to identify positive clones

The DNA purified from the positive bacterial clones were screened by DNA sequencing. Samples for DNA sequencing were prepared in 200 µl PCR tubes (Table 4) and sequenced at in-house 'Genomics Service Unit' of Faculty of Biology, LMU Munich. The protocol used for DNA sequencing was called 'Cycle, Clean, Run'. DNA primers having annealing temperature in the range of 52°C to 60°C and bind 100bp upstream of the region to be sequenced were chosen.

Table 4: Sample preparation for DNA sequencing

S. No.	Ingredient	Volume (7 µl)
1.	DNA template	1 µl (having 150-300 ng)
2.	Sequencing Primer	1 µl (having 2-10 pmol)
3.	10 mM Tris/Cl, pH 8.5 (no EDTA)	5 µl

3.4.7 DNA purifications by commercial kits

Correct bacterial clones identified by DNA sequencing were cultured again, either in 3 ml LB broth containing selection antibiotic to obtain smaller quantities of purified plasmid (mini-preps) or in 25 ml LB broth having selection antibiotic for getting higher plasmid yields (midi-preps). Plasmid purifications were performed by following manufacturer's instructions. Mini-preps to obtain plasmids for microinjection in *C. elegans* gonads were performed by using PureLink Quick Plasmid Miniprep Kit (Invitrogen, K2100-01). Midi or mini-preps to purify plasmids for transfection in HeLa cells were carried out using Qiagen Plasmid Mini Kit (#12125) or Qiagen Plasmid Midi Kit (#12145).

3.5 Immunoblotting

For immunoblotting, cells were washed with 1x PBS, scratched off the surface, collected in an eppendorf tube and pelleted by spinning at 4000 rpm for 5 mins at 4°C. Cell pellet was resuspended in 1x Laemmli sample buffer and incubated at 95°C for 10min. For immunoblotting adult worms, 30-40 worms were picked and washed multiple times in M9 buffer. Sample buffer was added and worms were incubated at 95°C for 5 mins and sonicated for 20 mins. All protein samples were resolved by SDS-PAGE under reducing conditions and were immobilized to PVDF membrane (Merck Millipore, PVH00010) by wet transfer method. Membranes were blocked with 4% milk powder-PBST solution for 1 hour at room temperature and incubated with desired primary antibodies listed in Table 11 (Section 3)

overnight at 4°C. Membranes were washed four times with PBST and incubated with appropriate HRP-conjugated secondary antibodies listed in Table 11 (Section 3) for 1hr at room temperature. After four washes with PBST, protein bands were visualized using enhanced chemiluminescence (ECL) and imaged with BioRad ChemiDoc XRS+ system.

3.6 Fluorescence Microscopy

HeLa cells were filmed live in Nunc™ Lab-Tek™ (Thermo Scientific) or ibidi treat-well (ibidi) chambered coverglass dishes at 37°C. Culture medium was replaced with CO_2 independent medium supplemented with 10% FBS and stable 2mM L-glutamine prior to imaging. During live-cell imaging the temperature was maintained at 37°C using a heated microscope chamber. To image *C. elegans* embryos, adult hermaphrodites were dissected in 4µl M9 buffer on a coverslip (18x18mm) which was inverted onto a glass slide having 2% agarose pad. *rga-3/4*Δ mutant embryos, being partially osmosensitive, were imaged in L-15 blastomere culture medium (Edgar and Goldstein, 2012) without the pressure of a coverslip (Zanin et al., 2013). Adult worms were dissected in a 4µl drop of L-15 medium on a coverslip (24x50mm) which was mounted on a metal slide (Monen et al., 2005) having a small hole in the center. A thin Vaseline ring was created around the drop to act as spacer and a smaller coverslip (18x18mm) was placed on the Vaseline ring. All details of the microscopes used and images acquired by them are summarized in Table 15. All images were processed in Fiji and Adobe Photoshop Element, graphs were plotted in Prism and figures were prepared in Affinity Designer.

3.7 Generation of Antibodies

To generate a polyclonal antibody against human anillin protein, sequence encoding anillin amino acids 417-687 (Piekny and Glotzer, 2008b) was cloned into pGEX-4T plasmid containing a GST tag. Expression of GST-anillin$^{417\text{-}687}$ fusion protein was induced in BL21 cells for 4hrs at 37°C and GST-anillin$^{417\text{-}687}$ was purified over glutathione-sepharose column by affinity chromatography (Figure 7B). The purified antigen was used to immunize rabbits by Davids Biotechnology GmbH. The serum obtained from the immunized rabbits was incubated with GST-coupled SulfoLink resin overnight at 4°C to deplete anti-GST antibodies (Figure 7A and C). The depleted of anti-GST antibodies was then incubated with GST-Anillin$^{417\text{-}687}$-coupled SulfoLink resin to trap and purify anti-anillin antibodies. Antibodies bound to the SulfoLink resin were eluted in 0.2M glycine pH 2.5 and immediately neutralized by 1M TrisHCl pH 8.5. The eluted antibodies were concentrated and the buffer

was exchanged to 1xPBS by using Pierce Protein Concentrator (10K MWCO; Life Technologies, 88527). The purified antibodies were mixed with equal volume of glycerol and stored at -20°C. Purified anti-anillin antibodies were tested and found to be suitable for Western Blotting and Immunofluorescence applications (Figure 7D and E). The specificity of the purified antibody can be seen on the western blot shown in Figure 9B, where immune-reactive band of anillin is nearly absent upon depletion of anillin by RNAi in HeLa cell extracts. Immunofluorescence analysis, similarly, showed absence of anillin signal in cells treated with anillin siRNA but not in control cells (Figure 7D).

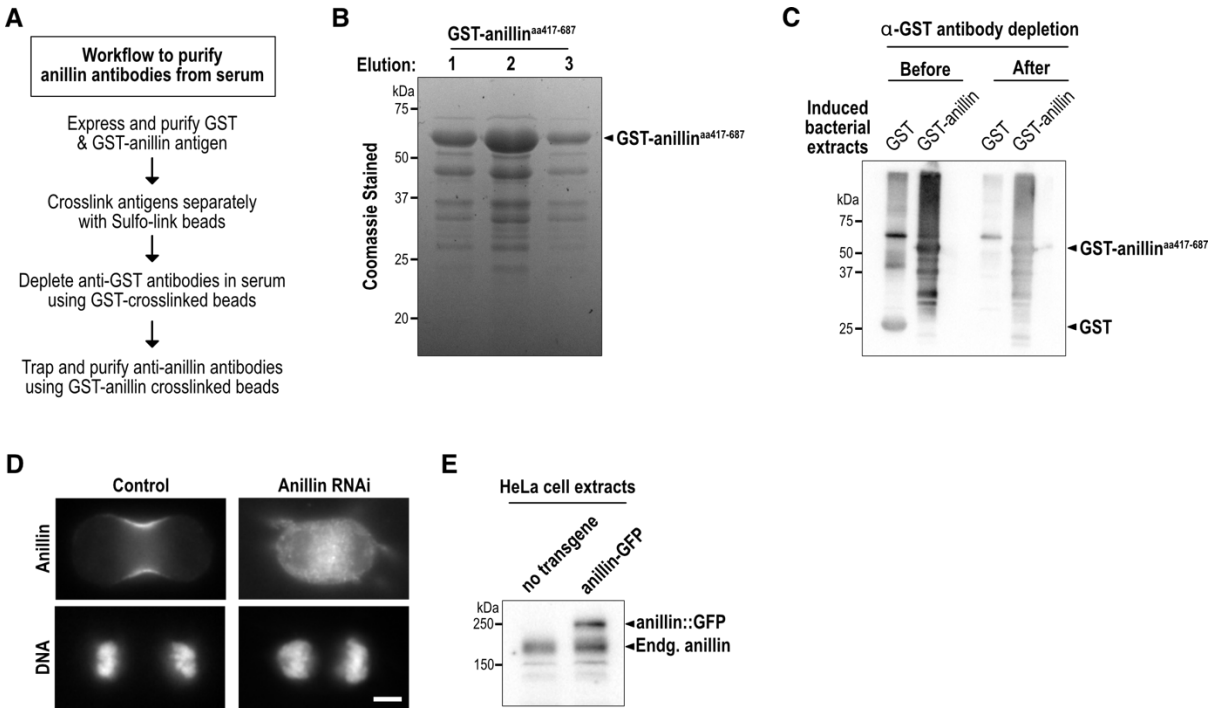

Figure 7: Purification of anti-anillin polycolonal antibodies from serum of immunized rabbits. (**A**) Workflow showing major steps of antibody purification. (**B**) Purification of anillin polypeptide to serve as an antigen to facilitate antibody purification. GST-tagged human anillin polypeptide (amino acids 417–687) was expressed in BL21 cells and purified with glutathione-sepharose beads. (**C**) Western Blot showing strong depletion of GST-antibodies from the rabbit serum. (**D**) Fluorescence images of control and anillin depelted HeLa cells stained with anillin antibodies and Hoechst. (**E**) Immunoblots of parental HeLa cells or cells expressing anillin::GFP to test the purified anillin antibodies.

To generate a polyclonal anti-MP-GAP antibody, MP-GAP cDNA was cloned into pGEX-6P1. The expression of GST-MP-GAP was induced from pGEX-6P1 in BL21 cells for 4hrs at 37°C and purified antigen was injected into rabbits by Thermo Scientific (antigen was expressed and purified by Dr. Shirin Bahmanyar). To purify MP-GAP antibodies from the

serum, MP-GAP cDNA was again cloned in to pGEX-4T plasmid as the previous pGEX-6P1 was not available in the lab stock. GST and MP-GAP antigens were purified by inducing pGEX-4T in BL21 cells for 4 hrs at 37°C and purified using glutathione-sepharoase column (Figure 8A). Purified antigens were coupled with SulfoLink resin by following the manufacturer's instructions. The serum containing anti-GST and anti-MP-GAP antibodies was run through GST-coupled SulfoLink resin to deplete anti-GST antibodies (Figure 8B). The serum, thus, depleted of anti-GST antibodies was passed through GST-MP-GAP-coupled SulfoLink resin (expressed using pGEX-4T plasmid) to trap and purify anti-MPGAP antibodies. Antibodies bound to the SulfoLink resin were eluted in 0.2M glycine pH 2.5 and immediately neutralized by 1M TrisHCl pH 8.5. The eluted antibodies were concentrated and the buffer was exchanged to 1xPBS by using Pierce Protein Concentrator (10K MWCO; Life Technologies, 88527). The purified antibodies were mixed with equal volume of glycerol and stored at -20°C. Purified anti-MPGAP antibodies were tested and found to be suitable for Western Blotting (Figure 8C). The specificity of the purified antibody can be seen on the western blot shown in Figure 8C, where immune-reactive band of MP-GAP is nearly absent upon depletion of MP-GAP by RNAi in HeLa cell extracts.

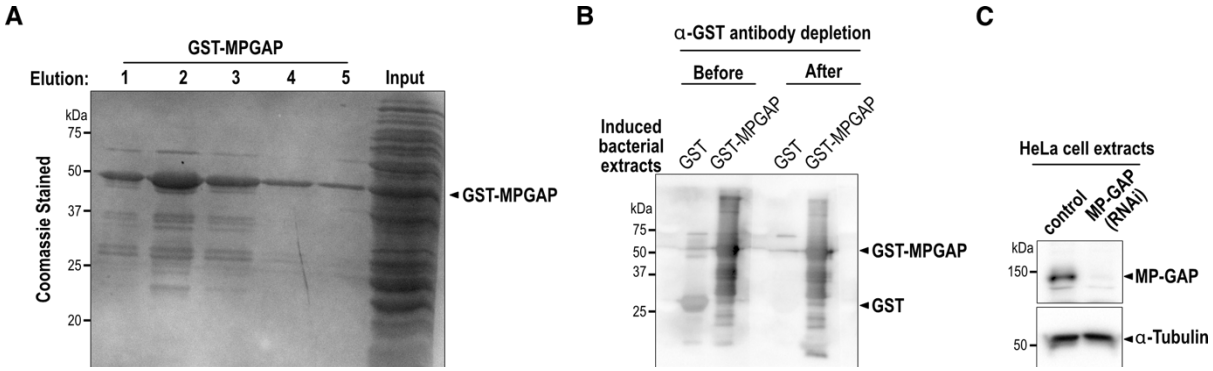

Figure 8: Purification of anti-MP-GAP polycolonal antibodies from serum of immunized rabbits. (**A**) Purification of GST-tagged MP-GAP to serve as an antigen to facilitate antibody purification. GST-tagged human MP-GAP polypeptide was expressed in BL21 cells and purified with glutathione-sepharose beads. (**B**) Western Blot showing strong depletion of GST-antibodies from the rabbit serum. (**C**) Immunoblots of control and MP-GAP RNAi treated HeLa cells. α-tubulin was used as a loading control.

3.8 Statistical Analysis

Statistical analysis for the RNAi screen was performed in Knime using two-tailed student's t-test. For all other experiments appropriate statistical test was performed in Prism as indicated in the figure legend and normal distribution of the data was checked by Shapiro-Wilk test. Mean values are shown with error bars representing either SEM or SD as indicated in the figure legends.

3.9 Data analysis with Knime

Knime (http://www.knime.org) is a free and open-source software that utilizes graphical user interface and modular data pipeline for data analysis. I used knime to calculate mean anillin or myosin fluorescence intensity in HeLa cells and *C. elegans* early embryos as well as anillin, myosin and RhoA zone width in HeLa cells. Knime was also used to analyse all the data of RNAi screen and check statistical significance by student's t-test. Raw pixel intensities measured by drawing cortical linescans in Fiji were imported in to Knime and fed into a data analysis pipeline to calculate mean fluorescence intensities on equatorial and polar cortex as well as zone width. Before calculating mean fluorescence intensities, cytoplasmic fluorescence intensity was subtracted from each value to account for slight variations in expression of fluorescent proteins and immunostainigs. I established the data analysis pipeline with the help of our collaborator Martin Stoeter of MPI-CBG.

Table 5: HeLa cell lines

Cell Line	Background	Description	Reference/ Established by
HeLa Parental	HeLa "Kyoto"	No transgene insertion	
EZ5	HeLa "Kyoto"	Expression of mouse anillin-FLAP from integrated BAC, clonal cell line obtained by FACS.	Zanin et. al. 2013
HeLa Flp-In TRex	HeLa	No transgene insertion	Tighe et al., 2004
Generated cell lines			
EZ56	HeLa "Kyoto"	Expression of mouse anillin-FLAP from integrated BAC and mKate2-α-tubulin from integrated transgene. Clonal cell line obtained by FACS.	S. Mangal
EZ88	HeLa Flp-In TRex	Expression of mNeonGreen-PKN2	S. Mangal

EZ101	HeLa Flp-In TRex	Expression of Sept7-mNeonGreen	S. Mangal

Table 6: *C. elegans* strains

Strain name	Genotype	Reference/ Generated by
N2	Wild type (ancestral)	
EG6699	*ttTi5605* II; *unc-119(ed3)* III; *oxEx1578*	Frøkjær-Jensen et al., 2008
EG8078	*oxTi185* I; *unc-119(ed3)* III	Frøkjær-Jensen et al., 2014
EG8081	*unc-119(ed3)* III; *oxTi177* IV.	Frokjaer-Jensen et al., 2014
MDX29	*ani-1(mon7[mNeonGreen^3xFlag::ani-1])* III	Descovich et. al., 2018
ZAN23	*nmy-2(cp13[nmy-2::gfp + LoxP])* I; *unc-119(ed3)* III; *ltIs37 [pAA64; pie-1/mCherry::his-58; unc-119 (+)]* IV	E. Zanin
ZAN295	*ani-1(mon7[mNeonGreen^3xFlag::ani-1])* III; *[mex-5::mCherry::tubulin]* IV	E. Zanin
OD184	*ltIs108 [pOD564/pFM005; pie-1::LAP::AIR-1^{WT} reencoded; unc-119(+)]*	F. Motegi
OD1359	*unc-119(ed3)* III; *ltSi716 [pOD1935/pDC208; Pmex-5::EBP-2::GFP::tbb-2; cb-unc-119(+)]* I	Wang et al., 2015
Generated worm strains		
ZAN286	*estSi71 [pAC257;pmex-5::LifeAct::mKate2:tbb2; cb-unc-119(+)]* IV; *rga-4(ok1935) unc-62(e644) rga-3(ok1988)* V/*nT1[qIs51]*(IV;V)	S. Mangal
ZAN308	*pkn-1(ok1673)* X; *ani-(mon7[mNeonGreen^3xFlag::ani-1]* III; *[mex-5::mCherry::tubulin]* IV	S. Mangal
ZAN87	*estSi50[pEZ156;pmex-5::frb::gfp::ph::tbb2; cb-unc-119(+)]I; unc-119(ed3) III*	S. Mangal
ZAN98	*estSi54[pEZ159;pmex-5::mCherry::fkbp12::tbb2; cb-unc-119(+)]II; unc-119(ed3) III*	S. Mangal
ZAN101	*estSi50[pEZ156;pmex-5::frb::gfp::ph::tbb2; cb-unc-119(+)]I; estSi54[pEZ159;pmex-5::mCherry::fkbp12::tbb2; cb-unc-119(+)]II; unc-119(ed3) III*	S. Mangal

Table 7: Bacterial strains used from laboratory stock

Strain name	Purpose
DH5α	Transformation of DNA
BL21	Expression of recombinant proteins
OP50	Feeding and culturing *C. elegans* worms

Table 8: siRNAs to knockdown gene expression

Gene	Sequence	Company	Cat. No.
Non-Targeting	Sequence not known	Dharmacon	D-001810-01-20
PKN2	GAAUGUGAGUGCUGUUCAA	Dharmacon	J-004612-13
SEPT7	UGAAUUCACGCUUAUGGUA	Dharmacon	J-011607-06
ARHGAP11a pool (MP-GAP)	AUUACAGGCUGCAGUAGUA, GGUAUCAGUUCACAUCGAU, GAUCGCAGGAGACAUGAAA, AAGCGUACAUUGCCAGUAG	Dharmacon	L-021122-00
Anillin	CGAUGCCUCUUUGAAUAAATT	Life Technologies	Custom-made
Control siRNAs used in the screen			
ECT2 pool	GCACUCACCUUGUAGUUGA, CAGAGGAGAUUAAGACUAU, UAACAGCAAUCGCAAACGA, GUAAUGAGUCGUCUUUCUA	Dharmacon	J-006450-05 to J-006450-08; manually pooled
MP-GAP pool	AUUACAGGCUGCAGUAGUA, GGUAUCAGUUCACAUCGAU, GAUCGCAGGAGACAUGAAA, AAGCGUACAUUGCCAGUAG	Dharmacon	J-021122-05 to J-021122-08; manually pooled

Table 9: Primers for dsRNA production for *C. elegans*

Gene	Oligonucleotide 1	Oligonucleotide 2	Template	dsRNA conc. mg/ml
pkn-1	TAATACGACTCACTA TAGGGATGGACCACC AAGTAAGCTTG	TAATACGACTCACT ATAGGGAGGTGGTT TTGGGATGAGTCC	Genomic DNA	3.06
unc-59	TAATACGACTCACTA TAGGTGGGAGCCAAT AGTGAACTAC	TAATACGACTCACT ATAGGCGATTCTTC TCATTCTTCGGC	Genomic DNA	1.0
unc-61	TAATACGACTCACTA TAGGAGCGTGTTAAT GTGATCCCAG	TAATACGACTCACT ATAGGTCCAGTCTC TCCATCTCCAATC	Genomic DNA	1.0
tpxl-1	TAATACGACTCACTA TAGGACGTCGGTGAG	TAATACGACTCACT ATAGGTGTACACAT	cDNA	0.58

	CAAATTGAC	ATGATGGCACAGG		
nmy-2	TAATACGACTCACTA TAGGAATTGAATCTC GGTTGAAGGAA	TAATACGACTCACT ATAGGACTGCATTT CACGCATCTTATG	cDNA	0.36
hcp-4	TAATACGACTCACTA TAGGGGAAATGTAC GGAGCGAAAAC	TAATACGACTCACT ATAGGGTTGGTGGG TCCAATATTAC	cDNA	0.64
rga-3 *rga-4*	TAATACGACTCACTA TAGGGCAACGCGTCG AAACATCG	TAATACGACTCACT ATAGGGTTGGAGTG GCAGTTGGAGTG	Genomic DNA	2.9
saps-1	TAATACGACTCACTA TAGGGACTCAAAATA GCAAGCAACTTCTG	TAATACGACTCACT ATAGGGGAAGGTTG TCCCGCCGAGG	cDNA	2.8
pph-6	TAATACGACTCACTA TAGGGGTATTCGACG TTCTTCCAATTGG	TAATACGACTCACT ATAGGGTTAGAGGA AATACGGAGCAACG	cDNA	2.0

T7 sequences are underlined.

Table 10: Plasmids

Plasmid Name	Plasmid backbone	Description
Addgene Plasmid #37132	pN1	Used to amplify mKate2 sequence
Addgene Plasmid #40201	pcDNA6	Used to amplify pcDNA6 plasmid backbone
Addgene Plasmid #31930	pEGFP	Used to amplify α-tubulin sequence
EZ76	pGEX-6P1	Encodes for GST::MP-GAP and used for anillin antibody generation
pAC257	pCFJ151	Encodes for LifeAct-mKate2
pEZ299	pcDNA5/FRT/TO	Encodes for RNAi resistant NG-PKN2
MosSCI co-injection plasmids		
pCFJ601	-	Encodes *Peft-3*::transposase.
pMA122	-	Encodes *Phsp*::peel-1
pGH8	-	Encodes *prab-3*::mcherry (pan-neuronal)
pCFJ90	-	Encodes *pmyo-2*::mcherry (pharynx-muscle)
pCFJ104	-	Encodes *pmyo-3*::mcherry (body-muscle)
Generated plasmids		
pEZ154	pGEX-4T	Encodes for GST::anillin$^{417-687}$ and used for anillin antibody generation
pEZ170	pCDNA6	Encodes mKate2::α-tubulin
pEZ229	pGEX-4T	Encodes for GST::MP-GAP and used for anillin antibody generation
pEZ292	pCDNA5/FRT/TO	Encodes for RNAi resistant Sept7-NG
pEZ266	pCDNA5/FRT/TO	Encodes for RNAi resistant PKN2

pEZ156	pCFJ350	Encodes for FRB-GFP-PH
pEZ159	pCFJ350	Encodes for mCherry-FKBP12

Table 11: Antibodies

Antibody	Raised in	Dilution		Supplier and Cat. No.	Fixative
		W.B.	I.F.		
Primary Antibodies					
Septin-7	Rabbit	1:1000	1:100	Tecan, JP18991	Methanol
pMLC (Ser19)	Rabbit	-	1:100	Cell Signaling Technology, 3671	4% formaldehyde
Anillin	Rabbit	1:3000	1:3000	Self-generated	Methanol
PKN2	Rabbit	1:1000	1:100	Abcam, ab138514	Methanol
α-Tubulin	Mouse	1:10000	1:250	Sigma, T6199	4% formaldehyde
RhoA (26C4)	Mouse	1:250	1:50	Santa Cruz, sc-418	10% TCA
Ect2	Mouse	1:250	-	Santa Cruz, sc-514750	-
Plk1(F-8)	Mouse	1:250	1:50	Santa Cruz, sc-17883	Methanol
pH3 (Ser28)	Rat	-	1:1000	Sigma, H9908	4% formaldehyde
pLATS2 (Ser83)	Mouse	-	1:1000	Cyclex, CY-M1020	4% formaldehyde
AIR-1	Rabbit	-	1:100	Hannak et. al., 2001	Methanol
Secondary Antibodies					
Alexa Fluor 488 anti-mouse	Goat	-	1:1000	Thermo Fischer	-
Alexa Fluor 488 anti-rabbit	Goat	-	1:1000	Thermo Fischer	-
Alexa Fluor 568 anti-rabbit	Goat	-	1:1000	Thermo Fischer	-
Alexa Fluor 568 anti-rat	Goat	-	1:1000	Thermo Fischer	-
Alexa Fluor 594 anti-rabbit	Goat	-	1:1000	Thermo Fischer	-
Rabbit-HRP	Goat	1:20000	-	Biorad	-
Mouse-HRP	Goat	1:20000	-	Biorad	-

Table 12: Reagents

Reagent	Supplier	Cat. No.
384-well µClear plates	Greiner Bio-one	781097
Opti-MEM	Thermo Fischer	31985070
INTERFERin	Polyplus	409-10
Lipofectamine RNAiMAX	Life Technologies	13778030
DMEM	Thermo Scientific	61965059
FBS (screening)	PAN Biotech	P30-3306
FBS	Thermo Scientific	10270106
Penicillin/Streptomycin	Merck	A2212
Thymidine	Sigma	T1895
MG132	Calbiochem	474790
Formaldehyde (screening)	Roth	4979.1
Formaldehyde	Thermo Scientific	28908
Plk1 inhibitor BI2536	Selleckchem	S1109
Nocodazole	Cayman	13857
X-tremeGENE 9	Roche	06365779001
Blasticidin	InvivoGen	ant-bl-1
Hygromycin	Sigma	H3274
Tetracycline	Sigma	T7660
AURKA inhibitor MK5108	Selleckchem	S2770
AZD1152-HQPA	Sigma	SML0268
poly-L-lysine	Sigma	P1524
CO_2 independent medium	Thermo Scientific	18045054
L-glutamine	A&E Scientific	M11-004
SulfoLink Resin	Thermo Scientific	20401
Propyl-gallate	Sigma	P3130
Leibovitz L-15 Medium	Thermo Scientific	11415-049
Inulin	Sigma	I3754
6x EZ-Vision	VWR	N472-KIT
DpnI	NEB	R0176L
Gibson Mix	NEB	4767707
Phusion Polymerase	NEB	M0530L
Phusion Buffer	NEB	-

Table 13: Kits to generate and purify dsRNA

Kit Name	Supplier	Cat. No.
MEGAscript T7 Transcription	Thermo Scientific	AM1334
MEGAclea Transcription Clean-Up	Thermo Scientific	AM1908

Qiagen Plasmid Mini Kit	Qiagen	12125
Qiagen Plasmid Mini Kit	Qiagen	12145
PureLink Quick Plasmid Miniprep Kit	Invitrogen	K2100-01
Nucleospin Gel and PCR cleanuo	Macherey and Nagel	740609250

Table 14: Buffers and Solutions

Solution	Composition
10x PBS	25.6g $Na_2HPO_4 \cdot 7H_2O$ 80g NaCl 2g KCl 2g KH_2PO_4. Adjust to 1L with ddH_2O
10x TBS	2g KCl 80g NaCl 30g Tris-Base Adjust the pH to 7.4 with HCl Adjust to 1L with ddH_2O
4x Resolving buffer	18.17g Tris 24 ml 1M HCl 0.4g SDS Adjust to pH 8.8 with HCl Adjust to 100ml with ddH_2O
4x Stacking buffer	6g Tris 38.5ml 1M HCl 0.4g SDS Adjust to pH 6.8 with HCl Adjust to 100ml with ddH_2O
10x Running buffer	30.3g Tris 144g Glycine Adjust to 1L with ddH_2O
Transfer buffer	200ml 100% Ethanol 100ml Running buffer Adjust to 1L with ddH_2O
Coomassie staining solution	100ml 100% Methanol 50ml Glacial Acetic Acid 0.5g Brilliant Blue Adjust to 500 ml with ddH2O
Coomassie destaining solution	250ml 100% Ethanol 50ml Glacial Acetic Acid Adjust to 500 ml with ddH_2O

2x Sample buffer	2ml 4x stacking buffer 4ml 10% SDS 140µl β-Mercaptoethanol 4ml 50% Glycerol 100µl Saturated Bromophenol blue solution
2x Freezing solution for *C. elegans* (Prepared by Lab Technicians)	5.58g NaCl 6.8g KH_2PO_4 300ml Glycerol 0.56ml NaOH to pH 6.0 MilliQ H_2O to 1 L Add 60µL of 1M $MgSO_4$ to 200 ml before use
M9 (Prepared by Lab Technicians)	6g Na_2HPO_4 3g KH_2PO_4 0.5g NaCl 1.0g NH_4Cl Adjust to 1L with ddH_2O
Mouting medium	4% n-Propyl-Gallate 90% Glycerol Prepare in 1x PBS
2x Freezing solution for HeLa cells	1.5ml DMEM medium 2.5ml FBS 1ml DMSO
L-15 blastomere culture medium	6ml Leibovitz L-15 media 1ml of HEPES (0.25M pH 7.4) 1ml Inulin Solution 2ml FBS
NETN Extraction buffer	4ml 1M Tris HCL pH 8.0 4ml 5M NaCl 10ml 10% NP-40 Adjust to 200ml with ddH_2O
LB Broth (Prepared by Lab Technicians except when required in large quantities)	10g Tryptone 5g Yeast extract 10g NaCl 800ml MilliQ H2O
Solution-1 (Prepared by Lab Technicians)	9ml 20% Glucose 5ml 1M Tris-HCl pH 8.0 8ml 0.25M EDTA adjust volume to 200ml with ddH2O
Solution-2 (Prepared by Lab Technicians)	200µl 10M NaOH 1ml 10% SDS MilliQ H2O to 10ml

Solution-3 (Prepared by Lab Technicians)	29.5ml glacial acetic acid KOH pellets to pH 4.8 MilliQ H2O to 100ml
TE Buffer (Prepared by Lab Technicians)	10 mM Tris-HCL 1 mM EDTA adjust pH to 8.0 with HCl adjust volume to 1 L with ddH2O

Table 15: Microscopes

Microscope	Equipment	Manufacturer
UltraVIEW VoX spinning disk confocal microscope (Used for Figure 9C, 19D, 25B, 26F, 38B-C, 43A)	*Lasers:* 405 nm, 442 nm, 488 nm, 514 nm, 561 nm, 640 nm *Objective:* 63x 1.4 NA Plan-Apochromat oil immersion *Camera:* Hamamatsu EMCCD C9100-50 *Software:* Volocity 6.1.1 software	Perkin Elmer
Nikon eclipse Ti spinning disk confocal microscope (Used for Figure 24B, 24D, 24G, 27A, 30A, 31A, 31D, 32A, 33B, 36A, 36C, 40C, 40D)	*Lasers:* 405 nm, 488 nm, 561 nm, 640 nm *Objective*: 100x 1.45 NA Plan-Apochromat oil immersion objective *Camera:* Andor DU-888 X-11056 *Software:* NIS Elements 4.51	Nikon
Leica TCS SP5 microscope (Used for Figure 9A (right), 20B, 20D, 22A, 22E, 26B, 26D, 33A, 36B, 37B, 39A, 39F, 41, 42B)	*Lasers:* Diode laser 405 nm (25 mW) Argon Laser 458 nm, 476 nm, 488 nm and 514 nm (5mW) DPSS Laser 561 nm (10 mW) HeNe Laser 594 nm (2.5 mW) *Objectives:* HCX PL APO Lambda Blue 63x 1.4 oil *Software:* Leica Application Suite Software 2.7.2	Leica
CV7000 high-throughput spinning disk confocal microscope (Used for Figure 9A (left), 10B, 12D, 15-17)	*Lasers:* 405 nm, 488 nm, 561 nm, 640 nm *Objevtive:* 40x 0.95 NA air 10x NA 0.4 *Camera:* Andor Neo sCMOS	Yokogawa

4. Results

4.1 RNAi Screen to discover novel regulators of cytokinesis

4.1.1 Establishing screening methodology

To identify the new regulators of cytokinesis in our RNAi screen, we analysed the cortical patterning of anillin at the cell cortex during anaphase in HeLa cells. Anillin is known to bind active RhoA and mimic its localization (Sun et al., 2015; Piekny and Glotzer, 2008). Anillin was visualized by using a previously established HeLa cell line expressing mouse anillin::GFP (Zanin et al., 2013) which was simply fixed and imaged (Figure 9A), thereby serving as a faster alternative to lengthy and time-consuming immunofluorescence assay. Since mitotic spindle plays a crucial role in regulating the cortical localization of anillin during anaphase (Section 1.3; Green et al., 2012), I introduced a stable integration of mKate2::α-tubulin in the cell line expressing anillin::GFP (Figure 9A). Visualizing mitotic spindle could help to identify overt spindle abnormalities (if present) in the shortlisted candidates. To obtain a cell line with homogenous expression of anillin::GFP and mKate2::α-tubulin single clones were generated by Fluorescence-activated cell sorting (FACS) and a colony having homogenous expression of the fluorescent proteins was identified, amplified and used in our experiments (named as EZ56, see Section 3, Table 5).

To assess whether the mouse anillin::GFP is functional, I depleted endogenous human anillin using a siRNA that selectively targets human anillin but not the mouse transgene. Anillin is required to link different components of the contractile ring and anillin depletion results in cytokinesis failure which causes an accumulation of bi- and multi-nucleated cells (Piekny and Glotzer, 2008). Consistent with the previous reports, anillin knockdown in HeLa cells led to a dramatic increase in the number of bi- (51% as compared to 6% in control) and multi-nucleated cells (27% as compared to 2% in control) (Figure 9C). Importantly, the increase in the number of bi- and multinucleated cells was rescued by the mouse anillin::GFP (15%

binucleated cells and 2% multinucleated cells), suggesting that the mouse transgenes is functional (Figure 9C). Furthermore, the Western Blot analysis showed that the expression level of mouse anillin::GFP was similar to that of the endogenous anillin (Figure 9B). Finally, mouse anillin::GFP localized to the cell equator during anaphase similar to the endogenous anillin (Figure 9A). Together, these three characteristics features of our cell line make it an excellent tool to study the cortical patterning of anillin in anaphase.

In non-synchronized cell populations, the number of anaphase cells is about 1% (Figure 9E). To analyze the cortical accumulation of anillin in adequate number of cells, it was crucial to increase the number of cells in anaphase in our fixed samples. To this end, I tested various cell cycle synchronization protocols such as single thymidine block, double thymidine block and MG132-induced metaphase arrest either in isolation or in different combinations. Concentrations of thymidine and MG132 were also optimized to achieve higher synchrony in the cell cycle. The resulting optimized synchronization workflow that was used in our experiments is shown in Figure 9D. Briefly, 24 hours after cell plating and siRNA transfection, cells were incubated with 0.5mM thymidine for 16 hours, released for 8 hours by washing out thymidine and treated again with 0.5mM thymidine for 16 hours. Thymidine was again washed off and cells were allowed to continue in cell cycle for 7.5 hours. Lastly, 5μM MG132 was added for two hours to allow accumulation of cells in metaphase followed by MG132 wash out and release of cells in to anaphase. Cells were fixed with formaldehyde 110 mins after MG132 washout and DNA was stained with DAPI. Using this procedure, we increased the number of anaphase cell to 15% percent (Figure 9E) from 1% in non-synchronous cells.

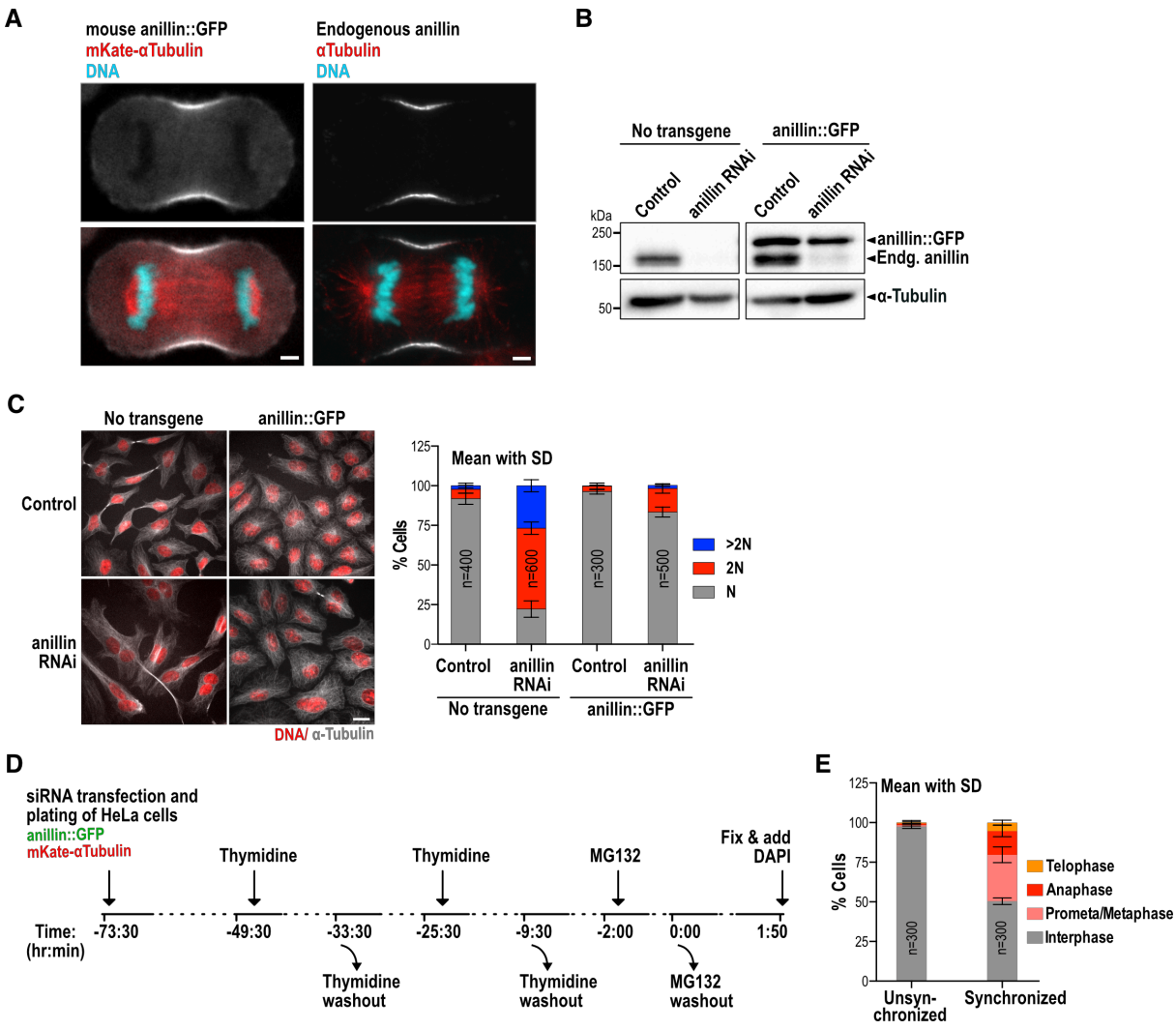

Figure 9: Characterization of anillin::GFP cell line and experimental workflow for the RNAi screen. (**A**) Confocal images of HeLa cells showing localization of transgenic anillin::GFP, mKate-α-tubulin, DNA (left) and stained endogenous anillin, α-tubulin and DNA (right) during anaphase. (**B**) Immunoblots of parental HeLa cells or cells expressing anillin::GFP after treatment with control or anillin siRNA. α-tubulin was used as loading control. (**C**) Confocal images (left) of parental HeLa and anillin::GFP expressing cells that were treated with control or anillin siRNA and stained with α-tubulin antibody and Hoechst. Graph (right) showing percentage of mono, bi and multi-nucleated cells for different treatment conditions. (**D**) Schematic showing experimental workflow of the screen. HeLa cells expressing anillin::GFP and mKate2::α-tubulin were seeded and cell cycle was synchronized by combination of double thymidine and MG132 treatments. Cells were fixed and DNA was stained with DAPI. (**E**) Plot showing percentage of cells in interphase, metaphase, anaphase and telophase with or without cell cycle synchronization. Scale bar is 5μm. Error bars are SD and n = number of cells.

4.1.2 Controls for the RNAi screen

To identify cytokinesis regulators, we wanted to analyse changes in patterning of anillin during anaphase upon knockdown of different genes. In control anaphase cells, anillin is enriched at the cell equator and is nearly absent from the cell poles (Figure 9A). To examine our ability to detect the expected phenotypes, I induced abnormal localization of anillin by depleting or inhibiting known regulators of cytokinesis like Plk1, Ect2, MP-GAP (Figure 2) using the procedure we developed for the RNAi screen (Section 3.1). Cells were plated and transfected in 384-well plates (Figure 12A) using automated plate dispensers and washers as described in material and methods (Section 3.1). The automation and optimization of plate washers and dispensers was carried out by Martin Stoeter at MPI-CBG. The cell cycle was synchronized as shown in Figure 9D and imaging was performed as shown in Figure 12D. Accumulation of anillin::GFP was quantified at the cell equator and poles by drawing a line around the entire cell cortex (Figure 9A). These positive controls can be broadly categorized into following two categories:

4.1.2.1 Reduced anillin accumulation at cell equator

Cortical localization of anillin is dramatically reduced upon depletion of RhoA-GEF Ect2 (Tatsumoto et al., 1999), or by Polo-like kinase 1 (PLK1) inhibition with small-molecule inhibitor BI2536 (Petronczki et al., 2007). As shown in Figure 10B and C, depletion of Ect2 led to substantial reduction in anillin::GFP accumulation at the cell equator. Similarly, PLK1 inhibition during anaphase using 100nM BI2536 caused significant decrease in the mean anillin::GFP intensity at the cell equator.

4.1.2.2 Increased anillin accumulation at cell poles

It is known that the microtubule asters prevent accumulation of anillin at the cell poles (D'Avino et al., 2015; Dassow, 2009; Green et al., 2012). Consistent with this, elimination of astral microtubules by treating anaphase cells with low dose of nocodazole (70nM) for 10 minutes resulted in significantly higher accumulation of anillin::GFP at the cell poles (Figure 10B and D). MP-GAP, a RhoA GTPase-activating protein, inactivates RhoA by converting it back to its GDP-bound state from GTP-bound state, thereby, acting as a negative regulator of RhoA signalling during cytokinesis. Depletion of MP-GAP in the absence of microtubule asters has been shown to result in polar accumulation of anillin (Zanin et al., 2013), suggesting that MP-GAP plays a role in restraining anillin localization to the cell equator. However, in my experiments depletion of MP-GAP alone was sufficient to cause a

significant increase in polar accumulation of anillin::GFP (Figure 10B and D), which is consistent with the role of MP-GAP in the inhibitory signalling but defies the notion that this inhibitory function is crucial only in the absence of microtubule asters. Since the depletion efficiency of MP-GAP in the earlier study was only shown for the GFP-tagged transgene and not for endogenous protein, it is possible that residual endogenous MP-GAP accounted for the lower penetrance of the observed phenotype. To investigate this possibility, I compared the depletion level of endogenous MP-GAP attained by the published older RNAi treatment with the newly optimized RNAi conditions of our screen on a Western Blot using MP-GAP antibodies that were purified by myself. The differences in the two experimental conditions are summarized in Figure 11A. Indeed, the comparison showed that while MP-GAP was nearly completely depleted using the new RNAi conditions, a significant amount of the protein was present after RNAi knockdown using the old treatment conditions (Figure 11B). Thus, the observed discrepancy in the penetrance of MP-GAP phenotype can be explained by the better knockdown of MP-GAP in my experiments. Regardless, these results show that abnormalities in anillin localization during anaphase in the positive controls can be reliably detected in our screening assay.

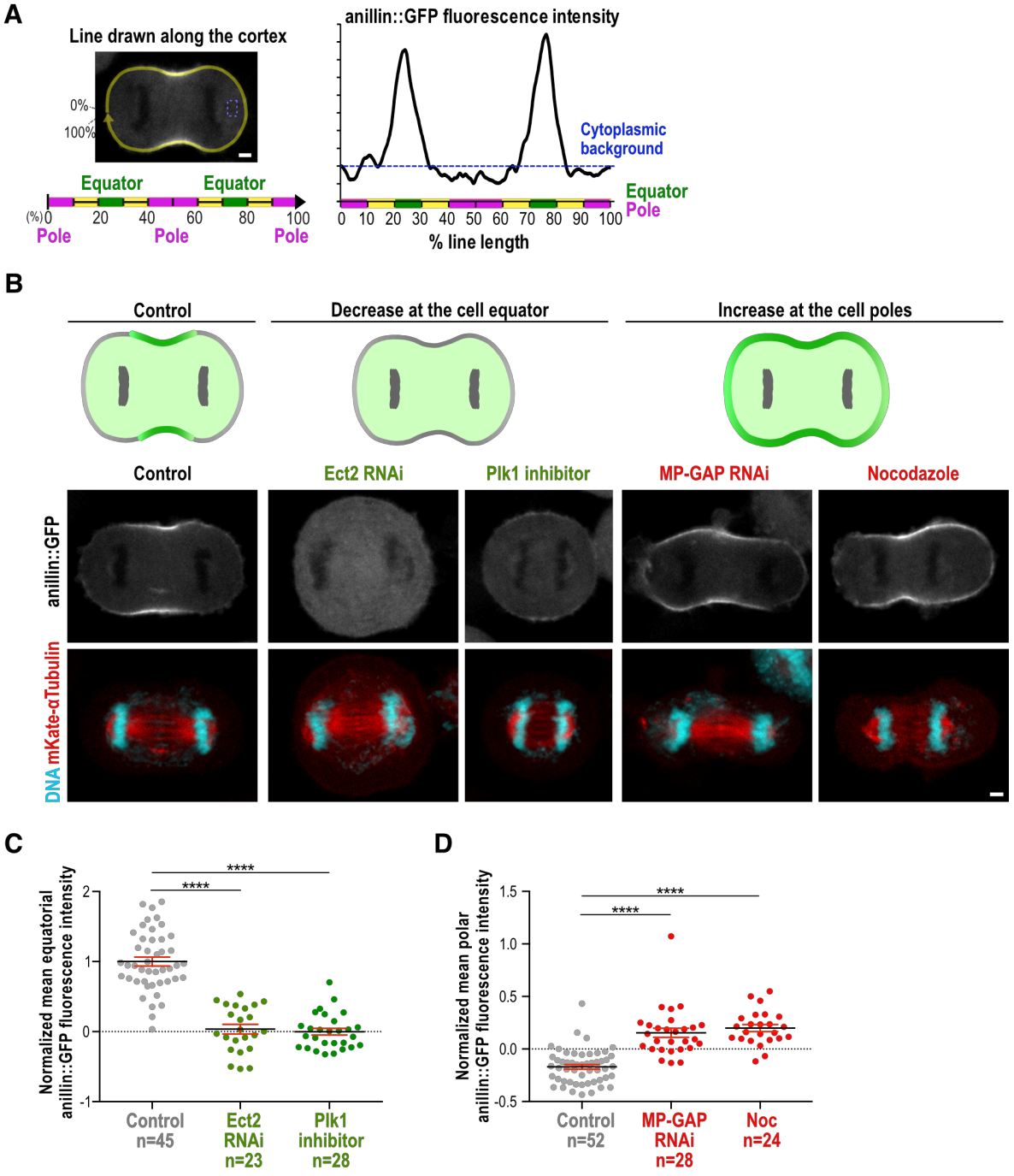

Figure 10: Quantification of cortical anillin::GFP in controls for the screen. (**A**) Anillin::GFP localization was analysed at the cell cortex by drawing a linescan (8 pixels wide) around the cell (start 0% and end 100%) and subtracting the mean cytoplasmic background intensity from the linescan. Mean fluorescence intensity was calculated for the polar (0-10%, 40-60%, and 90-100%) and equatorial (20-30%, 70-80%) cortex. (**B**) Schematics and representative images illustrating possible anillin localization defects expected to occur in the RNAi screen after knockdown of genes regulating cortical patterning of anillin. (**C**) Graphs plot the normalized mean anillin::GFP intensity at the cell equator in control, Ect2 depleted and Plk1 inhibitor-treated (BI2536) cells. p-values were calculated by Student's t test (****, $P < 0.0001$). (**D**) Graphs plot the normalized mean anillin::GFP intensity at the cell poles in control, MP-GAP depleted and nocodazole treated cells. p-values

were calculated by Kolmogorov-Smirnov test (****, P < 0.0001). All error bars are SEM and n = number of cells. All values were normalized to the mean anillin::GFP intensity at the cell equator in control. Scale bar is 5μm.

A

	Old conditions	New conditions
Transfection Reagent	Oligofectamine	Interferin
Transfection Method	Forward	Reverse
siRNA Conc.	200nM	10nM
Knockdown duration	48 hours	72 hours
Cell cycle synchronized	No	Yes

B

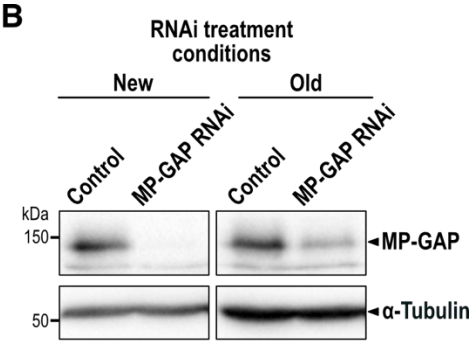

Figure 11: Comparison of MP-GAP knockdown efficiency with two different siRNA transfection protocols. (**A**) Table summarizing key differences in old and new experimental conditions for RNAi-mediated knockdown. **(B)** Immunoblots comparing MP-GAP knockdown efficiency achieved by the two siRNA transfection methods new and old. In the old method, 200nM siRNA was mixed with oligofectamine in optimem and added to the cells 24 hours after seeding. Cells were incubated for 48 hours at 37°C. In the new method used in our RNAi screen, 10nM siRNA was mixed with INTERFERin in optimem and cell suspension was added. Cell cycle was synchronized and total duration of RNAi treatment was 72 hours at 37°C. α-tubulin was used as a loading control.

4.1.3 Performing the primary screen

After establishing the screening workflow, I performed the RNAi screen at the Screening Facility of Max Planck Institute of Molecular Cell Biology and Genetics (MPI-CBG) with the help of Dr. Martin Stoeter. We transfected the HeLa cells expressing anillin::GFP and mKate2::α-tubulin with Dharmacon druggable human genome library, where four different siRNAs were pooled to target one gene. The library covers 7,553 genes that are considered to be potential targets for drugs and includes kinases, phosphatases, proteases, GPCRs (G-protein coupled receptors), ubiquitin ligases etc. and therefore serve as an excellent collection of genes for RNAi screen. After siRNA transfection, cells were synchronized in cell cycle and fixed by following the workflow depicted in the Figure 9D. DNA was stained with DAPI and cytoplasm was stained with CellMask Blue, so that it could be used for segmenting cells in automated image analysis. In total, 7,553 genes were knockdown which were distributed on thirty-three 384-well plates (Figure 12A). Positive controls (MP-GAP, Ect2, nocodazole and BI2536), negative control (mock) and siRNA transfection controls (Eg5 and GFP) were included on every screening plate. Eg5 or kinesin-like protein 11 (KIF11) is a plus-end-

directed motor protein which is required for assembly of bipolar mitotic spindle (Blangy et al., 1995). Eg5 depletion leads to pronounced cell death after cells arrest in mitosis due to formation of monopolar spindles (Blangy et al., 1995; Chin and Herbst, 2006; Mayer et al., 1999; Tao et al., 2005). Eg5 RNAi phenotype is so strong that it can be visualized simply by observing samples under a compound microscope equipped with 10x objective. Thus, Eg5 serves as an excellent control to monitor RNAi transfection efficiency while performing the experiments.

To assess the RNAi knockdown efficiency, Martin Stoeter imaged the screening plates using 10x objective of high-throughput imaging microscope Yokogawa CV7000 and performed automated image analysis using Cell Profiler and Knime. He segmented individual cells in the images of Eg5, Ect2, and GFP siRNA-treated wells by using fluorescence signal of cytoplasmic stain CellMask blue, DAPI-stained nuclei, and nuclear anillin::GFP. Then he measured the number of cells as well as integral anillin::GFP intensity on these images. The numeric raw data was exported into Knime, where Z scores were calculated by using an automated data analysis workflow. Z-score is the number of standard deviations a given data point lies from the mean and Z-scores are a way to compare 'experimental' population to a 'control' population. If a Z-score is 0, it indicates that the data point is identical to the mean. Z-scores may have positive or negative values, with a positive value indicating the score is above the mean and a negative score indicating it is below the mean. In the screening controls, Eg5 knockdown was expected to result in pronounced cell death phenotype (Blangy et al., 1995; Chin and Herbst, 2006; Mayer et al., 1999; Tao et al., 2005). Indeed, Eg5 RNAi led to a marked decrease in the cell count as compared to the controls (Figure 12B). Similarly, GFP RNAi led to a strong decrease in the integrated nuclear anillin::GFP intensity as compared to the controls (Figure 12C). Ect2 RNAi, however, resulted in an increase in the integrated nuclear anillin::GFP intensity due to accumulation of multinucleated cells formed as a result of failed cytokinesis (Figure 12C). After ensuring high knockdown efficiency, screening plates were imaged on CV7000 (Yokogawa) spinning disk confocal microscope using 40x air objective. Six positions were imaged for each well and ten Z-planes were acquired for each channel namely anillin::GFP, mKate2::α-tubulin and DAPI (Figure 12D).

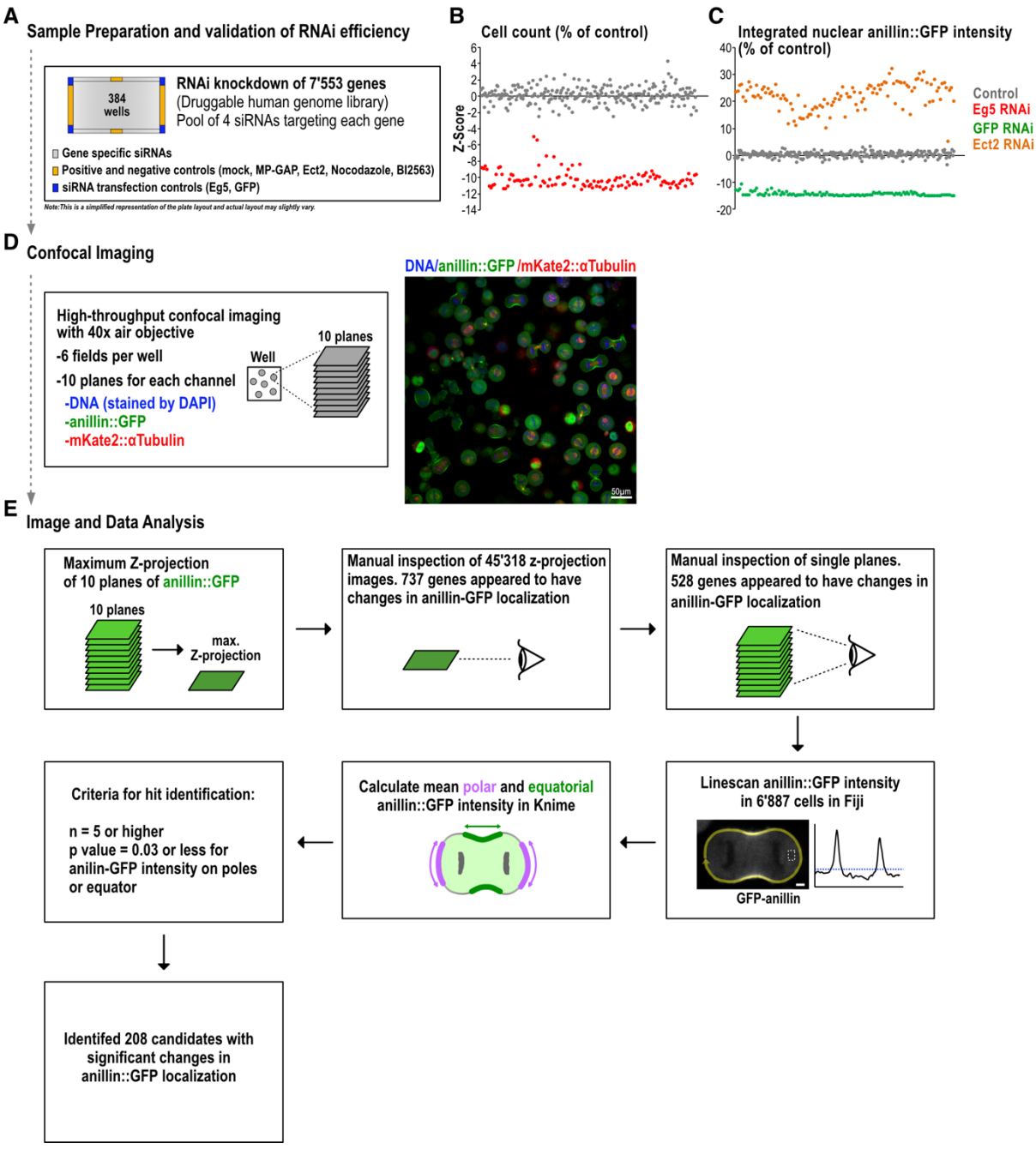

Figure 12: Workflow of the RNAi screen. (**A**) Gene specific and control siRNAs were transferred to 384 well assay plates and mixed with the transfection reagent. HeLa cells expressing anillin::GFP and mKate2::α-tubulin were seeded and cell cycle was synchronized as shown in Figure 9D. (**B**, **C**) Distribution of Z scores for cell count and integrated nuclear GFP intensity for positive controls on the screening plates. (**D**) Six fields of view were imaged for every well using a high-throughput confocal microscope equipped with 40x objective, acquiring ten optical sections for each channel. The example image on the right shows merge of anillin::GFP (green), mKate2::α-tubulin (red) and DNA (blue). Scale bar is 50µm. (**E**) Maximum Z-projection images were generated for anillin::GFP channel which were manually inspected to identify anillin localization defects. Genes were further shortlisted by inspecting individual planes of Z-projections and linescans were manually drawn to quantitatively analyze the localization of anillin::GFP in anaphase cells. Mean

anillin::GFP fluorescence intensity at the equatorial and polar cortex was calculated in Knime and compared to negative controls to identify statistically significant changes.

There were a few known regulators of cell division among the genes that were knockdown in the primary screen. To check whether the phenotypes caused by inhibiting these genes could be reproduced in the primary screen, I compared their published phenotypes to that observed in the primary screen (Table 16). Total number of cells in six 40x images of each well were manually counted and classified as interphase, prometaphase/metaphase and anaphase cells. In addition, percentage of mono-, bi- and multinucleated cells was measured on 10x images where elevated numbers multinucleated cells were seen. Plk1 is involved in regulating different steps of cell division like mitotic checkpoints, centrosome maturation, bipolar spindle assembly, and cytokinesis (Colicino and Hehnly, 2018). Depletion of Plk1 in HeLa cells was previously reported to inhibit cell proliferation, induce G2/M arrest and apoptosis (Liu and Erikson, 2003b; 2003a; Liu et al., 2006). Consistently, Plk1 depletion in the primary screen led to a strong reduction in the number of surviving cells after 72 hours of transfecting Plk1 siRNA (39 cells as compared to >450 cells in control; Table 16). Due to insufficient number of mitotic cells, it is not possible to comment on whether Plk1 depletion also induced bipolar spindle formation. Another group of microtubule-based motor proteins called Kinesins play crucial role in chromosome alignment, formation and elongation of bipolar spindle (Zhu et al., 2005). In HeLa cells, Eg5 and KIF2A RNAi increased the proportion of cells with monopolar spindles, whereas KIF18A and CENP-E (Kinesin 7 family member) RNAi led to misaligned chromosomes at the metaphase plate. In addition, KIF2A depletion was reported to inhibit cell proliferation in MDA-MB-231 breast cancer cell line (Wang et al., 2014). Depletion of Eg5 (Blangy et al., 1995; Chin and Herbst, 2006; Mayer et al., 1999; Tao et al., 2005), KIF18A (Janssen et al., 2018; Zhang et al., 2010) and inhibition of CENP-E (Qian et al., 2010; Schaar et al., 1997) were also shown to result in increased cell death. In the primary screen, depletion of all the four kinesins (Eg5, KIF18A, KIF2A and CENP-E) led to increased cell death (>120 cells survived as compared to more than 450 cells in control; Table 16). Again, as very few mitotic cells were found (Table 16) in Eg5 and KIF2A depleted wells, it is not possible to comment on the spindle abnormality phenotype. Also, the high throughput imaging conditions in the primary screen were optimised for quantification of anillin::GFP and are not suitable to detect small changes in chromosome misalignment. Therefore, whether CENP-E and KIF18A RNAi caused errors in chromosome alignment cannot be addressed. Next, Polo-like kinase 4 (Plk4) is mainly involved in centriole duplication and its depletion leads to progressive reduction in the number of centriole within

a cell (Bettencourt-Dias et al., 2005; Habedanck et al., 2005). As centrioles were not fluorescently-tagged or immunostained, this phenotypes could not be investigated. However, in the screen, a marked decrease in the number of anaphase cells (and not metaphase) was observed after Plk4 RNAi (4 anaphase cells as compared to 22-23 in control; Table 16), indicating towards abnormalities in cell cycle progression. Depletion of another cell cycle regulator BUB1B (Budding Uninhibited By Benzimidazoles 1B), which inhibits progression into anaphase until all the kinetochores are properly attached to the mitotic spindle (Cleveland et al., 2003), led to a strong reduction in the number of metaphase and not anaphase cells (51 metaphase cells compared to >200 in controls; Table 16). This seems to be consistent with the findings of Meraldi et. al., who showed that depletion of BUB1B in HeLa cells accelerated the mitotic progression into anaphase (Meraldi et al., 2004). Also, BUB1B RNAi resulted in mild multinucleation phenotype (20% multinucleated cells compared to 3% to 8% in controls; Table 16). Finally, phenotypes of two related-kinases, Aurora A and Aurora B, which have many regulatory roles from interphase to abscission were also investigated in the primary screen. Aurora A is required for entry into mitosis, maturation and separation of centrosomes, bipolar spindle assembly, chromosome alignment and cytokinesis (Marumoto et al., 2005). Aurora B is involved in chromosome alignment at metaphase plate, satisfying spindle assembly checkpoint (SAC), sister chromatid separation and cytokinesis (Marumoto et al., 2005; Willems et al., 2018). Depletion of both Aurora A (Marumoto et al., 2003) and Aurora B (Delaval et al., 2004) was reported to result in accumulation of multinucleated cells. Consistently in the primary screen, Aurora A and Aurora B depletion resulted in 18% and 30% multinucleated cells respectively as compared to 3% to 8% multinucleated cells in control (Table 16). Aurora B depletion also led to reduced number of mitotic cells (anaphase and metaphase; Table 16) as compared to controls, which could be due to apoptotic fate of polyploid cells. In addition to the multinucleation phenotype, Aurora A depletion was expected to increase the number of cells having multipolar spindles and decrease the number of anaphase cells due to mitotic arrest in G2M (Marumoto et al., 2003). But, these two phenotypes were not observed in the primary screen, indicating that Aurora A was not properly depleted. Overall, the phenotypes observed after knocking down these cell cycle genes were similar to that published in previous reports.

Table 16: Cell count of some mitotic regulators in the primary screen

		Number of Cells				
Gene Symbol	**Plate**	**Interphase**	**Prometa & Metaphase**	**Anaphase**	**Total**	**Observation**
PLK1	301	26	13	0	39	Increased cell death
KIF2A	319	95	17	0	112	Increased cell death
KIF18A	319	95	17	0	112	Increased cell death
Eg5	312	100	19	0	119	Increased cell death
CENP-E	313	92	45	4	141	Increased cell death
PLK4	308	221	133	4	358	No overt phenotype
BUB1B	308	308	51	15	299	19.8% Multinucleated cells
AURKA	301	255	145	17	417	18% Multinucleated cells
AURKB	308	236	73	6	315	30% Multinucleated cells
Control	312	242	217	23	482	3% to 8% multinucleated cells
Control	313	315	276	30	621	
Control	301	208	238	22	468	
Control	319	262	202	23	487	
Control	308	266	236	19	521	

To identify the candidate genes, we had initially planned for our collaborator Martin Stoeter to perform automated image analysis in Cell Profiler. The image analysis workflow was envisioned to consist of two main parts: (a) segmentation and identification of anaphase cells and (b) measuring cortical anillin localization in the identified anaphase cells. To segment individual cells and classify them into anaphase or metaphase, fluorescent signals of DAPI, mKate-tubulin, cytoplasmic cell mask blue and cell membrane (stained by wheat-germ agglutinin) were used in a workflow having over 40 modules. However, when the classification obtained using this pipeline was compared with manual classification, Martin Stoeter found that many anaphase cells were not recognized and more worryingly, about 40% of the cells were wrongly classified into anaphase. To determine errors committed by the automated analysis, he manually classified more than 3700 cells in the images bearing segmentation boundaries overlaid by the software. The nature of these errors prompted him to use unique morphological characteristics of anaphase cells to exclude wrongly identified anaphase cells. Cells in anaphase are elongated with progressive indentation at centre of the cell. Notably, the two segregating DNA masses are largely parallel to each other and are similar in area and intensity. This strategy of filtering out wrong anaphase cells during data analysis increased the accuracy of automated image analysis to 87 percent. However, the

anaphase cells missed by the image analysis program could not be recovered. This analysis was performed on maximum intensity Z-projections of 10 confocal planes. This is because anaphase cells were present in different Z planes and it was not possible to automatically identify and select best Z-planes from every stack. Generating maximum z-projection solved these problems, but, it led to other difficulties in image segmentation. Cells originally not in the same Z-plane, frequently appeared sticking together in a Z-projection image. Such closely lying objects were extremely difficult to segment and led to high error rate or contributed to the proportion of anaphase cells that were not recognized by the program. We lowered the cell density in our samples to minimize cell clumping. But, it led to decrease in the number of anaphase cells in the samples. One solution could be to identify and remove undesired objects (round cells, bright objects etc.) from each image in a stack and then create z-projection for further analysis, but this approach would increase the image processing time by many folds. Alternatively, 3D-segmentation (in Fiji) could be used on the entire stack to segment and identify the anaphase cells. However, we were unable to test the latter two approaches due to complexities involved. Overall, we were unsuccessful in developing an automated image analysis program for the RNAi screen. As a result, I had to carry out manual image analysis to identify the candidates controlling anillin localization in anaphase cells.

First, I generated maximum Z-projections of anillin channel by collapsing ten anillin::GFP planes into one image (Figure 12E). This resulted in six anillin::GFP images for each gene corresponding to the six positions that were imaged within a well. In total, 45,318 images were generated for 7,553 genes and I visually inspected all the images to identify candidates causing an increase in anillin::GFP at the cell poles or decrease in anillin::GFP at the cell equator. In this way, 737 candidates were shortlisted which appeared to have changes in anillin::GFP localization during anaphase. For these 737 candidates, I repeated the visual inspection on the single planes of anillin::GFP images that were previously used to generate the Z-projections (44,220 images) and further shortlisted 528 candidate genes. Then, I linescaned all the anaphase cells present for each candidate in Fiji (6,887 cells) and calculated the mean anillin::GFP intensity at the equator and at the cell poles in Knime using an automated data analysis workflow. Manual calculation of mean anillin fluorescence intensities at equator and poles is very tedious, repetitive and time-consuming task. It was nearly impossible to perform manual calculations for more than 6000 cells. Therefore, with the help of Martin Stoeter, I established a data analysis workflow in Knime to calculate different parameters like mean anillin fluorescence intensity at equator and poles, anillin zone

width at equator, and distance between two DNA masses in anaphase cells using the raw pixel values obtained from linescans in Fiji.

On an average, 12±5 anaphase cells for control and 11±5 anaphase cells for shortlisted genes were measured (genes having less than 5 anaphase cells were excluded from the analysis). Quantitative and statistical analysis (student's t-test; p-value cut-off for significance 0.03 or less) revealed 208 candidates having significant changes in anillin localization at the poles and/or equator (Figure 12E). Out of 208 candidates, 139 genes resulted in an increase in anillin::GFP at cell poles, 38 genes caused an increase in anillin::GFP at cell equator and 52 genes led to decrease in anillin::GFP at the cell equator (Figure 13). Out of 38 genes that led to increased anillin::GFP at the cell equator, 20 genes also resulted in increased anillin::GFP at the cell poles (Figure 13). On the other hand, out of 52 genes that led to decreased anillin::GFP at the cell equator, only 1 gene led to an increase in anillin::GFP at the cell poles (Figure 13). Please note that the list of all 208 candidates is not shown in my thesis as many of these genes are under further investigation in the laboratory.

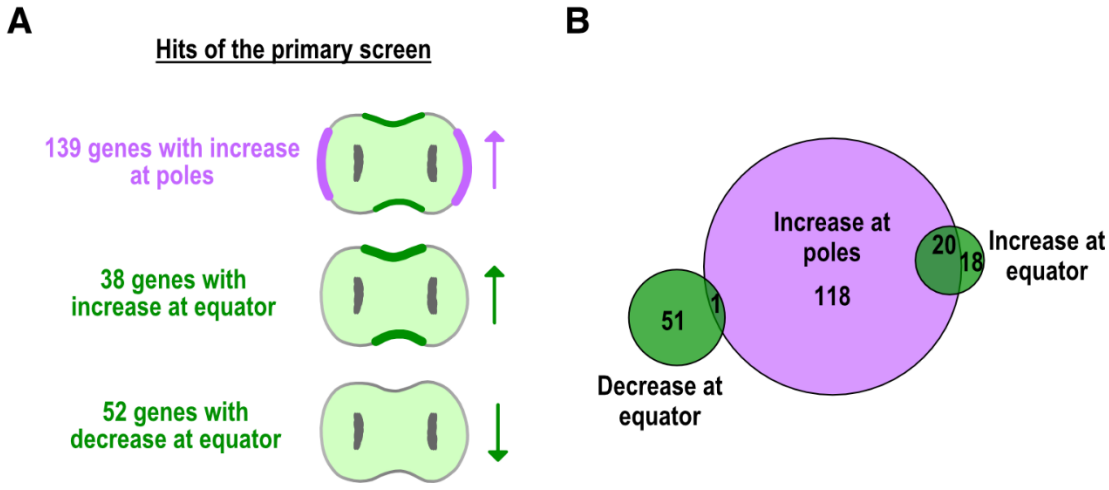

Figure 13: Summary of candidates identified in the primary. (**A**) Schematic showing classification of genes identified in the primary screen into three phenotypic categories. (**B**) Venn Diagram illustrating the overlap of identified genes in different phenotypic classes.

4.1.4 Performing the secondary screen

To further confirm the 208 candidate genes identified in the primary screen, a secondary screen was performed. Cells were transfected with pool of four siRNAs targeting a gene from Dharmacon library and cell cycle was synchronized as in the primary screen. Screening

plates were imaged on CV7000 (Yokogawa) spinning disk confocal microscope using 40x air objective. Eleven positions were imaged for each well and ten Z-planes were acquired for anillin::GFP, mKate2::α-tubulin and DAPI. The experiment was performed by Cordula Andree a senior technician at the Screening Facility of MPI-CBG and imaging was carried out by Martin Stoeter. To measure the cortical localization of anillin::GFP during anaphase, I linescaned 12±5 anaphase cells for each candidate in Fiji (3,334 cells) and calculated the mean anillin::GFP intensity at the equator and at the cell poles using automated data analysis workflow in Knime (Figure 14A). Among 208 candidate genes, two could not be analysed as they had less than two anaphase cells. Quantitative and statistical analysis (student's t-test; $p<0.05$) revealed 21 candidates having significant changes in anillin localization at the poles or equator (Figure 14A-C; Table 17-18) and showed same trend as in the primary screen. Out of 21 candidates, 7 genes resulted in an increase in anillin::GFP at cell poles (Figure 14E and 15; Table 17), 2 genes caused an increase in anillin::GFP at cell equator (Figure 14D and 17; Table 18) and 12 genes led to decrease in anillin::GFP at the cell equator (Figure 14D and 16; Table 18).

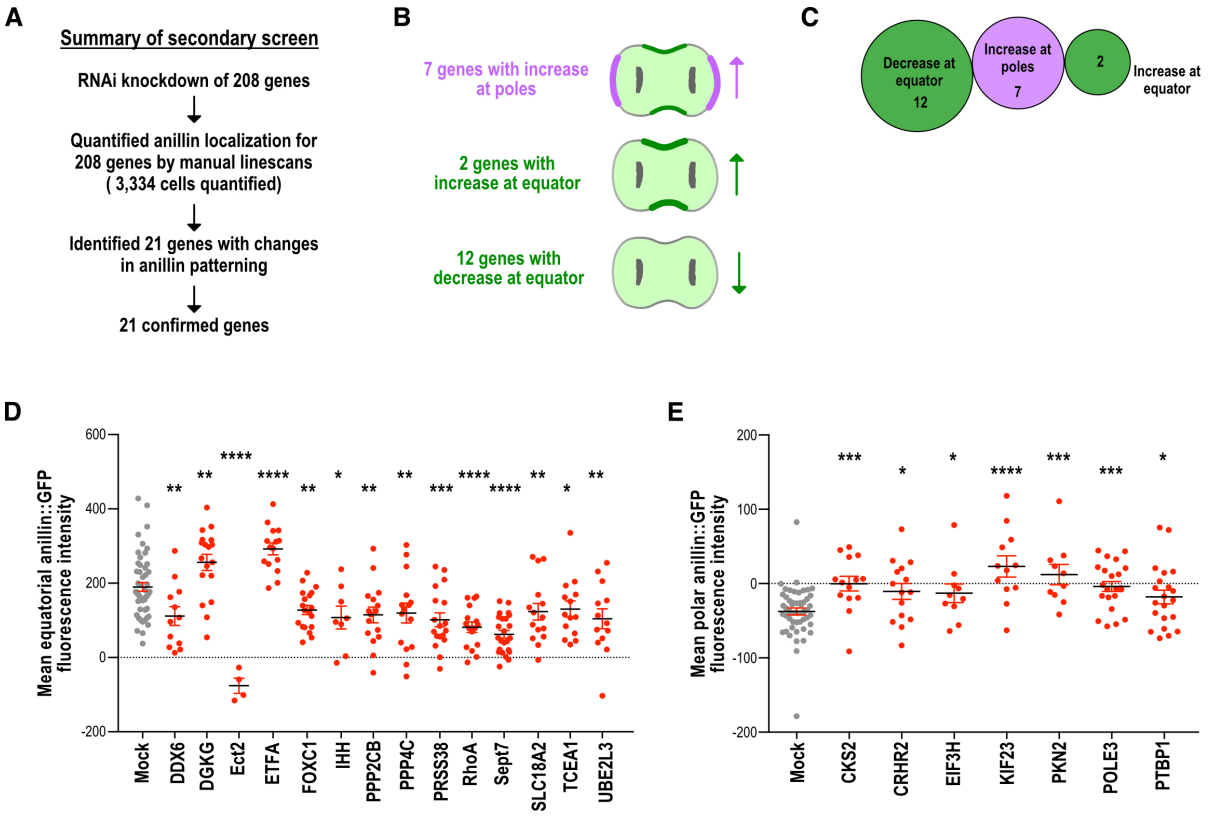

Figure 14: Summary of outcome of the secondary screen. (**A**) Flow chart depicting procedure for confirming the candidates genes identified in the primary screen. (**B**) Schematic representation of genes confirmed in the secondary screen into three phenotypic classes. (**C**) Venn Diagram illustrating the overlap of identified genes in different phenotypic classes. Graphs showing mean anillin::GFP intensity at (**D**) the cell equator and (**E**) at the cell

poles after RNAi knockdown of 21 candidate genes. Pixel intensities were measured by drawing a linescan (8 pixels wide) around the cell cortex in Fiji and mean values were calculated in Knime. All the differences are statistically significant and were tested by Student's t-test (****, P < 0.0001; ***, P < 0.001; **, P <0.01; *, P < 0.05). p-values are reported in Tables 17 and 18. All error bars are SEM. Scale bar is 5µm.

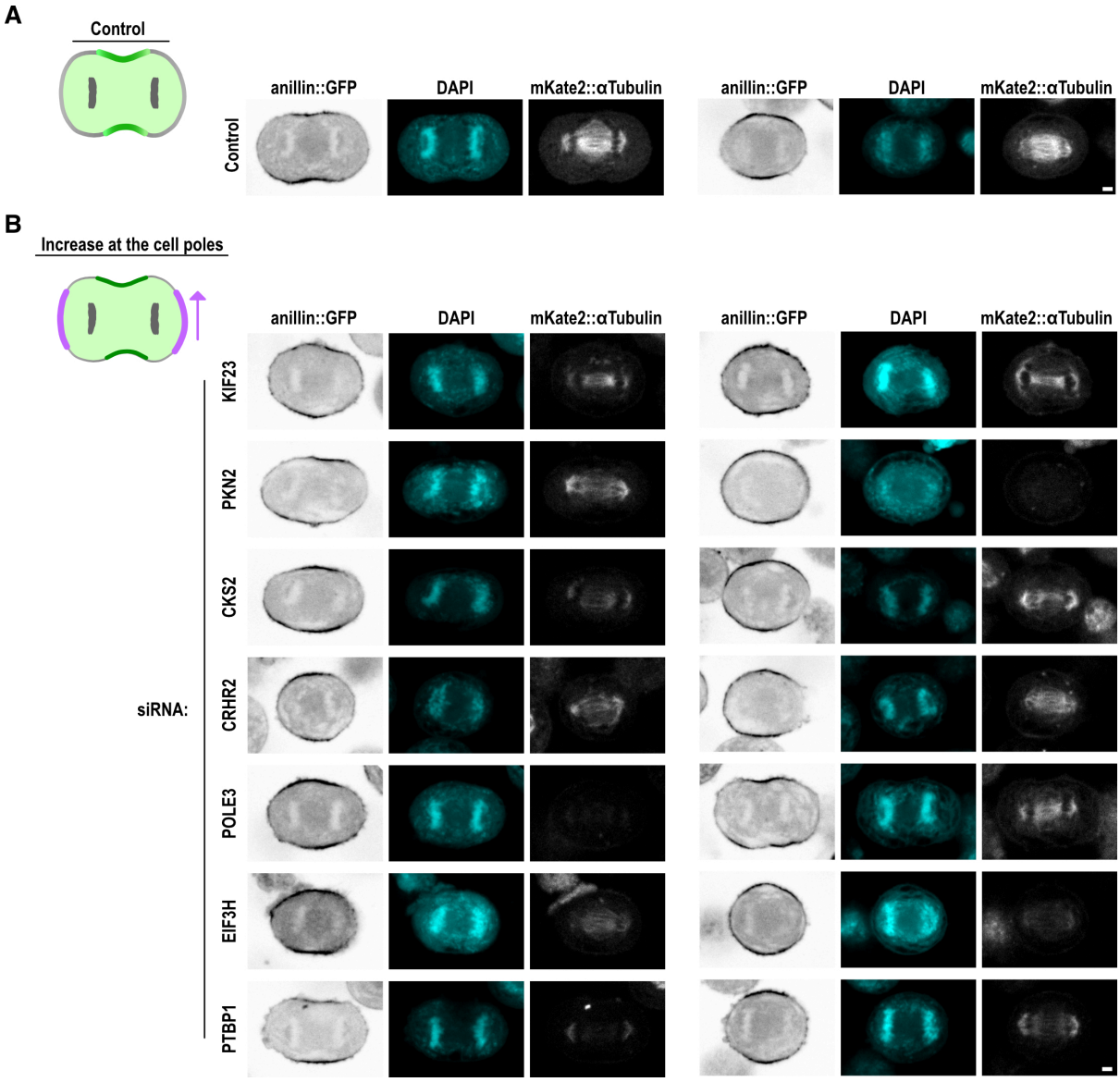

Figure 15: Example images of candidate genes having increased anillin::GFP localization at cell poles. Confocal images of HeLa cells expressing anillin::GFP (inverted grayscale image), mKate2::αTubulin (grayscale image) and DAPI-stained DNA (cyan) treated with (**A**) control or (**B**) gene-specific siRNAs. Scale bar is 5µm.

Table 17: Candidates confirmed in the secondary screen having significantly different anillin::GFP intensity at the cell poles

			Secondary Screen					Primary Screen				
S. No.	**Gene Name**	**Gene Symbol**	**n**	**Mean Intensity**	**Mean Intensity of Mock**	**Trend**	**p-value**	**n**	**Mean Intensity**	**Mean Intensity of Mock**	**Trend**	**p-value**
1	CDC28 protein kinase regulatory subunit 2	CKS2	14	-0.010	-37.4	increase	0.0006	13	3.6	-47.5	increase	0.0026
2	corticotropin releasing hormone receptor 2	CRHR2	15	-10.6	-37.4	increase	0.0125	12	5.9	-28.7	increase	0.0183
3	eukaryotic translation initiation factor 3, subunit H	EIF3H	10	-13.0	-37.4	increase	0.0462	9	-16.8	-49.0	increase	0.0120
4	kinesin family member 23	KIF23	12	23.2	-37.4	increase	0.0000	9	42.5	-48.8	increase	0.0000
5	protein kinase N2	PKN2	10	12.2	-37.4	increase	0.0001	12	6.7	-47.5	increase	0.0014
6	polymerase (DNA directed), epsilon 3, accessory subunit	POLE3	22	-3.9	-37.4	increase	0.0002	9	10.8	-57.7	increase	0.0003
7	polypyrimidine tract binding protein 1	PTBP1	21	-17.9	-37.4	increase	0.0421	13	-30.8	-48.8	increase	0.0142

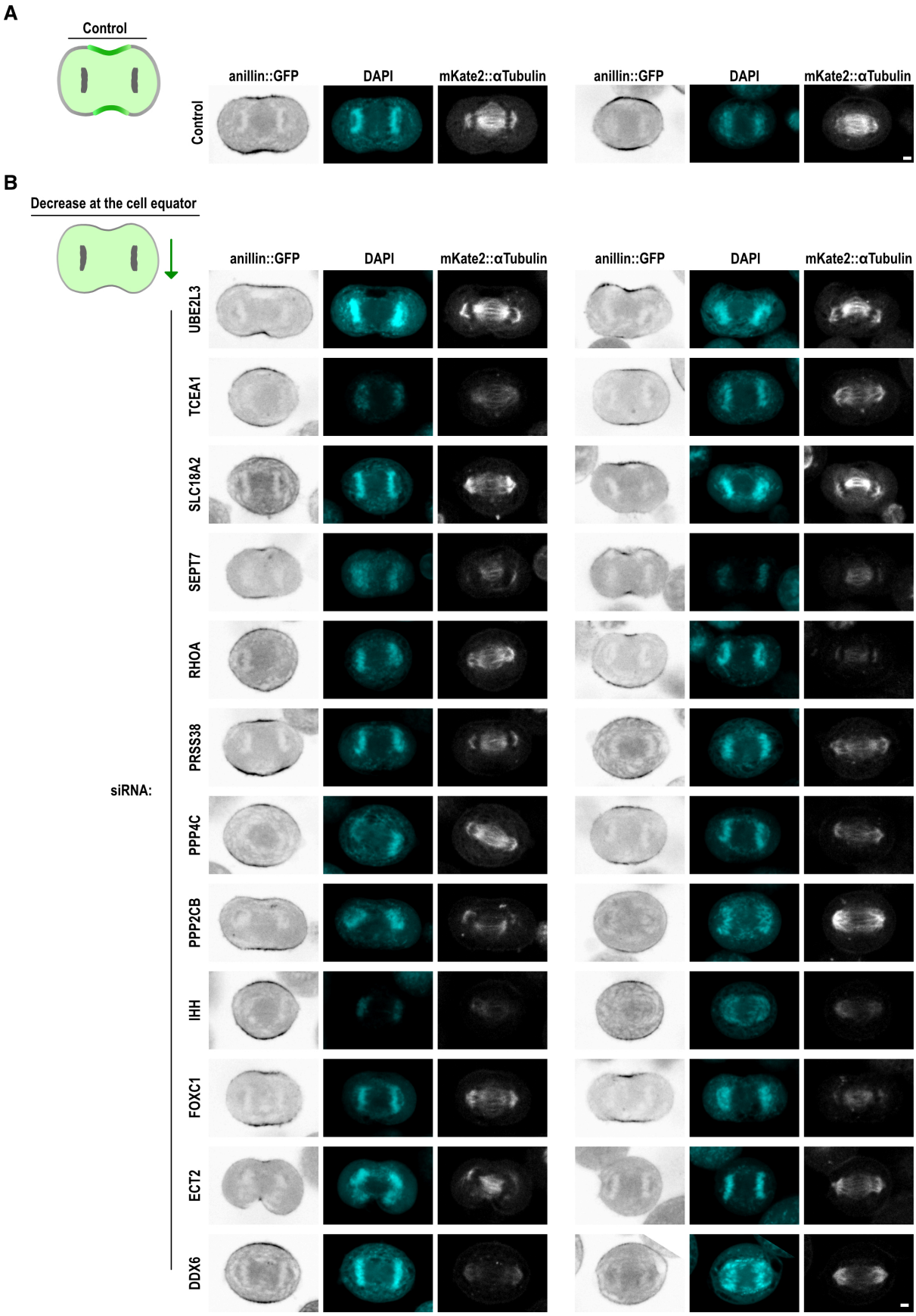

Figure 16: Example images of candidate genes having decreased anillin::GFP localization at cell equator. Confocal images of HeLa cells expressing anillin::GFP

(inverted grayscale image), mKate2::αTubulin (grayscale image) and DAPI-stained DNA (cyan) treated with (**A**) control or (**B**) gene-specific siRNAs. Scale bar is 5μm.

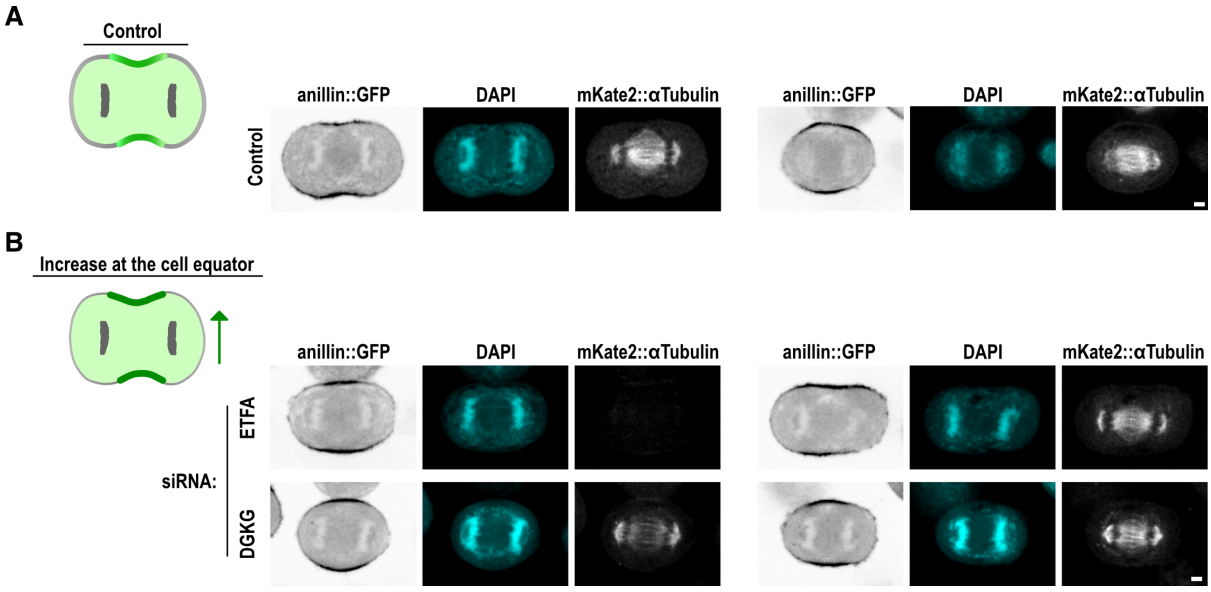

Figure 17: Example images of candidate genes having increased anillin::GFP localization at cell equator. Confocal images of HeLa cells expressing anillin::GFP (inverted grayscale image), mKate2::αTubulin (grayscale image) and DAPI-stained DNA (cyan) treated with (**A**) control or (**B**) gene-specific siRNAs. Scale bar is 5μm.

Table 18: Candidates confirmed in the secondary screen having significantly different anillin::GFP intensity at the cell equator

			Secondary Screen					Primary Screen				
S. No.	**Gene Name**	**Gene Symbol**	**n**	**Mean Intensity**	**Mean Intensity of Mock**	**Trend**	**p-value**	**n**	**Mean Intensity**	**Mean Intensity of Mock**	**Trend**	**p-value**
1	DEAD box helicase 6	DDX6	12	111.6	189.9	decrease	0.0051	8	149.3	235.1	decrease	0.0096
2	diacylglycerol kinase, gamma 90kDa	DGKG	18	256.2	189.9	increase	0.0062	23	411.9	298.2	increase	0.0161
3	epithelial cell transforming 2	ECT2	4	-75.7	189.9	decrease	0.0000	7	-67.8	210.2	decrease	0.0000
4	electron-transfer-flavoprotein, alpha polypeptide	ETFA	15	292.5	189.9	increase	0.0000	11	343.3	235.1	increase	0.0002
5	forkhead box C1	FOXC1	19	127.9	189.9	decrease	0.0037	12	103.0	220.2	decrease	0.0002
6	indian hedgehog	IHH	8	107.6	189.9	decrease	0.0124	22	239.2	373.6	decrease	0.0000
7	protein phosphatase 2, catalytic subunit, beta isozyme	PPP2CB	16	114.9	189.9	decrease	0.0026	8	224.0	373.6	decrease	0.0009
8	protein phosphatase 4, catalytic subunit	PPP4C	15	119.8	189.9	decrease	0.0086	9	264.3	373.6	decrease	0.0103
9	protease, serine, 38	PRSS38	18	101.4	189.9	decrease	0.0002	10	253.3	373.6	decrease	0.0026
10	ras homolog family member A	RHOA	16	81.6	189.9	decrease	0.0000	11	164.3	235.1	decrease	0.0102
11	septin 7	SEPT7	24	62.5	189.9	decrease	0.0000	19	153.7	210.2	decrease	0.0192
12	solute carrier family 18 (vesicular monoamine transporter), member 2	SLC18A2	15	123.6	189.9	decrease	0.0091	10	57.4	169.9	decrease	0.0147
13	transcription elongation factor A (SII), 1	TCEA1	14	130.4	189.9	decrease	0.0204	8	80.9	220.2	decrease	0.0076
14	ubiquitin-conjugating enzyme E2L 3	UBE2L3	13	104.3	189.9	decrease	0.0021	11	178.6	242.2	decrease	0.0198

In set of screened genes were KIF23 (or MKLP1), Ect2 and RhoA that are expected to change anillin localization based on the current literature. KIF23 was shown to inhibit the RhoA localization on cell poles and thus KIF23 depletion was expected to increase the anillin levels at the poles (Yüce et al., 2005). Ect2 and RhoA depletions were expected to reduce anillin recruitment to the cell equator. As expected, Ect2 and RhoA knockdown significantly reduced anillin::GFP accumulation at the equator (Table 18, Figure 14D and 16) and KIF23 knockdown increased the anillin::GFP at cell poles (Table 17, Figure 14E and 15), both in primary and secondary screens, thereby, confirming the robustness of our screening workflow. Further, Ect2 and Kif23 depletion led to 62% and 33% multinucleated cells mainly due to failed of cytokinesis, consistent with previous reports (Su et al., 2011; Yüce et al., 2005). Knockdown of 2 other candidate genes PRSS38 (Serine Protease 38) and PPP2CB (Protein Phosphatase 2 Catalytic Subunit B) resulted in 17% and 19% multinucleated cells respectively (Table 22). [Here, it should be noted that a comprehensive analysis was not performed to identify genes which resulted in multinucleated cells upon their knockdown. Instead, images from primary screen were manually inspected and genes that led to overt multinucleation defects were shortlisted. 100-200 cells were manually counted for the shortlisted genes and classified as mono-, bi-, multinucleated. Separate multinucleation analysis was not performed for the genes confirmed in the secondary screen].

Table 22: List of candidate genes showing multinucleation upon knockdown

S.No	Gene Name	% Multinucleated cells
1.	ECT2	62
2.	KIF23	33
3.	PRSS38	17
4.	PPP2CB	19
5	Control	3-8

For the identified 21 candidates, anillin zone width, length of the spindle midzone (Figure 18B) and cell circumference were also calculated in primary and secondary screen (Tables 19-21). Length of the spindle midzone was measured to find out if the anillin localization defect in 21 candidates was a consequence of changes in the dimension of the spindle midzone. Cell circumference was also measured for the same reason to determine whether the observed changes in anillin localization were a side-effect of changes in cell size.

The zone width of anillin::GFP was defined as the width of peak of anillin::GFP fluorescence intensity at half the maximum value (Figure 18A). RhoA and Septin7, having significantly reduced anillin::GFP localization at the cell equator, were also found to have significantly reduced anillin::GFP zone width as compared to the controls (Table 19). Conversely, KIF23 or MKLP1 having significantly higher anillin localization on the cell poles, were also found to have significantly broader zone of anillin::GFP at the cell equator (Table 19). Remaining 18 candidate genes did not show any significant difference in anillin::GFP zone at the cell equator (Table 19).

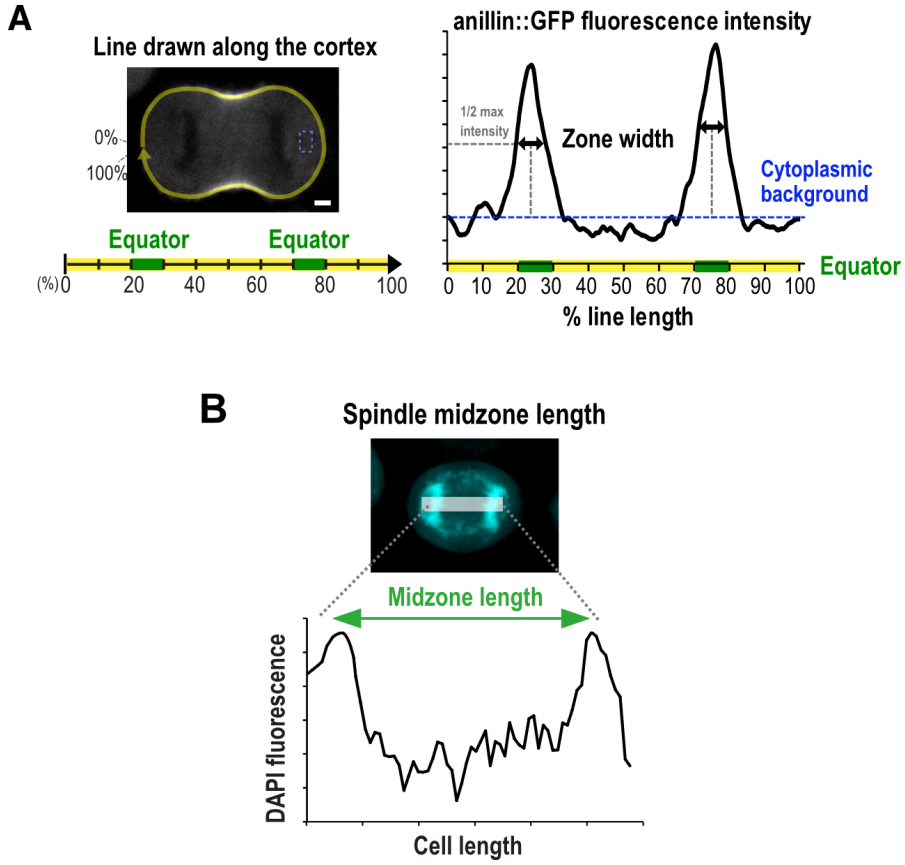

Figure 18: Quantification of anillin zone width and spindle midzone length. (A) Anillin::GFP localization was analysed at the cell cortex by drawing a linescan (8 pixels wide) around the cell (start 0% and end 100%). Mean cytoplasmic background intensity was subtracted from the linescan. The anillin zone width was defined as the width of peak at half maximum anillin fluorescence intensity. (**B**) The length of the spindle midzone was measured by drawing linescans (8 pixel wide) across the center of the cell. Using the pixel intensities of DAPI fluorescence signal, distance between the two maxima of DAPI fluorescence intensity was calculated in Knime and referred to as spindle midzone length.

To measure the length of spindle midzone, a linescan was drawn across the two masses of DNA in Fiji (Figure 18B). The DAPI pixel intensity profiles were imported into Knime and

the length of spindle midzone was defined as the distance between two intensity peaks. None of the 21 candidates were found to have significant changes in the length of spindle midzone as compared to the controls (Table 20). Similarly, 19/21 candidates did not show any significant changes in the cell perimeter (Table 21). Knockdown of only two candidate genes KIF23 and POLE3, both of which resulted in increased localization of anillin::GFP on the cell poles, led to slight decrease and increase in the cell perimeter, respectively (Table 21). Next, to determine any abnormalities in the mitotic spindle caused by knockdown of 21 candidate genes, I attempted to measure mKate2::αTubulin fluorescence intensity in the same cells where anillin::GFP was quantified. However, the expression of mKate2::αTubulin was quite variable as compared to anillin::GFP and thus not suitable for meaningful quantifications. The manual analysis of images did not show any overt abnormalities in the mitotic spindle after knockdown of these 21 candidate genes. In addition, abnormalities in chromosome segregation and position of metaphase plate were not apparent in the manual analysis of images of DAPI channel. Overall, the changes in anillin::GFP localization observed for 21 candidate genes do not seem to be a consequence of aberrant mitotic spindle, or spindle midzone, but needs to be further validated in future experiments.

Table 19: Zone width of anillin::GFP at cell equator during anaphase measured for 21 candidates in primary and secondary screen

		Secondary Screen					Primary Screen					Confirmed Trend
S. No.	Gene Symbol	n	Zone width	Zone width of Mock	p-value	Trend	n	Zone width	Zone width of Mock	p-value	Trend	
1	DDX6	12	0.128	0.130	ns	no change	8	0.125	0.108	ns	no change	no change
2	DGKG	18	0.148	0.130	ns	no change	23	0.154	0.124	0.0220	increase	no change
3	ECT2	4	0.000	0.130	0.0000	decrease	7	0.006	0.123	2.6E-06	decrease	decrease
4	ETFA	15	0.148	0.130	ns	no change	11	0.106	0.108	ns	no change	no change
5	FOXC1	19	0.125	0.130	ns	no change	12	0.098	0.115	ns	no change	no change
6	IHH	8	0.141	0.130	ns	no change	22	0.106	0.105	ns	no change	no change
7	PPP2CB	16	0.107	0.130	ns	no change	8	0.115	0.105	ns	no change	no change
8	PPP4C	15	0.102	0.130	ns	no change	9	0.105	0.105	ns	no change	no change
9	PRSS38	18	0.120	0.130	ns	no change	10	0.098	0.105	ns	no change	no change
10	RHOA	16	0.084	0.130	0.0000	decrease	11	0.087	0.108	0.0088	decrease	decrease
11	SEPT7	24	0.085	0.130	0.0000	decrease	19	0.090	0.123	0.0291	decrease	decrease
12	SLC18A2	15	0.092	0.130	0.0069	decrease	10	0.097	0.115	ns	no change	no change
13	TCEA1	14	0.107	0.130	ns	no change	8	0.096	0.115	ns	no change	no change
14	UBE2L3	13	0.125	0.130	ns	no change	11	0.119	0.108	ns	no change	no change
15	CKS2	14	0.156	0.130	0.0390	increase	13	0.143	0.124	ns	no change	no change
16	CRHR2	15	0.177	0.130	0.0013	increase	12	0.118	0.105	ns	no change	no change
17	EIF3H	10	0.155	0.130	ns	no change	9	0.149	0.111	ns	no change	no change
18	KIF23	12	0.220	0.130	0.0048	increase	9	0.222	0.115	0.0050	increase	increase
19	PKN2	10	0.190	0.130	ns	no change	12	0.109	0.124	ns	no change	no change
20	POLE3	22	0.157	0.130	ns	no change	9	0.112	0.115	ns	no change	no change

21	PTBP1	21	0.146	0.130	ns	no change	13	0.136	0.115	ns	no change	no change

Table 20: Length of spindle midzone for for 21 candidates in primary and secondary screen

		Primary Screen					Secondary screen					Confirmed Trend
S. No.	**Gene Symbol**	**n**	**Mean normalized spindle midzone length**	**Mean normalized spindle midzone length of Mock**	**p-value**	**Trend**	**n**	**Mean normalized spindle midzone length**	**Mean normalized spindle midzone length of Mock**	**p-value**	**Trend**	
1	DDX6	8	0.572	0.515	0.001	increase	12	0.472	0.474	0.985	No change	No change
2	DGKG	23	0.485	0.520	0.039	decrease	18	0.477	0.474	0.762	No change	No change
3	ECT2	7	0.573	0.558	0.632	No change	4	0.421	0.474	0.115	No change	No change
4	ETFA	11	0.495	0.515	0.207	No change	15	0.458	0.474	0.412	No change	No change
5	FOXC1	12	0.584	0.549	0.104	No change	19	0.448	0.474	0.202	No change	No change
6	IHH	22	0.499	0.488	0.339	No change	8	0.481	0.474	0.864	No change	No change
7	PPP2CB	8	0.502	0.488	0.492	No change	16	0.477	0.474	0.785	No change	No change
8	PPP4C	9	0.475	0.488	0.340	No change	15	0.428	0.474	0.233	No change	No change
9	PRSS38	10	0.492	0.488	0.919	No change	18	0.490	0.474	0.257	No change	No change
10	SEPT7	19	0.548	0.558	0.496	No change	24	0.512	0.474	0.010	Increase	No change
11	RHOA	11	0.501	0.515	0.410	No change	16	0.449	0.474	0.175	No change	No change
12	SLC18A2	10	0.556	0.528	0.380	No change	15	0.470	0.474	0.918	No change	No change
13	TCEA1	8	0.562	0.549	0.622	No change	14	0.476	0.474	0.810	No change	No change
14	UBE2L3	11	0.524	0.508	0.489	No change	13	0.492	0.474	0.310	No change	No change
15	CKS2	13	0.473	0.520	0.017	decrease	14	0.498	0.474	0.149	No change	No change
16	CRHR2	12	0.458	0.488	0.020	decrease	15	0.498	0.474	0.160	No change	No change
17	EIF3H	9	0.568	0.549	0.375	No change	10	0.485	0.474	0.556	No change	No change

18	KIF23	9	0.513	0.549	0.141	No change	12	0.481	0.474	0.655	No change	No change
19	PKN2	12	0.484	0.520	0.073	No change	10	0.444	0.474	0.185	No change	No change
20	POLE3	9	0.562	0.528	0.285	No change	22	0.458	0.474	0.387	No change	No change
21	PTBP1	13	0.568	0.549	0.364	No change	21	0.458	0.474	0.386	No change	No change

Table 21: Perimeter of anaphase cells for 21 candidates in primary and secondary screen

		Primary Screen					Secondary Screen					Confirmed Trend
S. No.	**Gene symbol**	**n**	**Mean cell circumfrence (AU)**	**Mean cell circumfrence of Mock (AU)**	**p-value**	**Trend**	**n**	**Mean cell circumfrence (AU)**	**Mean normalized distance of Mock (AU)**	**p-value**	**Trend**	
1	DDX6	8	4.841	5.123	0.145	No change	12	5.276	5.482	0.203	No change	No change
2	DGKG	23	4.618	4.943	0.000	decrease	18	5.204	5.482	0.054	No change	No change
3	ECT2	7	6.004	5.306	0.000	increase	4	5.323	5.482	0.560	No change	No change
4	ETFA	11	5.488	5.123	0.007	increase	15	5.502	5.482	0.924	No change	No change
5	FOXC1	12	5.224	5.378	0.263	No change	19	5.244	5.482	0.076	No change	No change
6	IHH	22	5.313	5.184	0.367	No change	8	5.057	5.482	0.038	decrease	No change
7	PPP2CB	8	4.865	5.184	4.01E-08	decrease	16	5.765	5.482	0.069	No change	No change
8	PPP4C	9	5.903	5.184	1.66E-05	increase	15	5.397	5.482	0.571	No change	No change
9	PRSS38	10	5.081	5.184	0.313	No change	18	5.251	5.482	0.093	No change	No change
10	SEPT7	19	5.359	5.306	0.610	No change	24	5.299	5.482	0.057	No change	No change
11	RHOA	11	5.265	5.123	0.239	No change	16	5.661	5.482	0.443	No change	No change
12	SLC18A2	10	5.184	5.359	0.412	No change	15	5.550	5.482	0.676	No change	No change

13	TCEA1	8	4.897	5.378	0.000	decrease	14	5.522	5.482	0.827	No change	No change
14	UBE2L3	11	4.829	5.056	0.074	No change	13	5.395	5.482	0.590	No change	No change
15	CKS2	13	4.927	4.943	0.991	decrease	14	5.501	5.482	0.925	No change	No change
16	CRHR2	12	5.181	5.184	0.779	decrease	15	5.423	5.482	0.696	No change	No change
17	EIF3H	9	4.995	5.279	0.067	decrease	10	5.188	5.482	0.096	No change	No change
18	KIF23	9	5.215	5.378	0.308	decrease	12	5.178	5.482	0.007	decrease	decrease
19	PKN2	12	5.368	4.943	0.051	increase	10	4.259	5.482	0.125	No change	No change
20	POLE3	9	6.042	5.359	0.000	increase	22	5.781	5.482	0.031	increase	increase
21	PTBP1	13	5.185	5.378	0.153	decrease	21	5.385	5.482	0.433	No change	No change

4.1.5 Brief overview of the candidate genes

In the RNAi screen, 21 genes were identified to be important for normal localization of anillin at the cell cortex. These genes perform different functions in the cell and only 5 genes namely RhoA, Ect2, Sept7, PKN2 and KIF23 are known to be directly involved in cytokinesis. Six genes are mainly involved in regulating transcription and translation. DDX6 (DEAD-Box Helicase 6) is involved in capping of mRNA during degradation and depletion of DDX6 leads to stabilization of transcripts and activation of translation (Jonas and Izaurralde, 2013). FOXC1 (Forkhead Box C1) encodes a transcription factor having DNA-binding forkhead domain which plays a role in diverse cellular and developmental processes (Elian et al., 2018). Some mutations of FOXC1 have also been linked to cancer phenotypes (Elian et al., 2018). TCEA1 (Transcription Elongation Factor A1) plays an important role in rescuing the transcription when RNA Polymerase is blocked to move forward on the template strand (Fish and Kane, 2002; Kettenberger et al., 2003). eIF3h (Eukaryotic Translation Initiation Factor 3 Subunit H) is required for stable assembly of eIF-3 complex which is involved in the initiation of protein synthesis (Masutani et al., 2007). POLE3 (DNA Polymerase Epsilon 3) is a histone fold domain bearing protein which interacts with similar protein POLE4 to contribute in proper DNA transcription and replication (Bellelli et al., 2018). PTBP1 (Polypyrimidine Tract Binding Protein 1) plays role in post-transcriptional regulation of processes like mRNA splicing, translational initiation and mRNA stability (Romanelli et al., 2013). The list of candidate genes also includes two phosphatases. PPP2CB (Protein Phosphatase 2 Catalytic Subunit Beta) is catalytic subunit of Protein Phosphatase 2A (PP2A) and is involved in regulating many cellular processes including protein translation, stress response, apoptosis and cell cycle (Janssens and Goris, 2001). PP2A can modulate activities of many kinases like MAP-kinase, Cyclin-dependent kinases (CDKs), Protein kinase A (PKA), Protein Kinase B (PKB) and Protein Kinase C (Janssens and Goris, 2001). Similar to PPP2CB, PPP4C (Protein Phosphatase 4 Catalytic Subunit) is also implicated in many cellular processes such as maturation of centrosomes, cell migration, apoptosis and regulation of Rho GTPases Cdc42 and Rac1 (Cohen et al., 2005; Martin-Granados et al., 2008). DGKG (Diacylglycerol Kinase Gamma), catalyses phosphorylation of diacylglycerol (DAG) to form phosphatidic acid (PA) which is a secondary messenger having many downstream targets including protein kinase C (Mérida et al., 2017). DGK family in mammals comprises of ten members which are classified into 5 subtypes and DGKA (Diacylglycerol Kinase Alpha) is implicated to have a role in tumour progression (Mérida et al., 2017). CKS2 (Cyclin-Dependent Kinases Regulatory Subunit 2), binds to catalytic subunit of cyclin dependent kinases (Cdk) and is important for their function. CKS2 is

required for metaphase/anaphase transition of first meiosis in mice germ cells (Spruck et al., 2003). In addition, CKS2 has been shown to be upregulated in different malignant tumours (You et al., 2015). Remaining genes in the list have miscellaneous functions. ETFA is alpha subunit of heterodimeric electron transfer flavoproteins (ETF) which shuttles electrons between flavoprotein dehydrogenases (involved in mitochondrial fatty acid and amino acid catabolism) and the respiratory chain (Roberts et al., 1996; Salazar et al., 1997). Indian Hedgehog Homolog (IHH) is a member of Hedgehog family of proteins and plays broad range of roles in developmental processes (Varjosalo and Taipale, 2008). SLC18A2 (Solute Carrier Family 18 Member A2) encodes vesicular monoamine transporter 2 (VMAT2). SLC18A2 is involved in transport of neurotransmitters like dopamine, histamine, serotonin into synaptic vesicles (Rilstone et al., 2013). UBE2L3 (Ubiquitin Conjugating Enzyme E2 L3) as the name suggests is a member of E2 ubiquitin-conjugating enzyme family and is involved in ubiquitinating different proteins in a cell (Moynihan et al., 1996). CRHR2 (Corticotropin Releasing Hormone Receptor 2) belongs to the G-protein coupled receptor 2 family, and binds to corticotropin releasing hormone (CRH) thereby coordinating endocrine responses (Hillhouse and Grammatopoulos, 2006). PRSS38 (Serine Protease 38) has serine endopeptidase activity and not much is known about it.

Two of the most promising candidates confirmed in the screen are Protein Kinase N2 (PKN2) and Septin 7 (Sept7). PKN2 depletion resulted in increased anillin::GFP accumulation at the polar cell cortex indicating towards a role of PKN2 in restricting anillin localization at cell equator during anaphase (Table 17, Figure 14E and 15). PKN2 Ser/Thr Kinase is known to be an effector protein in Rho/Rac signalling pathway and it directly binds to active Rho GTPases (Amano et al., 1996; Flynn et al., 1998; Maesaki et al., 1999; Shibata et al., 1996; Vincent and Settleman, 1997) through the first two N-terminal HR1 domains (Flynn et al., 1998; Maesaki et al., 1999; Shibata et al., 1996). Protein kinase N (PKN) proteins are evolutionarily well conserved and its homologues in *Drosophila* and *C. elegans* (PKN-1) have also been shown to bind active Rho/Rac (Betson and Settleman, 2007; Lu and Settleman, 1999; Qadota et al., 2011). Moreover, PKN2 localizes to the cleavage furrow and mid-body during cytokinesis in HeLa cells in Ect2-dependent manner (Schmidt et al., 2007). Another interesting candidate is Septin 7 and its depletion led to reduced anillin::GFP accumulation at the cell equator (Table 18, Figure 14D and 16). Sept7 is a member of conserved Septin family proteins which is required for normal organization of cytoskeleton (Kremer et al., 2007). Septin proteins are present in the contractile ring and are known to colocalize with actin (Kinoshita et. al., 2002), bind anillin via C-terminal PH domain

(Oegema at. al. 2000; Kinoshita et. al., 2002; Field et al., 2005) and directly interact with myosin II (Joo et. al., 2007). Since Sept7 directly binds anillin and PKN2 binds RhoA, these two candidates were ideal choice to begin further experiments for their characterization in more detail.

4.1.6 PKN2 prevents anillin accumulation at the cell poles

Depletion of PKN2 resulted in increased anillin levels at the cell poles in the primary and secondary screens (Table 17, Figure 14E and 15). In addition to PKN2, PKN1 and PKN3 are also expressed in HeLa cells (Palmer et al., 1994; Mukai, 2003). To investigate whether PKN1 and PKN3 have a similar function in regulating anillin localization in anaphase, I measured cortical anillin::GFP levels on the images acquired in the primary screen after PKN1 and PKN3 RNAi and found no significant difference as compared to the control (Figure 19A). Thus, in the light of this preliminary data PKN2 appears to have a specific role in restricting anillin localization to the cell equator. To further confirm this phenotype, I depleted PKN2 by using only one siRNA instead of a pool of four siRNAs and performed live cell imaging (Figure 19B and C). Similar to findings in the two screens, PKN2 depletion resulted in significant increase in the levels of anillin::GFP at the cell poles without any change in zone width and equatorial levels of anillin::GFP (Figure 19D-G), all of which were measured 8 minutes after anaphase onset. Since PKN2 depletion did not increase overall cytoplasmic levels of anillin::GFP as compared to controls (Figure 19H), it seems that PKN2 specifically inhibits anillin localization on the cell poles. The PKN2 RNAi phenotype was also confirmed by depletion of PKN2 using a different siRNA (s1117) from another manufacturer (Figure 19I-L). As before, PKN2 depletion by s1117 siRNA resulted in significant increase in anillin::GFP levels on cell poles (Figure 19J) without any changes in equatorial levels of anillin::GFP (Figure 19K) and its zone width (Figure 19L).

Finally, to verify that the PKN2 RNAi phenotype is specific and not due to an off-target effect of siRNAs, inducible RNAi resistant NG::PKN2 transgene was generated and integrated into the HeLa-FRT host cell line by flippase-mediated recombination (Figure 20A). Consistent with a previous report (Schmidt et al., 2007), NG::PKN2 localized at equatorial cortex in anaphase cells similar to the endogenous PKN2 (Figure 20B). As expected, RNAi knockdown of PKN2 (Figure 20C) resulted in an increase of endogenous anillin at the cell poles and this phenotype was rescued by the expression of RNAi resistant NG-tagged PKN2 transgene induced upon addition of tetracycline (Figure 20C-E).

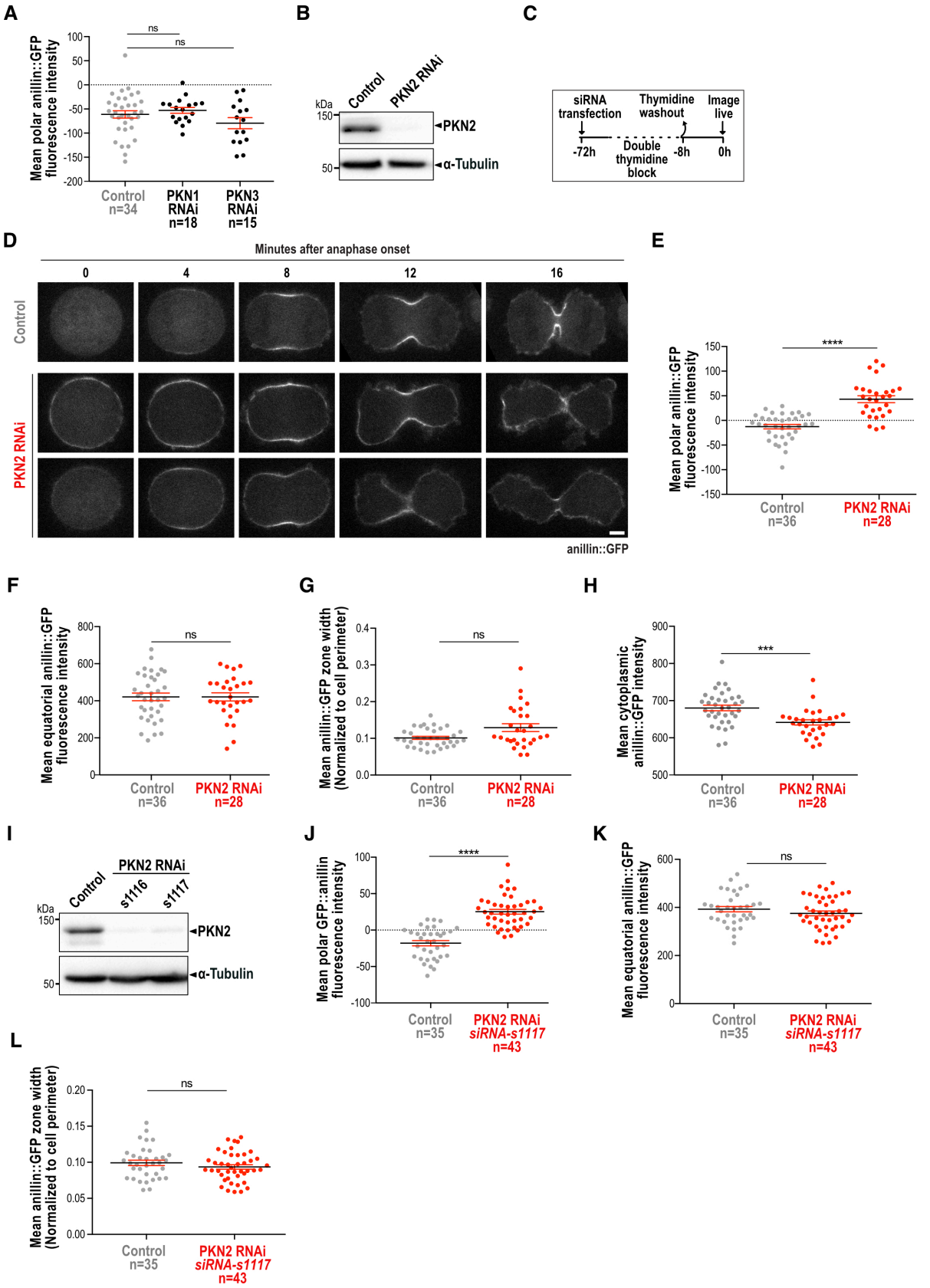

Figure 19: PKN2 inhibits localization of anillin-GFP at the polar cortex in HeLa cells. (**A**) Mean polar anillin::GFP intensity in control, PKN1 and PKN3 depleted cells that was measured in primary screen. (**B**) Immunoblots of HeLa cells expressing anillin::GFP after treatment with control or PKN2 siRNA probed for PKN2 and α-tubulin as a loading control.

(**C**) Schematic illustrating protocol used to transfect and synchronize cells for live cell imaging experiments. (**D**) Time lapse confocal images of HeLa cells expressing anillin::GFP treated with control (n=36) or PKN2 (n=28) siRNA. (**E,F**) Graphs showing mean anillin::GFP intensity at the cell poles and equator respectively in control and PKN2 depleted cells. (**G**) Graphs showing mean anillin::GFP zone width in control and PKN2 depleted cells. (**H**) Graph showing the mean cytoplasmic anillin::GFP intensity in control and PKN2 RNAi cells. (**I**) Immunoblot showing depletion of PKN2 with two different siRNAs s1116 and s1117. α-tubulin was used as loading control. (**J,K,L**) Plots showing mean anillin::GFP intensity at the cell poles and equator as well as anillin::GFP zone width in control and PKN2 depleted cells by siRNA s1117. All pixel intensities were measured by drawing a linescan (8 pixels wide) around the cell cortex in Fiji and mean values were calculated in Knime. All p-values were calculated by Student's t test (****, $P < 0.0001$; ***, $P < 0.001$), except in (G) where statistical significance was checked by Kolmogorov Smirnov Test. All scale bars are 5µm. All error bars are SEM unless otherwise stated and n = number of cells.

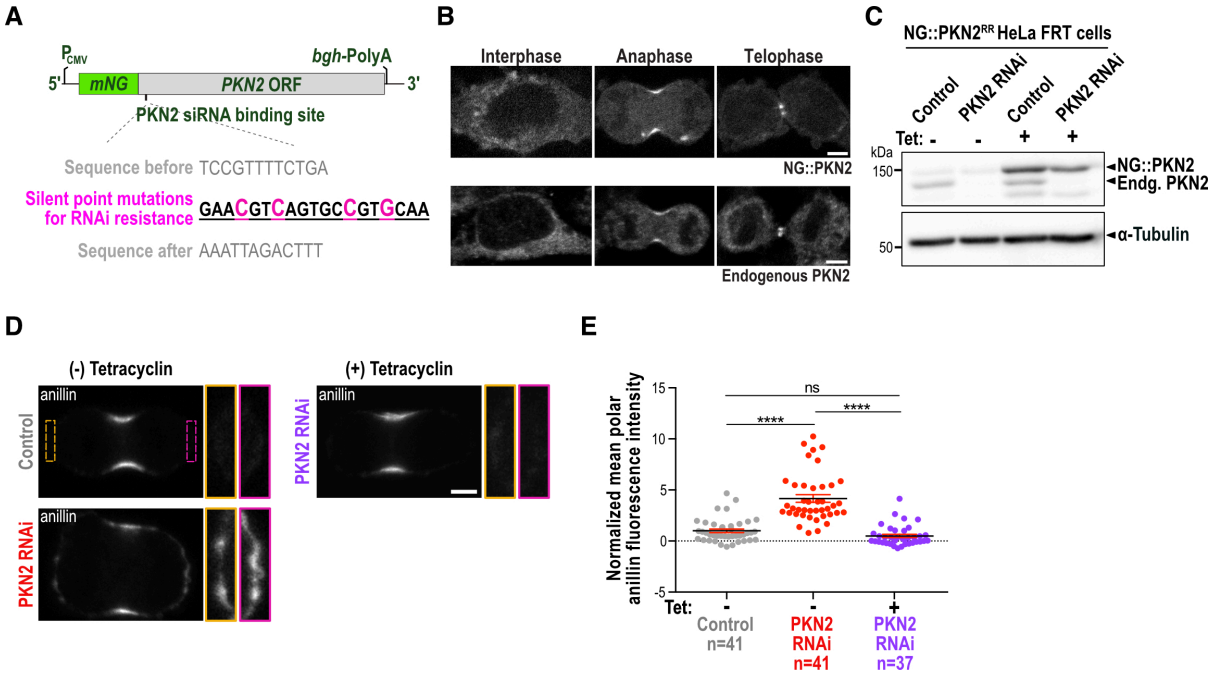

Figure 20: RNAi resistant NG::PKN2 rescues the phenotype of PKN2 depletion in HeLa cells. (**A**) Schematics showing RNAi resistant PKN2 transgene tagged with mNeonGreen. To confer RNAi resistance four silent mutations were introduced in the PKN2 siRNA binding site by site-directed mutagenesis. The transgene was inserted in pCDNA5/FRT/TO plasmid and integrated into HeLa FRT host cell line for inducible expression of mNG::PKN2^{RR}. (**B**) Confocal images of mNG::PKN2^{RR} cells induced by addition of tetracycline (top) or parental HeLa cells fixed and stained with anti-PKN2 antibodies (bottom). (**C**) Immunoblots of induced or non-induced mNG::PKN2^{RR} cells after treatment with control or PKN2 siRNA probed for PKN2 and α-tubulin as a loading control. (**D**) Confocal images of non-induced control cells (n=41) or PKN2 depleted cells with (n=37) or without mNG::PKN2^{RR} induction (n=41) stained with anti-anillin antibody. (**E**) Graphs showing mean normalized anillin intensity at the cell poles for treatments performed in (D). Pixel intensities were measured by drawing a linescan (7 pixels wide) around the cell cortex in Fiji and mean values were

calculated in Knime. Values were normalized to the mean anillin::GFP intensity at the cell poles. p-values were calculated by Kruskal-Wallis multiple comparisons test (with Dunn's post-hoc test) (*** P<0.001; **** P < 0.0001). All scale bars are 5μm. All error bars are SEM unless otherwise stated and n = number of cells.

In addition to quantifying cortical levels of anillin::GFP, I also used the live-cell imaging data to measure the rate and timing of furrow ingression in PKN2 depleted cells. To quantify the furrow closure rate, I measured the distance between ingressing fronts of a furrow starting from anaphase onset until complete ring closure at 2 minute intervals (Figure 21A). This analysis revealed that the rate of furrow closure in PKN2 depleted cells was indistinguishable from the control cells (Figure 21B). Also, the total time from anaphase onset to complete furrow ingression did not significantly vary between control and PKN2 depleted cells (Figure 21C). Previously, Schmidt et. al. reported 32% binucleation in PKN2 depleted HeLa-S3 cells owing to failure of abscission (Schmidt et al., 2007) after complete furrow ingression. In my live-cell recordings of PKN2 depleted cells that varied in duration from 74 minutes to 182 minutes, only 1/28 cells failed abscission and 27/28 cells did not show an absicision defect (Figure 21D). To reproduce the observations of Schmidt et al., I further performed a multinucleation assay by depleting PKN2 in HeLa parental cells for 72 hours followed by fixation with formaldehyde. Manual counting of mononucleated and multinucleated cells revelaed only 9% multinucleation (n = 205 cells) in PKN2 depleted cells as compared to 4% in control (n = 263 cells). Thus, the role of PKN2 in abscission could not be confirmed in my experiments in HeLa cells, reasons for which are discussed later in 'Discussion' section. Overall, this data shows that PKN2 inhibits anillin accumulation at cell poles during anaphase without affecting timing and rate of cytokinetic furrow closure.

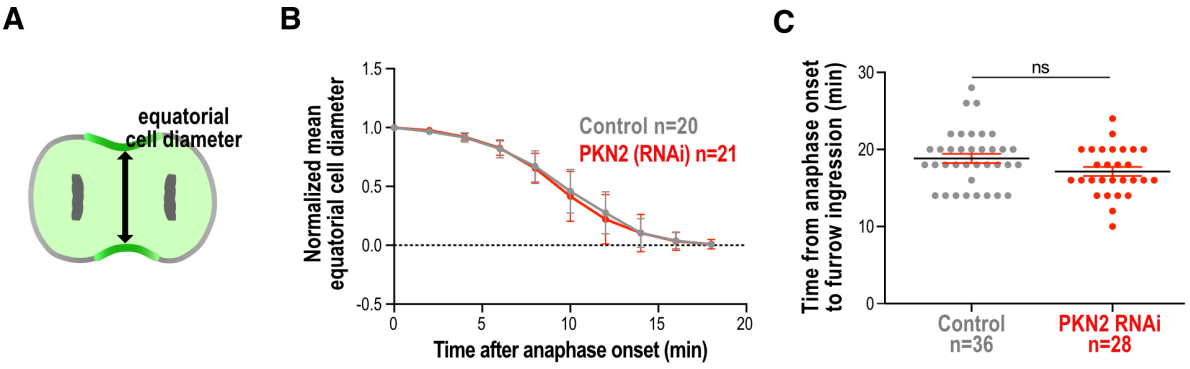

D

Cytokinesis defects after PKN2 RNAi

	Control			PKN2 RNAi		
Duration (mins)	74	84	182	74	84	182
n	10	7	19	8	7	13
Phenotype	Normal	Normal	Normal	Normal	Normal	1/13 abscission defect

Figure 21: PKN2 depletion does not alter furrow ingression dynamics in HeLa cells. (A) Schematic showing the method used to measure cell diameter at the equator in the cells on time lapse movies shown in Figure 19D. (**B**) Graph showing normalized mean equatorial cell diameter over time after anaphase onset. Error bars are SD. (**C**) Graph depicting time (in mins) from furrow onset to furrow ingression in control and PKN2 depleted cells. Error bars are SEM. Statistical significance was tested by Kolmogorov Smirnov test. (**D**) Table summarizing late cytokinesis defects after control or PKN2 RNAi observed during live cell imaging of indicated time duration in cells expressing anillin::GFP.

PKN2 is known to be an effector protein in Rho/Rac signalling pathway and directly binds to active Rho GTPases (Amano et al., 1996; Flynn et al., 1998; Maesaki et al., 1999; Shibata et al., 1996; Vincent and Settleman, 1997). Therefore, it is possible that PKN2 might directly inhibit RhoA accumulation at the cell poles, which in turn could prevent anillin recruitment to the cell poles. To investigate this possibility, HeLa cells were treated with PKN2 siRNA, fixed and stained with anti-RhoA antibodies. RhoA was not found to be increased at the cell poles after PKN2 knockdown (Figure 22A and C), however, the RhoA fluorescence signal at the cell poles was rather weak which could compromise the ability to capture small differences. Therefore, the possibility of PKN2 inhibiting RhoA accumulation at cell poles cannot be ruled out. On the other hand, PKN2 RNAi led to a significant increase in RhoA accumulation at the cell equator (Figure 22A and B) without a significant change in RhoA zone width (Figure 22D), suggesting that PKN2 inhibits RhoA at the cell equator. Increase in active RhoA accumulation at cell equator is expected to result in a rise in active myosin II and anillin at the cell equator. To analyze the cortical levels of active myosin II, I depleted PKN2 in HeLa cells and immunostained phosphorylated myosin light chain 2,

pMLC2(Ser19). Similar to RhoA, equatorial levels of pMLC2(Ser19) were found to be significantly increased (Figure 22E and F) in PKN2 depleted cells without any change in zone width (Figure 22H) and pMLC2(Ser19) levels at poles (Figure 22E and G). Although, anillin::GFP accumulation increased at the cell poles upon PKN2 depletion, it did not increase at the cell equator (Figure 19D-F). To resolve this conundrum, I analysed cellular levels of anillin after PKN2 RNAi on a Western Blot. Surprisingly, the levels of endogenous anillin and anillin::GFP were strongly reduced upon PKN2 knockdown (Figure 23A and B), indicating towards a novel role of PKN2 in maintaining anillin protein stability. This phenotype was also confirmed by four out of six different siRNAs, each targeting a distinct site on PKN2 mRNA (Figure 23C). In addition, cellular levels of other cytokinesis regulators like Plk1 and Ect2 was not altered upon PKN2 RNAi (Figure 23D) and RNAi resistant NG::PKN2 partially rescued the anillin level in absence of the endogenous PKN2 (Figure 23E). Conversely, anillin depletion did not change PKN2 levels in parental HeLa cells and cells expressing anillin::GFP (Figure 23F), thereby, suggesting that PKN2 is required for stable expression of anillin and not vice versa. As a result, an increase in anillin::GFP levels could not be detected at the cell equator upon PKN2 depletion and the rise in anillin::GFP at the cell poles was probably underestimated.

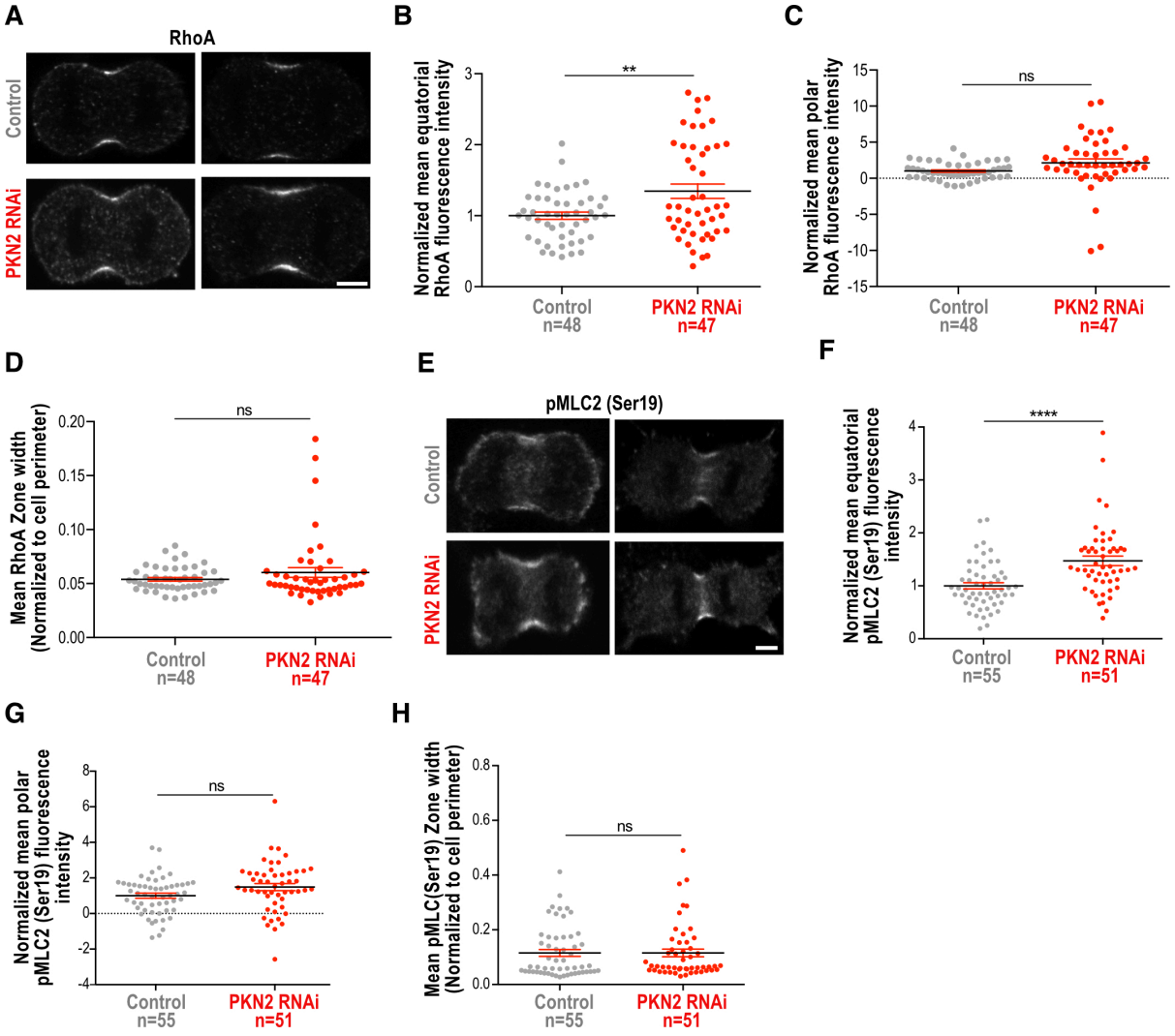

Figure 22: PKN2 inhibits equatorial accumulation of RhoA and phosphorylated myosin in HeLa cells. (**A**) Confocal images of HeLa cells treated with control (n=48) or PKN2 (n=47) siRNA and stained with anti-RhoA antibody. (**B,C,D**) Graphs showing normalized mean RhoA intensity at cell equator, cell poles and RhoA zone width in control and PKN2 depleted cells. (**E**) Confocal images of HeLa cells treated with control (n=55) or PKN2 (n=51) siRNA and stained with anti-pMLC2 (Ser19) antibody to visualize phosphorylated myosin light chain. (**F,G,H**) Graphs showing normalized mean phosphorylated myosin light chain pMLC(Ser19) intensity at cell equator, cell poles and pMLC(Ser19) zone width in control and PKN2 depleted cells. All pixel intensities were measured by drawing a linescan (4 pixels wide) around the cell cortex in Fiji and mean values were calculated in Knime. p-values were calculated by Kolmogorov-Smirnov test (**, $P < 0.01$; ****, $P < 0.0001$). All scale bars are 5µm.

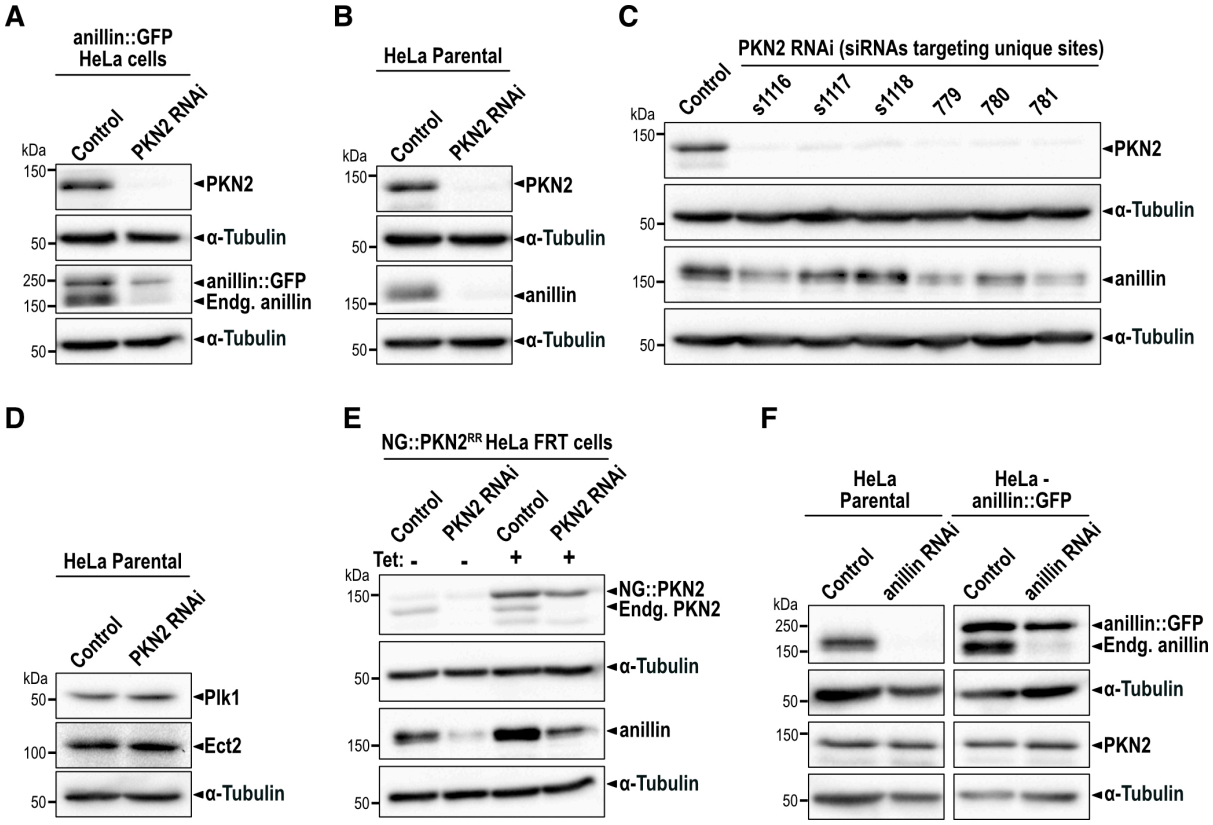

Figure 23: PKN2 is required for stable expression of anillin in HeLa cells. (**A,B**) Immunoblots of parental HeLa cells or cells expressing anillin::GFP after treatment with control or PKN2 siRNA probed for PKN2 and anillin. (**C**) Western Blots showing anillin levels after PKN2 depletion by six different siRNAs. (**D**) Immunoblots comparing Plk1 and Ect2 levels in PKN2 depleted cells with control. (**E**) Immunoblots of induced or non-induced mNG::PKN2^{RR} cells after treatment with control or PKN2 siRNA probed for PKN2 and anillin. (**F**) Immunoblot showing PKN2 levels in cells treated with control or anillin RNAi. α-tubulin was used as loading control in all the Blots.

Protein kinase N (PKN) proteins are evolutionarily well conserved and its orthologues in *Drosophila* and *C. elegans* (PKN-1) have also been shown to bind active Rho/Rac (Amano et al., 1996; Betson and Settleman, 2007; Lu and Settleman, 1999; Qadota et al., 2011). Based on homology search performd by Qadota et al. in 2011, PKN-1 is the only known orthologue of human PKN, and the human and *C. elegans* PKN proteins are 38% identical comparing the overall protein sequences and 71% identical comparing only the kinase domains (Qadota et al., 2011). Moreover, human and *C. elegans* PKN proteins also share structural features like RhoA binding N-terminal HR1 repeats, C2-like domain in the middle and a C-terminal kinase domain (Qadota et al., 2011; Flynn et al., 1998; Maesaki et al., 1999; Shibata et al., 1996). Therefore, I set out to investigate whether the function of PKN-1 is conserved in *C. elegans* one-cell embryos during the first cytokinesis. To achieve this, I depleted PKN-1 by

injecting dsRNA into young adult worms and performed live-cell imaging on one-cell embryos 40-48 hours after dsRNA injections. As shown in Figure 24B and C, PKN-1 depletion caused excessive membrane blebbing during late anaphase of first cell division. To further confirm this phenotype, I ordered a *pkn-1* mutant strain from CGC having a 1064 base-pairs long region between fourth and seventh exon replaced with 18 bp long sequence, leading to premature stop inside C2-like domain (Figure 24A). It is not known whether this is a null mutant but if a truncated protein would form, it would lack kinase domain. Similar to *pkn-1(RNAi)*, *pkn-1* mutant also showed excessive membrane blebbing during late anaphase of first embryonic division (Figure 24C). Next, I investigated the affect of *pkn-1(RNAi)* on the levels of polar accumulation of Neon-green tagged-anillin during first cell division. PKN-1 depletion led to a mild increase in NG::Anillin levels on the anterior and posterior poles during anaphase but not on the equatorial cortex (Figure 24D-F), similar to the phenotype in HeLa cells. To determine if this trend is also true for other contractile ring proteins downstream of RhoA, I imaged embryos expressing non-muscle myosin II (NMY-2::GFP) in PKN-1 depleted one-cell embryos. Similar to NG::anillin, the cortical levels of NMY-2::GFP were also significantly increased on the poles (Figure 24G and H). However, unlike NG::anillin, equatorial levels of NMY-2::GFP were also found to be increased in PKN-1 depleted embryos (Figure 24G and H). These results indicate that PKN-1 inhibits the polar accumulation of anillin and NMY-2 during the first division of *C. elegans* early embryos, probably by regulating RhoA activity. Further, the role of human PKN2 in preventing anillin accumulation at the cell poles during anaphase seems to be conserved in *C. elegans*.

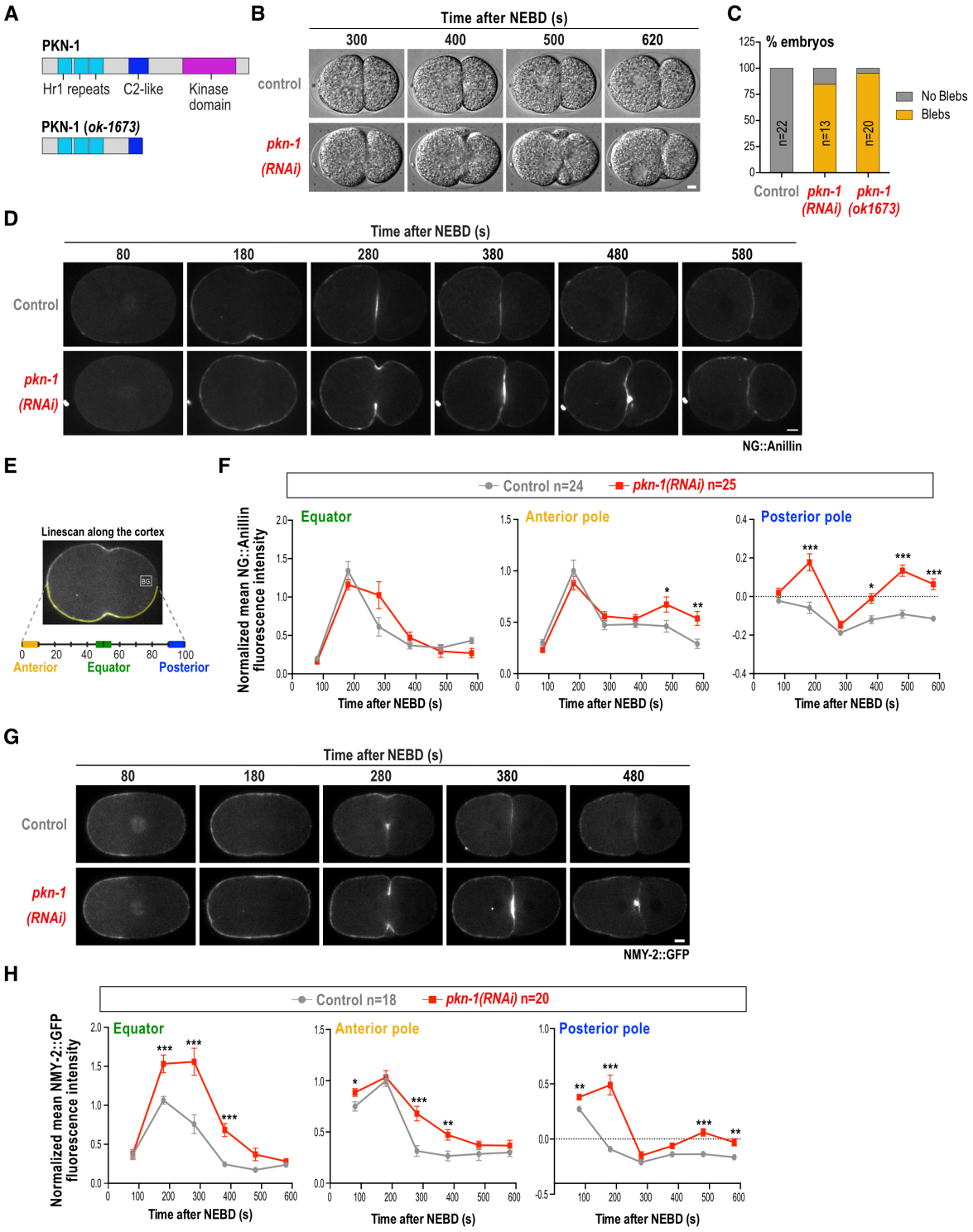

Figure 24: PKN-1 inhibits anillin accumulation at the polar cortex in first cell division of *C. elegans* embryos. (A) Schematic representation of products of wild-type *pkn-1* and mutant *pkn-1*(*ok1673*) genes. This representation was adapted from Qadota et al., 2011. (**B**) Time-lapse DIC images of the first cell division in *C. elegans* embryos in control (n=22) and PKN-1 depleted (n=13) embryos. (**C**) Graph shows percentage of embryos having blebs at cell equator during first division in control, *pkn-1(RNAi)* and *pkn-1(ok1673)* mutant. (**D**). Time-lapse confocal images of control (n=12) or PKN-1 depleted (n=13) embryos expressing endogenously-tagged NG-anillin. (**E**) Schematic showing the linescan method used to

quantify NG-anillin fluorescence at the anterior, posterior and equatorial cortex. The mean cytoplasmic background (BG) was subtracted and the mean fluorescence intensity was normalized by dividing by the mean anterior intensity in control at 180s. (**F**) Graphs show normalized NG-anillin fluorescence intensity over time at the equator as well as anterior and posterior poles. (**G**) Time-lapse confocal images of control (n=9) or PKN-1 depleted (n=10) embryos expressing endogenously-tagged NMY-2::GFP. (**H**) Graphs show normalized NMY-2::GFP fluorescence intensity over time at the anterior and posterior poles, and at the cell equator. In all the graphs, anillin fluorescence intensity was normalized to the mean anterior fluorescence intensity in controls 180s after NEBD. All pixel intensities were measured by drawing a linescan (8 pixels wide) around the cell cortex in Fiji and mean values were calculated in Knime. All time points are seconds after NEBD and all scale bars are 5µm. All error bars are SEM and n = number of linescans. All p-values were calculated by student's t-test (* $p<0.05$; ** $p<0.01$; *** $P < 0.001$).

4.1.7 Septin 7 promotes anillin recruitment at the cell equator

Depletion of Septin 7 resulted in strong reduction of anillin levels at the cell equator in the primary and secondary screens (Figure 14D and 16, Table 18). Sept7, a member of conserved Septin family proteins, is required for normal organization of cytoskeleton (Kremer et al., 2007). To investigate whether other members of Septin family proteins have a similar function in regulating anillin localization in anaphase, I measured cortical anillin::GFP levels on the images acquired in the primary screen after Sept1, Sept3, Sept4, Sept5, Sept6, Sept9 and Sept11 RNAi and found no significant difference when compared to the control (Table 23). This preliminary data indicates a specific role of Sept7 in recruiting anillin at the cell equator.

Table 23: Anillin::GFP intensity at the cell equator in cells depleted of different septin family members was measured on images of the primary screen.

RNAi	Mean GFP Intensity	n	RNAi	Mean GFP Intensity	n	p value
SEPT1	319.37	9	Control	258.95	28	**0.272815**
SEPT3	199.27	8	Control	227.84	37	**0.631648**
SEPT4	278.19	5	Control	227.84	37	**0.503405**
SEPT5	162.99	2	Control	171.54	22	**0.917513**
SEPT6	293.90	5	Control	227.84	37	**0.405312**
SEPT9	178.96	2	Control	215.46	35	**0.706409**
SEPT11	236.54	13	Control	202.26	29	**0.148962**

The Sept7 phenotype was further investigated in live-cell imaging experiments after ensuring nearly complete depletion of Sept7 by Western Blotting (Figure 25A). Similar to the screen, Sept7 depletion led to a significant reduction in the level of anillin::GFP at the cell equator and equatorial anillin zone width, 8 minutes after anaphase onset (Figure 25B-D). Importantly, cytoplasmic (Figure 25E) and cellular (Figure 25A) levels of anillin did not change after Sept7 depletion suggesting that Sept7 promotes anillin recruitment to the equatorial cortex.

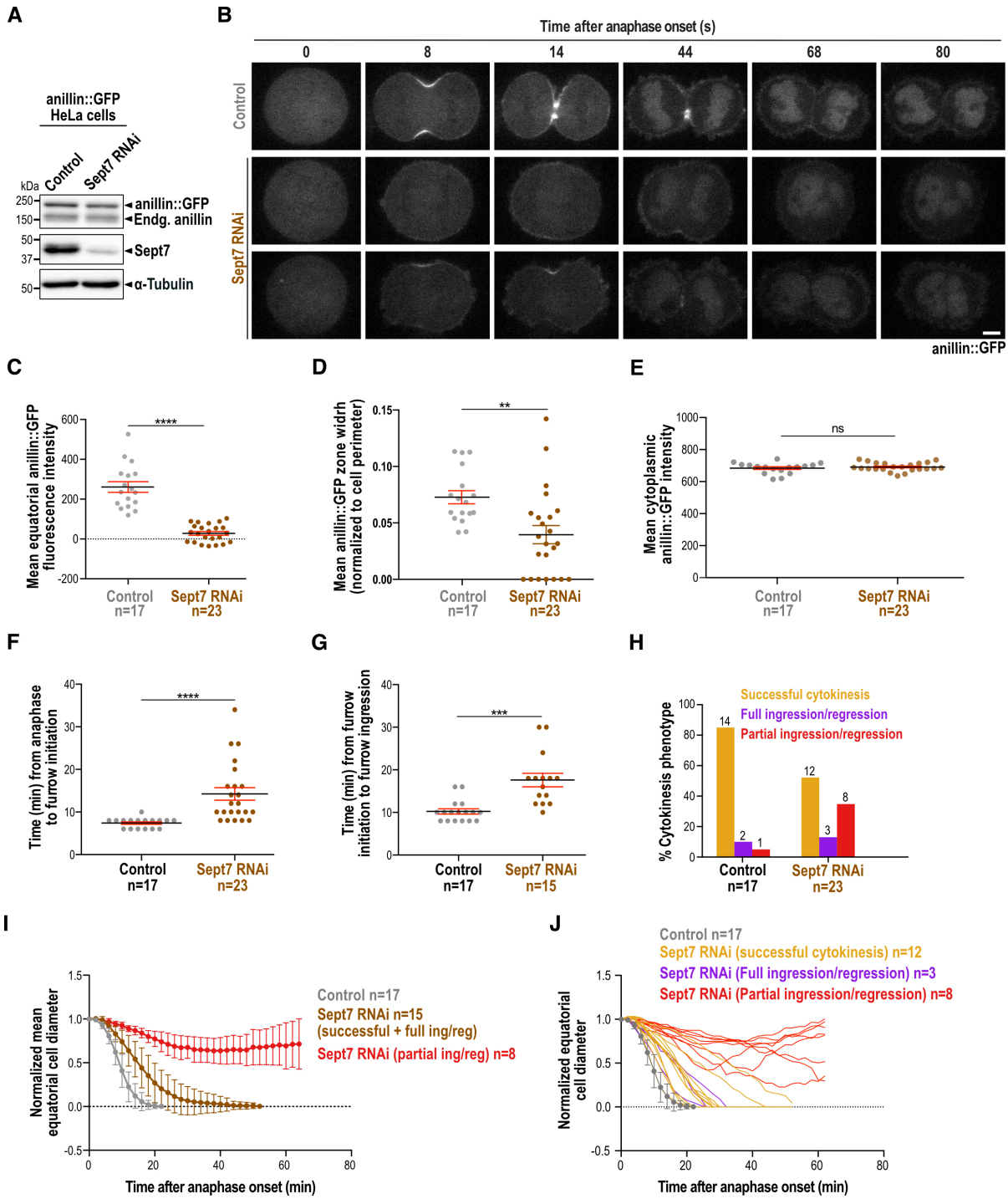

Figure 25: Septin 7 is required for localization of anillin::GFP at the equatorial cortex in HeLa cells. (**A**) Immunoblots of HeLa cells expressing anillin::GFP after treatment with control or SEPT7 siRNA probed for anillin, SEPT7 and α-tubulin as a loading control. (**B**) Time lapse confocal images of HeLa cells expressing anillin::GFP, treated with control (n=17) or SEPT7 (n=23) siRNA. (**C**) Graph showing mean anillin::GFP intensity at the cell equator in control and SEPT7 depleted cells. p-values were calculated by Student's t test (****, $P < 0.0001$). (**D**) Graph showing anillin::GFP zone width at the cell equator in control and Septin 7 depleted cells. Pixel intensities were measured by drawing a linescan (6 pixels wide) around the cell cortex in Fiji and mean values were calculated in Knime. (**E**) Graph showing mean cytoplasmic anillin::GFP intensity in control and SEPT7 depleted cells. (**F**) Graphs showing time (min) from anaphase onset to furrow initiation in control (n=17) and SEPT7 depleted (n=23) cells. (**G**) Graphs showing time (min) from anaphase onset to complete furrow ingression in control (n=17) and SEPT7 depleted (n=15) cells. p-values in (E) and (F) were calculated by Kolmogorov-Smirnov test (**** $P < 0.0001$; *** $p<0.001$). Error bars are SD. (**H**) Graph showing different cytokinesis defects observed after SEPT7 RNAi as compared to controls. (**I,J**) Plots showing dynamics of furrow closure in control and SEPT7 depleted cells. Graph in (H) shows mean values with SD and graph in (I) shows traces for individual cells. All pixel intensities were measured by drawing a linescan (8 pixels wide) around the cell cortex in Fiji and mean values were calculated in Knime. All scale bars are 5μm. All error bars are SEM unless otherwise stated and n = number of cells.

To confirm that the reduction of cortical anillin was due to depletion of Sept7 and not an off-target effect, I generated and integrated an RNAi resistant NeonGreen-tagged Sept7 transgene into the HeLa-FRT host cell line (Figure 26A). Septin proteins are present in the contractile ring and are known to colocalize with actin and anillin (Kinoshita et. al., 2002, Oegema at. al. 2000, Joo et. al., 2007). Similar to these reports, live-cell imaging of NG::Sept7 and immunostaining of endogenous Sept7 revealed cortical localization of Sept7 during anaphase (Figure 26B). RNAi knockdown of Sept7 resulted in decreased recruitment of endogenous anillin at the cell equator which was rescued by the expression of RNAi resistant NG::Sept7 transgene induced by tetracycline addition (Figure 26C-E). Thus, this data shows that Sept7 is required for anillin recruitment to the equatorial cortex and that the phenotype is not caused by an off-target effect of the siRNA. To further test whether the decrease in anillin accumulation at the cell equator in Sept7 depleted cells is a consequence of reduced Ect2 localization to the spindle midzone, Sept7 was depleted in HeLa cells expressing Ect2::GFP followed by live-cell imaging. No change was detected in the mean fluorescence intensity of Ect2::GFP at the spindle midzone (Figure 26F), suggesting that Sept7 plays a direct role in recruitment and/or maintenance of anillin at the cell equator.

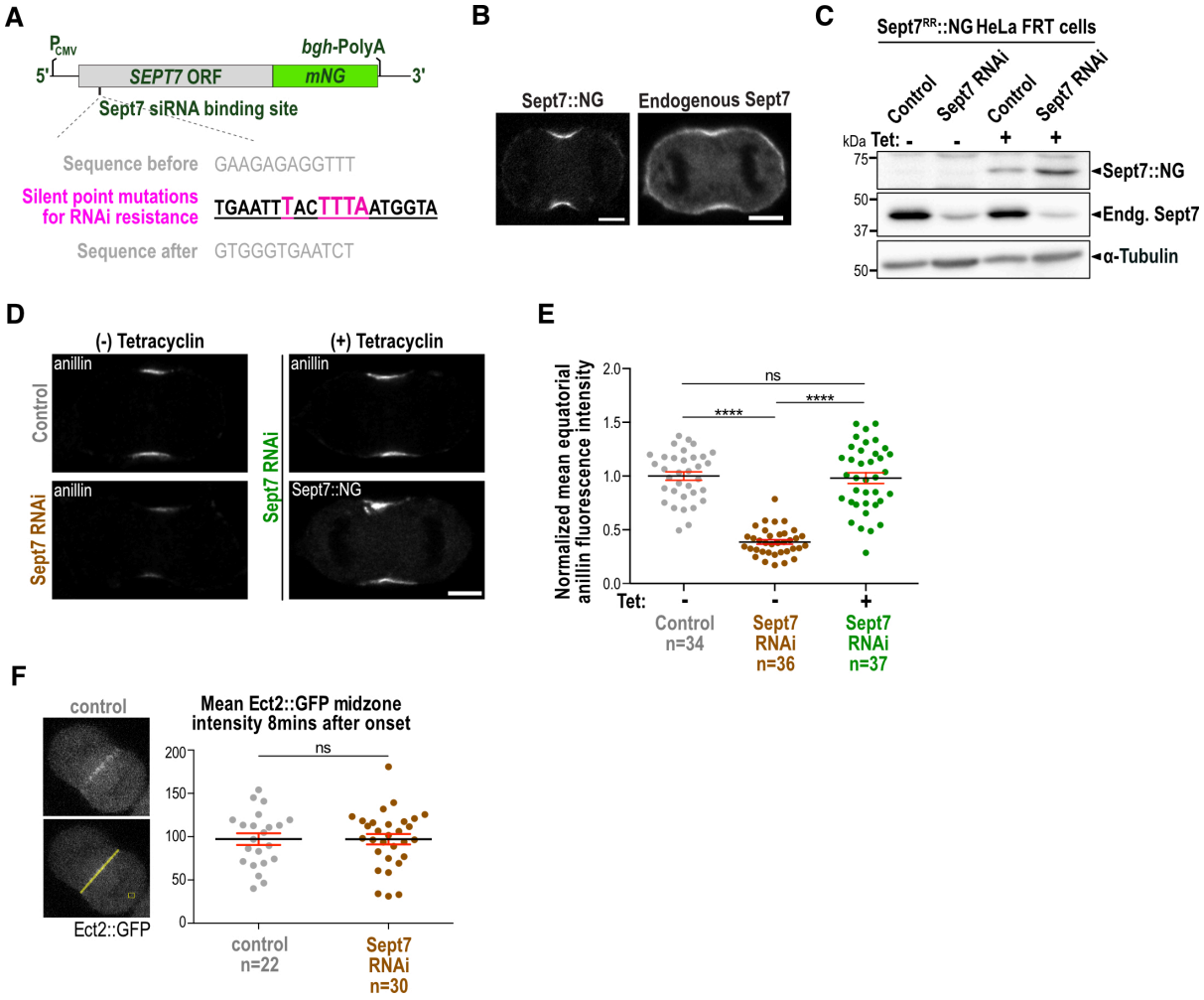

Figure 26: RNAi resistant SEPT7::NG rescues the phenotype of Septin 7 depletion in HeLa cells. (A) Schematics showing RNAi resistant SEPT7 transgene tagged with mNeonGreen. To confer RNAi resistance five silent mutations were introduced in the SEPT7 siRNA binding site by site-directed mutagenesis. The transgene was inserted in pCDNA5/FRT/TO plasmid and integrated into HeLa FRT host cell line for inducible expression of SEPT7^{RR}-mNG. (**B**) Confocal images of SEPT7^{RR}-mNG cells induced by addition of tetracycline or parental HeLa cells fixed and stained with anti-SEPT7 antibodie. (**C**) Immunoblots of induced or non-induced SEPT7^{RR}-mNG cells after treatment with control or SEPT7 siRNA probed for SEPT7 and α-tubulin as a loading control. (**D**) Confocal images of non-induced control cells (n=34) or SEPT7 depleted cells with (n=36) or without mNG-PKN2^{RR} induction (n=37) stained with anti-anillin antibody. (**E**) Graphs showing mean normalized anillin intensity at the cell equator for treatments performed in (D). Pixel intensities were measured by drawing a linescan (7 pixels wide) around the cell cortex in Fiji and mean values were calculated in Knime. Values were normalized to the mean anillin intensity at the cell equator and p-values were calculated by Kruskal-Wallis multiple comparisons test (with Dunn's post-hoc test; **** $P < 0.0001$). (**F**) Graph showing mean Ect2::GFP intensity at the spindle midzone in control and Septin 7 depleted cells measured 8 minutes after anaphas onset. All scale bars are 5µm. All error bars are SEM unless otherwise stated and n = number of cells.

Sept7 depletion was previously shown to result in incomplete cytokinesis and multinucleation in fibroblasts (Menon et al., 2014), however, the dynamics of furrow formation and the cause of this phenotype remains elusive. Indeed, live-cell imaging of Sept7 depleted cells revealed that 5/27 cells (18%) showed full furrow ingression followed by regression and 8/27 cells (30%) formed partially ingressing furrows (Figure 25H). Then, I measured the time taken after anaphase onset to form and ingress the cleavage furrow and found that Sept7 depletion strongly delayed the cleavage furrow formation and ingression (Figure 25F and G). This finding was corroborated by measuring rate of furrow ingression and regression (Figure 25I and J) as depicted in Figure 21A. Rate of furrow ingression was notably slower in Sept7 depleted cells as compared to the controls (Figure 25I and J), thereby, suggesting that Sept7 promotes furrow ingression by binding and stabilizing anillin at the cytokinetic furrow.

Next, I investigated whether septins have a similar function of anillin recruitment to the cell cortex during first embryonic division of *C. elegans*. Depleting UNC-59 and UNC-61, the only septins expressed in *C. elegans*, led to a significant reduction in cortical accumulation of NG::Anillin, both at equator and polar cortex (Figure 27A and B). In addition, time taken from furrow intiation to complete furrow closure was signififcantly increased in UNC-59 and UNC-61 depleted embryos as compared to the controls. Similarly, the rate of cleavage furrow ingression was also slower in UNC-59 and UNC-61 depleted embryos (Figure 27C and D), just like in HeLa cells. These findings suggest that Sept7 promotes furrow formation and recruits anillin to the cell equator in HeLa cells and *C. elegans*.

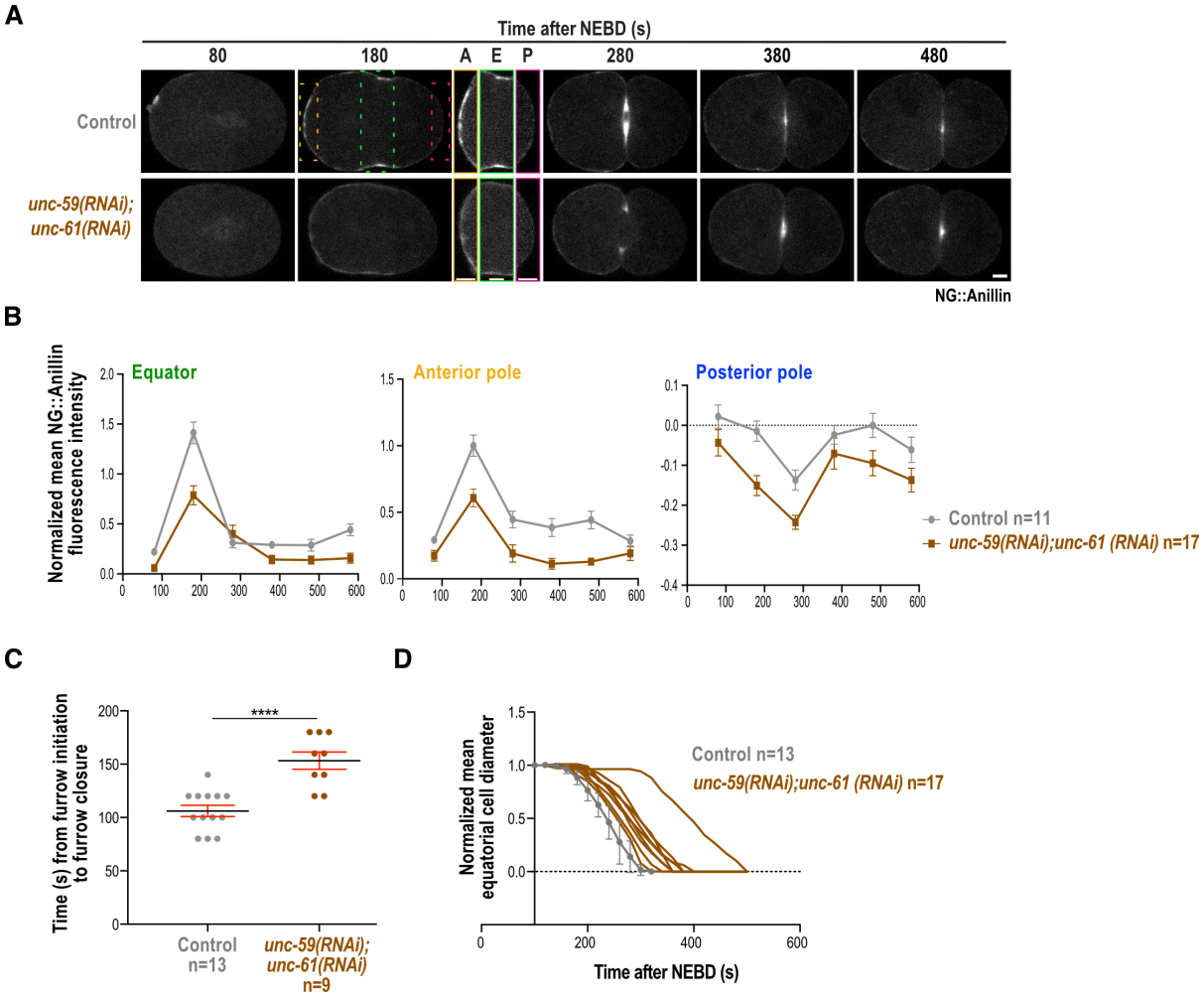

Figure 27: *C. elegans* septins UNC-59 and UNC-61 promote anillin accumulation at the cell cortex during first cell division. (**A**) Time-lapse confocal images of control (n=6) or *unc-59 & unc-61 (RNAi)* embryos (n=9) expressing endogenously-tagged NG::anillin. For the embryo 180s after NEBD, magnified images are shown of anterior pole (yellow), equator (green) and posterior pole (magenta). (**B**) Graphs plot normalized NG::anillin fluorescence intensity over time at the anterior and posterior poles, and at the cell equator. NG::anillin intensity was measured as shown in Figure 24E. Mean fluorescence intensity was normalized by dividing by the mean anterior intensity in control at 180s. Error bars are SEM and n = number of linescans. (**C**) Graph showing time (in sec) from furrow initiation to furrow ingression in control and *unc-59(RNAi);unc-61(RNAi)* embryos. p-value was calculated by Student's t-test (**, P < 0.01). Error bars are SEM and n = number of embryos. (**D**) Plot showing dynamics of furrow closure in control and *unc-59(RNAi);unc-61(RNAi)* embryos. All pixel intensities were measured by drawing a linescan (8 pixels wide) around the cell cortex in Fiji and mean values were calculated in Knime. In all the graphs, anillin fluorescence intensity was normalized to the mean anterior fluorescence intensity in controls 180s after NEBD. Error bars are SD and n = number of embryos. All time points are seconds after NEBD and all scale bars are 5μm.

4.2 Aurora A inhibits anillin localization on the polar cortex during cytokinesis in *C. elegans* one-cell embryos and HeLa cells

[A portion of data presented in this section has already been published by us in the Journal of Cell Biology. The detailed citation is as follows:

Mangal, S., Sacher, J., Kim, T., Osório, D.S., Motegi, F., Carvalho, A.X., Oegema, K., and Zanin, E. (2018). TPXL-1 activates Aurora A to clear contractile ring components from the polar cortex during cytokinesis. The Journal of Cell Biology *217*, 837–848.

Figures have been reproduced or modified with the permission of Rockefeller University Press and the permission email is attached in the Appendix.]

4.2.1 TPXL-1 clears the contractile ring protein anillin and f-actin from the polar cortex independent of its function in regulating spindle length

During cytokinesis formation of contractile ring is regulated by the anaphase spindle. While the central spindle promotes the accumulation of contractile ring proteins like anillin on the equatorial cortex (D'Avino et al., 2015; Dassow, 2009; Green et al., 2012), inhibitory signals of unknown molecular identity arising from astral microtubules prevent the accumulation of these proteins on the polar cortex (Figure 28A) (D'Avino et al., 2015; Dassow, 2009; Green et al., 2012).

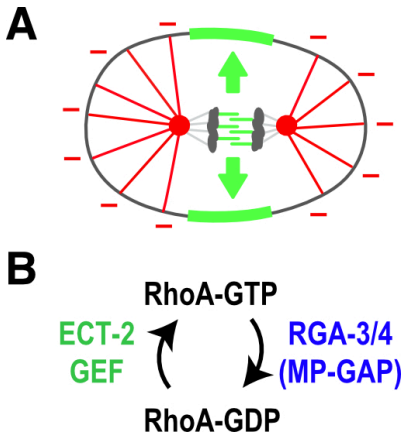

Figure 28: Anaphase spindle regulates the assembly of contractile ring. (**A**) Stimulatory signals promote the accumulation of contractile ring proteins at the equatorial cortex and unknown signals from astral microtubules prevent accumulation of contractile ring proteins on the polar cortex, thereby ensuring correct position for formation of the contractile ring. (**B**) ECT-2 converts RhoA to active GTP bound state and RGA-3/4 (homolog of human MP-GAP) antagonizes RhoA activation by converting it back to inactive GDP-bound state.

To identify the genes involved in the inhibitory signalling cascade in *C. elegans*, my PhD supervisor Dr. Esther Zanin established an assay to monitor the removal of GFP::anillin from the polar cortex during the first division (Figure 29A and B). Anillin was chosen because it colocalizes with and binds to active RhoA (Piekny and Glotzer, 2008) and its recruitment to the cell cortex is independent of myosin II (Maddox et al., 2005), thereby allowing us to study the cortical patterning even in absence of cortical contractility. This assay was performed in *rga-3/4*Δ mutant embryos to increase the cortical levels of GFP::anillin. RGA-3/4 are the two major GTPase activating proteins (GAPs) that oppose RhoA activation during cytokinesis, and are homologs of human MP-GAP (Figure 29B) (Zanin et al., 2013). In addition, NMY-2 was depleted by RNAi to prevent geometrical rearrangements in the cortex due to myosin-based expansion and compression. Using this assay Dr. Zanin discovered that, while in controls GFP::anillin was cleared from the anterior cortex during late anaphase (Figure 29A and B), *tpxl-1(RNAi)* prevented GFP::anillin clearing from the anterior pole after anaphase onset (Figure 29C), suggesting that TPXL-1 has a role in polar clearing during anaphase.

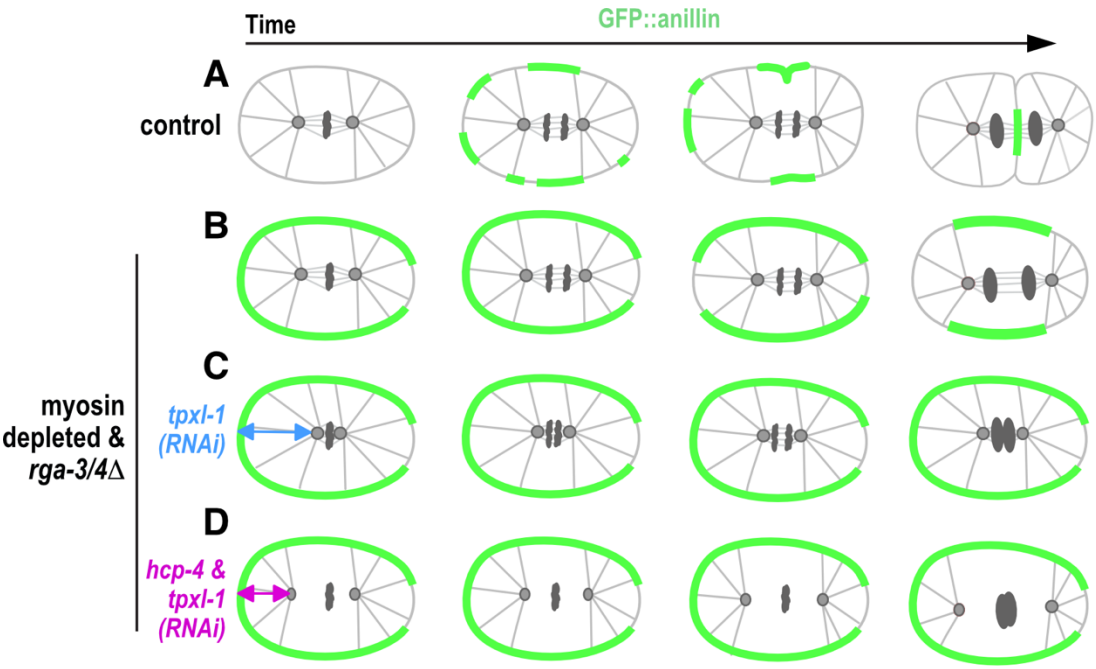

Figure 29: TPXL-1 is required for polar clearing of anillin in *C. elegans* one-cell embryos. Schematics showing the localization of GFP::anillin during first division in (**A**) control and (**B-D**) myosin-depleted *rga-3/4*Δ embryos treated with *tpxl-1(RNAi)* or *hcp-4 & tpxl-1(RNAi)*. Blue and magenta double headed arrows mark the distance between centrosome and polar cortex. (Experiments performed by Esther Zanin)

TPXL-1 depletion leads to formation of short spindles and thereby increases the anterior pole and centrosome distance (Özlü et al., 2005). To restore the distance between the centrosome and polar cortex, myosin II, HCP-4 and TPXL-1 were co-depleted in *rga-3/4*Δ embryos. Kinetochore assembly is disrupted in *hcp-4(RNAi)* embryos which weakens the connection between centrosome and chromosomes. As a result, the position of centrosome is restored by the cortical pulling forces acting on the centrosome asters (Lewellyn et al., 2010; Özlü et al., 2005). Despite restoration of the distance between centrosome and polar cortex, GFP::anillin was not cleared from the anterior pole in *hcp-4 & tpxl-1(RNAi)* embryos (experiment performed by Dr. Zanin) (Figure 29B-D), suggesting that TPXL-1 plays a direct role in polar clearing. To investigate whether TPXL-1 is also involved in clearing of other contractile ring proteins from the anterior pole, I repeated the experiments and followed the localization of filamentous actin (f-actin) using a f-actin binding probe LifeAct fused to mKate2 (Riedl et al., 2008). Imaging myosin depleted & *rga-3/4*Δ embryos expressing LifeAct::mKate2, revealed clearing of f-actin from the anterior pole in *hcp-4(RNAi)* but not in *hcp-4 & tpxl-1(RNAi)* embryos (Figure 30) similar to anillin. Based on these findings, we concluded that TPXL-1 plays a direct role in polar clearing of anillin and f-actin during anaphase independent of its role in regulating spindle length.

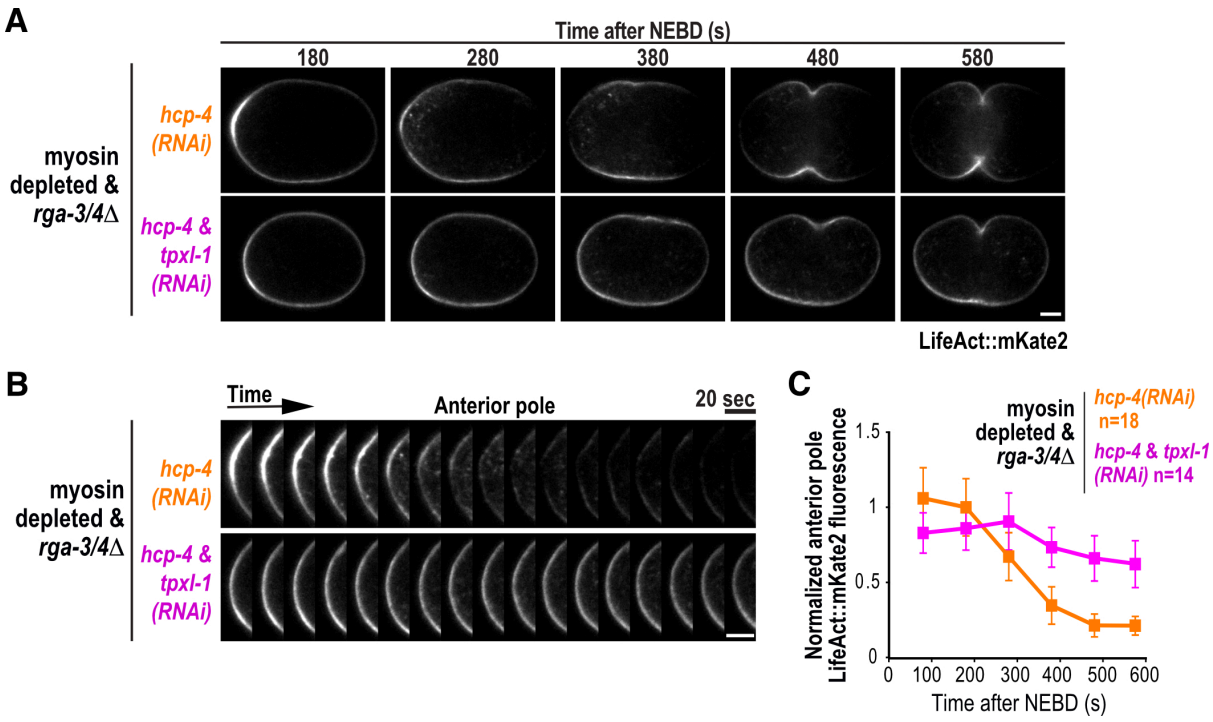

Figure 30: TPXL-1 is required for polar clearing of f-actin in *C. elegans* one-cell embryos. (**A**) Time-lapse confocal images of myosin depleted *rga-3/4*Δ embryos expressing LifeAct::mKate2 treated with *hcp-4(RNAi)* (n=9) or *hcp-4 & tpxl-1(RNAi)* (n=7). (**B**) Kymographs of embryos shown in (A) starting from 180s after NEBD at 20s time interval.

(**C**) Graph showing normalized mean fluorescence intensity of LifeAct::mKate2 at anterior poles over time. LifeAct::mKate2 fluorescence intensity was normalized to the mean anterior fluorescence intensity in controls 180s after NEBD. Pixel intensities were measured by drawing a linescan (8 pixels wide) around the cell cortex in Fiji as shown in Figure 24E and mean values were calculated in Knime. Error bars are SEM and n = number of linescans. Scale bars is 5µm. Figure has been reproduced from Mangal et. al. 2018, with the permission of Rockefeller University Press.

4.2.2 TPXL-1 localizes to astral microtubules but is dispensable for their growth and nucleation

We analysed the localization of TPXL-1 by immunofluorescence and live cell imaging and consistent with a previous report (Özlü et al., 2005), Dr. Zanin showed that TPXL-1 localized to pericentriolar material (PCM) and astral microtubules during metaphase. In addition, she observed that TPXL-1 localization at the astral microtubules became more pronounced during anaphase, coinciding with the timepoint of polar clearing. TPXL-1 and its vertebrate homolog TPX2 have been shown to play different roles in regulating microtubule dynamics in *C. elegans* and *X. laevis,* respectively. In *C. elegans*, TPXL-1 RNAi led to the formation of short spindle without altering microtubule density, nucleation or growth rates in metaphase (Srayko et al., 2005) (Greenan et al., 2010). In contrast, TPX2 was shown to promote microtubule nucleation from existing microtubule in *Xenopus* egg extracts (Petry et al., 2013).

As already discussed in the previous chapter (Section 1.6), microtubules play an important role in regulating cortical accumulation of contractile ring proteins during anaphase. Therefore, to rule out the possibility that the observed polar clearing defect (Figure 29C-D and 30) was a consequence of altered microtubule dynamics in TPXL-1 depleted embryos, I set out to measure microtubule nucleation and growth rates in embryos expressing the microtubule plus end-binding protein EBP-2::GFP. The assay was established and carried out as described previously (Srayko et al., 2005). Briefly, the metaphase or anaphase embryos were filmed live for 2 minutes by exposing them to light for 400 ms without any intervals. A half circle of 9 µm radius was drawn centred around the anterior centrosome and kymographs were generated along the half circle for 1 minute recording (Figure 31A). To confirm that our assay is working reliably, I compared the microtubule nucleation and growth rates of metaphase with anaphase in control embryos. Consistent with prior work (Srayko et al., 2005), the microtubule nucleation increased and growth rate decreased in early (160-220s after NEBD) and late anaphase (255-315s after NEBD) as compared to metaphase (Figure 31A-C). Next, I analysed microtubule nucleation and growth rate in myosin depleted and

tpxl-1 & hcp-4(RNAi) embryos during the anaphase interval when polar clearing occurs (255-315s after NEBD) and found no difference as compared to the control (Figure 31D and E). Similarly, the number of microtubules that reached anterior cortex were indistinguishable from the control (blue line) (Figure 31D and F). Microtubule growth rate in *tpxl-1 & hcp-4*(RNAi) embryos was slightly higher rather than being lower than the control (Figure 31G). Finally, the microtubule nucleation and growth rates measured in myosin depleted & *rga-3/4(RNAi)* embryos were identical to the control (Figure 31D-G). RGA-3/4 were depleted by RNAi because *ebp-2::gfp* transgene was silenced in the *rga-3/4*Δ mutant. We confirmed that cortical accumulation and subsequent clearing of anillin from the anterior pole in *rga-3/4(RNAi)* embryos was similar to *rga-3/4*Δ mutant (experiment performed by Jennifer Sacher and image analysis by myself; Figure 32). These results show that neither TPXL-1 depletion nor RGA-3/4 inhibition impedes microtubule dynamics which could in turn slow down the process of polar clearing. Therefore, we concluded that TPXL-1 is involved in polar clearing of anillin independent of its function in regulating spindle length.

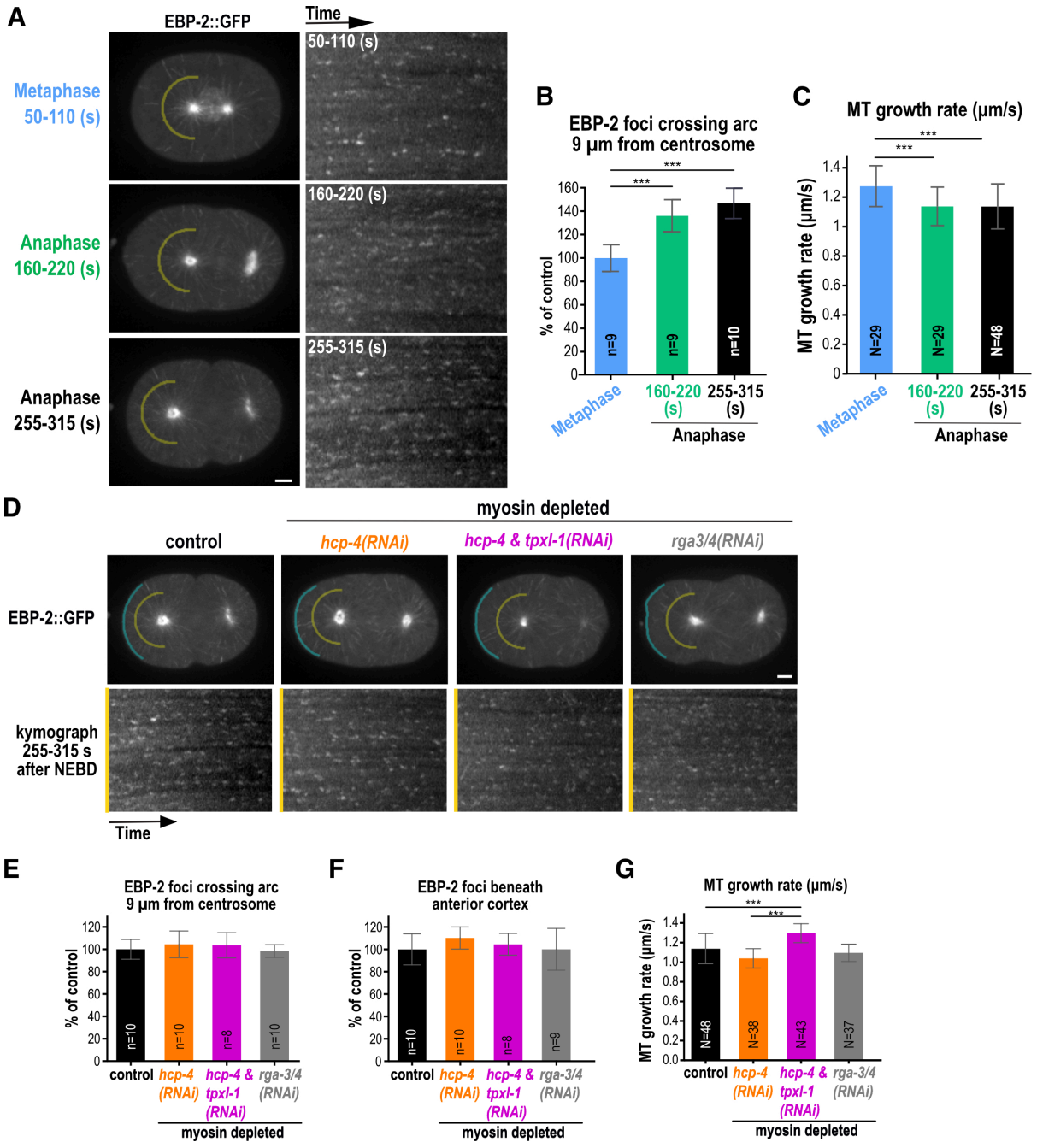

Figure 31: TPXL-1 is not required for nucleation and growth of astral microtubules in *C. elegans* one-cell embryos. (**A**) Projections of EBP-2::GFP images (left) acquired at 400ms intervals for a period of 4s in metaphase (n=9), early anaphase (160-220s after NEBD; n=9) and late anaphase (255-315s after NEBD; n=10). Gamma of 1.2 was applied in photoshop to visualize the EBP-2::GFP foci without saturating the aster centers. Kymographs (right) were generated for the entire 1 min movie along the yellow arc placed 9 microns away from the anterior centrosome and were used to quantify the microtubule nucleation. (**B-C**) Graphs show percentage of EBP2::GFP foci crossing the yellow arc in (B) as compared to the control (metaphase) and microtubule growth rates respectively. (**D**) Projections of EBP-2::GFP images (top) acquired at 400ms intervals for a period of 4s in control (n=10) and myosin depleted embryos alongwith *hcp-4(RNAi)* (n=10), *hcp-4 tpxl-1(RNAi)* (n=8), rga-3/4*(RNAi)* (n=10). Gamma of 1.2 was applied in photoshop to visualize the EBP-2::GFP foci

without saturating the aster centers. Kymographs (bottom) were generated along the yellow arc placed 9 microns away from the anterior centrosome as well as the blue arc beneath the anterior cortex for the entire 1 min movie. (**E-F**) Graphs show number of EBP-2::GFP foci crossing the yellow and blue arc respectively and (**G**) microtubule growth rates. Error bars are SD and p values are two-tailed student's t-test (***, $p < 0.001$). n = number of embryos in (B, E, F) and N = number of micrtotubles tracked in three or more embryos per treatment. Scale bars is 5µm. Figure has been reproduced from Mangal et. al. 2018, with the permission of Rockefeller University Press.

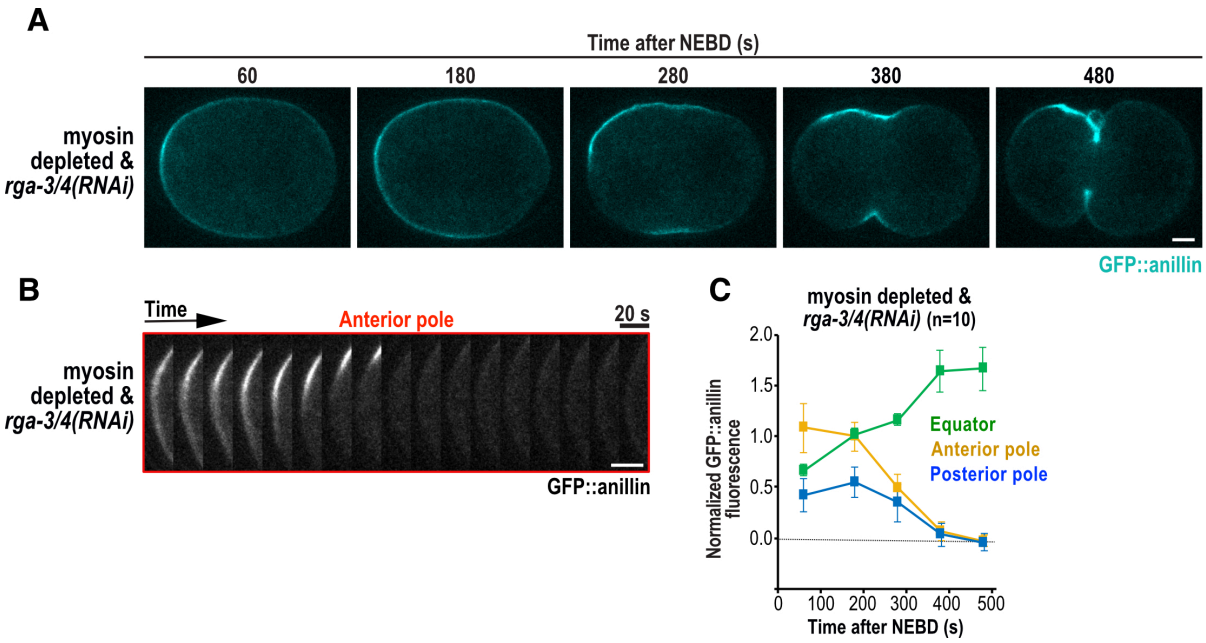

Figure 32: Anillin is actively cleared from polar cortex after anaphase onset in myosin depleted *rga-3/4(RNAi)* embryos. (**A**) Time-lapse confocal images of myosin depleted *rga-3/4*Δ embryos expressing GFP::anillin treated (n=5). (**B**) Kymographs of embryos shown in (A) starting from 180s after NEBD at 20s time interval. (**C**) Graph showing normalized mean fluorescence intensity of GFP::anillin at polar and equatorial cortex over time. GFP::anillin fluorescence intensity was normalized to the mean anterior fluorescence intensity in controls 180s after NEBD. Pixel intensities were measured by drawing a linescan (8 pixels wide) around the cell cortex in Fiji and mean values were calculated in Knime. Error bars are SEM and n = number of linescans. Scale bars is 5µm. Figure has been reproduced from Mangal et. al. 2018, with the permission of Rockefeller University Press.

4.2.3 Aurora A activation by TPXL-1 is required for polar clearing

TPXL-1 is known to activate and recruit Aurora A (AIR-1 in *C. elegans*) to microtubules where it stabilizes microtubules that connect kinetochores to spindle pole (Özlü et al., 2005). Consistent with prior work (Özlü et al., 2005), I confirmed that endogenous Aurora A^{AIR-1} (Figure 33A) and GFP::Aurora A^{AIR-1} (Figure 33B) localized to astral microtubules and pericentriolar material (PCM) during metaphase and anaphase, similar to TPXL-1. Furthermore, TPXL-1 depletion abrogated the GFP::Aurora A^{AIR-1} localization to astral

microtubules and strongly reduced its localization to the PCM (Figure 33A), confirming that localization of Aurora A to astral microtubules and PCM depends on TPXL-1.

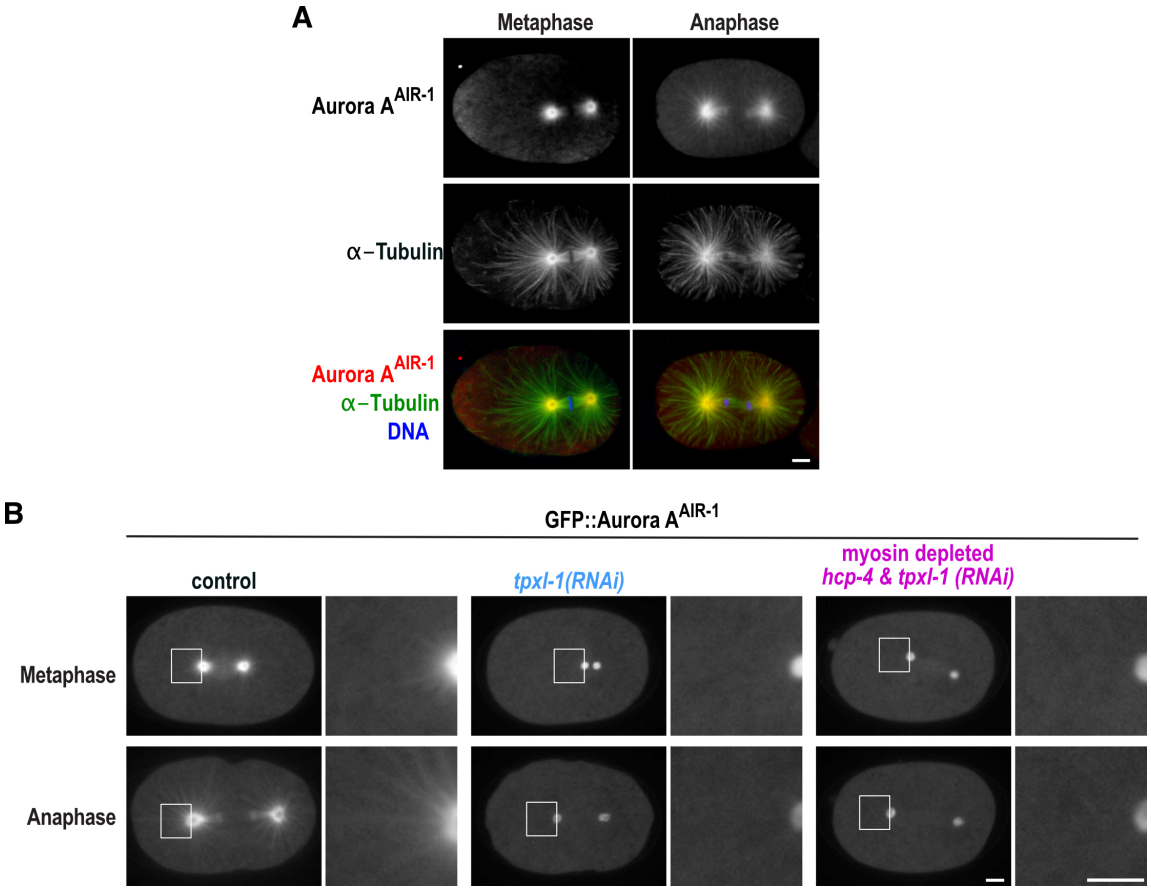

Figure 33: Endogenous and GFP-tagged AuroraA^{AIR-1} localizes to astral microtubule during anaphase in TPXL-1 dependent manner. (**A**) Representative confocal images of fixed metaphase (n=5) and anaphase (n=5) embryos stained for α-tubulin, Aurora A^{AIR-1} and DNA. Gamma of 1.5 was applied in photoshop to visualize the astral microtubules without saturating the centrosomes. (**B**) Confocal images showing GFP::AuroraA^{AIR-1} in control (n=14), *tpxl-1(RNAi)* (n=10) and myosin depleted *hcp-4 tpxl-1(RNAi)* (n=11) embryos during anaphase. Gamma of 2.0 was applied in photoshop to visualize the astral microtubules without saturating the centrosomes. Scale bars is 5μm. This figure is reproduced from my published research paper with the permission of the Journal JCB (Mangal et. al. 2018). Figure has been reproduced from Mangal et. al. 2018, with the permission of Rockefeller University Press.

To determine whether recruitment and activation of Aurora A by TPXL-1 is required for polar clearing, Dr. Zanin abolished their interaction by generating a previously described TPXL-1 transgene in which phenylalanine 15 and 18 were mutated to aspartic acid (TPXL-1^{FD}; (Bird and Hyman, 2008; Özlü et al., 2005). Then the transgene was crossed into *rga-3/4*Δ worms expressing mKate2::anillin and polar clearing of anillin in myosin, TPXL-1 and

HCP-4 co-depleted embryos was analyzed. While mKate2::anillin was cleared from the anterior pole in TPXL-1^{WT} embryos after anaphase onset, anillin accumulation continued to increase in embryos expressing TPXL-1^{FD} (Figure 34). Thus, we concluded that the activation of Aurora A by TPXL-1 is required for polar clearing (Figure 35).

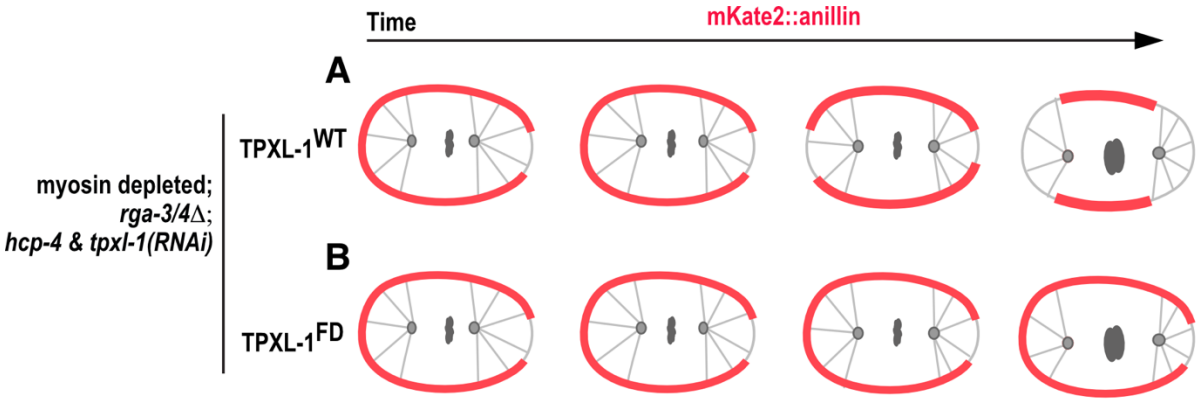

Figure 34: Aurora A activation by TPXL-1 is required for polar clearing of anillin in *C. elegans* one-cell embryos. Schematics showing the polar clearing of mKate2::anillin during anaphase myosin-depleted *rga-3/4Δ hcp-4 tpxl-1(RNAi)* embryos expressing (**A**) TPXL-1^{WT} or (**B**) Aurora A binding defective TPXL-1^{FD}.

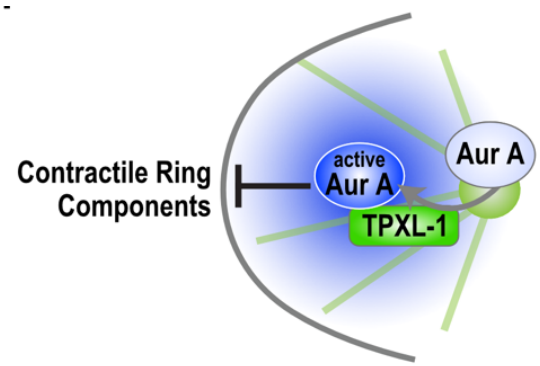

Figure 35: Model for Aurora A mediated clearing of contractile ring proteins from polar cortex. Avtivation of Aurora A on the astral microtubules by TPXL-1 generates a pool of diffusible signal that inhibits accumulation of contractile ring proteins on the polar cortex. Figure has been reproduced from Mangal et. al. 2018, with the permission of Rockefeller University Press.

It is possible that TPXL-1 activates Aurora A on the astral microtubules which then diffuses to the adjacent polar cortex where it clears the contractile ring proteins either directly or by phosphorylating downstream substrates (Figure 35). Consistent with our idea, prior work has shown that Aurora A forms a gradient around spindle poles in *Drosophila* S2 cells (Ye et al., 2015) and exhibits high centrosomal turnover rates in HeLa cells and *C. elegans* early embryos (Portier et al., 2007; Stenoien et al., 2003). Intriguingly, increased activation of Aurora A by inhibiting protein phosphatase 6 (PP6), a negative regulator of Aurora A (Zeng et al., 2010), led to ectopic accumulation of Aurora A on the cell cortex (Kotak et al., 2016) and reduced cell contractility (Afshar et al., 2009). To confirm these previous findings, I depleted PP6 phosphatase catalytic subunit PPH-6 or its associated subunit SAPS-1 in embryos expressing GFP::Aurora A^{AIR-1}. As previously shown by Kotak and colleagues, live imaging revealed ectopic accumulation of GFP::Aurora A^{AIR-1} on the cell cortex after anaphase onset in *pph-6(RNAi)* or *saps-1(RNAi)* embryos (Figure 36A). Although the GFP::Aurora A^{AIR-1} signal was clearly visible on the ingressing furrows where two cell membranes were juxta-positioned, the signal was rather weak on the polar cortex. Immunofluorescence analysis, however, resolved this issue and ectopic accumulation of Aurora A^{AIR-1} was clearly visible all around the cell cortex in *saps-1(RNAi)* embryos (Figure 36B), confirming the notion that increased activation of Aurora A leads to ectopic localization on the cell cortex. Based on these findings, I speculate that small amounts of Aurora A could localize to the cell cortex in wild-type embryos which are not detected owing to its transient nature and technological bottlenecks. If Aurora A is involved in clearing anillin from the cell poles, then ectopic localization of Aurora A on the cell cortex should lead to lower cortical accumulation of anillin. Indeed, much less GFP::anillin localized to the anterior pole in PPH-6 or SAPS-1 depleted embryos (Figure 36C-E) from anaphase (120s after NEBD) until complete furrow ingression. The accumulation of GFP::anillin on the equatorial cortex was also reduced in PPH-6 or SAPS-1 depleted embryos (Figure 36C-E) from anaphase until 220s after NEBD when furrow starts to ingress. Changes in anillin accumulation on the posterior pole was not measured as only trace amount of anillin localizes on the posterior pole in control embryos. These findings support our hypothesis that TPXL-1 activates Aurora A on the astral microtubules which diffuses to the adjacent cell poles and clears contractile ring proteins from the polar cell cortex.

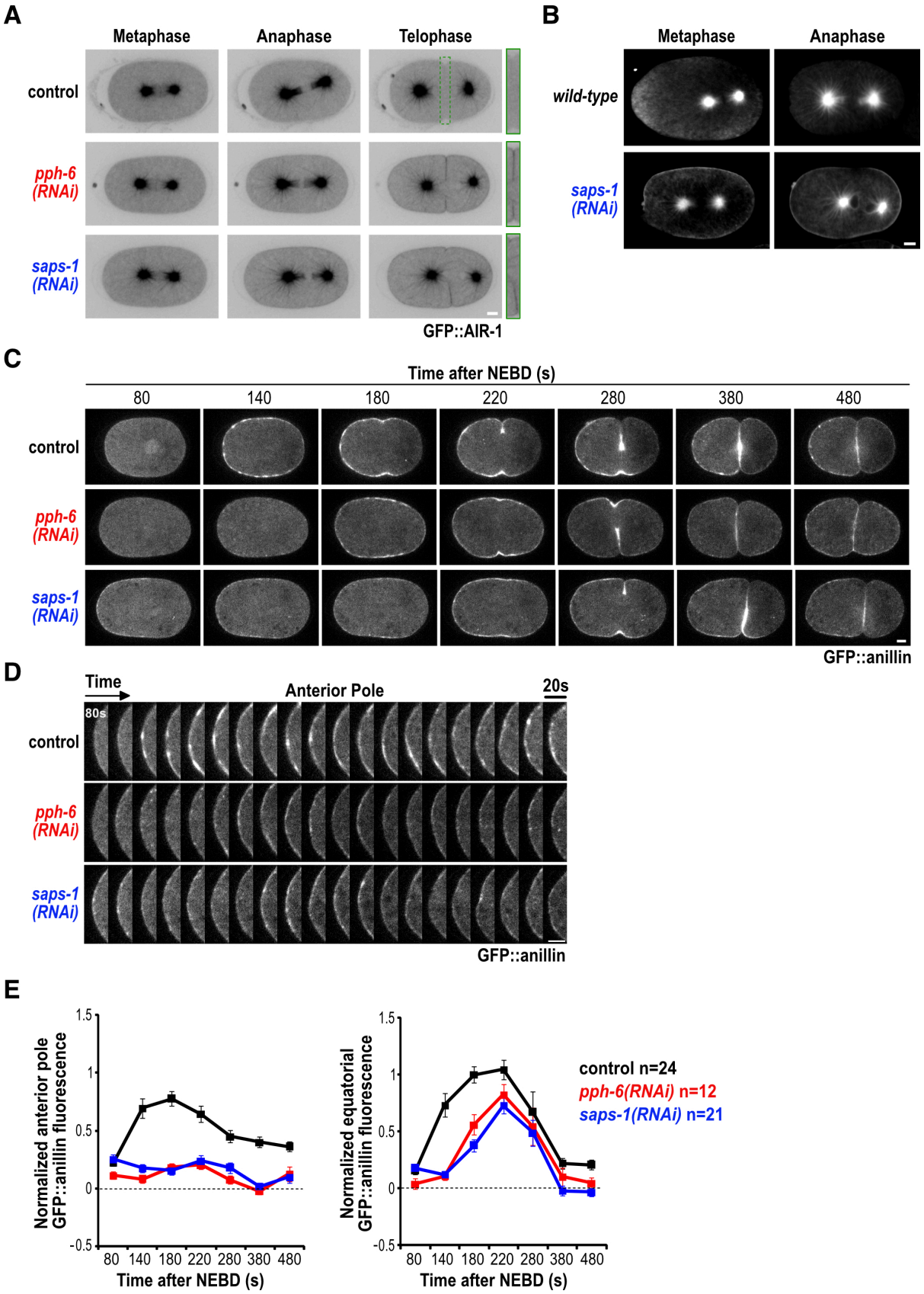

Figure 36: Ectopic accumulation of Aurora A^{AIR-1} on the cell cortex inhibits Anillin localization. (**A**) Representative confocal images of control, *pph-6 (RNAi)*, *saps-1 (RNAi)* embryos expressing GFP::AIR-1 in metaphase, anaphase and telophase. Green boxes on the right enclose magnified section of equator region during telophase. Gamma of 2.0 was

applied in photoshop to visualize the astral GFP::AIR-1 signal without saturating the centrosomes. (**B**) Representative confocal images of fixed wild-type and *saps-1(RNAi)* embryos in metaphase and anaphase stained for Aurora A^{AIR-1}. Gamma of 0.8was applied in Fiji to visualize the astral GFP::AIR-1 without saturating the centrosomes. (**C**) Timelapse confocal images showing GFP::anillin localization in control (n=12), *pph-6(RNAi)* (n=6) and *saps-1(RNAi)* (n=11). (**D**) Kymographs of embryos shown in (C) starting from 80s after NEBD at 20s time interval. (**E**) Graph showing normalized mean fluorescence intensity of GFP::anillin at polar and equatorial cortex over time. GFP::anillin fluorescence intensity was normalized to the mean equatorial fluorescence intensity in controls 180s after NEBD. Pixel intensities were measured by drawing a linescan (8 pixels wide) around the cell cortex in Fiji as shown in Figure 24E and mean values were calculated in Knime. Error bars are SEM and n = number of linescans. Scale bars is 5µm.

4.2.4 Aurora A inhibits anillin localization at cell poles in human cells

In vertebrates Aurora A localizes to centrosomes and astral microtubules (Kufer et al., 2002; Joukov et al., 2010; Roghi et al., 1998; Gopalan et al., 1997; Kimura et al., 1997) similar to Aurora A^{AIR-1} localization in *C. elegans* embryos (Özlü et al., 2005). In addition, Aurora A localization to astral microtubules, but not on the PCM surrounding centrosomes, is dependent on vertebrate homolog of TPXL-1 called TPX2 (Bird and Hyman, 2008). Several previous studies have shown that depolymerization of astral microtubules extends the equatorial localization of RhoA and other contractile ring proteins towards the cell poles (Bement et al., 2005; Foe and von Dassow, 2008; Murthy and Wadsworth, 2008; von Dassow et al., 2009, Zanin et al., 2013). In light of these observations, we wanted to investigate whether Aurora A plays a similar role in preventing accumulation of contractile ring proteins on the polar cortex in human cells as in *C. elegans* embryos. Since Aurora A has many functions in cell cycle like bipolar spindle assembly, spindle midzone formation and centrosome maturation (Nikonova et al., 2012), its depletion results in pleiotropic phenotypes that hinder the analysis of cortical patterning in anaphase. To overcome this problem, I used a highly specific chemical inhibitor of Aurora A to acutely inhibit its kinase activity in mitotic cells. As active site of Aurora A is very similar to its closely-related Aurora B kinase which is implicated in chromosome segregation and cytokinesis (Carmena et al., 2012), we based our choice of chemical inhibitors on a report that analysed selectivity of ten Aurora inhibitors (de Groot et al., 2015). Using an immunofluorescence assay that measured phosphorylation of Aurora A substrate LATS2 (Ser83) and Aurora B substrate histone H3 (Ser28), de Groot and colleagues identified MK-5108 and AZD1152-HQPA (AZD) as most selective inhibitors of Aurora A and B respectively (de Groot et al., 2015). Next, we used this published assay to optimize the concentration and duration of MK-5108 and AZD treatments in HeLa cells. I

confirmed that treatment of HeLa cells with 10µM MK-5108 for 30-60 minutes strongly inhibited Aurora A activity evident from significant reduction in centrosome pLATS2 (Ser83) intensity and had minimal effect on Aurora B as shown by mild decreased in chromosomal pH3 (Ser28) intensity (Figure 37A-D). Conversely, treatment with the AZD for 2-3 hours strongly inhibited Aurora B activity with only mild effects on Aurora A (Figure 37A-D).

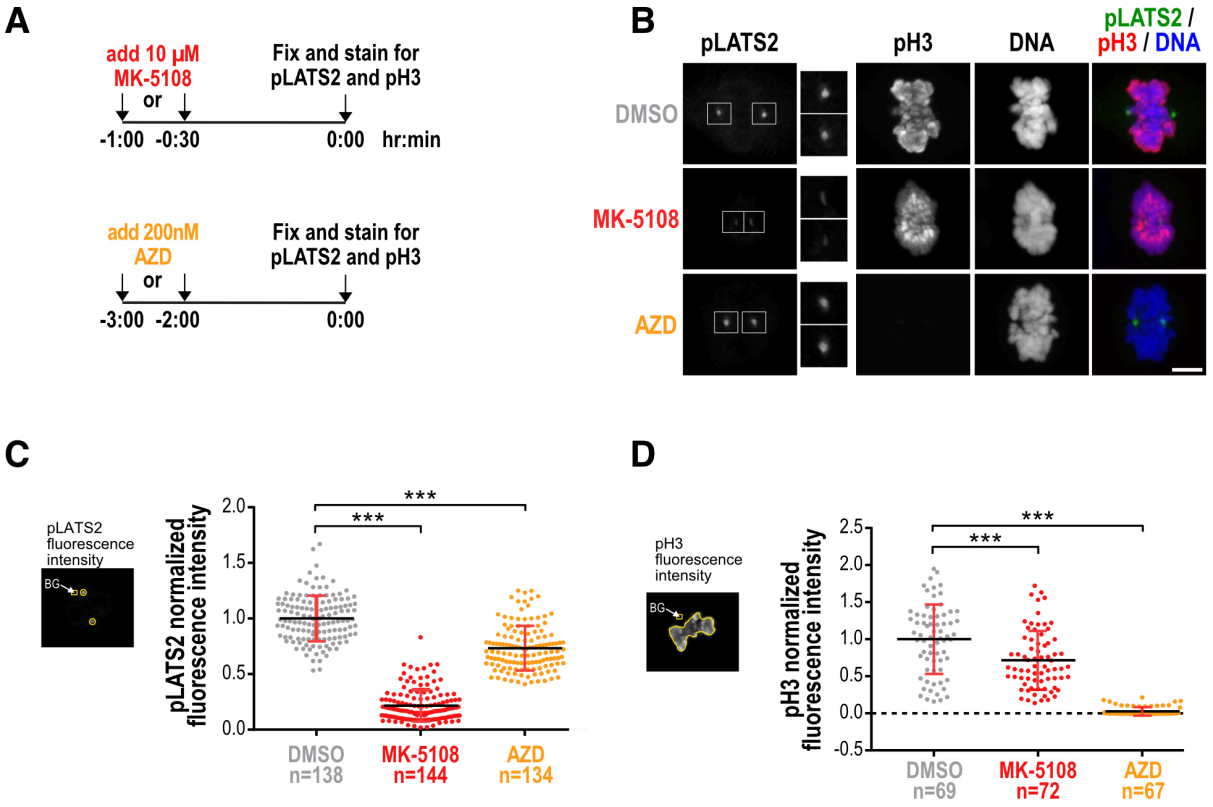

Figure 37: Establishing conditions for selective Aurora A inhibition in HeLa cells. (**A**) Schematics illustrating the procedures used for inhibitor treatments. Aurora A was inhibited by treatment with 10µM MK-5108 for 60 or 30min and Aurora B was inhibited by treatment with 200 nM AZD for 2 or 3hrs. (**B**) Maximum intensity projections of confocal immunofluorescence images of MK-5108, AZD or DMSO treated HeLa cells stained for pLATS2, pH3 and Hoechst (DNA). (**C-D**) Normalized mean fluorescence intensity of pLATS2 at centrosomes (C) and pH3 on chromosomes (D) is plotted for the indicated conditions. All values were normalized to the mean value in DMSO-treated control cells and error bars are SD. In (C) n = number of centrosomes and in (D) n = number of cells. All p values are obtained by student's t-test (***p<0.001) and scale bars are 5µm.

To investigate the involvement of Aurora A in clearing contractile ring proteins from polar cortex in human cells, HeLa cells expressing anillin::GFP were treated with MK-5108, AZD, or DMSO as a control and filmed live during anaphase (Figure 38A and B). Treatment with MK-5108 and AZD led to mitotic arrest in ~60% and ~30% cells respectively. To ensure

strong but selective inhibition of Aurora activity, I analyzed cells that entered anaphase between 25 and 60 minutes after MK-5108 addition and between 2 and 3 hours after AZD addition. The accumulation of anillin::GFP at the cell cortex was measured by drawing linescans 8 minutes after anaphase onset as shown in Figure 10A. We found that Aurora A, but not Aurora B, inhibition led to increased accumulation of anillin::GFP on the polar cortex (Figure 38B-D) and a wider zone of anillin::GFP at the cell equator (Figure 38F). This increase cannot be attributed to a global rise in cortical accumulation of anillin::GFP as its levels were slightly reduced at the equatorial cortex in both, Aurora A and B inhibited cells (Figure 38E). Alternatively, broader anillin zone at the cell equator could be caused by longer spindle midzone as anillin zone width and spindle midzone length are thought to be correlated (Hu et al., 2011). However, when I measured the spindle midzone length after Aurora A inhibition, it was found to be decreased, rather than increased, consistent with previous studies (Reboutier et al., 2013; Lioutas and Vernos, 2013) (Figure 38G and H). To ensure that the increase in polar anillin was not caused by a weak spindle midzone in Aurora A inhibited cells as reported by few previous studies (Reboutier et al., 2013; Lioutas and Vernos, 2013), I analysed localization of Plk1 and endogenous anillin after MK-5108 treatment. Plk1 was chosen because it is a key cytokinesis regulator that localizes to midzone and promotes cell contractility. The analysis revealed that Plk1 localized to the spindle midzone in two third of the cells (53/80; Figure 39A) treated with MK-5108 even though the length of spindle midzone was significantly reduced as compared to the controls (Figure 39E). Importantly, in these 53 cells having midzone localized Plk1, anillin formed a wider zone at cell equator (Figure 39D) and anillin accumulation at cell poles was increased (Figure 39B). Similar to live-cell imaging experiments (Figure 38E), increase in polar anillin accumulation was not due to a global rise in cortical accumulation of anillin as anillin levels were slightly reduced at the equatorial cortex in Aurora A inhibited cells (Figure 39C). Thus, this data indicates that Aurora A inhibits anillin localization on cell poles independent of the weak midzone phenotype.

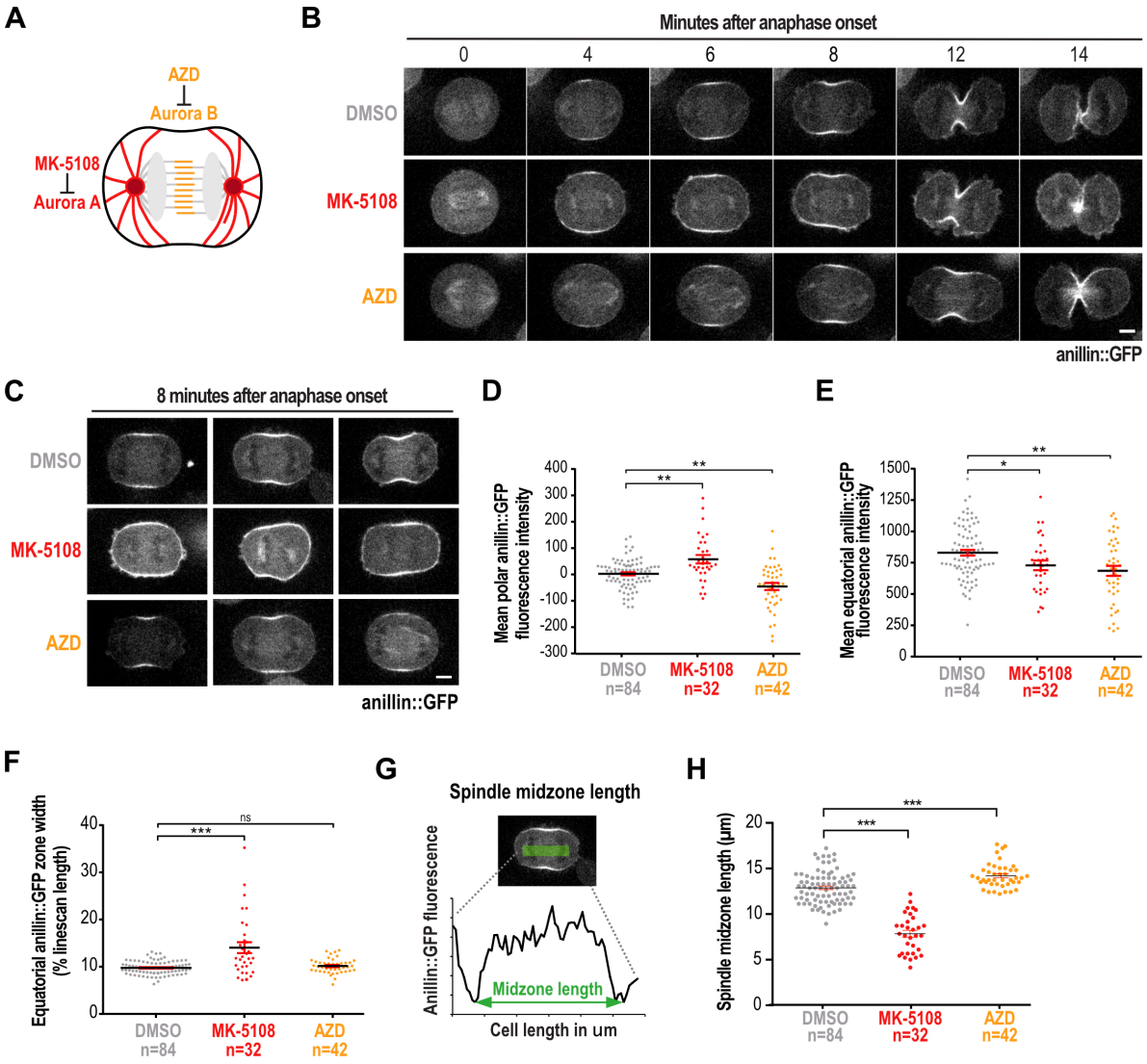

Figure 38: Aurora A restricts anillin accumulation to a narrow zone at the cell equator in HeLa cells. (**A**) Aurora A localizes to the centrosome and the centrosomal microtubule asters and is inhibited by MK-5108. Aurora B localizes to the spindle midzone and is inhibited by AZD. (**B**) Time-lapse confocal images of HeLa cells expressing anillin::GFP that were treated with DMSO (control), 10µM MK-5108 or 200nM AZD. (**C**) More confocal images of 8 min after anaphase onset are shown. (**D-F**) Graphs showing the mean anillin::GFP intensity at the cell poles (D), at cell equator (E) and width of the equatorial anillin::GFP zone (F) for cells subjected to the indicated conditions. Pixel intensities in (D-F) were measured by drawing a linescan (8 pixels wide) around the cell cortex in Fiji and mean values were calculated in Knime. (**G**) The length of the spindle midzone was measured 8 minutes after anaphase onset from linescans across the center of the cell. Spindle midzone length was defined as the distance between the two minima of anillin::GFP fluorescence intensity measured by drawing a 15 pixel wide line in Fiji. (**H**) Graph plotting spindle midzone length for the indicated conditions. All error bars are SEM and n = number of cells. All p values are calculated with student's t-test (***p<0.001, **p<0.01, *p<0.05, not significant (ns) p>0.05) and all scale bars are 5µm.

Selective disassembly of astral microtubules with nocodazole, is known to broaden the localization of anillin at the cell equator in HeLa cells (Zanin et al., 2013). To determine if broader anillin zone and increased anillin at the polar cortex in Aurora A inhibited cells was due to attenuated asters, microtubules were stained and imaged on a confocal microscope. Treatment with 70nM Nocodazole for 10 minutes, similar to MK-5108 treatment, led to increased anillin accumulation at cell poles (Figure 39B) and a wider zone of anillin (Figure 39D) at the cell equator despite having a shorter spindle midzone (Figure 39E). However, unlike nocodazole treated cells (n=39) where astral microtubules were barely visible, microtubule asters in MK-5108 treated cells (n=65) appeared similar to those in control (n=46; Figure 39F). Thus, Aurora A seems to inhibit anillin accumulation at cell poles without severely affecting the microtubule asters. Overall, I conclude that Aurora A, restricts the accumulation of anillin to a narrow zone at the cell equator and inhibits its localization at the cell poles, suggesting that the role of Aurora A activity in polar clearing of contractile ring proteins in *C. elegans* embryos is conserved in humans.

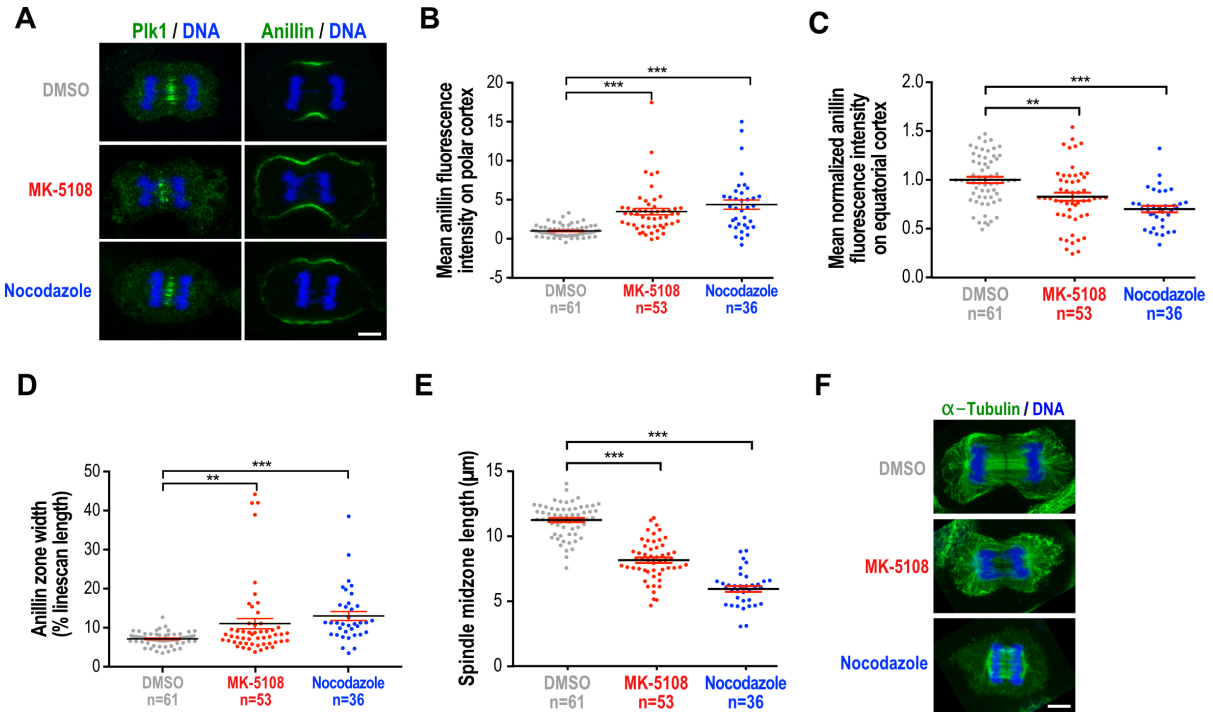

Figure 39: Aurora A inhibition results in accumulation of endogenous anillin on the polar cell cortex in HeLa cells. (**A**) Confocal images of fixed DMSO, 10µM MK-5108 or 70M nocodazole treated HeLa cells that were stained for Plk1, anillin and DNA. (**B**) Graphs showing mean anillin fluorescence intensity on the polar cortex in cells treated with DMSO, MK-5108 and Nocodazole. (**C**) Plots showing mean normalized anillin fluorescence intensity on the equatorial cortex in cells subjected to indicated conditions and (**D**) and mean anillin zone width. Anillin intensities in (B-D) were measured by drawing a linescan (9 pixel wide) around the cell cortex in Fiji and mean intensities were calculated in Knime. Anillin intensity

in (C) was normalized to mean anillin intensity in DMSO treated cells. (**E**) Graph showing length of spindle midzone in cells subjected to the indicated conditions. (**F**) Confocal images of HeLa cells treated with DMSO (n = 46), 10μM MK-5108 (n = 65) or 70M nocodazole (n = 39) and stained for α-tubulin and DNA. All error bars are SEM and n = number of cells. All p values are calculated with student's t-test (***p<0.001, **p<0.01, not significant (ns) p>0.05) and all scale bars are 5μm.

4.3 Rapamycin-induced protein dimerization in *C. elegans*

[Data presented in this section has already been published by us in the microPublication Biology Journal. The detailed citation is as follows:

Mangal, S., Zielich, J., Lambie, EJ., Zanin E. (2018). Rapamycin-induced protein dimerization as a tool for C. elegans research. Micropublication: biology. https://doi.org/10.17912/W2BH3H.

The Figure has been reproduced with the permission of microPublication Biology Journal and the permission email is attached in the Appendix.]

To further investigate the role of TPXL-1 and Aurora A in clearing anillin and f-actin from the cell poles, I wanted to target TPXL-1 and Aurora A to the cell membrane by inducing dimerization with a membrane bound protein or domain. In biological research, especially cell culture systems, rapamycin induced protein dimerization has been extensively used (DeRose, Miyamoto, & Inoue, 2013; Voß, Klewer, & Wu, 2015) to regulate expression, localization (Boeckeler, Rosse, Howell, & Parker, 2010), stability (Janse, Crosas, Finley, & Church, 2004) and activity of proteins including transcription factors (Pollock, Giel, Linher, & Clackson, 2002), kinases (Karginov & Hahn, 2011), Cre recombinase (Jullien, Sampieri, Enjalbert, & Herman, 2003), and RhoA GTPase signaling (Inoue, Heo, Grimley, Wandless, & Meyer, 2005). Rapamycin was first isolated in 1972 from *Streptomyces hygroscopicus* (Vézina, Kudelski, & Sehgal, 1975), and has attracted much attention of researchers owing to its immunosuppressant properties. Rapamycin, naturally, binds to FK506 binding protein FKBP12, which in turn binds to the FRB (FKBP12-rapamycin binding) domain of mammalian target of rapamycin (mTOR). Thus, forming a heterodimer of FRB and FKBP12 domains containing proteins linked by rapamycin (Choi, Chen, Schreiber, & Clardy, 1996; Putyrski & Schultz, 2012). Rapmycin induced protein dimerization seemed to be an appealing choice for two reasons. Firstly, I could fuse TPXL-1 or Aurora A with FKBP-12 domain and cell membrane binding pleckstrin homology (PH) domain with the FRB domain of mTOR to target TPXL-1 or Aurora A to the cell membrane in presence of rapamycin.

Secondly, I could inject rapamycin into the gonads of the worms to incorporate rapamycin into the cytoplasm of newly formed oocytes and the otherwise impermeable embryos. However, to my knowledge, rapamycin induced protein dimerization was not previously used in *C. elegans*.

To establish this technique in *C. elegans*, the cDNA sequences of human FKBP12 (CR542168) and FRB (NM_004958) domains were codon optimized (Redemann et al., 2011) for high expression in *C. elegans*. In addition, introns were added between amino acids 25(K)-26(G) in FRB and amino acids 35(K)-36(K) in FKBP12. Since rapamycin binding with mTOR kinase may cause pleiotropic phenotypes, I mutated 'threonine' 2098 to 'leucine' in the FRB domain which allows the binding of rapamycin derivatives that do not interact with mTOR kinase (Bayle et al., 2006). The resulting DNA sequence was synthesized by Eurofins Genomics. Next, the codon-optimized FRB domain was fused with GFP::PH (Audhya et al., 2005) to anchor FRB domain to the plasma membrane and FKBP12 domain with mCherry on the N-terminus. Both the transgenes, FRB::GFP::PH and mCherry::FKBP-12, were put under the control of *mex-5* promoter and the *tbb-2* 3′ UTR (Zeiser, Frøkjær-Jensen, Jorgensen, & Ahringer, 2011) and, were integrated on chromosomes I and II, respectively, using the MosSCI method (Frøkjær-Jensen et al., 2008; Figure 40A).

Imaging of adult worm gonads showed that mCherry::FKBP12 localized to the cytoplasm and nucleus, and FRB::GFP::PH localized to the plasma membrane, in both the germ line and early embryos (Figure 40C and D) as we expected. However, upon injection of 1mM rapamycin into the pachytene region of germ line (by Dr. Jeffery Zielich; Figure 40B), mCherry::FKBP12 also localized to the plasma membrane similar to FRB::GFP::PH in all analysed germ lines (Figure 40C) and early embryos (Figure 40D). This shift in localization of mCherry::FKBP-12 was not seen when DMSO (the solvent used to dissolve rapamycin) was injected into the gonads of adult worms (Figure 40C and D). These findings suggest that, rapamycin successfully induced heterodimerization of FRB and FKBP12 domain containing transgenic proteins at the plasma membrane, as FRB domain was anchored there by pleckstrin homology domain (PH). In my experiments, injection of rapamycin into the germ line did not cause any embryonic lethality (DMSO, n = 281 progenies; rapamycin, n = 302 progenies). Further, rapamycin did not seem to alter in gonad morphology (n = 29 gonads) and early embryonic divisions (n = 17 embryos), however, this needs to be further tested and quantified.

In summary, we established a rapamycin-inducible dimerization system in *C. elegans* which can be used to target, theoretically, any protein including TPXL-1 and Aurora A to the plasma membrane. This method could also be further adapted to control activity and stability of proteins. However, due to lack of time, I was not able to employ this method for targeting TPXL-1 and Aurora A to the cell membrane and observing changes in anillin localization.

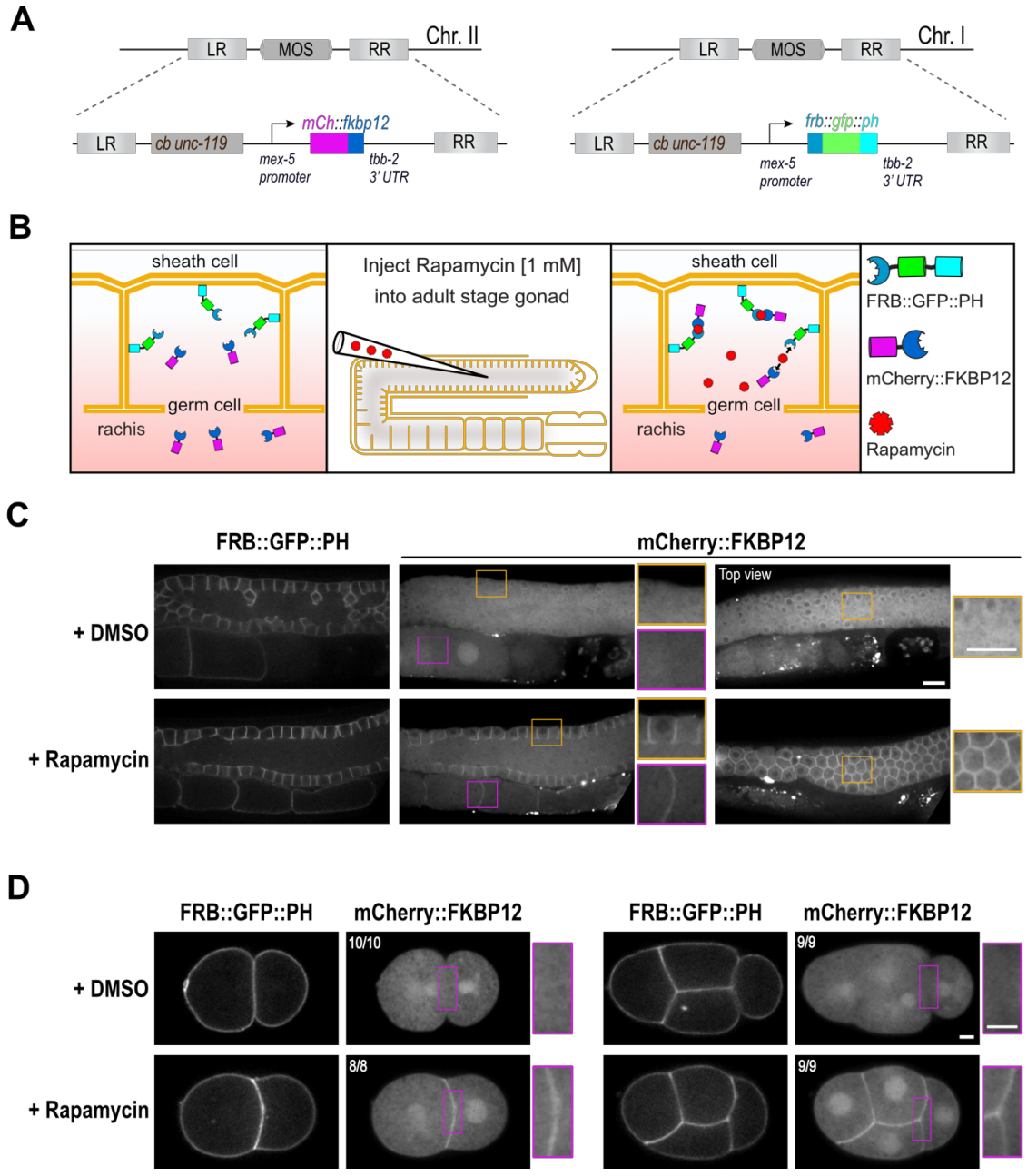

Figure 40. Rapamycin mediated dimerization of cytosolic mCherry::FKBP12 and FRB::GFP::PH at the plasma membrane in *C. elegans* gonad and early embryos. (A) Schematic representation of mCherry-tagged FKBP12 and GFP-PH-tagged FRB transgenes that were integrated into chromosome II and chromosome I respectively by single copy MosSCI insertion. The transgenes were kept under the control of the *mex-5* promoter and *tbb-2* 3′ UTR. **(B)** Schematic illustration of rapamycin-induced dimerization of FRB::GFP::PH

and mCherry::FKBP12 in *C. elegans* gonad. In the absence of rapamycin, mCherry::FKBP12 is present in the cytoplasm and FRB::GFP is tethered to the plasma membrane by FRB domain. Injection of 1 mM rapamycin into the gonad, induces heterodimerization of FKBP12 and FRB domains, resulting in translocation of mCherry-FKBP12 from cytoplasm to the plasma membrane. **(C)** Representative confocal images of gonad of an adult *C. elegans* worm expressing FRB and FKBP12 fusion proteins that were injected with DMSO (n=19) or 1 mM rapamycin (n=29) and imaged 2-3 hours after injection. n = number of gonads. Yellow and magenta insets show magnified view of two regions of the gonad, germ cells and oocytes respectively. Scale bar 10 μm. **(D)** Confocal images of 2-cell and 4-cell *C. elegans* embryos excised from adult worms that were injected into the gonad 2-3 hours before imaging either with DMSO (2-cell embryo n = 10; 4-cell embryo n = 9) or with 1 mM rapamycin (2-cell embryo n = 8; 4-cell embryo n = 9). Magenta inset shows magnified view of the plasma membrane between the two adjacent cells in the embryo. Scale bar 5μm. The figure has been reproduced with the permission of microPublication Biology Journal.

5. Discussion and Outlook

Precise temporal and spatial regulation of cytokinesis is key to successful cell division and maintaining the genome integrity. This robust control over contractile ring assembly and ingression is facilitated by active signalling between mitotic spindle and the cell cortex (Green et al., 2012). Based on experimental evidences, it is widely believed that spindle midzone stimulates the localization of contractile ring proteins at the cell equator (Cao and Wang, 1996; Kawamura, 1977; Nishimura and Yonemura, 2006; Somers and Saint, 2003; Wheatley and Wang, 1996; Yüce et al., 2005; Zhao and Fang, 2005) (Figure 3A), whereas microtubule asters deliver inhibitory signal(s) that prevent the localization of contractile ring proteins at the cell poles (Bement et al., 2005; Foe and Dassow, 2008; Mangal et al., 2018; Murthy and Wadsworth, 2008; Rodrigues et al., 2015; Werner et al., 2007; Zanin et al., 2013; Zhou and Wang, 2008) (Figure 3C). However, the identity of such aster derived inhibitory molecules(s) remains elusive. In addition, regulation of cortical patterning during cytokinesis is not properly understood and insights on how Ect2 and RhoA are activated in a narrow equatorial zone have just begun to emerge. For example, a recent study in *Drosophila* S2 cells showed that Plk1, Aurora B and centralspindlin localize to plus-tips of equatorial microtubule asters which recruit Ect2 to the equatorial cortex and activate RhoA (Verma and Maresca, 2019). The aim of my thesis was to identify signalling molecules that play a role in promoting and inhibiting localization of contractile ring proteins at cell equator and poles, respectively. I chose to investigate this question in two model systems, the human HeLa cell line and the one-cell embryos of the nematode *C. elegans* using a variety of genetic, biochemical and fluorescence microscopy techniques. These two model systems have well annotated genomes, established tools for genetic manipulations, and are amenable to quantitative confocal microscopy. Using these two model systems together offers many advantageous as the main components of their cell cycle machinery are largely conserved and the observations from one model system can be validated in the other.

5.1 RNAi Screen identified 18 new regulators of cytokinesis in human cells

To identify novel regulators of cortical patterning during cytokinesis high-throughput RNAi screen was performed in HeLa cells in collaboration with Dr. Marc Bickle and Dr. Martin Stoeter of MPI-CBG, Dresden. HeLa cells were chosen over *C. elegans* worms due to their easier handling, convenient RNAi protocol, permeability to chemical compounds and amenability to high-throughput imaging. Previous screens have mainly relied on multinucleation phenotype to identify regulators of cytokinesis (Eggert et al., 2004; Kittler et al., 2004; 2007; Mukherji et al., 2006; Neumann et al., 2006; 2010; Sönnichsen et al., 2005). For example, Eggert et al. treated *Drosophila* cells with 19,470 dsRNAs and 51,000 chemical molecules but only analysed number of binucleated and multinucleated cells to identify cytokinesis regulators (Eggert et al., 2004). Similarly, Kittler et al. treated HeLa cells with endoribonuclease-prepared siRNAs (esiRNAs) library covering 17,828 genes and performed DNA content analysis by laser scanning cytometry to analyse ploidy after gene knockdown (Kittler et al. 2007). Mukherji et al. treated U2OS cells with siRNA library covering the entire human genome and analysed phenotypes like total number of cells, cells in G1, S, G2/M phases, percentage of cells with altered ploidy etc. Since the drastic changes in ploidy mainly result from cytokinesis failure, latter two screens only revealed regulators which are required for successful completion of mitosis. It should be noted that abnormal cortical patterning of contractile ring proteins does not always result in cytokinesis failure. Depletion of MP-GAP, the only known RhoA GTPase which counteracts RhoA activation during cytokinesis, does not lead to increased multinucleation (Zanin et al., 2013). Thus, cytokinesis failure is not always a good terminal readout to identify regulators of cytokinesis. A more comprehensive genome-wide RNAi screen was performed in *C. elegans* by Sönnichsen et al. to identify genes regulating first two embryonic cell divisions (Sönnichsen et al., 2005). 5000 genes that led to embryonic lethality were further tested by differential interference contrast (DIC) time-lapse microscopy to link genes with various abnormal phenotypes. For example, polar body extrusion, pronuclear migration, spindle assembly and elongation, sister chromatid separation, asymmetry of division, cytokinesis etc. Although DIC time-lapse microscopy proved to be very useful for assessment of different processes during cell division, subtle defects in cortical dynamics and changes in cortical patterning of contractile ring proteins could not be investigated. Moreover, knockdown of genes that do not result in embryonic lethality can still play a role in regulating contractile ring assembly and ingression. A similar genome-wide RNAi screen was also performed in HeLa cells expressing H2B-GFP where epifluorescence time-lapse microscopy was performed to

identify phenotypes like chromosome segregation errors, premature nuclear assembly and cytokinesis failure (Neumann et al., 2010). Again, cytokinesis failure was largely judged on the basis of number of binuclear cells. Importantly, a contractile ring marker such as RhoA or anillin has never been used in any of the previous screens to analyse cortical patterning during anaphase when contractile ring is assembled. The reasons behind this can only be speculated. Firstly, anaphase lasts for very short duration of approximately 15 minutes in HeLa cells, which makes it extremely challenging to have high number of anaphase cells in fixed samples (Figure 19D, 38B). Secondly, most RNAi screens employ automated image analysis to obtain quantitative phenotypic data from the acquired images. Identifying anaphase cells with >95% accuracy and measuring fluorescence intensity of contractile ring proteins on cell cortex with automated workflows is very difficult. Thirdly and most importantly, RNAi screens are financially expensive as large quantities of expensive reagents, latest microscopes and multi-disciplinary experienced research team are required. Thus, laboratories prefer to investigate several aspects of a process to get maximum value out of their investment and enhance the probability of finding interesting candidates. We overcame some of these challenges and developed a semi-automated high-throughput screening workflow to analyse the cortical localization of contractile ring marker anillin during anaphase (Figure 9D, 10A and 12). The number of anaphase cells were increased by synchronizing cell cycle using a combination of thymidine and MG132 treatments (Figure 9D). Since mitotic cells are loosely attached to the well surface and can be detached merely by a shake off, Martin Stoeter developed a gentler wash protocol on liquid handling robot Tecan 384. This liquid handling station is different from conventional plate washers which cannot be programmed for gentler wash cycles. We used this workflow to screen a set of 7,553 genes, which comprises the druggable human genome library, in HeLa cells expressing anillin::GFP and mKate2::α-tubulin (Figure 12). This subset of Dharmacon genome-wide siRNA library was interesting to test as it includes kinases, phosphatases, proteases, GPCRs (G-Protein coupled receptors), ubiquitin ligases etc. Anillin was chosen because it binds to active RhoA and mimic RhoA localization (Piekny and Glotzer, 2008), thereby, serving as a proxy marker for active RhoA. To identify the candidates that altered anillin localization upon gene knockdown, Martin Stoeter made rigorous efforts to establish an automated image analysis workflow. But all the attempts in this regard failed to achieve desired results and images were analysed manually. It is worth noting that anillin localization in anaphase cells has never been investigated on such a large scale and this makes our RNAi screen stand out from all the previous screens. In the primary screen, 45,318 images were manually inspected and 6,887 cells for 528 shortlisted genes were manually quantified by drawing linescans as

shown in Figure 10A. Data analysis performed using automated workflow in Knime, led to identification of 208 candidates having significant changes in anillin localization at the poles and/or equator (Figure 12E and 13). These 208 candidates were further validated in secondary screen by following the same procedure as in the primary screen. In the secondary screen, 21 candidate genes (10%) caused the same anillin localization defects as in the primary screen. Previous RNAi screens performed in HeLa cells by Neumann et al. and Kittler et al. confirmed 46% and 78% of the genes, respectively, that were identified in the primary screen. Considering that the pool of four siRNAs used for RNAi-mediated gene knockdown in primary and secondary screens had identical sequence, catalogue and lot numbers, it is surprising to have such a low number of confirmed candidates. The individual siRNAs were mixed again for the secondary screen and therefore, this pool cannot be said to be identical to that in the primary screen. However, unless, major pipetting errors occurred while pooling the siRNAs for the secondary screen, it cannot be speculated as a cause of low reproducibility. Further, it is not reasonable to believe that low or poor transfection efficiency led to reproducibility problems in the secondary screen as RhoA, Ect2, KIF23 and MP-GAP depletion lead to expected phenotypes. But, the probability of well-to-well variation in transfection efficiency cannot be ruled out. The influence of off-targets effects on reproducibility can be eliminated as same siRNAs were used in primary and secondary screen. In the primary screen, variations in expression level of anillin::GFP were observed between different batches of the screening plates that were processed on different days. To take this into consideration, siRNA treated library wells were always compared to the controls of the same batch. Thus, batch to batch variations in anillin::GFP levels cannot be accounted for the issue of low reproducibility. In both screens, anillin::GFP was measured in early and late anaphase cells having not more than 50 percent (approximately) furrow ingression. Since the accumulation of anillin::GFP increases from early anaphase to late anaphase, it is possible that this contributed to some variability in our assay which in turn negatively impacted the reproducibility rate. Another factor affecting reproducibility could be the low number of analysed cells. For 53/208 candidates genes shortlisted in the primary screen, only 5-10 anaphase cells could be analysed by linescans.

To further investigate reasons for low reproducibility, I turned back to the list of 208 candidates identified in the primary screen. While 14/90 (or 15%) genes that resulted in altered anillin::GFP localization at the cell equator were confirmed, only 7/139 (or 5%) genes altering polar anillin::GFP localization were confirmed in the secondary screen (Figure 13, 14 and 41). This means that rate of reproducibility was much lower for the candidates that

showed changes in polar localization of anillin. Here it is important to note that mean anillin::GFP fluorescence intensity at cell poles is always negative in controls, as cytoplasmic background is subtracted to correct for cell to cell variation in the expression of transgenic protein (Figure 14). In the primary screen, 103/139 genes had significantly higher anillin accumulation at cell poles yet the mean polar anillin::GFP fluorescence intensities were still negative (Figure 41). Out of these 103 genes, only 2 (or <2%) genes were confirmed in the secondary screen. Whereas, from remaining 36 genes which had positive mean value for anillin::GFP fluorescence, 5 (or 14%) genes were confirmed in the secondary screen (Figure 41). This comparative analysis shows that applying cut-off solely based on statistical significance value was not sufficient for this phenotype and a suitable threshold value should have been applied on the data. This observation, however, is not true for the 90 genes that were identified to have more (38 genes) or less (52 genes) anillin on equatorial cell cortex upon knockdown in the primary screen (Figure 13 and 41). While 12/52 (or 23%) genes leading to decreased anillin localization at cell equator were confirmed, only 2/38 (or 5%) genes leading to increase in anillin localization at cell equator were confirmed in the secondary screen (Figure 41). The magnitude of change in mean anillin::GFP intensity upon knockdown of majority of the genes was at least 0.5 folds but still only few of them were confirmed. Overall, the cause(s) leading to low reproducibility in the RNAi screen are not entirely clear and remain open for further analysis in the near future.

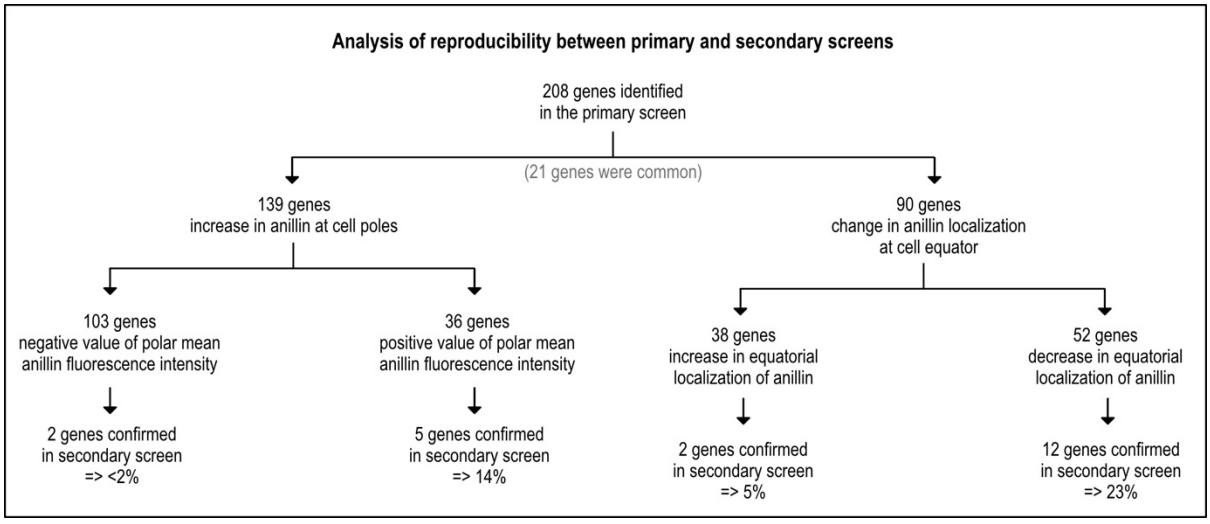

Figure 41: Analysis of reproducibility between primary and secondary screen. Genes confirmed in primary and secondary screen were classified into phenotypic classes and percentage of total number of genes confirmed for each phenotype was calculated.

Out of 21 candidates, Ect2, RhoA and MKLP1 (or KIF23) are known regulators of cytokinesis. Since Ect2 was also used as RNAi control, it was reassuring but not surprising to have Ect2 in the list of confirmed candidates. Nevertheless, in total, 19 new regulators of cytokinesis signalling were revealed in the RNAi screen. For all the 21 candidates, other parameters linked with cortical localization of anillin such as anillin zone width, length of the spindle midzone (Figure 18B) and cell circumference were measured in primary and secondary screen (Tables 19-21). 18/21 candidate genes did not show any significant changes in anillin::GFP zone width at the cell equator upon knockdown (Table 19). RhoA and Sept7 having reduced anillin::GFP localization at cell equator also had significantly narrower zone width, while KIF23 having increased anillin::GFP on cell poles had broader zone at the cell equator (Table 19). Thus, the changes in anillin zone width for RhoA, Sept7 and KIF23 are in line with the changes observed in anillin localization at cell equator and poles. Length of spindle midzone was also measured to investigate abnormalities in its elongation, however, none of the 21 candidates were found to have any significant changes in the length of spindle midzone as compared to the controls (Table 20). Similarly, cell perimeter for most candidate genes (19/21) remained unchanged (Table 21) suggesting that knockdown of 19 genes did not affect size of anaphase cells. Overall, the changes in anillin::GFP localization observed for 21 candidate genes were not caused by altered midzone length or changes in cell size.

The 18 new genes identified to be important for normal localization of anillin at the cell cortex during anaphase can be categorized into different classes based on their function. Six genes DDX6, FOXC1, TCEA1, eIF3h, POLE3 and PTBP1 regulate transcription, translation or stability of mRNA. Briefly, FOXC1 encodes a transcription factor (Elian et al., 2018), TCEA1 rescues blocked RNA Polymerase on template strands (Fish and Kane, 2002; Kettenberger et al., 2003), eIF3h is involved in initiation of protein synthesis (Masutani et al., 2007), POLE3 contributes in DNA transcription and replication (Bellelli et al., 2018), PTBP1 and DDX6 play role in post-transcriptional regulation of mRNA (Romanelli et al., 2013; Jonas and Izaurralde, 2013). While DDX6, FOXC1 and TCEA1 depletion led to decreased anillin::GFP localization at cell equator, depletion of eIF3h, POLE3 and PTBP1 resulted in increased anillin::GFP accumulation at cell poles. The direct role of these six transcription and translation regulators in regulating anillin localization is difficult to delineate as their depletion can simultaneously change the levels of many cellular proteins and disrupt multiple cellular processes. It is possible that these candidate genes directly upregulate or downregulate the levels of anillin and other contractile ring proteins. For example, PTBP1 is a regulator of alternate splicing of Formin homology 2 domain containing 3 (FHOD3) mRNA

which is involved in polymerization of actin filament in cardiomyocytes (Pamela et. al., 2018). Alternatively, these genes could be involved in regulating the levels of specific signaling molecules that in turn control localization or stability of contractile ring proteins including anillin. Cellular levels of contractile ring proteins like anillin, actin and septin 7 should be determined by Western Blotting in cells depleted of DDX6, FOXC1, TCEA1, eIF3h, POLE3 and PTBP1 proteins to examine whether the changes in anillin localization were caused by changes in overall protein level. Then, thorough literature review and bioinformatic analysis is required to identify the role of these six candidate genes in regulating transcription and translation of known regulators of cytokinesis. If a downstream cytokinesis regulator is found to be controlled by any of these six candidate genes, then further studies could be carried out to investigate how this downstream effector controls anillin localization at cell cortex during cytokinesis.

Three candidate genes encode kinases DGKG, PKN2, CKS2. PKN2 is an effector protein of RhoA signalling pathway and is known to interact with RhoA (Amano et al., 1996). PKN2 and its *C. elegans* orthologue were further studied in HeLa cells and *C. elegans,* respectively, and therefore are discussed in more detail in Section 5.2. DGKG phosphorylates diacylglycerol (DAG) to form phosphatidic acid (PA) (Shulga et al., 2011). DAG is produced by hydrolysis of phosphatidylinositol-4,5-bisphosphate (PIP2) by phospholipase C (PLC) (Shulga et al., 2011). Besides serving as an intermediate for lipid biosynthesis, DAG activates protein Kinase C (PKC), which is known to phosphorylate and activate myosin light chain (Logan and Mandato, 2012; Varlamova et al., 2001). Since DAG can be synthesized in other ways (Eichmann and Lass, 2015), depletion of DGKG may not result in significantly lower levels of DAG and reduced PKC signalling. Thus, it is unlikely that reduced PKC activation by DAG led to the increase in equatorial anillin::GFP localization in the RNAi screen. Interestingly, DGKG has been shown to colocalize and interact with Rac1 and serve as Rac1 suppressor during lamellipodium formation (Tolias et al., 1998; Tsushima et al., 2004). Rac1 is a negative regulator of cytokinesis (Jordan and Canman, 2012) and expression of constitutively active Rac1 in HeLa cells was shown to result in multinucleated cells (Yoshizaki et al., 2004). If DGKG depletion led to increased activation of Rac1 during anaphase in the RNAi screen, then an increase in the number of multinucleated cells would be expected. Visual inspection of 10x images of DGKG RNAi well did not reveal any significant rise in multinucleated cells. It is possible that the increase in Rac1 activation upon DGKG depletion was only marginal and could not impede cytokinetic furrow ingression. As a result, multinucleated cells were not observed after DGKG depletion in the RNAi screen. It should also be considered that active Rac1 is excluded from the cell equator and mainly

localizes at cell poles during anaphase (Jordan and Canman, 2012), which makes it difficult to implicate a role of increased Rac1 activation in promoting anillin accumulation at cell equator. To clear the confusion, active Rac1 localization should be investigated in HeLa cells after DGKG depletion. Another possibility is that depletion of DGKG somehow leads to an increase in the levels of PIP2, a precursor of DAG. PIP2 is known to localize at ingressing cytokinetic furrow and promote anillin localization at the furrow by interact with its PH domain (Liu et al., 2012). In addition, PIP2 promotes actin polymerization by uncapping actin monomers and inactivating cofilin which depolymerizes actin filaments (Logan and Mandato, 2012). Thus, an increase in PIP2 levels upon DGKG depletion would clearly explain the reason for increase in anillin::GFP accumulation at cell equator. In future experiments, cortical localization of PIP2 and other contractile ring proteins like f-actin, septin 7 and myosin II should be investigated in DGKG depleted cells.

CKS2 is a cyclin dependent kinases (CDK) interacting protein which has been frequently observed to be upregulated in different malignant tumours (You et al., 2015). The two paralogs CKS1 and CKS2 have redundant function in G2-M phase transition as they promote transcription of important cell cycle genes encoding CDK1, cyclin B1, cyclin A (Martinsson-Ahlzén et al., 2008). In the RNAi screen, CKS2 depletion was found to result in increased anillin::GFP localization at the cell poles. Since CKS2 is associated with CDKs, it could be involved in phosphorylating cytokinesis regulators downstream of CDKs. But, there is not much known about CKS2 phosphorylation sites in proteins that regulate cell cycle or cytokinesis. Therefore, it is difficult to speculate how CKS2 inhibits anillin localization at cell poles during anaphase.

Two candidate genes encode phosphatases PPP2CB and PPP4C. PPP2CB is a catalytic subunit of Protein Phosphatase 2A (PP2A) that plays an important role during cytokinesis and mitotic exit. PP2A, which is inhibited indirectly by CDK1, gets activated in anaphase once CDK1 activity decreases (Holder et al., 2019). Depletion of PPP2CB in the RNAi screen led to decreased anillin localization at the cell equator. This phenotype can be explained on the basis of role of PP2A in triggering localization of PRC1 and CPC to spindle midzone. During metaphase, CDK1 phosphorylates INCENP directly and Histone H3 through haspin kinase which results in docking of CPC to the chromatin. At anaphase onset when CDK1 activity declines, PP2A dephosphorylates INCENP directly and promotes dephosphorylation of Histone H3 though PP1, thereby, allowing CPC to translocate from chromatin to spindle midzone. CPC, then, phosphorylates MKLP1 of centralspindlin and releases 14-3-3 binding, thereby allowing multimerization of centralspindlin and its stable recruitment to the spindle midzone (Douglas et al., 2010; Giet and Glover, 2001; Guse et al.,

2005; Hauf et al., 2003; Hu et al., 2008; Kaitna et al., 2000; Severson et al., 2000; Verbrugghe and White, 2004; Zhu et al., 2005). In addition, PP2A antagonizes the inhibitory phosphorylation of PRC1 by CDK1 and induces PRC1 recruitment to the spindle midzone (Holder et al., 2019). PRC1 stabilizes the overlapping microtubules of spindle midzone and gets phosphorylated by Plk1 (Neef et al., 2007; 2003), thereby, promoting Plk1 localization to the spindle midzone. Plk1 further phosphorylates centralspindlin's CYK-4 subunit (Burkard et al., 2009; Wolfe et al., 2009) which then binds and recruits RhoA GEF Ect2 to the spindle midzone. This binding relieves autoinhibition of Ect2 by its BRCT domains and Ect2 is loaded on the adjoining cell membrane where it activates RhoA and directs the accumulation of contractile ring proteins like anillin, actin and myosin (Burkard et al., 2009; Chalamalasetty et al., 2006; Tatsumoto et al., 1999; Wolfe et al., 2009). In addition to recruitment of PRC1 to the spindle midzone, PP2A also plays a role in relocalization of CPC (containing Aurora B) from chromatin to the spindle midzone (Holder et al., 2019). Thus depletion of PPP2CB would compromise spindle midzone assembly and midzone localization of CPC, ultimately leading to reduced cortical accumulation of contractile ring proteins including anillin. In future experiments, it would be interesting to analyse localization of CPC, Plk1, PRC1, Ect2, RhoA and contractile ring proteins in cells depleted of PPP2CB. If the hypothesis proposed above is correct, then PPP2CB depletion is expected to result in decreased accumulation of Ect2 and RhoA on equatorial cortex and reduced localization of Ect2 on spindle midzone.

The next candidate gene, PPP4C, is catalytic subunit of Protein Phosphatase 4 and depletion of PPP4C in the RNAi screen led to decreased anillin localization at the cell equator. PPP4C localizes to the centrosomes in *C. elegans* and *Drosophila* and to pericentriolar material in human cells (Brewis et al., 1993; Helps et al., 1998; Sumiyoshi et al., 2002). PPP4C in *C. elegans, Drosophila* and human cells was shown to be required for centrosome maturation and mitotic spindle assembly (Brewis et al., 1993; Cohen et al., 2005; Han et al., 2009; Helps et al., 1998; Martin-Granados et al., 2008; Sumiyoshi et al., 2002). Depletion of PPP4C also reduced localization of γ-tubulin on the centrosomes in *C. elegans* and human cells (Martin-Granados et al., 2008; Sumiyoshi et al., 2002), thereby, severely affecting nucleation of microtubules. It is likely that defective spindle midzone or absence of stable microtubules which originate from centrosomes and stimulate RhoA activation at equatorial cortex, leads to lower anillin accumulation at cell equator in PPP4C depleted cells (Figure 3A and B). As a result less anillin is accumulated at the equatorial cell cortex. However, in the RNAi screen no overt spindle defects were seen in PPP4C depleted HeLa cells. This could be due to lower RNAi knockdown efficiency of PPP4C which was enough to reduce anillin accumulation at

cell equator but not sufficient to induce major spindle assembly defects. In future experiments, RNAi knockdown conditions should be optimised to achieve stronger PPP4C depletion. Thereafter, immunofluorescence analysis should be performed to analyse mitotic spindle, microtubule asters, spindle midzone and localization of Ect2, RhoA and anillin.

One candidate gene Septin 7 is a component of contractile ring and was investigated in more detail in HeLa cells and *C. elegans* one-cell embryos. Role of Septin 7 in regulating anillin localization at cell cortex is discussed below in section 5.3. Two candidate genes encode proteins that have enzymatic activity – Ubiquitin conjugating enzyme E2 UBE2L3 and serine endopeptidase PRSS38 and remaining four genes play important roles in other miscellaneous cellular processes. SLC18A2 encodes a transmembrane transporter of neurotransmitters, IHH is a signalling molecule, CRHR2 is a member of G-Protein Coupled Receptors 2 family that binds to corticotropin releasing hormone, ETFA shuttles electrons between dehydrogenases and the respiratory chain (Roberts et al., 1996; Salazar et al., 1997). Considering the known functions of these six candidate genes in cellular processes especially CRHR2, ETFA, and SLC18A2 which have roles not related to cytokinesis, it is difficult to speculate how these genes control cortical localization of anillin during cytokinesis. Although it is challenging to implicate a role of remaining candidates genes in cytokinesis, they present an excellent opportunity to link new proteins and signalling pathways with the existing network of cytokinesis signalling. As a starting point, anillin levels should be determined after depleting UBE2L3, PRSS38, SLC18A2, CRHR2, ETFA and IHH to understand whether changes in anillin localization were caused by changes in overall protein level. Immunofluorescence analysis should be performed to analyse the localization of these proteins during anaphase as it could provide insights on how they could regulate anillin localization. It would also be important to analyze localization of RhoA, Ect2 and other contractile ring proteins in cells depleted of these six candidate proteins. Finally, in the future it would also be interesting to screen rest of the genome if the automated image analysis can be established successfully.

5.2 PKN2 inhibits anillin accumulation at the cell poles

Depletion of PKN2, but not PKN1 and PKN3, resulted in increased anillin::GFP levels at the cell poles in the primary and secondary screens without any change in equatorial localization and zone width (Table 17, Figure 14E, 15 and 19A). PKN2 depletion phenotype was further confirmed in live-cell imaging experiments by using two different PKN2-targeting siRNAs (Figure 19). In addition, endogenous anillin staining in fixed HeLa cells that were treated with PKN2 siRNA also showed increased anillin localization on the cell poles (Figure 20).

Importantly, expression of RNAi resistant NeonGreen-tagged PKN2 transgene rescued this phenotype and restored the polar anillin levels similar to that in controls (Figure 19D and E). Thus, PKN2 depletion phenotype was specific and not due to RNAi off-target effects. Moreover, this polar increase was not due to global rise in anillin levels as PKN2 depletion did not increase mean cytoplasmic anillin::GFP intensity as compared to controls (Figure 19H). Since PKN proteins are evolutionarily well conserved, the role of *C. elegans* orthologue PKN-1 (Qadota et al., 2011) in regulating cortical anillin localization was examined. Indeed, RNAi-mediated depletion of PKN-1 in *C. elegans* one-cell embryos led to an increase in NG::Anillin levels on the anterior and posterior poles during anaphase but not on the equatorial cortex (Figure 24D-F). In HeLa cells, PKN2 depletion did not result in any other cytokinesis defects. The rate and timing of furrow ingression was similar between control and PKN2 depleted cells (Figure 21B). Similarly, the total time from anaphase onset to complete furrow ingression was not different between control and PKN2 depleted cells (Figure 21C). Schmidt et. al. have previously reported abscission defects in PKN2 depleted HeLa-S3 cells which in turn result in 32% binucleated cells (Schmidt et al., 2007). Inconsistent with this report, only 9% multinucleated cells were observed after PKN2 RNAi in my multinucleation assay and no significant evidence of abscission failure was found in long duration live-cell recordings of PKN2 depleted cells (Figure 21D). Schmidt et al. did not perform experiments to rescue the abscission defect caused by PKN2 RNAi, therefore the contribution of RNAi off-target effects to this phenotype cannot be ruled out. But, there could be other reasons underlying this discrepancy such as differences in siRNAs or experimental procedures and can only be resolved after thorough investigation.

PKN2 is effector protein of RhoA signalling pathway and is known to interact with RhoA (Amano et al., 1996; Flynn et al., 1998; Maesaki et al., 1999; Shibata et al., 1996; Vincent and Settleman, 1997). Shibata et al. showed direct interaction between RhoA and PKN2 using yeast two-hybrid system and Amano et al. showed binding of PKN2 with RhoA in COS7 cells followed by its activation. In addition, genetic and structural studies by Flynn et al. and Maesaki et al. have identified RhoA binding domains in the N-terminus of PKN2. Specifically, HR1a and HR1b but not HR1c domains in N-terminal region of PKN2 were shown to interact with RhoA (Flynn et al., 1998). These observations led to the hypothesis that PKN2 could prevent anillin localization at cell poles by inhibiting RhoA. Immunofluorescence analysis in PKN2 depleted cells showed significant increase in RhoA localization at the cell equator but not at cell poles (Figure 22A-C). But it is noteworthy that the RhoA fluorescence signal at the cell poles was rather weak which could compromise the ability to capture small differences. These findings suggest that PKN2 inhibits RhoA at least

at the cell equator and the notion that PKN2 inhibits RhoA at cell poles remains open for future investigation. Since anillin binds to active RhoA and mimics its localization, it was surprising to observe increased RhoA levels at cell equator without any change in equatorial anillin localization. This conundrum was solved by analysing cellular levels of anillin in PKN2 depleted cells by Western Blotting. The results showed strong reduction in levels of endogenous and GFP-tagged anillin after PKN2 knockdown by six different siRNAs (Figure 23A-C), thereby, unravelling a novel role of PKN2 in stable expression of anillin. As the global anillin levels fell in absence of PKN2, increase in equatorial anillin localization could not be observed and perhaps the rise in anillin at cell poles was underestimated. Immunofluorescence analysis of myosin II localization carried out by staining pMLC(Ser19) in PKN2 depleted cells revealed increased accumulation of myosin II at cell equator but not on cell poles (Figure 22E-G). In *C. elegans* one-cell embryos, PKN-1 depletion also led to an increase in equatorial and polar levels of NMY-2::GFP (Figure 24G and H). Based on above-mentioned and previously published findings, a preliminary model can be proposed to explain how PKN2 plays a role in regulating cortical patterning during cytokinesis (Figure 42). At anaphase onset, active RhoA induces the assembly of contractile ring by promoting cortical localization of proteins like anillin and myosin II. At the same time, PKN2 binding to RhoA induces PKN2 activation either by autophosphorylation or by a kinase yet to be identified. PKN2 could either inhibit RhoA activity to regulate the cortical levels of anillin and myosin II or control their localization by directly or indirectly phosphorylating them. In addition, PKN2 could also control cellular levels of anillin independent of RhoA. It should be noted that this is a preliminary model and there is not sufficient experimental evidence in my thesis to strongly support this model.

Future experiments should focus on answering two main questions. First, why does PKN2 depletion result in substantial drop in cellular levels of anillin. The main reasons behind reduced protein levels are decreased transcription or translation and increased protein degradation. Levels of anillin mRNA in control and PKN2 depleted cells can be measured by performing real-time quantitative PCR (RT-qPCR) and the results will reveal whether anillin is transcriptionally regulated by PKN2. Anillin levels are known to peak in mitosis and drop significantly during mitotic exit by proteasomal degradation after its ubiquitination by anaphase promoting complex/cyclosome (APC/C^{cdh1}) (Zhao and Fang, 2005b). There is a possibility that PKN2 stabilizes anillin by inhibiting ubiquitination which can be checked on Western Blot using anti-ubiquitin antibodies. PKN2 could stabilize anillin by directly binding with it and/or by phosphorylating downstream targets (possibly including anillin). Interestingly, anillin is phosphorylated in mitosis by different mitotic kinases like CDK1,

Plk1, Aurora B (Kim et al., 2017). To examine the role of PKN2 kinase activity in stabilizing anillin, RNAi resistant kinase-dead PKN2 should be generated (Lim et al., 2008; Udo et al., 2000) and expressed in cells depleted of endogenous PKN2. If the anillin levels can be rescued by kinase-dead PKN2, then the role of PKN2 kinase activity could be ruled out in stabilizing anillin. To investigate whether PKN2 binds anillin, PKN2 should be immunoprecipitated and samples should be immunoblotted with anti-anillin antibodies. Alternatively, immunoprecipitated PKN2 can be analysed by mass spectrometry to identify binding partners of PKN2 including anillin.

Second important question to be investigated in future studies is how does PKN2 inhibit cortical localization of anillin and active myosin. Kim et al. have shown that phosphorylation of anillin on S635 adjacent to the AH domain is required for recruitment of anillin to the equatorial cortex during anaphase (Kim et al., 2017). This leads to the possibility that PKN2 somehow inhibits the phosphorylation of anillin on S635 and when PKN2 is depleted more anillin is phosphorylated on S635. As a result, higher amount of anillin localizes at the cell cortex ultimately leading to increase in anillin levels at the cell poles. This hypothesis is consistent with the observations that PKN2, anillin and RhoA localize at the equatorial cell cortex and that RhoA interacts with both anillin and PKN2. Another possibility is that PKN2 binds to anillin and this physical binding sequesters anillin away from RhoA. To support this notion, it would be essential to show anillin-PKN2 interactions by immunoprecipitation or yeast two-hybrid method. In HeLa cells, PKN2 depletion led to increased equatorial accumulation of pMLC(Ser19). Similarly, Ferreira et al. have shown that nurse cells of *Drosophila* egg chambers have increased cortical accumulation of phosphorylated (active) myosin in *pkn* mutant flies during the process of nurse cell dumping (Ferreira et al., 2014). Based on these observations, it is reasonable to hypothesize a role of PKN2 in inhibiting myosin phosphorylation and activation. To investigate the molecular mechanism, Ferreira et al. immunoprecipitated myc-tagged Pkn and performed mass spectrometry but failed to identify any protein that regulates phosphorylation of myosin (Ferreira et al., 2014). The data was not presented in their article and, therefore, it would still be interesting to repeat such an experiment in HeLa cells. Lastly, it is possible that PKN2 antagonizes RhoA activity by inhibiting cortical localization of RhoA. Since RhoA triggers the accumulation of anillin and myosin at the cell cortex, altering cortical levels of RhoA would lead to changes in anillin and myosin localization. In support of this hypothesis, equatorial accumulation of RhoA was found to be increased in cells depleted of PKN2, but, RhoA could not be properly stained on cell poles. Future experiments should try to optimize conditions for RhoA immunostainings or establish a tool to track RhoA localization in live-cell microscopy. Finally, the two

isoforms of PKN2, PKN1 and PKN3, may alleviate the phenotypes observed in PKN2 depleted HeLa cells. Although individual knockdown of PKN1 and PKN3 did not lead to anillin localization defects, it would be important to co-deplete all three PKNs and analyse if this results in stronger phenotypes. Such depletions could be performed in different combinations and the outcome would shed light on the functional redundancy of PKN1-3 in regulating anillin localization. In summary, a new function of previously known RhoA/Rac effector PKN2 was identified in regulating the cortical accumulation of contractile ring components during cytokinesis.

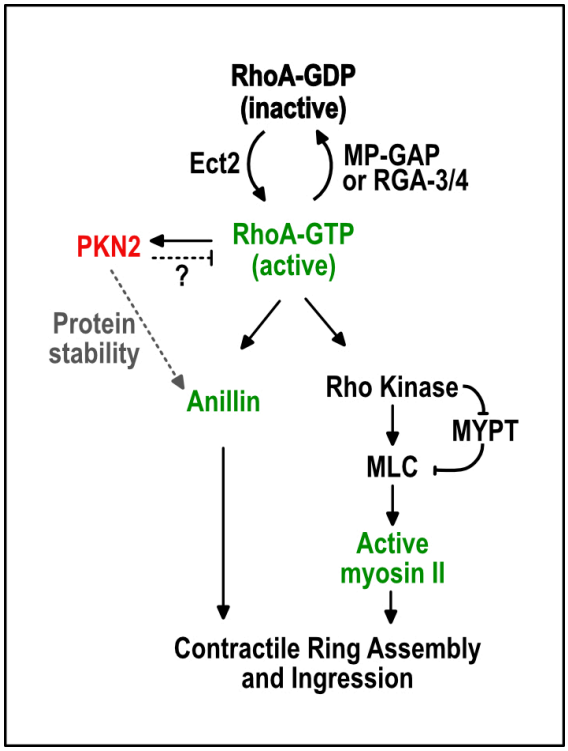

Figure 42: Preliminary model for role of PKN2 in cytokinesis signalling. PKN2 interacts with RhoA (Amano et al., 1996) which induces its activation by autophosphorylation or by other unknown kinase. PKN2 in turn could inhibit RhoA thereby controlling cortical accumulation of anillin and myosin II. In addition, PKN2 regulates anillin by controlling its protein stability.

5.3 Septin 7 promotes anillin localization at the cell equator

Septin 7 is a member of conserved Septin family proteins which are required for normal organization of cytoskeleton (Kremer et al., 2007). There are 13 Septin genes in human cells which are divided into four groups based on homology in their protein sequences (Valadares et al., 2017). Septin 2 group consists of Sept1, 2, 4, 5; Septin 3 group comprises of Sept3, 9, 12; Septin 6 group has Sept6, 8, 10, 11, 14 and Septin 7 group has only Sept7. Septin proteins

oligomerize into heteromeric complexes to form non-polar filaments that become a part of cytoskeleton. In the RNAi screen, depletion of Septin 7 resulted in strong reduction of anillin levels at the cell equator and significantly narrower anillin zone in the primary and secondary screens (Figure 14D and 16, Table 18). However, depletion of other Septin proteins Sept1, Sept3, Sept4, Sept5, Sept6, Sept9 and Sept11 did not affect anillin::GFP localization at cell cortex (Table 23). Remaining septin genes could not be screened as the siRNAs targeting them were not present in the druggable genome library. Since Sept9 and Sept11 are present all around the cell cortex in anaphase (Estey et al., 2010), similar to Sept7, it was surprising to not see anillin localization defects after their depletion. It should be noted that Sept4,5,6,9 depleted samples had few anaphase cells (less than 6 cells; Table 23) and therefore, the quantitative data obtained from these genes is not very reliable. To draw firm conclusions, Sept1, Sept3, Sept4, Sept5, Sept6, Sept9 and Sept11 should be depleted again and their depletion should be monitored by Western Blotting. Then, in these samples, anillin localization should be analysed by immunofluorescence or by live-cell imaging. Here it is important to note that septin filaments in human cells are made of repetitive units of hexameric or octameric septin complexes. The configuration of hexameric complex is Sept7–Sept6–Sept2–Sept2–Sept6–Sept7 and octameric complex is Sept9–Sept7–Sept6–Sept2–Sept2–Sept6–Sept7–Sept9 where each Septin protein can be substituted by another Septin protein of the same group (Ribet et al., 2017; Sellin et al., 2011; Sirajuddin et al., 2007). Interestingly, Sept7 is the only member in its group and, therefore, depletion of only Sept7 is likely to disrupt the septin filaments. This can explain why Sept7 RNAi, but not others, led to a strong defect in anillin localization. In future experiments it would be interesting to see whether co-depletion of all septin proteins belonging to the same group can lead to phenotypes mimicking that of Sept7. Regardless, Sept7 phenotype was further confirmed in live-cell imaging experiments (Figure 25A). In addition, anillin staining in fixed HeLa cells that were treated with Sept7 siRNA also lead to decreased anillin localization at cell equator (Figure 26C-E). Importantly, expression of RNAi resistant Neon-tagged Sept7 transgene rescued this phenotype and restored the equatorial anillin levels similar to that in controls (Figure 26C-E). Thus, Sept7 depletion phenotype was specific and not an off-target effect of RNAi. This strong decrease in equatorial anillin localization in Sept7 depleted cells was not due to global drop in cytoplasmic (Figure 25E) or cellular (Figure 25A) levels of anillin. Further, imaging HeLa cells expressing Ect2::GFP after Sept7 RNAi did not affect mean fluorescence intensity of Ect2::GFP at the spindle midzone (Figure 26F). However Ect2 membrane localization could not be analysed as Ect2::GFP did not localize at the cell membrane in this particular cell line and remains to be investigated in future. Kremer et al.

have shown that Sept7 depletion in interphase HeLa cells leads to increase in microtubule stability (Kremer et al., 2007; Valadares et al., 2017). As mitotic spindle plays an important role in regulating cortical accumulation of contractile ring proteins (Section 1.3), it will be important to analyse the affect of Sept7 RNAi on microtubule stability in HeLa cells. As a starting point, α-tubulin should be immunostained after Sept7 RNAi and spindle midzone microtubule intensities should be measured on confocal images. Later, more complicated experiments like microtubule tip-tracking using fluorescently-tagged EB2 can be performed to precisely measure nucleation and growth rates of microtubules. Another interesting experiment would be to artificially stabilize the microtubules by Taxol treatment in control and Sept7 depleted cells. Nevertheless, the anillin localization defect in Sept7 RNAi cells is rather strong and it is likely that Sept7 plays a direct role in recruitment and/or maintenance of anillin at the cell equator. Since *C. elegans* genome encodes for two Septin proteins namely UNC-59 and UNC-61, their function in regulating anillin recruitment to the cell cortex was examined during first embryonic division. Similar to HeLa cells, depleting UNC-59 and UNC-61, led to a significant reduction in cortical accumulation of NG::Anillin, both at equatorial and polar cortex (Figure 27A and B). In 2004, Menon et al. showed that depletion of Sept7 in fibroblasts leads to incomplete cytokinesis and multinucleation (Menon et al., 2014). But they did not measure the dynamics of furrow ingression. Consistent with this report, depletion of Sept7 in HeLa cells led to furrow regression after partial or complete furrow ingression in 48 percent cells (Figure 25H). In addition, the rate of furrow ingression rate was much slower (Figure 25I and J) and time taken after anaphase onset to form and ingress the cleavage furrow was significantly longer. Similarly in *C. elegans* one-cell embryos, co-depletion of septin proteins UNC-59 and UNC-61 led to significantly slower furrow ingression (Figure 27C and D). Together, these findings suggest that Sept7 promotes assembly and ingression of contractile ring by recruiting anillin to the cell equator in HeLa cells and *C. elegans*.

Septin proteins are important component of contractile ring that localize at the equatorial cell cortex similar to anillin, myosin II, f-actin and RhoA and also at the cell poles (Figure 26B; Estey et al., 2010). Previous reports have shown that septins bind with C-terminus of anillin in *Drosophila* (Field et al., 2005) and human cells (Oegema at. al. 2000; Kinoshita et. al., 2002). In addition, Septin2 directly binds with myosin II which is important for myosin II activation (Joo et. al., 2007). Based on current literature and above-mentioned experimental findings, a preliminary model can be proposed to explain how Sept7 plays a role in regulating cortical patterning during cytokinesis (Figure 43). At anaphase onset, active RhoA induces the assembly of contractile ring by promoting cortical localization of proteins like anillin and

myosin II. Sept7 and/or other septins either promote anillin recruitment to the equatorial cortex or stabilize its equatorial localization as septin depletion reduces cortical accumulation of anillin in HeLa cells (Figure 25B) and *C. elegans* one-cell embryo (Figure 27A and B). Similarly, anillin localization at the cleavage furrows was found to be severely impaired during cellularization in developing *Drosophila* embryos that expressed mutant septin *pnut* (Adam et al., 2000). Conversely, anillin also plays a similar role in recruiting or stabilizing sept7 and/or other septins at the equatorial cortex. Indeed, anillin depletion in *Drosophila* cells reduced the localization of septin (Pnut) at the cleavage furrow (D'Avino et al., 2008; Hickson and O'Farrell, 2008). Likewise, mutations that modified PH domain of anillin resulted in decreased accumulation of septin (Pnut) at the cellularization front of developing *Drosophila* embryos (Field et al., 2005). In this way, anillin and septin promote mutual recruitment of each other to the equatorial cortex during anaphase and contribute in building a stable contractile ring. In future it would be interesting to perform partial anillin depletions in HeLa cells and analyze whether septin localization at the cell equator is reduced. Previous studies have shown that anillin RNAi leads to unstable cleavage furrow formation which suffers from severe oscillations (Straight et al., 2005; Piekny and Glotzer, 2008). These oscillations are probably due to weak cortical cytoskeleton which cannot support the cell membrane through the tension that builds up during anaphase. Although depletion of Sept7 in HeLa cells substantially reduced the equatorial accumulation of anillin, cleavage furrow oscillations were not observed (Figure 25B). It seems that the small amount of anillin which is recruited to the equatorial cortex, probably by interaction with PIP2, is enough to stabilize the cell membrane-contractile ring interactions during anaphase, thereby, preventing cleavage furrow oscillations. Interestingly, chimeric anillin having its PH domain replaced by PH domain of PLC localizes to cleavage furrow in PIP2 dependent manner and rescues furrow oscillation phenotype without recruiting septin proteins to the cleavage furrow (Liu et al., 2012). Overall, the data suggests that both septin and anillin play an important role in proper assembly and ingression of the contractile ring.

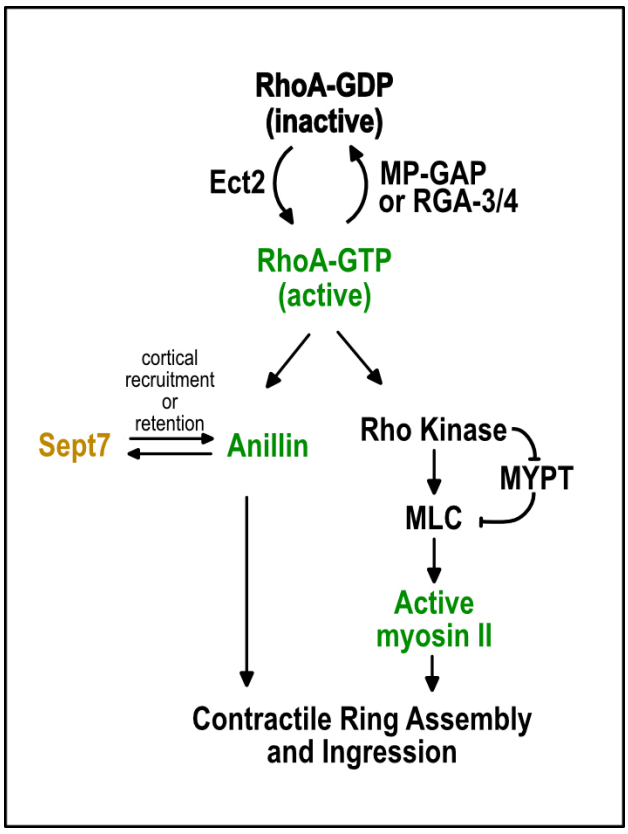

Figure 43: Preliminary model for role of Sept7 in cytokinesis signalling. During cytokinesis Sept7 binds with anillin and promotes its localization or retention at equatorial cell cortex. Conversely, anillin also promotes Sept7 localization at the cell equator. Thus, anillin and septin promote mutual recruitment of each other to the equatorial cortex and contribute in building a stable contractile ring.

5.4 Aurora A inhibits anillin localization at cell poles

In *C. elegans* one-cell embryos, anillin accumulates at the equator and anterior pole after anaphase onset (Figure 29A). While the anillin levels on equatorial cortex stays high until furrow ingression, the localization of anillin on the anterior pole decreases over time (Figure 29A). To identify genes involved in removing anillin and other contractile ring proteins from the anterior pole, my PhD advisor Dr. Esther Zanin established an assay to monitor the removal of GFP::anillin from the anterior pole during the first division of *C. elegans* embryos (Figure 29B). This assay was performed in *rga-3/4*Δ mutant embryos depleted of myosin to increase the cortical levels of GFP::anillin and prevent geometrical rearrangements caused by furrow ingression, respectively (Figure 29A and B). The embryos were imaged live on a confocal microscope and the cortical GFP::anillin fluorescence was quantified by performing linescans along the cortex from anterior to posterior pole as shown in Figure 24E. It should be noted that posterior pole of one-cell embryos was not analyzed because much less anillin localized on posterior pole. As expected, much higher amounts of GFP::anillin accumulated

at the equator and anterior poles in myosin depleted & *rga-3/4*Δ embryos as compared to control or myosin depleted embryos (Mangal et. al., 2018). Importantly, during anaphase GFP::anillin was cleared from the anterior pole similar to control or myosin depleted embryos. These results support the hypothesis that decrease in anillin localization on anterior poles during anaphase progression is mediated by an active clearing mechanism. Using this assay, Dr. Esther Zanin found that TPXL-1 (activator of Aurora A) plays a role in clearing anillin from the anterior poles as *tpxl-1(RNAi)* in myosin and *rga-3/4*Δ embryos prevented GFP::anillin clearing from the anterior pole after anaphase onset (Figure 29C; Mangal et. al., 2018). The function of TPXL-1 in clearing anillin from anterior pole was independent of short spindles that occur after *tpxl-1(RNAi)* as restoring the centrosome-pole distance by co-depleting HCP-4 did not rescue polar anillin levels to match that in controls (Figure 29B-D; Mangal et. al., 2018). To further investigate whether TPXL-1 also plays a similar role in clearing other contractile ring proteins from the anterior pole, I investigated the localization of f-actin in myosin depleted & *rga-3/4*Δ embryos using f-actin binding probe LifeAct::mKate2 after *hcp-4 & tpxl-1(RNAi)*. Similar to the role of TPXL-1 in clearing anillin, TPXL-1 was also found to be involved in clearing f-actin from the anterior pole (Figure 30). Thus, indicating towards a generic role of TPXL-1 in clearing contractile ring proteins from the anterior pole and serving as a spatial regulator of contractile ring assembly. To ensure that polar clearing defect of *tpxl-1(RNAi)* was not due to changes in microtubule dynamics, microtubule nucleation and growth rates were measured in embryos expressing the EBP-2::GFP using a previously established assay (Srayko et al., 2005). Importantly, TPXL-1 depletion did not change microtubule nucleation and growth rate in myosin depleted and *tpxl-1 & hcp-4(RNAi)* embryos during the interval when polar clearing occurs (255-315s after NEBD; Figure 31D and E). All these findings cumulatively suggest that polar clearing of anillin and f-actin by TPXL-1 was independent of its role in regulating length of mitotic spindle. TPXL-1 is known to activate and recruit Aurora A to microtubules (Özlü et al., 2005). To determine whether activation of Aurora A by TPXL-1 is required for polar clearing, Dr. Zanin abolished Aurora A and TPXL-1 interaction by using a previously described TPXL-1 transgene (TPXL-1^{FD}; Bird and Hyman, 2008; Özlü et al., 2005) in myosin depleted *rga-3/4*Δ *tpxl-1 & hcp-4(RNAi)* embryos (Figure 34; Mangal et al., 2018). While fluorescently-tagged anillin was cleared from the anterior pole in TPXL-1^{WT} embryos after anaphase onset, anillin accumulation continued to increase in embryos expressing TPXL-1^{FD} (Figure 29B-D). Thus, activation of Aurora A by TPXL-1 is required for polar clearing (Figure 35). Finally, I demonstrated that Aurora A has conserved function in restricting anillin localization on the cell poles in human cells. Depletion of Aurora A in the

RNAi screen only led to mild multinucleation phenotype and other known defects like multipolar spindles and G2M arrest (Marumoto et al., 2003) were not observed. Therefore, it seemed that Aurora A was not properly depleted in the RNAi screen. Nevertheless, since depletion of Aurora A leads to many pleiotropic effects it would not have been easy to analyse anillin localization defects in Aurora A depleted cells. This problem was solved using a highly specific chemical inhibitor of Aurora A MK5108 to acutely inhibit its kinase activity in mitotic cells. Treatment of cells with MK5108 led to increased accumulation of anillin::GFP on the polar cortex (Figure 38B-D) and a wider zone of anillin::GFP at the cell equator (Figure 38F). Immunofluorescence analysis of endogenous anillin also confirmed the same phenotype in cells having normal spindle midzone visualized by staining Plk1. Thus, Aurora A inhibits anillin localization on cell poles in HeLa cells similar to that in *C. elegans*. In future, more experiments should be performed to confirm these findings as the current evidence in HeLa cells is solely based on chemical inhibition. Although, treatment condition with MK5108 was optimised to specifically inhibit Aurora A, some cross-inhibition of closely related Aurora B was still observed. The future experiments should aim to inhibit Aurora A specifically without affecting other kinases using analog-sensitive (as) allele of Aurora A (Reboutier et al., 2013).

But how does Aurora A inhibit the localization of anillin and f-actin on the polar cortex in human cells and *C. elegans* one-cell embryos? One possibility is that active Aurora A diffuses to adjacent polar cortex from astral microtubules and clears anillin or f-actin either directly or by phosphorylating downstream effectors (Figure 35). In line with this hypothesis, both TPXL-1 and Aurora A localized to astral microtubules and pericentriolar material (PCM) during metaphase and anaphase (Figure 33B; Özlü et al., 2005) and their localization on asters was enriched upon anaphase onset, coinciding with the phase of polar clearing. Prior work has shown activity gradient of Aurora A around spindle poles in *Drosophila* S2 cells (Ye et al., 2015) which rectified incorrect kinetochore-MT attachments by phosphorylating kinetochore localized Ndc80 complex. Importantly, *Drosophila* Aurora A is not regulated by TPX2 but still forms an activity gradient around the spindle poles (Goshima, 2011). This implies that *C. elegans* and human Aurora A can form stronger activity gradients with the help of TPXL-1 and TPX2 respectively, which recruit and activate Aurora A on spindle microtubules (Ye et al., 2015). Such Aurora A gradients are partly possible due to high centrosomal turnover rates of Aurora A in HeLa cells (Stenoien et al., 2003) and *C. elegans* one-cell embryos (Portier et al., 2007). Fluorescence recovery after photobleaching (FRAP) experiments in HeLa cells have revealed that centrosomal GFP::Aurora A turns-over

faster than NuMA with half time of 3 seconds as compared to 20-30 seconds of NuMA (Stenoien et al., 2003). In human cells, NuMA (Nuclear mitotic apparatus protein) mainly localizes to spindle poles during metaphase, but undergoes a pronounced enrichment at polar cortex during anaphase (Kiyomitsu and Cheeseman, 2013; Kotak and Gönczy, 2013). Since Aurora A turns-over much faster than NuMA, it is likely that Aurora A can also localize to the adjacent polar cell cortex and facilitate clearing of anillin and f-actin. Indeed, increased activation of Aurora A by inhibition of PP6 in *C. elegans* was reported to cause ectopic accumulation of Aurora A on the cell cortex (Kotak et al., 2016) and reduced contractility in early embryos (Afshar et al., 2009). Consistent with this report, immunofluorescence analysis and live cell imaging of PPH-6 or SAPS-1 (subunits of PP6) depleted embryos confirmed ectopic accumulation of endogenous or GFP-tagged or Aurora A on the cell cortex during cytokinesis (Figure 36A-B). In addition, anillin accumulation on poles and equator was significantly reduced in PPH-6 or SAPS-1 depleted embryos (Figure 36C-E) suggesting that increased Aurora A activation inhibits anillin localization at the cell cortex. To further investigate the role of TPXL-1 and Aurora A in clearing anillin and f-actin from the cell poles, both these proteins should be targeted to the cell membrane by inducing dimerization with a membrane bound protein or domain. The targeting must be inducible as constitutive membrane targeting of these proteins can lead to pleiotropic phenotypes. For *C.* elegans, this can be easily achieved by using rapamycin induced protein dimerization system established and described in section 4.3. TPXL-1 or Aurora A should be fused with FKBP12 and crossed into the strain expressing FRB::GFP::PH and mKate2::anillin. In the presence of rapamycin, TPXL-1 or Aurora A fusion proteins would dimerize with the membrane bound FRB::GFP::PH leading to their ectopic localization on the cell cortex. Following mKate2-anillin by live imaging in these embryos would reveal whether ectopic localization of TPXL-1 and Aurora A, without inhibiting PP6, can result in anillin localization defects. A similar rapamycin inducible protein dimerization system can be optimised in human cells for targeting TPX2 or Aurora A to the cell membrane. In future, it would also be interesting to establish a FRET (Fluorescence resonance energy transfer)-based sensor for monitoring Aurora A activity in human cells and *C. elegans* one-cell embryos during anaphase especially at the polar cortex. Overall, the above-mentioned findings favour a model in which TPXL-1 activates Aurora A on the astral microtubules, which then diffuses to the adjacent cell poles and clears contractile ring proteins from the polar cell cortex (Figure 35). It is, however, not clear whether Aurora A directly inhibits polar localization of contractile ring proteins or this inhibitory action is routed through other downstream signalling molecules, and remains to be answered in future studies.

5.5 Summary

The thesis aimed to identify new regulators of cytokinesis which promote or inhibit cortical localization of contractile ring proteins during cytokinesis. To achieve this goal, high-content RNAi screen was performed in human cells and localization of anillin::GFP localization was manually inspected or quantified in anaphase cells after knockdown of each gene. The screen was performed in collaboration with Dr. Marc Bickle and Dr. Martin Stoeter of MPI-CBG, Dresden, Germany. Out of 7,553 genes that were screened 21 genes were identified to play a role in regulating anillin localization at cell poles or equator. Two candidate genes PKN2 and Sept7 and their *C. elegans* homologues were further studied by employing confocal live-cell imaging and immunofluorescence analysis. While PKN2 inhibited anillin localization on the cell poles, Sept7 promoted anillin accumulation at the cell equator. Interestingly, their *C. elegans* homologues PKN-1 and UNC-59/UNC-61 played similar roles in regulating anillin location during first embryonic cell division. Precise molecular mechanisms to explain how PKN2 and Sept7 regulate anillin localization could not established but preliminary models have been proposed based on the experimental data and previously published findings (Figure 42 and 43). Besides the RNAi screen, role of Aurora A in preventing localization of contractile ring proteins anillin and f-actin on the cell poles was also investigated in human cells and *C. elegans* one-cell embryos. Dr. Esther Zanin, the advisor of this thesis, had established a role of TPXL-1 and Aurora A in clearing anillin from the polar cortex in *C. elegans* one-cell embryos. TPXL-1 was found to perform a similar role in polar clearing of f-actin, suggesting a generic role of Aurora A in removal of contractile ring proteins from polar cortex. Measurement of microtubule dynamics in TPXL-1 depleted embryos revealed that anillin clearing defect observed in TPXL-1 depleted embryos was not due to altered microtubule dynamics. Further, ectopic localization of Aurora A to the cell cortex achieved by inhibiting Protein Phosphatase 2A (PP2A) led to a significant reduction in anillin localization at cell equator and poles. Consistent with findings in *C. elegans*, inhibition of Aurora A in HeLa cells by small molecular inhibitor MK-5108 resulted in increased accumulation of anillin on the polar cortex. Based on these findings, it was proposed that TPXL-1 activates Aurora A on the microtubule asters which diffuses to the adjacent cell poles and inhibits localization of contractile ring proteins (Figure 35). Overall, the goal of the thesis was met in identifying new regulators of cytokinesis, but detailed mechanistic insights behind their function remain open for future studies.

References

Adam, J.C., Pringle, J.R., and Peifer, M. (2000). Evidence for functional differentiation among Drosophila septins in cytokinesis and cellularization. Mol. Biol. Cell *11*, 3123–3135.

Amano, M., Mukai, H., Ono, Y., Chihara, K., Matsui, T., Hamajima, Y., Okawa, K., Iwamatsu, A., and Kaibuchi, K. (1996). Identification of a putative target for Rho as the serine-threonine kinase protein kinase N. Science *271*, 648–650.

Audhya, A., Hyndman, F., McLeod, I. X., Maddox, A. S., Yates, J. R., Desai, A., & Oegema, K. (2005). A complex containing the Sm protein CAR-1 and the RNA helicase CGH-1 is required for embryonic cytokinesis in Caenorhabditis elegans. The Journal of Cell Biology, *171*(2), 267–279.

Basant, A., Lekomtsev, S., Tse, Y.C., Zhang, D., Longhini, K.M., Petronczki, M., and Glotzer, M. (2015). Aurora B kinase promotes cytokinesis by inducing centralspindlin oligomers that associate with the plasma membrane. Developmental Cell *33*, 204–215.

Bastos, R.N., Penate, X., Bates, M., Hammond, D., and Barr, F.A. (2012). CYK4 inhibits Rac1-dependent PAK1 and ARHGEF7 effector pathways during cytokinesis. The Journal of Cell Biology *198*, 865–880.

Bayle, J. H., Grimley, J. S., Stankunas, K., Gestwicki, J. E., Wandless, T. J., & Crabtree, G. R. (2006). Rapamycin Analogs with Differential Binding Specificity Permit Orthogonal Control of Protein Activity. Chemistry & Biology, *13*(1), 99–107.

Bellelli, R., Belan, O., Pye, V.E., Clement, C., Maslen, S.L., Skehel, J.M., Cherepanov, P., Almouzni, G., and Boulton, S.J. (2018). POLE3-POLE4 Is a Histone H3-H4 Chaperone that Maintains Chromatin Integrity during DNA Replication. Mol. Cell *72*, 112–126.e115.

Bement, W.M., Benink, H.A., and Dassow, von, G. (2005). A microtubule-dependent zone of active RhoA during cleavage plane specification. The Journal of Cell Biology *170*, 91–101.

Bement, W.M., Miller, A.L., and Dassow, von, G. (2006). Rho GTPase activity zones and transient contractile arrays. Bioessays *28*, 983–993.

Betson, M., and Settleman, J. (2007). A rho-binding protein kinase C-like activity is required for the function of protein kinase N in Drosophila development. Genetics *176*, 2201–2212.

Bettencourt-Dias, M., Hildebrandt, F., Pellman, D., Woods, G., and Godinho, S.A. (2011). Centrosomes and cilia in human disease. Trends Genet. *27*, 307–315.

Bettencourt-Dias, M., Rodrigues-Martins, A., Carpenter, L., Riparbelli, M., Lehmann, L., Gatt, M.K., Carmo, N., Balloux, F., Callaini, G., and Glover, D.M. (2005). SAK/PLK4 is required for centriole duplication and flagella development. Curbio *15*, 2199–2207.

Bieling, P., Telley, I.A., and Surrey, T. (2010). A minimal midzone protein module controls formation and length of antiparallel microtubule overlaps. Cell *142*, 420–432.

Bird, A.W., and Hyman, A.A. (2008). Building a spindle of the correct length in human cells requires the interaction between TPX2 and Aurora A. The Journal of Cell Biology *182*, 289–300.

Biron, D., Alvarez-Lacalle, E., Tlusty, T., and Moses, E. (2005). Molecular model of the contractile ring. Phys. Rev. Lett. *95*, 098102.

Boeckeler, K., Rosse, C., Howell, M., & Parker, P. J. (2010). Manipulating signal delivery - plasma-membrane ERK activation in aPKC-dependent migration. Journal of Cell Science, *123*(Pt 16), 2725–2732.

Brennan, I.M., Peters, U., Kapoor, T.M., and Straight, A.F. (2007). Polo-like kinase controls vertebrate spindle elongation and cytokinesis. PLoS ONE *2*, e409.

Brewis, N.D., Street, A.J., Prescott, A.R., and Cohen, P.T. (1993). PPX, a novel protein serine/threonine phosphatase localized to centrosomes. The EMBO Journal *12*, 987–996.

Burkard, M.E., Maciejowski, J., Rodriguez-Bravo, V., Repka, M., Lowery, D.M., Clauser, K.R., Zhang, C., Shokat, K.M., Carr, S.A., Yaffe, M.B., et al. (2009). Plk1 self-organization and priming phosphorylation of HsCYK-4 at the spindle midzone regulate the onset of division in human cells. Plos Biol *7*, e1000111.

Burkard, M.E., Randall, C.L., Larochelle, S., Zhang, C., Shokat, K.M., Fisher, R.P., and Jallepalli, P.V. (2007). Chemical genetics reveals the requirement for Polo-like kinase 1 activity in positioning RhoA and triggering cytokinesis in human cells. Proceedings of the National Academy of Sciences *104*, 4383–4388.

Calvert, M.E.K., Wright, G.D., Leong, F.Y., Chiam, K.-H., Chen, Y., Jedd, G., and Balasubramanian, M.K. (2011). Myosin concentration underlies cell size-dependent scalability of actomyosin ring constriction. The Journal of Cell Biology *195*, 799–813.

Canman, J.C. (2009). Cytokinetic astralogy. The Journal of Cell Biology *187*, 757–759.

Canman, J.C., Cameron, L.A., Maddox, P.S., Straight, A., Tirnauer, J.S., Mitchison, T.J., Fang, G., Kapoor, T.M., and Salmon, E.D. (2003). Determining the position of the cell division plane. Nature *424*, 1074–1078.

Canman, J.C., Lewellyn, L., Laband, K., Smerdon, S.J., Desai, A., Bowerman, B., and Oegema, K. (2008). Inhibition of Rac by the GAP Activity of Centralspindlin Is Essential for Cytokinesis. Science *322*, 1543–1546.

Cao, L.G., and Wang, Y.L. (1996). Signals from the spindle midzone are required for the stimulation of cytokinesis in cultured epithelial cells. Mol. Biol. Cell *7*, 225–232.

Cabernard, C., Prehoda, K.E., and Doe, C.Q. (2010). A spindle-independent cleavage furrow positioning pathway. Nature *467*, 91–94.

Carmena, M., Ruchaud, S., and Earnshaw, W.C. (2009). Making the Auroras glow: regulation of Aurora A and B kinase function by interacting proteins. Current Opinion in Cell Biology *21*, 796–805.

Carmena, M., Wheelock, M., Funabiki, H., and Earnshaw, W.C. (2012). The chromosomal passenger complex (CPC): from easy rider to the godfather of mitosis. Nat Rev Mol Cell Biol *13*, 789–803.

Castrillon, D.H., and Wasserman, S.A. (1994). Diaphanous is required for cytokinesis in Drosophila and shares domains of similarity with the products of the limb deformity gene. Development *120*, 3367–3377.

Carvalho, A., Desai, A., and Oegema, K. (2009). Structural memory in the contractile ring makes the duration of cytokinesis independent of cell size. Cell *137*, 926–937.

Chalamalasetty, R.B., Chalamalasetty, R.B., Hummer, S., Hummer, S., Nigg, E.A., Nigg, E.A., Sillje, H.H.W., and Sillje, H.H.W. (2006). Influence of human Ect2 depletion and overexpression on cleavage furrow formation and abscission. Journal of Cell Science *119*, 3008–3019.

Chan, E., and Nance, J. (2013). Mechanisms of CDC-42 activation during contact-induced cell polarization. Journal of Cell Science *126*, 1692–1702.

Chen, W., Foss, M., Tseng, K.-F., and Zhang, D. (2008). Redundant mechanisms recruit actin into the contractile ring in silkworm spermatocytes. Plos Biol *6*, e209.

Choi, J., Chen, J., Schreiber, S. L., & Clardy, J. (1996). Structure of the FKBP12-rapamycin complex interacting with the binding domain of human FRAP. Science, *273*(5272), 239–242.

Cleveland, D.W., Mao, Y., and Sullivan, K.F. (2003). Centromeres and kinetochores: from epigenetics to mitotic checkpoint signaling. Cell *112*, 407–421.

Cohen, P.T.W., Philp, A., and Vázquez-Martin, C. (2005). Protein phosphatase 4--from obscurity to vital functions. FEBS Letters *579*, 3278–3286.

Colicino, E.G., and Hehnly, H. (2018). Regulating a key mitotic regulator, polo-like kinase 1 (PLK1). Cytoskeleton (Hoboken) *75*, 481–494.

D'Avino, P.P., Giansanti, M.G., and Petronczki, M. (2015). Cytokinesis in animal cells. Cold Spring Harbor Perspectives in Biology *7*, a015834.

D'Avino, P.P., Savoian, M.S., and Glover, D.M. (2004). Mutations in sticky lead to defective organization of the contractile ring during cytokinesis and are enhanced by Rho and suppressed by Rac. The Journal of Cell Biology *166*, 61–71.

D'Avino, P.P., Takeda, T., Capalbo, L., Zhang, W., Lilley, K.S., Laue, E.D., and Glover, D.M. (2008). Interaction between Anillin and RacGAP50C connects the actomyosin contractile ring with spindle microtubules at the cell division site. Journal of Cell Science *121*, 1151–1158.

Dassow, von, G. (2009). Concurrent cues for cytokinetic furrow induction in animal cells. Trends in Cell Biology *19*, 165–173.

Davoli, T., and de Lange, T. (2011). The Causes and Consequences of Polyploidy in Normal Development and Cancer. Annu. Rev. Cell Dev. Biol. *27*, 585–610.

Delaval, B., Ferrand, A., Conte, N., Larroque, C., Hernandez-Verdun, D., Prigent, C., and Birnbaum, D. (2004). Aurora B -TACC1 protein complex in cytokinesis. Oncogene *23*, 4516–4522.

DeRose, R., Miyamoto, T., & Inoue, T. (2013). Manipulating signaling at will: chemically-inducible dimerization (CID) techniques resolve problems in cell biology. *Pflugers Archiv :* European Journal of Physiology, *465*(3), 409–417.

Dewhurst, S.M., McGranahan, N., Burrell, R.A., Rowan, A.J., Grönroos, E., Endesfelder, D., Joshi, T., Mouradov, D., Gibbs, P., Ward, R.L., et al. (2014). Tolerance of whole-genome doubling propagates chromosomal instability and accelerates cancer genome evolution. Cancer Discov *4*, 175–185.

Douglas, M.E., Davies, T., Joseph, N., and Mishima, M. (2010). Aurora B and 14-3-3 coordinately regulate clustering of centralspindlin during cytokinesis. Curr. Biol. *20*, 927–933.

Drechsel, D.N., Hyman, A.A., Hall, A., and Glotzer, M. (1997). A requirement for Rho and Cdc42 during cytokinesis in Xenopus embryos. Curbio *7*, 12–23.

Eichmann, T.O., and Lass, A. (2015). DAG tales: the multiple faces of diacylglycerol--stereochemistry, metabolism, and signaling. Cell. Mol. Life Sci. *72*, 3931–3952.

Eggert, U.S., Kiger, A.A., Richter, C., Perlman, Z.E., Perrimon, N., Mitchison, T.J., and Field, C.M. (2004). Parallel chemical genetic and genome-wide RNAi screens identify cytokinesis inhibitors and targets. PLoS Biol. *2*, e379.

Eggert, U.S., Mitchison, T.J., and Field, C.M. (2006). Animal cytokinesis: from parts list to mechanisms. Annu. Rev. Biochem. *75*, 543–566.

Elian, F.A., Yan, E., and Walter, M.A. (2018). FOXC1, the new player in the cancer sandbox. Oncotarget *9*, 8165–8178.

Estey, M.P., Di Ciano-Oliveira, C., Froese, C.D., Bejide, M.T., and Trimble, W.S. (2010). Distinct roles of septins in cytokinesis: SEPT9 mediates midbody abscission. The Journal of Cell Biology *191*, 741–749.

Euteneuer, U., and McIntosh, J.R. (1980). Polarity of midbody and phragmoplast microtubules. The Journal of Cell Biology *87*, 509–515.

Evangelista, M., Pruyne, D., Amberg, D.C., Boone, C., and Bretscher, A. (2002). Formins direct Arp2/3-independent actin filament assembly to polarize cell growth in yeast. Nature Cell Biology *4*, 260–269.

Ferreira, T., Prudêncio, P., and Martinho, R.G. (2014). Drosophila protein kinase N (Pkn) is a negative regulator of actin-myosin activity during oogenesis. Developmental Biology *394*, 277–291.

Field, C.M., Coughlin, M., Doberstein, S., Marty, T., and Sullivan, W. (2005). Characterization of anillin mutants reveals essential roles in septin localization and plasma membrane integrity. Development *132*, 2849–2860.

Fish, R.N., and Kane, C.M. (2002). Promoting elongation with transcript cleavage stimulatory factors. Biochim. Biophys. Acta *1577*, 287–307.

Foe, V.E., and Dassow, von, G. (2008). Stable and dynamic microtubules coordinately shape the myosin activation zone during cytokinetic furrow formation. The Journal of Cell Biology *183*, 457–470.

Frøkjær-Jensen, C., Wayne Davis, M., Hopkins, C.E., Newman, B.J., Thummel, J.M., Olesen, S.-P., Grunnet, M., and Jorgensen, E.M. (2008). Single-copy insertion of transgenes in Caenorhabditis elegans. Nat Genet *40*, 1375–1383.

Gaillard, J., Neumann, E., Van Damme, D., Stoppin-Mellet, V., Ebel, C., Barbier, E., Geelen, D., and Vantard, M. (2008). Two microtubule-associated proteins of Arabidopsis MAP65s promote antiparallel microtubule bundling. Mol. Biol. Cell *19*, 4534–4544.

Ganem, N.J., Cornils, H., Chiu, S.-Y., O'Rourke, K.P., Arnaud, J., Yimlamai, D., Théry, M., Camargo, F.D., and Pellman, D. (2014). Cytokinesis Failure Triggers Hippo Tumor Suppressor Pathway Activation. Cell *158*, 833–848.

Giet, R., and Glover, D.M. (2001). Drosophila aurora B kinase is required for histone H3 phosphorylation and condensin recruitment during chromosome condensation and to organize the central spindle during cytokinesis. The Journal of Cell Biology *152*, 669–682.

Glotzer, M. (2004). Cleavage furrow positioning. The Journal of Cell Biology *164*, 347–351.

Glotzer, M. (2005). The molecular requirements for cytokinesis. Science *307*, 1735–1739.

Glotzer, M. (2009). The 3Ms of central spindle assembly: microtubules, motors and MAPs. Nat Rev Mol Cell Biol *10*, 9–20.

Goshima, G. (2011). Identification of a TPX2-like microtubule-associated protein in Drosophila. PLoS ONE *6*, e28120.

Green, R.A., Paluch, E., and Oegema, K. (2012). Cytokinesis in animal cells. Annu. Rev. Cell Dev. Biol. *28*, 29–58.

Gregory, S.L., Ebrahimi, S., Milverton, J., Jones, W.M., Bejsovec, A., and Saint, R. (2008). Cell division requires a direct link between microtubule-bound RacGAP and Anillin in the contractile ring. Curbio *18*, 25–29.

Guse, A., Mishima, M., and Glotzer, M. (2005). Phosphorylation of ZEN-4/MKLP1 by aurora B regulates completion of cytokinesis. Curbio *15*, 778–786.

Habedanck, R., Stierhof, Y.-D., Wilkinson, C.J., and Nigg, E.A. (2005). The Polo kinase Plk4 functions in centriole duplication. Nature Cell Biology *7*, 1140–1146.

Haga, R.B., and Ridley, A.J. (2016). Rho GTPases: Regulation and roles in cancer cell biology. Small GTPases *7*, 207–221.

Hakem, A., Sanchez-Sweatman, O., You-Ten, A., Duncan, G., Wakeham, A., Khokha, R., and Mak, T.W. (2005). RhoC is dispensable for embryogenesis and tumor initiation but essential for metastasis. Genes & Development *19*, 1974–1979.

Han, X., Gomes, J.-E., Birmingham, C.L., Pintard, L., Sugimoto, A., and Mains, P.E. (2009). The role of protein phosphatase 4 in regulating microtubule severing in the Caenorhabditis elegans embryo. Genetics *181*, 933–943.

Hauf, S., Cole, R.W., LaTerra, S., Zimmer, C., Schnapp, G., Walter, R., Heckel, A., van Meel, J., Rieder, C.L., and Peters, J.-M. (2003). The small molecule Hesperadin reveals a role for Aurora B in correcting kinetochore-microtubule attachment and in maintaining the spindle assembly checkpoint. The Journal of Cell Biology *161*, 281–294.

Heasman, S.J., and Ridley, A.J. (2008). Mammalian Rho GTPases: new insights into their functions from in vivo studies. Nat Rev Mol Cell Biol *9*, 690–701.

Helps, N.R., Brewis, N.D., Lineruth, K., Davis, T., Kaiser, K., and Cohen, P.T. (1998). Protein phosphatase 4 is an essential enzyme required for organisation of microtubules at centrosomes in Drosophila embryos. Journal of Cell Science *111 (Pt 10)*, 1331–1340.

Hickson, G.R.X., and O'Farrell, P.H. (2008). Rho-dependent control of anillin behavior during cytokinesis. The Journal of Cell Biology *180*, 285–294.

Hillhouse, E.W., and Grammatopoulos, D.K. (2006). The molecular mechanisms underlying the regulation of the biological activity of corticotropin-releasing hormone receptors: implications for physiology and pathophysiology. Endocr. Rev. *27*, 260–286.

Hodge, R.G., and Ridley, A.J. (2016). Regulating Rho GTPases and their regulators. Nat Rev Mol Cell Biol *17*, 496–510.

Holder, J., Poser, E., and Barr, F.A. (2019). Getting out of mitosis: spatial and temporal control of mitotic exit and cytokinesis by PP1 and PP2A. FEBS Letters *593*, 2908–2924.

Hu, C.-K., Coughlin, M., Field, C.M., and Mitchison, T.J. (2008). Cell polarization during monopolar cytokinesis. The Journal of Cell Biology *181*, 195–202.

Hu, C.-K., Coughlin, M., Field, C.M., and Mitchison, T.J. (2011). KIF4 regulates midzone length during cytokinesis. Curr. Biol. *21*, 815–824.

Hu, C.-K., Özlü, N., Coughlin, M., Steen, J.J., and Mitchison, T.J. (2012). Plk1 negatively regulates PRC1 to prevent premature midzone formation before cytokinesis. Mol. Biol. Cell *23*, 2702–2711.

Janssen, L.M.E., Averink, T.V., Blomen, V.A., Brummelkamp, T.R., Medema, R.H., and Raaijmakers, J.A. (2018). Loss of Kif18A Results in Spindle Assembly Checkpoint Activation at Microtubule-Attached Kinetochores. Curr. Biol. *28*, 2685–2696.e4.

Janssens, V., and Goris, J. (2001). Protein phosphatase 2A: a highly regulated family of serine/threonine phosphatases implicated in cell growth and signalling. Biochem. J. *353*, 417–439.

Janson, M.E., Loughlin, R., Loïodice, I., Fu, C., Brunner, D., Nédélec, F.J., and Tran, P.T. (2007). Crosslinkers and motors organize dynamic microtubules to form stable bipolar arrays in fission yeast. Cell *128*, 357–368.

Jantsch-Plunger, V., Gonczy, P., Romano, A., Schnabel, H., Hamill, D., Schnabel, R., Hyman, A.A., and Glotzer, M. (2000). CYK-4: A Rho family gtpase activating protein

(GAP) required for central spindle formation and cytokinesis. The Journal of Cell Biology *149*, 1391–1404.

Jonas, S., and Izaurralde, E. (2013). The role of disordered protein regions in the assembly of decapping complexes and RNP granules. Genes & Development *27*, 2628–2641.

Jordan, S.N., and Canman, J.C. (2012). Rho GTPases in animal cell cytokinesis: an occupation by the one percent. Cytoskeleton (Hoboken) *69*, 919–930.

Jordan, S.N., Davies, T., Zhuravlev, Y., Dumont, J., Shirasu-Hiza, M., and Canman, J.C. (2016). Cortical PAR polarity proteins promote robust cytokinesis during asymmetric cell division. The Journal of Cell Biology *212*, 39–49.

Joo, E., Surka, M.C., and Trimble, W.S. (2007). Mammalian SEPT2 is required for scaffolding nonmuscle myosin II and its kinases. Developmental Cell *13*, 677–690.

Kaitna, S., Mendoza, M., Jantsch-Plunger, V., and Glotzer, M. (2000). Incenp and an aurora-like kinase form a complex essential for chromosome segregation and efficient completion of cytokinesis. Curbio *10*, 1172–1181.

Kamasaki, T., Osumi, M., and Mabuchi, I. (2007). Three-dimensional arrangement of F-actin in the contractile ring of fission yeast. The Journal of Cell Biology *178*, 765–771.

Kawamura, K. (1977). Microdissection studies on the dividing neuroblast of the grasshopper, with special reference to the mechanism of unequal cytokinesis. Experimental Cell Research *106*, 127–137.

Kawashima, T., Hirose, K., Satoh, T., Kaneko, A., Ikeda, Y., Kaziro, Y., Nosaka, T., and Kitamura, T. (2000). MgcRacGAP is involved in the control of growth and differentiation of hematopoietic cells. Blood *96*, 2116–2124.

Kechad, A., Jananji, S., Ruella, Y., and Hickson, G.R.X. (2012). Anillin acts as a bifunctional linker coordinating midbody ring biogenesis during cytokinesis. Curr. Biol. *22*, 197–203.

Kettenberger, H., Armache, K.-J., and Cramer, P. (2003). Architecture of the RNA polymerase II-TFIIS complex and implications for mRNA cleavage. Cell *114*, 347–357.

Kim, H., Johnson, J.M., Lera, R.F., Brahma, S., and Burkard, M.E. (2017). Anillin Phosphorylation Controls Timely Membrane Association and Successful Cytokinesis. PLoS Genet *13*, e1006511.

Kishi, K., Sasaki, T., Kuroda, S., Itoh, T., and Takai, Y. (1993). Regulation of cytoplasmic division of Xenopus embryo by rho p21 and its inhibitory GDP/GTP exchange protein (rho GDI). The Journal of Cell Biology *120*, 1187–1195.

Kittler, R., Pelletier, L., Heninger, A.-K., Slabicki, M., Theis, M., Miroslaw, L., Poser, I., Lawo, S., Kozak, K., Wagner, J., et al. (2007). Genome-scale RNAi profiling of cell division in human tissue culture cells. Nat Cell Biol *9*, 1401–1412.

Kittler, R., Putz, G., Pelletier, L., Poser, I., Heninger, A.-K., Drechsel, D., Fischer, S., Konstantinova, I., Habermann, B., Grabner, H., et al. (2004). An endoribonuclease-prepared siRNA screen in human cells identifies genes essential for cell division. Nature *432*, 1036–1040.

Kotýnková, K., Su, K.-C., West, S.C., and Petronczki, M. (2016). Plasma Membrane Association but Not Midzone Recruitment of RhoGEF ECT2 Is Essential for Cytokinesis. CellReports *17*, 2672–2686.

Kurasawa, Y., Earnshaw, W.C., Mochizuki, Y., Dohmae, N., and Todokoro, K. (2004). Essential roles of KIF4 and its binding partner PRC1 in organized central spindle midzone formation. The EMBO Journal *23*, 3237–3248.

Lacroix, B., and Maddox, A.S. (2012). Cytokinesis, ploidy and aneuploidy. J. Pathol. *226*, 338–351.

Lewellyn, L., Dumont, J., Desai, A., and Oegema, K. (2010). Analyzing the effects of delaying aster separation on furrow formation during cytokinesis in the Caenorhabditis elegans embryo. Mol. Biol. Cell *21*, 50–62.

Lim, W.G., Chen, X., Liu, J.-P., Tan, B.J., Zhou, S., Smith, A., Lees, N., Hou, L., Gu, F., Yu, X.Y., et al. (2008). The C-terminus of PRK2/PKNgamma is required for optimal activation by RhoA in a GTP-dependent manner. Arch. Biochem. Biophys. *479*, 170–178.

Liu Ax, Cerniglia, G.J., Bernhard, E.J., and Prendergast, G.C. (2001). RhoB is required to mediate apoptosis in neoplastically transformed cells after DNA damage. Proceedings of the National Academy of Sciences *98*, 6192–6197.

Liu, J., Fairn, G.D., Ceccarelli, D.F., Sicheri, F., and Wilde, A. (2012). Cleavage furrow organization requires PIP(2)-mediated recruitment of anillin. Curr. Biol. *22*, 64–69.

Liu, X., and Erikson, R.L. (2003a). Polo-like kinase 1 in the life and death of cancer cells. Cell Cycle *2*, 424–425.

Liu, X., and Erikson, R.L. (2003b). Polo-like kinase (Plk)1 depletion induces apoptosis in cancer cells. Proceedings of the National Academy of Sciences *100*, 5789–5794.

Liu, X., Lei, M., and Erikson, R.L. (2006). Normal cells, but not cancer cells, survive severe Plk1 depletion. Molecular and Cellular Biology *26*, 2093–2108.

Logan, M.R., and Mandato, C.A. (2012). Regulation of the actin cytoskeleton by PIP2 in cytokinesis. Biology of the Cell *98*, 377–388.

Loïodice, I., Staub, J., Setty, T.G., Nguyen, N.-P.T., Paoletti, A., and Tran, P.T. (2005). Ase1p organizes antiparallel microtubule arrays during interphase and mitosis in fission yeast. Mol. Biol. Cell *16*, 1756–1768.

Loria, A., Longhini, K.M., and Glotzer, M. (2012). The RhoGAP Domain of CYK-4 Has an Essential Role in RhoA Activation. Curbio *22*, 213–219.

Lu, Y., and Settleman, J. (1999). The Drosophila Pkn protein kinase is a Rho/Rac effector target required for dorsal closure during embryogenesis. Genes & Development *13*, 1168–1180.

Ma, X., Kovács, M., Conti, M.A., Wang, A., Zhang, Y., Sellers, J.R., and Adelstein, R.S. (2012). Nonmuscle myosin II exerts tension but does not translocate actin in vertebrate cytokinesis. Proc. Natl. Acad. Sci. U.S.a. *109*, 4509–4514.

Mabuchi, I., Hamaguchi, Y., Fujimoto, H., Morii, N., Mishima, M., and Narumiya, S. (1993). A rho-like protein is involved in the organisation of the contractile ring in dividing sand dollar eggs. Zygote *1*, 325–331.

Mangal, S., Sacher, J., Kim, T., Osório, D.S., Motegi, F., Carvalho, A.X., Oegema, K., and Zanin, E. (2018). TPXL-1 activates Aurora A to clear contractile ring components from the polar cortex during cytokinesis. The Journal of Cell Biology *217*, 837–848.

Marumoto, T., Honda, S., Hara, T., Nitta, M., Hirota, T., Kohmura, E., and Saya, H. (2003). Aurora-A kinase maintains the fidelity of early and late mitotic events in HeLa cells. Journal of Biological Chemistry *278*, 51786–51795.

Marumoto, T., Zhang, D., and Saya, H. (2005). Aurora-A - a guardian of poles. Nat Rev Cancer *5*, 42–50.

Martin-Granados, C., Philp, A., Oxenham, S.K., Prescott, A.R., and Cohen, P.T.W. (2008). Depletion of protein phosphatase 4 in human cells reveals essential roles in centrosome maturation, cell migration and the regulation of Rho GTPases. The International Journal of Biochemistry & Cell Biology *40*, 2315–2332.

Masutani, M., Sonenberg, N., Yokoyama, S., and Imataka, H. (2007). Reconstitution reveals the functional core of mammalian eIF3. The EMBO Journal *26*, 3373–3383.

Martinsson-Ahlzén, H.-S., Liberal, V., Grünenfelder, B., Chaves, S.R., Spruck, C.H., and Reed, S.I. (2008). Cyclin-dependent kinase-associated proteins Cks1 and Cks2 are essential during early embryogenesis and for cell cycle progression in somatic cells. Molecular and Cellular Biology *28*, 5698–5709.

Meraldi, P., Draviam, V.M., and Sorger, P.K. (2004). Timing and checkpoints in the regulation of mitotic progression. Developmental Cell *7*, 45–60.

Mérida, I., Torres-Ayuso, P., Ávila-Flores, A., Arranz-Nicolás, J., Andrada, E., Tello-Lafoz, M., Liébana, R., and Arcos, R. (2017). Diacylglycerol kinases in cancer. Adv Biol Regul *63*, 22–31.

Miller, A.L., and Bement, W.M. (2009). Regulation of cytokinesis by Rho GTPase flux. Nature Publishing Group *11*, 71–77.

Mollinari, C., Kleman, J.-P., Saoudi, Y., Jablonski, S.A., Perard, J., Yen, T.J., and Margolis, R.L. (2005). Ablation of PRC1 by small interfering RNA demonstrates that cytokinetic abscission requires a central spindle bundle in mammalian cells, whereas completion of furrowing does not. Mol. Biol. Cell *16*, 1043–1055.

Motegi, F., and Sugimoto, A. (2006). Sequential functioning of the ECT-2 RhoGEF, RHO-1 and CDC-42 establishes cell polarity in Caenorhabditis elegans embryos. Nature Cell Biology *8*, 978–985.

Moynihan, T.P., Ardley, H.C., Leek, J.P., Thompson, J., Brindle, N.S., Markham, A.F., and Robinson, P.A. (1996). Characterization of a human ubiquitin-conjugating enzyme gene UBE2L3. Mamm. Genome *7*, 520–525.

Mukherji, M., Bell, R., Supekova, L., Wang, Y., Orth, A.P., Batalov, S., Miraglia, L., Huesken, D., Lange, J., Martin, C., et al. (2006). Genome-wide functional analysis of human cell-cycle regulators. Proc. Natl. Acad. Sci. U.S.a. *103*, 14819–14824.

Murthy, K., and Wadsworth, P. (2008). Dual role for microtubules in regulating cortical contractility during cytokinesis. Journal of Cell Science *121*, 2350–2359.

Neef, R., Gruneberg, U., Kopajtich, R., Li, X., Nigg, E.A., Sillje, H., and Barr, F.A. (2007). Choice of Plk1 docking partners during mitosis and cytokinesis is controlled by the activation state of Cdk1. Nature Cell Biology *9*, 436–444.

Neef, R., Preisinger, C., Sutcliffe, J., Kopajtich, R., Nigg, E.A., Mayer, T.U., and Barr, F.A. (2003). Phosphorylation of mitotic kinesin-like protein 2 by polo-like kinase 1 is required for cytokinesis. The Journal of Cell Biology *162*, 863–875.

Neumann, B., Held, M., Liebel, U., Erfle, H., Rogers, P., Pepperkok, R., and Ellenberg, J. (2006). High-throughput RNAi screening by time-lapse imaging of live human cells. Nat Meth *3*, 385–390.

Neumann, B., Walter, T., Hériché, J.-K., Bulkescher, J., Erfle, H., Conrad, C., Rogers, P., Poser, I., Held, M., Liebel, U., et al. (2010). Phenotypic profiling of the human genome by time-lapse microscopy reveals cell division genes. Nature *464*, 721–727.

Nikonova, A.S., Astsaturov, I., Serebriiskii, I.G., Dunbrack, R.L., and Golemis, E.A. (2012). Aurora A kinase (AURKA) in normal and pathological cell division. Cell. Mol. Life Sci. *70*, 661–687.

Nishimura, Y., and Yonemura, S. (2006). Centralspindlin regulates ECT2 and RhoA accumulation at the equatorial cortex during cytokinesis. Journal of Cell Science *119*, 104–114.

Oegema, K., and Mitchison, T.J. (1997). Rappaport rules: cleavage furrow induction in animal cells. Proceedings of the National Academy of Sciences *94*, 4817–4820.

Özlü, N., Srayko, M., Kinoshita, K., Habermann, B., O'Toole, E.T., Müller-Reichert, T., Schmalz, N., Desai, A., and Hyman, A.A. (2005). An Essential Function of the C. elegans Ortholog of TPX2 Is to Localize Activated Aurora A Kinase to Mitotic Spindles. Developmental Cell *9*, 237–248.

Lorenzi, P., Sangalli, A., Fochi, S., Dal Molin, A., Malerba, G., Zipeto, D., and Romanelli, M.G. (2019). RNA-binding proteins RBM20 and PTBP1 regulate the alternative splicing of FHOD3. The International Journal of Biochemistry & Cell Biology *106*, 74–83.

Pavicic-Kaltenbrunner, V., Mishima, M., and Glotzer, M. (2007). Cooperative assembly of CYK-4/MgcRacGAP and ZEN-4/MKLP1 to form the centralspindlin complex. Mol. Biol. Cell *18*, 4992–5003.

Petronczki, M., Glotzer, M., Kraut, N., and Peters, J.-M. (2007). Polo-like Kinase 1 Triggers the Initiation of Cytokinesis in Human Cells by Promoting Recruitment of the RhoGEF Ect2 to the Central Spindle. Developmental Cell *12*, 713–725.

Piekny, A.J., and Glotzer, M. (2008). Anillin is a scaffold protein that links RhoA, actin, and myosin during cytokinesis. Curbio *18*, 30–36.

Piekny, A.J., and Maddox, A.S. (2010). The myriad roles of Anillin during cytokinesis. Seminars in Cell and Developmental Biology *21*, 881–891.

Powers, J., Bossinger, O., Rose, D., Strome, S., and Saxton, W. (1998). A nematode kinesin required for cleavage furrow advancement. Curbio *8*, 1133–1136.

Prokopenko, S.N., Brumby, A., O'Keefe, L., Prior, L., He, Y., Saint, R., and Bellen, H.J. (1999). A putative exchange factor for Rho1 GTPase is required for initiation of cytokinesis in Drosophila. Genes & Development *13*, 2301–2314.

Qadota, H., Miyauchi, T., Nahabedian, J.F., Stirman, J.N., Lu, H., Amano, M., Benian, G.M., and Kaibuchi, K. (2011). PKN-1, a homologue of mammalian PKN, is involved in the regulation of muscle contraction and force transmission in C. elegans. J. Mol. Biol. *407*, 222–231.

Qian, X., McDonald, A., Zhou, H.-J., Adams, N.D., Parrish, C.A., Duffy, K.J., Fitch, D.M., Tedesco, R., Ashcraft, L.W., Yao, B., et al. (2010). Discovery of the First Potent and Selective Inhibitor of Centromere-Associated Protein E: GSK923295. ACS Med Chem Lett *1*, 30–34.

Raich, W.B., Moran, A.N., Rothman, J.H., and Hardin, J. (1998). Cytokinesis and midzone microtubule organization in Caenorhabditis elegans require the kinesin-like protein ZEN-4. Mol. Biol. Cell *9*, 2037–2049.

Rappaport, R. (1961). Experiments concerning the cleavage stimulus in sand dollar eggs. J. Exp. Zool. *148*, 81–89.

Rappaport, R. (1985). Repeated furrow formation from a single mitotic apparatus in cylindrical sand dollar eggs. J. Exp. Zool. *234*, 167–171.

Reboutier, D., Troadec, M.-B., Cremet, J.-Y., Chauvin, L., Guen, V., Salaun, P., and Prigent, C. (2013). Aurora A is involved in central spindle assembly through phosphorylation of Ser 19 in P150Glued. The Journal of Cell Biology *201*, 65–79.

Riedl, J., Crevenna, A.H., Kessenbrock, K., Yu, J.H., Neukirchen, D., Bista, M., Bradke, F., Jenne, D., Holak, T.A., Werb, Z., et al. (2008). Lifeact: a versatile marker to visualize F-actin. Nat Meth *5*, 605–607.

Ribet, D., Boscaini, S., Cauvin, C., Siguier, M., Mostowy, S., Echard, A., and Cossart, P. (2017). SUMOylation of human septins is critical for septin filament bundling and cytokinesis. The Journal of Cell Biology *216*, 4041–4052.

Rieder, C.L., Khodjakov, A., Paliulis, L.V., Fortier, T.M., Cole, R.W., and Sluder, G. (1997). Mitosis in vertebrate somatic cells with two spindles: implications for the metaphase/anaphase transition checkpoint and cleavage. Proceedings of the National Academy of Sciences *94*, 5107–5112.

Rilstone, J.J., Alkhater, R.A., and Minassian, B.A. (2013). Brain dopamine-serotonin vesicular transport disease and its treatment. N. Engl. J. Med. *368*, 543–550.

Roberts, D.L., Frerman, F.E., and Kim, J.J. (1996). Three-dimensional structure of human electron transfer flavoprotein to 2.1-A resolution. Proceedings of the National Academy of Sciences *93*, 14355–14360.

Rodrigues, N.T.L., Lekomtsev, S., Jananji, S., Kriston-Vizi, J., Hickson, G.R.X., and Baum, B. (2015). Kinetochore-localized PP1-Sds22 couples chromosome segregation to polar relaxation. Nature *524*, 489–492.

Romanelli, M.G., Diani, E., and Lievens, P.M.-J. (2013). New insights into functional roles of the polypyrimidine tract-binding protein. Int J Mol Sci *14*, 22906–22932.

Ruchaud, S., Carmena, M., and Earnshaw, W.C. (2007). Chromosomal passengers: conducting cell division. Nat Rev Mol Cell Biol *8*, 798–812.

Salazar, D., Zhang, L., deGala, G.D., and Frerman, F.E. (1997). Expression and characterization of two pathogenic mutations in human electron transfer flavoprotein. Journal of Biological Chemistry *272*, 26425–26433.

Schaar, B.T., Chan, G.K., Maddox, P., Salmon, E.D., and Yen, T.J. (1997). CENP-E function at kinetochores is essential for chromosome alignment. The Journal of Cell Biology *139*, 1373–1382.

Schmidt, O., and Teis, D. (2012). The ESCRT machinery. Curr. Biol. *22*, R116–R120.

Schmidt, A., Durgan, J., Magalhaes, A., and Hall, A. (2007). Rho GTPases regulate PRK2/PKN2 to control entry into mitosis and exit from cytokinesis. The EMBO Journal *26*, 1624–1636.

Schmutz, C., Stevens, J., and Spang, A. (2007). Functions of the novel RhoGAP proteins RGA-3 and RGA-4 in the germ line and in the early embryo of C. elegans. Development *134*, 3495–3505.

Schonegg, S., Constantinescu, A.T., Hoege, C., and Hyman, A.A. (2007). The Rho GTPase-activating proteins RGA-3 and RGA-4 are required to set the initial size of PAR domains in Caenorhabditis elegans one-cell embryos. Proceedings of the National Academy of Sciences *104*, 14976–14981.

Schroeder, T.E. (1990). The contractile ring and furrowing in dividing cells. Ann. N. Y. Acad. Sci. *582*, 78–87.

Sellin, M.E., Sandblad, L., Stenmark, S., and Gullberg, M. (2011). Deciphering the rules governing assembly order of mammalian septin complexes. Mol. Biol. Cell *22*, 3152–3164.

Severson, A.F., Baillie, D.L., and Bowerman, B. (2002). A Formin Homology protein and a profilin are required for cytokinesis and Arp2/3-independent assembly of cortical microfilaments in C. elegans. Curbio *12*, 2066–2075.

Severson, A.F., Hamill, D.R., Carter, J.C., Schumacher, J., and Bowerman, B. (2000). The aurora-related kinase AIR-2 recruits ZEN-4/CeMKLP1 to the mitotic spindle at metaphase and is required for cytokinesis. Curbio *10*, 1162–1171.

Sirajuddin, M., Farkasovsky, M., Hauer, F., Kühlmann, D., Macara, I.G., Weyand, M., Stark, H., and Wittinghofer, A. (2007). Structural insight into filament formation by mammalian septins. Nature *449*, 311–315.

Shulga, Y.V., Topham, M.K., and Epand, R.M. (2011). Regulation and functions of diacylglycerol kinases. Chem. Rev. *111*, 6186–6208.

Sit, S.-T., and Manser, E. (2011). Rho GTPases and their role in organizing the actin cytoskeleton. Journal of Cell Science *124*, 679–683.

Somers, W.G., and Saint, R. (2003). A RhoGEF and Rho family GTPase-activating protein complex links the contractile ring to cortical microtubules at the onset of cytokinesis. Developmental Cell *4*, 29–39.

Somma, M.P., Fasulo, B., Cenci, G., Cundari, E., and Gatti, M. (2002). Molecular dissection of cytokinesis by RNA interference in Drosophila cultured cells. Mol. Biol. Cell *13*, 2448–2460.

Sönnichsen, B., Koski, L.B., Walsh, A., Marschall, P., Neumann, B., Brehm, M., Alleaume, A.-M., Artelt, J., Bettencourt, P., Cassin, E., et al. (2005). Full-genome RNAi profiling of early embryogenesis in Caenorhabditis elegans. Nature *434*, 462–469.

Speliotes, E.K., Uren, A., Vaux, D., and Horvitz, H.R. (2000). The survivin-like C. elegans BIR-1 protein acts with the Aurora-like kinase AIR-2 to affect chromosomes and the spindle midzone. Mol. Cell *6*, 211–223.

Spruck, C.H., de Miguel, M.P., Smith, A.P.L., Ryan, A., Stein, P., Schultz, R.M., Lincoln, A.J., Donovan, P.J., and Reed, S.I. (2003). Requirement of Cks2 for the first metaphase/anaphase transition of mammalian meiosis. Science *300*, 647–650.

Srayko, M., Kaya, A., Stamford, J., and Hyman, A.A. (2005). Identification and Characterization of Factors Required for Microtubule Growth and Nucleation in the Early C. elegans Embryo. Developmental Cell *9*, 223–236.

Straight, A.F., Field, C.M., and Mitchison, T.J. (2005). Anillin binds nonmuscle myosin II and regulates the contractile ring. Mol. Biol. Cell *16*, 193–201.

Su, K.-C., Takaki, T., and Petronczki, M. (2011). Targeting of the RhoGEF Ect2 to the Equatorial Membrane Controls Cleavage Furrow Formation during Cytokinesis. Developmental Cell *21*, 1104–1115.

Sun, L., Guan, R., Lee, I.-J., Liu, Y., Chen, M., Wang, J., Wu, J.-Q., and Chen, Z. (2015). Mechanistic insights into the anchorage of the contractile ring by anillin and Mid1. Developmental Cell *33*, 413–426.

Sumiyoshi, E., Sugimoto, A., and Yamamoto, M. (2002). Protein phosphatase 4 is required for centrosome maturation in mitosis and sperm meiosis in C. elegans. Journal of Cell Science *115*, 1403–1410.

Takaishi, K., Sasaki, T., Kameyama, T., Tsukita, S., and Takai, Y. (1995). Translocation of activated Rho from the cytoplasm to membrane ruffling area, cell-cell adhesion sites and cleavage furrows. Oncogene *11*, 39–48.

Tatsumoto, T., Xie, X., Blumenthal, R., Okamoto, I., and Miki, T. (1999). Human ECT2 is an exchange factor for Rho GTPases, phosphorylated in G2/M phases, and involved in cytokinesis. The Journal of Cell Biology *147*, 921–928.

Tolias, K.F., Couvillon, A.D., Cantley, L.C., and Carpenter, C.L. (1998). Characterization of a Rac1- and RhoGDI-associated lipid kinase signaling complex. Molecular and Cellular Biology *18*, 762–770.

Touré, A., Dorseuil, O., Morin, L., Timmons, P., Jégou, B., Reibel, L., and Gacon, G. (1998). MgcRacGAP, a new human GTPase-activating protein for Rac and Cdc42 similar to

Drosophila rotundRacGAP gene product, is expressed in male germ cells. Journal of Biological Chemistry *273*, 6019–6023.

Tsushima, S., Kai, M., Yamada, K., Imai, S.-I., Houkin, K., Kanoh, H., and Sakane, F. (2004). Diacylglycerol Kinase γ Serves as an Upstream Suppressor of Rac1 and Lamellipodium Formation. Journal of Biological Chemistry *279*, 28603–28613.

Udo, H., Lam, C.K., Mori, S., Inouye, M., and Inouye, S. (2000). Identification of a substrate for Pkn2, a protein Ser/Thr kinase from Myxococcus xanthus by a novel method for substrate identification. J. Mol. Microbiol. Biotechnol. *2*, 557–563.

Valadares, N.F., d' Muniz Pereira, H., Ulian Araujo, A.P., and Garratt, R.C. (2017). Septin structure and filament assembly. Biophys Rev *9*, 481–500.

Varjosalo, M., and Taipale, J. (2008). Hedgehog: functions and mechanisms. Genes & Development *22*, 2454–2472.

Varlamova, O., Spektor, A., and Bresnick, A.R. (2001). Protein kinase C mediates phosphorylation of the regulatory light chain of myosin-II during mitosis. J. Muscle Res. Cell. Motil. *22*, 243–250.

Verbrugghe, K.J.C., and White, J.G. (2004). SPD-1 is required for the formation of the spindle midzone but is not essential for the completion of cytokinesis in C. elegans embryos. Curbio *14*, 1755–1760.

Verma, V., and Maresca, T.J. (2019). Microtubule plus-ends act as physical signaling hubs to activate RhoA during cytokinesis. eLife *8*, 309.

Vincent, S., and Settleman, J. (1997). The PRK2 kinase is a potential effector target of both Rho and Rac GTPases and regulates actin cytoskeletal organization. Molecular and Cellular Biology *17*, 2247–2256.

Wang, J., Ma, S., Ma, R., Qu, X., Liu, W., Lv, C., Zhao, S., and Gong, Y. (2014). KIF2A silencing inhibits the proliferation and migration of breast cancer cells and correlates with unfavorable prognosis in breast cancer. BMC Cancer *14*, 461–469.

Watanabe, S., Ando, Y., Yasuda, S., Hosoya, H., Watanabe, N., Ishizaki, T., and Narumiya, S. (2008). mDia2 induces the actin scaffold for the contractile ring and stabilizes its position during cytokinesis in NIH 3T3 cells. Mol. Biol. Cell *19*, 2328–2338.

Werner, M., Munro, E., and Glotzer, M. (2007). Astral signals spatially bias cortical myosin recruitment to break symmetry and promote cytokinesis. Curbio *17*, 1286–1297.

Wheatley, S.P., and Wang, Y. (1996). Midzone microtubule bundles are continuously required for cytokinesis in cultured epithelial cells. The Journal of Cell Biology *135*, 981–989.

Willems, E., Dedobbeleer, M., Digregorio, M., Lombard, A., Lumapat, P.N., and Rogister, B. (2018). The functional diversity of Aurora kinases: a comprehensive review. Cell Div *13*, 7–17.

Wolfe, B.A., Takaki, T., Petronczki, M., and Glotzer, M. (2009). Polo-like kinase 1 directs assembly of the HsCyk-4 RhoGAP/Ect2 RhoGEF complex to initiate cleavage furrow formation. Plos Biol *7*, e1000110.

Yamada, T., Hikida, M., and Kurosaki, T. (2006). Regulation of cytokinesis by mgcRacGAP in B lymphocytes is independent of GAP activity. Experimental Cell Research *312*, 3517–3525.

Yonemura, S., Hirao-Minakuchi, K., and Nishimura, Y. (2004). Rho localization in cells and tissues. Experimental Cell Research *295*, 300–314.

Yoshizaki, H., Ohba, Y., Parrini, M.-C., Dulyaninova, N.G., Bresnick, A.R., Mochizuki, N., and Matsuda, M. (2004). Cell type-specific regulation of RhoA activity during cytokinesis. Journal of Biological Chemistry *279*, 44756–44762.

You, H., Lin, H., and Zhang, Z. (2015). CKS2 in human cancers: Clinical roles and current perspectives (Review). Mol Clin Oncol *3*, 459–463.

Yüce, Ö., Piekny, A., and Glotzer, M. (2005). An ECT2-centralspindlin complex regulates the localization and function of RhoA. The Journal of Cell Biology *170*, 571–582.

Zanin, E., Desai, A., Poser, I., Toyoda, Y., Andree, C., Moebius, C., Bickle, M., Conradt, B., Piekny, A., and Oegema, K. (2013). A Conserved RhoGAP Limits M Phase Contractility and Coordinates with Microtubule Asters to Confine RhoA during Cytokinesis. Developmental Cell *26*, 496–510.

Zavortink, M., Contreras, N., Addy, T., Bejsovec, A., and Saint, R. (2005). Tum/RacGAP50C provides a critical link between anaphase microtubules and the assembly of the contractile ring in Drosophila melanogaster. Journal of Cell Science *118*, 5381–5392.

Zhang, B., Zhang, Y., Wang, Z., and Zheng, Y. (2000). The role of Mg2+ cofactor in the guanine nucleotide exchange and GTP hydrolysis reactions of Rho family GTP-binding proteins. Journal of Biological Chemistry *275*, 25299–25307.

Zhang, C., Zhu, C., Chen, H., Li, L., Guo, L., Jiang, W., and Lu, S.H. (2010). Kif18A is involved in human breast carcinogenesis. Carcinogenesis *31*, 1676–1684.

Zhao, W.-M., and Fang, G. (2005). MgcRacGAP controls the assembly of the contractile ring and the initiation of cytokinesis. Proc. Natl. Acad. Sci. U.S.a. *102*, 13158–13163.

Zhao, W.-M., and Fang, G. (2005b). Anillin is a substrate of anaphase-promoting complex/cyclosome (APC/C) that controls spatial contractility of myosin during late cytokinesis. Journal of Biological Chemistry *280*, 33516–33524.

Zhou, M., and Wang, Y.-L. (2008). Distinct pathways for the early recruitment of myosin II and actin to the cytokinetic furrow. Mol. Biol. Cell *19*, 318–326.

Zhu, C., and Jiang, W. (2005). Cell cycle-dependent translocation of PRC1 on the spindle by Kif4 is essential for midzone formation and cytokinesis. Proceedings of the National Academy of Sciences *102*, 343–348.

Zhu, C., Bossy-Wetzel, E., and Jiang, W. (2005). Recruitment of MKLP1 to the spindle midzone/midbody by INCENP is essential for midbody formation and completion of cytokinesis in human cells. Biochem. J. *389*, 373–381.

Zhu, C., Zhao, J., Bibikova, M., Leverson, J.D., Bossy-Wetzel, E., Fan, J.-B., Abraham, R.T., and Jiang, W. (2005). Functional analysis of human microtubule-based motor proteins, the

kinesins and dyneins, in mitosis/cytokinesis using RNA interference. Mol. Biol. Cell *16*, 3187–3199.

Zumdieck, A., Kruse, K., Bringmann, H., Hyman, A.A., and Jülicher, F. (2007). Stress generation and filament turnover during actin ring constriction. PLoS ONE *2*, e696.

Appendix

Figure 29-35 in section 4.2 were reproduced or adapted from our recently published research paper in the Journal of Cell Biology with the permission of Rockefeller University Press. The same has been mentioned in figure legends of the adapted and reproduced figures. The detailed citation of the paper is as follows:

Mangal, S., Sacher, J., Kim, T., Osório, D.S., Motegi, F., Carvalho, A.X., Oegema, K., and Zanin, E. (2018). TPXL-1 activates Aurora A to clear contractile ring components from the polar cortex during cytokinesis. The Journal of Cell Biology *217*, 837–84.

The permission to reuse the figures was seeked from the Rockefeller University Press as shown in the following email thread.

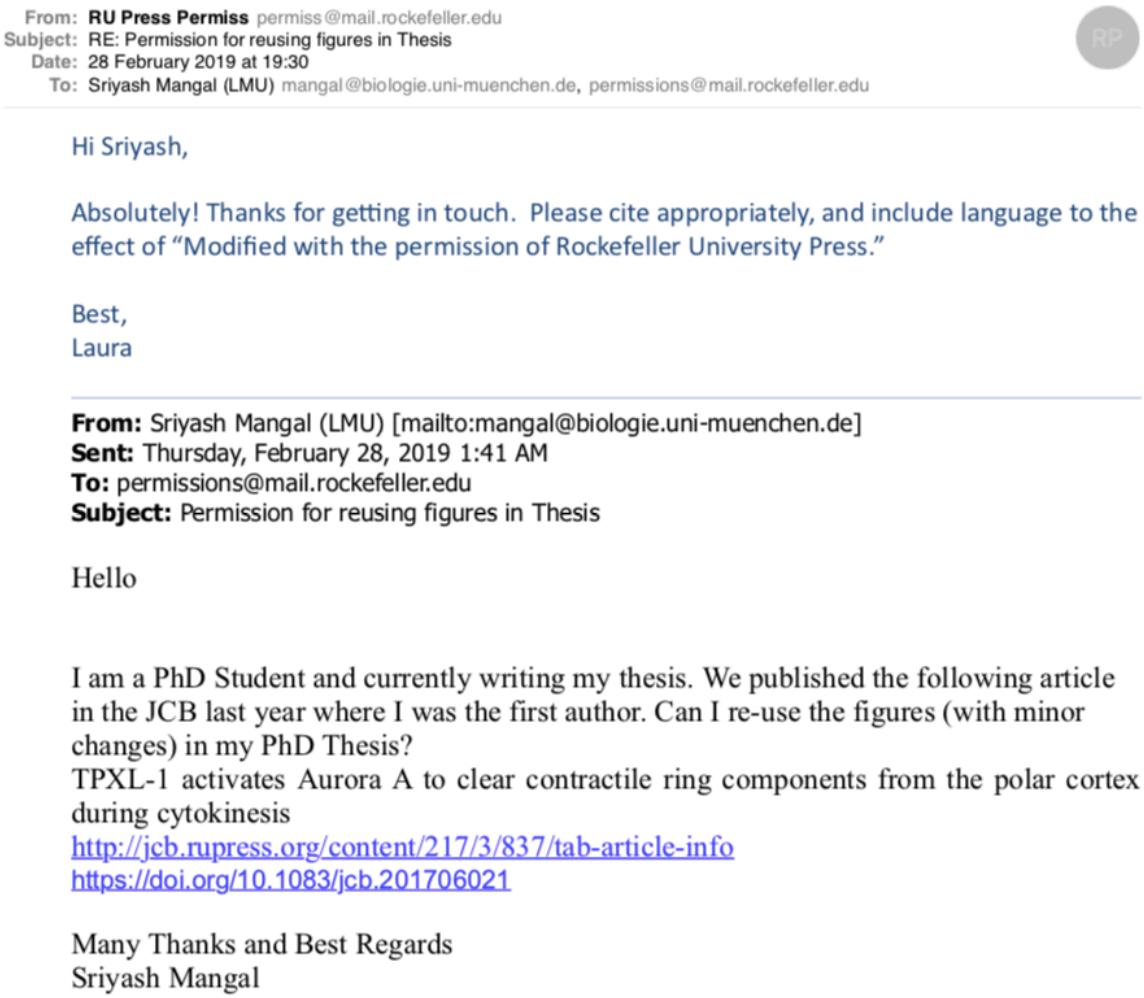

From: **RU Press Permiss** permiss@mail.rockefeller.edu
Subject: RE: Permission for reusing figures in Thesis
Date: 28 February 2019 at 19:30
To: Sriyash Mangal (LMU) mangal@biologie.uni-muenchen.de, permissions@mail.rockefeller.edu

Hi Sriyash,

Absolutely! Thanks for getting in touch. Please cite appropriately, and include language to the effect of "Modified with the permission of Rockefeller University Press."

Best,
Laura

From: Sriyash Mangal (LMU) [mailto:mangal@biologie.uni-muenchen.de]
Sent: Thursday, February 28, 2019 1:41 AM
To: permissions@mail.rockefeller.edu
Subject: Permission for reusing figures in Thesis

Hello

I am a PhD Student and currently writing my thesis. We published the following article in the JCB last year where I was the first author. Can I re-use the figures (with minor changes) in my PhD Thesis?
TPXL-1 activates Aurora A to clear contractile ring components from the polar cortex during cytokinesis
http://jcb.rupress.org/content/217/3/837/tab-article-info
https://doi.org/10.1083/jcb.201706021

Many Thanks and Best Regards
Sriyash Mangal

Figure 40 in section 4.3 was reproduced from our recently published research paper in the micoPublication Biology Journal with their permission. The detailed citation of the paper is as follows:

Mangal, S., Zielich, J., Lambie, EJ., Zanin E. (2018). Rapamycin-induced protein dimerization as a tool for C. elegans research. Micropublication: biology. https://doi.org/10.17912/W2BH3H.

The permission to reuse the figures was seeked from the micropublication Biology Journal as shown in the following email thread.

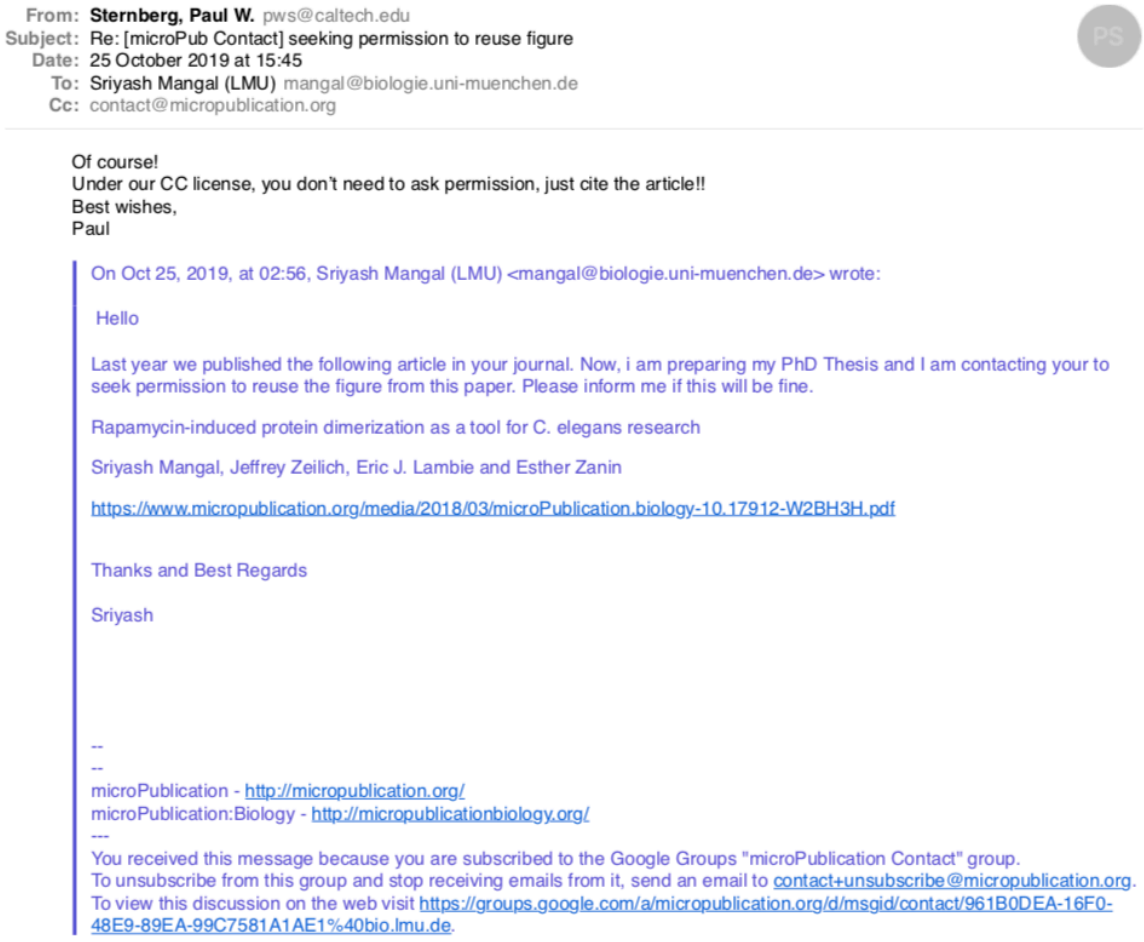

From: **Sternberg, Paul W.** pws@caltech.edu
Subject: Re: [microPub Contact] seeking permission to reuse figure
Date: 25 October 2019 at 15:45
To: Sriyash Mangal (LMU) mangal@biologie.uni-muenchen.de
Cc: contact@micropublication.org

Of course!
Under our CC license, you don't need to ask permission, just cite the article!!
Best wishes,
Paul

> On Oct 25, 2019, at 02:56, Sriyash Mangal (LMU) <mangal@biologie.uni-muenchen.de> wrote:
>
> Hello
>
> Last year we published the following article in your journal. Now, i am preparing my PhD Thesis and I am contacting your to seek permission to reuse the figure from this paper. Please inform me if this will be fine.
>
> Rapamycin-induced protein dimerization as a tool for C. elegans research
>
> Sriyash Mangal, Jeffrey Zeilich, Eric J. Lambie and Esther Zanin
>
> https://www.micropublication.org/media/2018/03/microPublication.biology-10.17912-W2BH3H.pdf
>
> Thanks and Best Regards
>
> Sriyash
>
> --
> --
> microPublication - http://micropublication.org/
> microPublication:Biology - http://micropublicationbiology.org/
> ---
> You received this message because you are subscribed to the Google Groups "microPublication Contact" group.
> To unsubscribe from this group and stop receiving emails from it, send an email to contact+unsubscribe@micropublication.org.
> To view this discussion on the web visit https://groups.google.com/a/micropublication.org/d/msgid/contact/961B0DEA-16F0-48E9-89EA-99C7581A1AE1%40bio.lmu.de.

SRIYASH MANGAL

42, Royal Avenue, Pocket-27, Sector-24, Rohini, Delhi, India
+91(0)8447356011/ email: sriyash29@gmail.com

EDUCATION

02-2015 to 01-2019: Ph.D. thesis in Cell and Developmental Biology, Ludwig Maximilian University of Munich, Germany. Supervisor: Dr. Esther Zanin

09-2012 to 09-2013: MSc Biomedical Sciences, University College London (UCL), England

08-2008 to 07-2012: B.Tech. Biotechnology, Amity University (Noida), India

RESEARCH EXPERIENCE

07-2014 to 12-2014: Researcher at Laboratory of Chromosome Biology, Max Planck Institute of Biochemistry, Munich, Germany

10-2013 to 12-2013: Honorary Research Assistant, Institute of Structural and Molecular Biology, UCL, London, UK.

03-2012 to 06-2012: Bachelor's Thesis at Haematopathology Lab, Rajiv Gandhi Cancer Institute and Research Center, New Delhi, India.

06-2011: Summer Intern, Blood Bank, Rajiv Gandhi Cancer Institute & Research Centre, India

05-2010 to 06-2010: Summer Intern, Division of Genetics, Maulana Azad Medical College and Lok Nayak Hospital, New Delhi, India.

06-2009 to 07-2009: Summer Intern, Genetic Stability Lab, National Bureau of Plant Genetic Resources, New Delhi, India.

PUBLICATIONS:

Mangal S, Stöter M, Andree C, Marc B, Zanin E. High content RNAi screen to discover and characterize novel regulators of cytokinesis. *Manuscript in preparation.*

Zielich J, **Mangal S**, Zanin E, Lambie EJ. (2018). Establishment of a CRISPR/Cas9-based strategy for inducible protein dimerization. *Micropublication biology* https://doi.org/10.17912/W2208R.

Mangal S, Zielich J, Lambie EJ, Zanin E. (2018). Rapamycin-induced protein dimerization as a tool for C. elegans research. *Micropublication biology* https://doi.org/10.17912/W2BH3H.

Mangal S, Sacher J, Kim T, Osório DS, Motegi F, Carvalho AX, Oegema K, Zanin E. (2018). TPXL-1 activates Aurora A to clear contractile ring components from the polar cortex during cytokinesis. *J. Cell Biol.* 217(3), 837–848.

Tsuchiya Y., Peak-Chew SY., Newell C., Miller-Aidoo S., **Mangal S.**, Zhyvoloup A., Bakovic J., Malanchuk O., Pereira GC., Kotiadis V., Szabadkai G., Duchen MR., Campbell M., Cuenca SR., Vidal-Puig A., James AM., Murphy MP., Filonenko V., Skehel M., Gout I. (2017). Protein CoAlation: a redox-regulated protein modification by coenzyme A in mammalian cells. *Biochem J.* 474(14), 2489-2508.

Rahman K., George S., **Mangal S.**, Mehta A. (2013). Simultaneous occurrence of chronic myeloid leukaemia and chronic lymphocytic leukemia- report of an unusual case. *Indian J Pathol Microbiol*. 56(4), 453-456.

TECHNICAL SKILLS:

a. High Content (large scale) RNAi screening with automated equipment.

b. Confocal Microscopy (Spinning Disk and Laser Scanning Microscopes from Leica, Nikon, Perkin Elmer, Yokogawa high throughput imaging system).

c. Model Organisms: Extensive experience in lab techniques used to work with mammalian cell lines, *C. elegans* worms & early embryos (crosses, single copy integration of transgene, microinjections) and Budding Yeast.

d. Common techniques in Molecular Biology and Biochemistry like Cloning (conventional method and Gibson), Western Blotting, IPs, Antibody and Antigen Purification.

e. Software: Fiji/ImageJ (including basic knowledge of writing Macros), automated data analysis software KNIME, plotting application GraphPad Prism, Affinity Designer (Adobe Illustrator alternative), Cell Profiler and other common programs used in a lab.

AWARDS & PRIZES:

a. Recipient of ASCB-EMBO travel award (2017) for attending ASCB-EMBO meeting in Philadelphia USA.
b. Best Student Prize in MSc Biomedical Sciences at UCL for the year 2012-2013.
c. Best Research Project Prize in MSc Biomedical Sciences at UCL for the year 2012-2013.
d. Gold Medal and DBT Biology Scholarship of INR 20,000 by the Government of India for scoring 100% in Biology in all India senior school certificate examination (2008).
e. Certificate of Merit for being among the top 0.1 per cent of successful candidates in Biology exam at All India senior school certificate examination (2008).
f. Certificate of Honour for being the school topper in Biology in the senior school certificate examination (2008).
g. Gold medal and Certificate of Merit for securing 1st rank in the school and 141st all India rank in the National Science Olympiad (2007).
h. Certificate of Honour for securing distinction in all 5 subjects in secondary school examination (2006).

CONFERENCES/WORKSHOPS:

07-2018: Workshop- Scientific Image Processing and Analysis
12-2017: Poster presentation at ASCB-EMBO Cell Biology Meeting, Philadelphia, USA.
06-2016: SLAS High-Content Screening Conference 2016, Dresden, Germany.
04-2016: Bio-Imaging Symposium, LMU, Munich
03-2016: International Meeting of the German Society for Cell Biology (DGZ), Munich.
07-2015: Cutting-Edge Technologies Symposium, LMU, Munich
06-2015: Workshop- Poster Design for scientific conferences
12-2014: Workshop- Scientific Writing
10-2014: Workshop- Time and Project Management
09-2014: Symposium: Career Opportunities in Research and Beyond
07-2014: Responsible Research Symposium, LMU, Munich
06-2012: Molecular Diagnostics: Challenges vis-à-vis Growth Potential organised by the Ministry of Science and Technology, Govt. of India.
12-2006: Poster Presentation on causes of Hepatitis at Hepatitis Day function held at G.B. Pant Hospital, New Delhi.